U.PORTO
FEUP FACULDADE DE ENGENHARIA
UNIVERSIDADE DO PORTO

Modelling and simulation of aerospace-grade non-crimp fabric composites

Rodrigo Duarte Carneiro

Thesis submitted to Universidade do Porto – Faculdade de Engenharia
in partial fulfillment of the requirements for the degree of
Master in Mechanical Engineering

Supervisor
Professor Albertino Arteiro

Mestrado em Engenharia Mecânica (MEM)
Departamento de Engenharia Mecânica (DEMec)
Faculdade de Engenharia (FEUP)
Universidade do Porto (UP)

© Porto, 2023

"Success is stumbling from failure to failure with no loss of enthusiasm."

Winston Churchill

Acknowledgements

Contemplating upon my five year academic journey at the Faculty of Engineering of the University of Porto nearing its end, I not merely find myself deeply grateful for the incredible opportunity I have been given, but additionally cherish the invaluable support and guidance I have received along the way.

Foremost, I wish to convey my deepest gratitude to my supervisor, Prof. Dr. Albertino Arteiro, whose expertise, wisdom, support and availability have been instrumental in the success of this thesis and my overall academic growth. I am profoundly grateful for the privilege of collaborating in this work, as well as the knowledge imparted throughout my degree, and hope to continue working in close proximity with such a distinguished academic.

I would like to express my profound gratitude to Prof. Dr. Carolina Furtado as well for generously providing the parametric `Python` python scripts employed in the material card identification process, which proved to be an instrumental resource in the completion of this work.

I am further indebted to all of my esteemed Professors, whose teachings I hold in the highest regard and intend to carry with me in all future endeavours. Moreover, I value the unwavering support of my colleagues, whom I am fortunate to count amongst my friends. Their constant encouragement and assistance drove me to pursue excellence, having played an integral part in shaping both my academic and personal life.

Lastly, I treasure the support, love, patience, belief and encouragement endowed on to me by my parents, Miguel and Odete, and my entire family. I wish to express a special note of gratitude to my elder sister, Rita, and to my girlfriend, Mariana, for their relentless support and guidance in both my academic and personal life.

Abstract

Within the aeronautical industry, due to their insurmountable in-plane mechanical properties, unidirectional prepreg laminates embody the standard composite materials. In spite of this, they represent a significant expense in the production of composite structures and are highly susceptible to impact damage. Thereby, as the paradigm within the sector shifts from maximising performance to more cost-conscious solutions, extensive research has been devoted to textile fabric reinforcements. In recent years, non-crimp fabric composites have emerged as an interesting solution. These materials are able to balance the dichotomy between high in-plane performance with improved impact resistance, reduced costs and ease of manufacturing. Nonetheless, their successful introduction hinges on structural substation campaigns, commonly reliant on testing and analysis. Testing alone is nevertheless extremely costly and time-consuming and, consequently, the development of accurate analytical and numerical models to aid this methodology is of the utmost importance.

In spite of the potential of non-crimp fabrics and the importance of numerical modelling, there is a clear knowledge gap in the available literature pertaining to the modelling and simulation of unidirectional non-crimp laminates. To this purpose, our work seeks to assess the validity of commonly used mesoscale modelling strategies for representative coupons, namely un-notched, open-hole. In addition, to achieve this, seeing as no material card has been reported for these composites, we further aim to ascertain the required computational parameters through the standard methodology, i.e., double-edge notched coupons. Lastly, we aim to conduct a preliminary assessment of an alternative modelling strategy for low velocity impact tests on thin laminates.

The numerical model herein adopted consists of a continuum damage model implemented within a finite element framework. In regard to the continuum mechanics methodology, intra- and interlaminar damage models are considered. The former, having been applied to every specimen, aligns itself with an extensively validated approach based on a phenomenological prediction of longitudinal, transverse and shear mechanisms. Concerning the latter, two strategies were used. For the un-notched, open-hole and double-edge notched coupons, an interlaminar cohesive zone model predicated upon a mode-dependent penalty stiffness was used, whereas for low velocity impact simulations, built-in Abaqus/Explicit cohesive surfaces were employed. Furthermore, although ply-by-ply discretization was contemplated across the finite element models, two modelling approaches were once more used. For the un-notched, open-hole and double-edge notched coupons, solid elements were considered, whereas for low velocity impact tests, conventional shell elements were selected.

The numerical results pertaining to the material card identification process show a remarkable correlation with the experimental ones. The predicted resistance values and slope of the size effect laws are within the standard 10% threshold commonly used in the aeronautical industry. The damage model responded accordingly to the changes made to the computational parameters

that govern the shape of the cohesive law. Furthermore, the damage onset and evolution were accurately predicted both in double-edge notched tension and compression, i.e., damage nucleated within the vicinity of the notch and extended across the width of the specimen up until catastrophic failure.

Concerning the validation tests, the numerical resistance obtained in plain tension is aligned with the experimental value, although discrepancies were noted in the damage evolution. Still, these differences agree with the alterations made to the delamination and in-plane shear response. On the other hand, in plain compression, both the strength value and damage history are precisely captured. In regard to the open-hole tests, a constant limitation was identified pertaining to the representation of size effects in both tension and compression, with this effect being more prevalent for the latter. Focusing on off-axis loading, although initially premature failure was detected for 30 and 60°, following alterations to the delamination and in-plane shear response, improvements in the damage evolution were evident. However, the values obtained in compression still fell outside the 10% threshold.

On the other hand, with respect to the low velocity impact simulations, poor results were nonetheless observed throughout the considered impact energies. Whilst for the smaller energy value tested, the maximum force and displacement are within the admissible threshold, augmenting the impact energy resulted in exponential growth in the errors identified. These results were explained by inadequate damage representations amidst the impact event. Thereby, the adopted standard modelling approach does not appear valid for extremely thin laminates, such as the one in study.

Ultimately, we were able to ascertain the material card parameters, and the results obtained support the validity of the adopted modelling methodology for the in-plane coupons. Notwithstanding, in light of the limitations identified, future research should focus on more comprehensively capturing hole size effects, compressive off-axis loading, and the out-of-plane response pertaining to low velocity impacts. Particularly, for the latter, alternative modelling strategies predicated upon solid elements could present great potential, and assessing the compression after impact response should also be taken into account.

Contents

Contents ix

List of Figures xiii

List of Tables xvii

List of Acronyms xix

I Introduction 1

1 Introduction 3
1.1 Background . . . 3
1.2 Thesis motivation . . . 5
1.3 Thesis objectives . . . 5
1.4 Thesis layout . . . 6

II State-of-art and literature review 9

2 Non-crimp fabric composites 11
2.1 Background & overview . . . 11
2.2 Manufacturing . . . 17
2.2.1 Preforming . . . 17
2.2.2 Liquid composite moulding processes . . . 19
2.2.2.1 Resin transfer moulding . . . 19
2.2.2.2 Vacuum-assisted resin transfer moulding . . . 20
2.2.2.3 Resin film infusion . . . 21
2.3 Mechanical performance . . . 22
2.3.1 In-plane properties . . . 22
2.3.2 Out-of-plane properties . . . 24

3 Numerical modelling of damage in composite materials 27
3.1 Introduction . . . 27
3.2 Damage mechanisms in composite materials . . . 29
3.3 Damage scale . . . 30
3.4 Cohesive zone models . . . 34
3.5 Continuum damage mechanics . . . 39
3.5.1 Continuum mechanics approach . . . 39

3.5.2 Idealisation of damage modes in composite materials . . . 42
3.5.3 CDM models applied to composite materials . . . 43
3.6 Numerical modelling of NCF composites . . . 49

III Numerical model 51

4 Composite damage model 53
4.1 Introduction . . . 53
4.2 Intralaminar damage model . . . 54
4.2.1 Constitutive law . . . 54
4.2.2 Damage laws . . . 56
4.2.3 Effect of through-thickness stresses . . . 59
4.2.4 In-situ strengths . . . 61
4.3 Interlaminar damage model . . . 66
4.3.1 Plain strength, open-hole & double edge-notched tests . . . 66
4.3.1.1 Constitutive model . . . 66
4.3.1.2 Mode dependent penalty stiffness . . . 67
4.3.1.3 Damage evolution law . . . 68
4.3.2 Low velocity impact tests . . . 68

5 Finite element model 73
5.1 Introduction . . . 73
5.2 Plain strength, open-hole and double-edge notched models . . . 74
5.3 Low velocity impact models . . . 77

IV Results & discussion 79

6 Material card identification 81
6.1 Double-edge notched tension . . . 81
6.1.1 Size effect law . . . 81
6.1.2 Damage onset & evolution history . . . 86
6.2 Double-edge notched compression . . . 88
6.2.1 Size effect law . . . 88
6.2.2 Damage onset & evolution history . . . 94
6.3 Material card . . . 96

7 Plain strength & open-hole tests 99
7.1 Plain tension . . . 99
7.1.1 Numerical prediction . . . 99
7.1.2 Damage onset & evolution history . . . 100
7.2 Plain compression . . . 105
7.2.1 Numerical prediction . . . 105
7.2.2 Damage onset & evolution history . . . 106
7.3 Open-hole tension . . . 108
7.3.1 Size effects . . . 108
7.3.1.1 Numerical prediction . . . 108
7.3.1.2 Damage onset & evolution history . . . 111
7.3.2 Off-axis loading . . . 114

7.3.2.1 Numerical prediction . . . 114
7.3.2.2 Damage onset & evolution history . . . 115
7.4 Open-hole compression . . . 119
7.4.1 Size effects . . . 119
7.4.1.1 Numerical prediction . . . 119
7.4.1.2 Damage onset & evolution history . . . 121
7.4.2 Off-axis loading . . . 124
7.4.2.1 Numerical prediction . . . 124
7.4.2.2 Damage onset & evolution history . . . 125

8 Low velocity impact tests **131**
8.1 Penalty stiffness sensitivity study . . . 131
8.2 Impact energy: 6.7J . . . 132
8.3 Impact energy: 13.4J . . . 134
8.4 Impact energy: 20.1J . . . 135

V Conclusions & future work **139**

9 Conclusions and future work **141**
9.1 Conclusions . . . 141
9.2 Future work . . . 145

References **147**

List of Figures

2.1 Timeline of composite material usage in aircrafts [10]. 12
2.2 Usage of composite materials on the Airbus A380 [15]. 12
2.3 Schematic of the inter-phase around a fibre, a UDPT (lamina), and laminae stacked in different orientations to form a laminate [16]. 13
2.4 Out-of-plane crimp of the fibre tows in a woven fabric [18]. 14
2.5 Non-crimp fabric schematic [15]. 16
2.6 Overview of different non-crimp fabric preforms [15]. 16
2.7 Non-course-wise multi-axial warp-knitting machine [15]. 18
2.8 Factors influencing the quality of an NCF laminate [15]. 18
2.9 Schematic of RTM [31]. 20
2.10 Schematic of VARTM [31]. 21
2.11 Schematic of RFI [10]. 21

3.1 Building-block approach test pyramid [57]. 28
3.2 Damage mechanisms in laminated composites [65]. 29
3.3 Schematic representation of the various scales involved in damage modelling [66]. 30
3.4 Top: FPZ of a quasi-brittle material. Middle: CZM concept. Bottom: stress distribution along the crack path for a constant cohesive law under pure mode I loading [80]. 35
3.5 Quasi-brittle bar of length L and cross-section A with a cohesive interface [65]. 36
3.6 Tri-linear cohesive law obtained by superposing two bi-linear laws [65]. 37
3.7 Mixed-mode cohesive law [65]. 37
3.8 Typical shear stress–strain response exhibiting multiple nonlinearities [65]. 40
3.9 Snap-back at constitutive level [65]. 41
3.10 3D kinking model [111]. 43
3.11 *In-situ* strength determined from the propagation of a slit crack in a ply [65]. . . . 43
3.12 FE modelling strategy based on the use of conventional shell elements, wherein h_p refers to the ply thickness [123]. 46

4.1 Composite intralaminar damage modes [52]. 54
4.2 Uniaxial response in: **a)** longitudinal tension, **b)** longitudinal compression, **c)** transverse tension/compression, **d)** in-plane shear (adapted from [8]). 59
4.3 Fibre kinking kinematics and effect of through-thickness stresses predicted by a 3D invariant-based failure criterion [8]. 60
4.4 Effect of hydrostatic pressure on the longitudinal in-plane shear response [8]. . . . 60
4.5 Effect of transverse compressive stresses on the longitudinal in-plane shear response [8]. 61
4.6 Ply *in-situ* strengths: transverse tensile strength, Y_T; transverse compressive strength, Y_C; transverse shear strength, S_T; in-plane longitudinal shear strength, S_L, [57]. . 61
4.7 Thick embedded ply [8]. 63

4.8 Thin embedded ply [8]. 64
4.9 Thin outer ply [8]. 65
4.10 $\sigma_{22} - \sigma_{12}$ failure envelope [8]. 65
4.11 System without (left) and with (right) cohesive elements [80, 124]. 70

5.1 Finite element models for plain tension and compression [8]. 76
5.2 Finite element models for open-hole tension and compression [8]. 76
5.3 Finite element models for double-edge notched tension and compression (adapted from Furtado et al. [8]). 76
5.4 Numerical model and BCs considered for the LVI simulations [80, 124]. 77
5.5 Modelling strategy pertaining to conventional shell elements linked to surface elements [80, 124]. 78

6.1 Tensile bi-linear cohesive laws: iterations 1-3. 83
6.2 DENT numerical size effect laws: **a)** iteration 1, **b)** iteration 2 **c)** iteration 3. 84
6.3 In-plane shear response fitting. 84
6.4 Revised size effect law for iteration 3 of the DENT models. 85
6.5 Numerical results for iteration 4 of the DENT models. 86
6.6 Damage onset and evolution history for the w = 10 mm DENT test. 88
6.7 *Post-mortem* for the w = 10 mm DENT test. 88
6.8 Compressive plateau cohesive laws: iterations 1-4. 90
6.9 Originally proposed longitudinal compression cohesive law [8]. 91
6.10 DENC numerical size effect laws: **a)** iteration 1, **b)** iteration 2 **c)** iteration 3, **d)** iteration 4. 92
6.11 Numerical results for iteration 5 of the DENC models. 93
6.12 Revised size effect law for iteration 5 of the DENC models. 94
6.13 Damage onset and evolution history for the w = 15 mm DENC test. 96
6.14 *Post-mortem* for the w = 15 mm DENC test. 96

7.1 Normalised numerical prediction obtained for the PT test. 100
7.2 PT load-displacement curve. 100
7.3 Comparison between the material card and original bi-linear cohesive laws and corresponding PT load-displacement curve. 101
7.4 Damage evolution for the material card cohesive law. 103
7.5 Damage evolution for the original cohesive law. 104
7.6 *Post-mortem* for the PT test. 105
7.7 Normalised numerical prediction obtained for the PC test. 106
7.8 Damage onset and evolution history for the PC test. 108
7.9 *Post-mortem* for the PC test. 108
7.10 Normalised numerical predictions obtained for the OHT tests pertaining to the hole size effects. 110
7.11 Original normalised numerical predictions obtained for the OHT tests pertaining to the hole size effects. 111
7.12 Damage onset and evolution history for the OHT test. 113
7.13 *Post-mortem* for the $d = 6$ mm OHT test. 114
7.14 OHT off-axis loading evolution. 115
7.15 Comparison between the OHT 30° off-axis load-displacement curves obtained for the original and material card parameters. 116
7.16 OHT 30° off-axis loading damage evolution for the original parameters. 118
7.17 OHT 30° off-axis loading damage evolution for the material card parameters. . . . 119

7.18 *Post-mortem* for the OHT 30° off-axis loading test: material card parameters. 119
7.19 OHC hole size effects: normalised plots. 121
7.20 Damage onset and evolution history for the $d = 6$ mm OHC test. 123
7.21 *Post-mortem* for the $d = 6$ mm OHC test. 124
7.22 OHC off-axis loading evolution. 125
7.23 Comparison between the OHC 60° off-axis load-displacement curves obtained for the original and material card parameters. 126
7.24 OHC 60° off-axis loading damage evolution for the original parameters. 127
7.25 OHC 60° off-axis loading damage evolution for the material card parameters. . . . 128
7.26 *Post-mortem* for the OHC 60° off-axis loading test: material card parameters. 129

8.1 LVI penalty stiffness sensitivity study. 132
8.2 Numerical LVI results: 6.7J impact energy. 133
8.3 Numerical LVI results: 13.4J impact energy. 135
8.4 Numerical LVI results: 20.1J impact energy. 136

List of Tables

5.1 Geometry of the plain strength models. 74
5.2 Geometries of the open-hole models. 74
5.3 Geometries of the double-edge notched models. 74
5.4 Lay-ups for the open-hole models. 75
5.5 Lay-ups for the double-edge notched models. 75
5.6 Maximum element sizes for each damage mechanism. 75

6.1 Numerical predictions for iteration 1 of the DENT models. 82
6.2 Numerical predictions for iteration 2 of the DENT models. 82
6.3 Numerical predictions for iteration 3 of the DENT models. 82
6.4 Revised numerical predictions for iteration 3 of the DENT models. 85
6.5 Numerical predictions for iteration 4 of the DENT models. 86
6.6 Numerical predictions for iteration 1 of the DENC models. 89
6.7 Numerical predictions for iteration 2 of the DENC models. 90
6.8 Numerical predictions for iteration 3 of the DENC models. 90
6.9 Numerical predictions for iteration 4 of the DENC models. 90
6.10 Numerical predictions for iteration 5 of the DENC models. 93
6.11 Revised numerical predictions for iteration 5 of the DENC models. 94
6.12 Ply elastic properties. 97
6.13 Ply strength properties. 97
6.14 Ply fracture toughness properties. 97
6.15 Ply geometrical parameters. 97
6.16 Ply friction parameters. 97
6.17 Ply *in-situ* properties. 98
6.18 Interlaminar penalty stiffness. 98
6.19 Interlaminar strength properties. 98
6.20 Interlaminar fracture toughness properties. 98
6.21 Interlaminar friction parameters. 98

7.1 Numerical prediction obtained for the PT test. 99
7.2 Numerical prediction obtained for the PC test. 105
7.3 Numerical predictions obtained for the OHT tests pertaining to the hole size effects. 109
7.4 Original numerical predictions obtained for the OHT tests pertaining to the hole size effects. 110
7.5 Original numerical predictions obtained for the OHT off-axis loading tests. 114
7.6 Material card numerical predictions obtained for the OHT off-axis loading tests. . 114
7.7 Numerical predictions for the OHC tests pertaining to the hole size effects. 120
7.8 Original numerical predictions obtained for the OHC off-axis loading tests. 124
7.9 Material card numerical predictions obtained for the OHC off-axis loading tests. . 124

List of Tables

8.1 Numerical predictions obtained for the LVI test: 6.7J impact energy. 132
8.2 Numerical predictions obtained for the LVI test: 13.4J impact energy. 134
8.3 Numerical predictions obtained for the LVI test: 20.1J impact energy. 135

List of Acronyms

- ACM ⇒ Advanced composite material
- BC ⇒ Boundary condition
- BVID ⇒ Barely visible impact damage
- CAEI ⇒ Compression after edge impact
- CAI ⇒ Compression after impact
- CDM ⇒ Continuum damage mechanics
- CFRP ⇒ Carbon fibre reinforced polymer
- COD ⇒ Crack opening displacement
- CZM ⇒ Cohesive zone model
- DDM ⇒ Discrete damage mechanics
- ERR ⇒ Energy release rate
- FE ⇒ Finite element
- FEA ⇒ Finite element analysis
- FPF ⇒ First-ply failure
- FPZ ⇒ Fracture process zone
- FRP ⇒ Fibre reinforced plastic
- ILSS ⇒ Interlaminar shear strength
- LCM ⇒ Liquid composite moulding
- LEFM ⇒ Linear elastic fracture mechanics
- LPF ⇒ Last-ply failure
- LVI ⇒ Low velocity impact
- MMB ⇒ Mixed-mode bending
- NCF ⇒ Non-crimp fabric
- OEM ⇒ Original equipment manufacturer
- OHT ⇒ Open-hole tension
- PC ⇒ Plain compression

List of Acronyms

- PT ⇒ Plain tension
- RFI ⇒ Resin film infusion
- ROM ⇒ Rule of mixtures
- RTM ⇒ Resin transfer moulding
- RVE ⇒ Representative volume element
- STDV ⇒ Standard deviation
- STF ⇒ Spread tow fabric
- STI ⇒ Stable time increment
- UDPT ⇒ Unidirectional fibre *prepreg* tape
- VARTM ⇒ Vacuum-assisted resin transfer moulding
- WCM ⇒ Wet-compressing moulding
- WWFE ⇒ Worldwide failure exercise
- X-FEM ⇒ Extended finite element method

Part I

Introduction

Chapter 1

Introduction

In the context of this introductory chapter, our foremost goal lies within furnishing the background pertaining to the present thesis, thereby highlighting its fundamental objectives, motivations, and structure. To this end, we commence with a brief discussion on the increasing significance of composite materials in the design and development of novel components, with a specific focus on their profound impact within the aeronautical sector. Subsequently, the motivation and objectives intrinsic to this thesis are presented. Lastly, we provide the structure governing its presentation.

1.1 Background

Composite materials are highly regarded as the materials of the future, poised to revolutionise a multitude of industries. These materials promise significant benefits, including enhanced safety, ease of use for a plethora of distinct objects and machines, and the potential for diverse applications across several fields of engineering, whilst additionally making strides towards the improvement of the paramount environmental concerns through cost savings [1].

As the term itself advocates, a *composite material* represents a departure from conventional macroscopic homogeneous materials (i.e., metals) and, at its core, arises from the macroscopic combination of two or more dissimilar materials, resulting in a third one boasting superior properties when compared to its individual constituents acting independently [2, 3]. Conventionally, such materials involve the incorporation of strong fibres (continuous or noncontinuous) or particles as reinforcement within a weaker matrix, responsible for uniformly distributing the reinforcements, sheltering them from environmental factors and transferring loads across the structure. Whilst several options are available for the design of composite materials, the term has nowadays become rather unanimous with the so-called *fibre reinforced plastics*, FRP, wherein endless fibres are embedded within a polymer matrix. Improvements over the years have, in addition, brought forth the use of advanced FRP, often fabricated as laminates, composed of multiple layers or plies oriented in specific directions that represent the standard within the aeronautical sector [2–4].

In spite of their seemingly recent emergence, composites have, in fact, existed for millennia. Nature itself offers a myriad of instances pertaining to such fibrous systems denoted in the structural composition of plants, animals, and the human body, e.g., trees with their leaves, birds with their wings, and fish with their fins all exemplify composite configurations. Moreover, the human body, on a fundamental level, embodies a complex composite structure comprised of the musculoskeletal

framework of bones, muscles, and tendons [5]. With respect to man-made composite materials, their historical trail further dates back to antiquity, with evidence found in ancient Egypt where stems retrieved from the papyrus plant were ingeniously laid up in two perpendicular layers to produce the first known man-made composite material, i.e., the papyrus paper. In contemporary mechanics terminology, the aforementioned fabric would be denoted as an asymmetric, cross-ply laminate [3, 5]. In subsequent epochs, these constituents were looked upon for optimising the performance of conventional weapons, e.g., with the Mongols devising the first composite bows, harnessing a combination of wood, bone, and animal tissues, bonded with animal glue, compressed and wrapped with birch bark. This innovation yielded bows of smaller proportions, exceptional manageability, and unrivalled power and precision. Meanwhile, Japanese samurai artisans crafted damask swords wherein a soft iron core was enveloped by a hardened steel exterior (forged in a U shape), imbuing the blades with a remarkable balance of toughness and superficial hardness [2, 3].

Notwithstanding, humanity lacked a compelling reason for devoting substantial amounts of time and ingenuity to enhance the manufacture and applicability of composite materials or fully explore their potential for centuries, i.e., a journey spanning from the early applications of fibrous composites by the Egyptians, to the introduction of advanced composites in the latter half of the 20^{th} century, a period covering roughly 6000 years, during which the advancements made in the past decades have far outpaced those of the preceding millennia [1, 5]. The seismic industrial shift towards advanced FRP commenced with the emergence of glass fibres in the 1930s, which found widespread application within the rapidly growing aeronautic and naval industries, particularly during World War II. The dawn of the space age in the 1950s further propelled their development, with the first patent for carbon fibre production being filled in the 1960s, followed by the introduction of boron and aramid fibres in the late 1960s and early 1970s, respectively [1, 3, 5].

In light of such advancements, the aerospace industry has, in recent decades, witnessed significant growth in composite technology, whose rapidly expanding applications have instilled great optimism for the future of these advanced materials. Deriving from several programs initiated by the US Air Force aimed at facilitating the introduction of composite structures in aircrafts, the F-111 horizontal stabiliser is seen as the pioneering flight-worthy composite component. Its production was subsequently followed by the introduction of composite parts (e.g., stabilisers and rudders) in several military aircrafts, such as the F-14, F-15, and F-16. It was in the early 1980s that composite materials were first extended into civil aviation (e.g., in the Boeing 767, Antonov 124, and Airbus A310-300) and, owing to a myriad of rapidly growing advancements, nowadays find themselves extensively employed in nearly all aircrafts [3, 6]. The increasing usage of advanced FRP has further seen a shift from non-load bearing applications to primary load-bearing structural applications [2]. A key driver behind this trend lies within their unrivalled stiffness, strength, fatigue, ballistic, thermal, corrosion, and electromagnetic properties that are always associated with weight reduction [2, 4, 7]. Their lightweight nature promotes/improves a far more sustainable lifestyle, a paramount factor that reinforces the adoption of composite materials as the significance of life cycle assessments is being exceedingly more recognised [3]. Their versatility is further remarkable and bolstered by the multitude of processing techniques available. These materials provide designers and engineers with remarkable flexibility in terms of both form and function, allowing for intricate geometries and compound curves to be seamlessly incorporated, ultimately maximising structural integrity and overall performance. In addition, advanced FRP facilitate the development of integrated designs, whereby parts or components can be manufactured in *"one shot"*, eliminating the need for laborious joining and fitting processes [2–4].

1.2 Thesis motivation

A thorough understanding of the mechanical performance of a given material system is a matter of the utmost importance within the aeronautical industry when designing novel composite structures in order to predict/evaluate how that component will respond to the various stimuli that it is probable to encounter during its lifetime. As a result, when new composite systems arise, resulting from the development of new manufacturing technologies, understanding their potential benefits and drawbacks is naturally paramount, in order to ensure their successful, i.e., safe introduction onto the market [3].

To this purpose, when a novel composite material emerges, structural substation campaigns are normally triggered according to a *building-block approach*, wherein numerous small, less expensive specimens are tested under simple loading scenarios to generate design allowables prior to evaluating its response for more complex structural details. However, this solution is, in its essence, extremely costly and time-consuming. As a result, the development of accurate analytical and numerical models to aid, or potentially supplant, this methodology is of the utmost importance [3, 8, 9].

One new technology of interest that has been witness to extensive research over the last few years is **non-crimp fabrics**, NCFs. The main advantage of these materials lies within significantly reducing manufacturing costs by allowing for liquid composite moulding methods and eliminating shelf-life and storage concerns. In addition, concerning their mechanical performance, although small reductions in the in-plane properties have been recorded, improvements in regard to damage tolerance and out-of-plane response over standard laminates have been observed. Thereby, NCFs are able to bridge the gap between two common types of reinforcement, namely, unidirectional *prepreg* tapes (aeronautic standard) and woven fabrics. Furthermore, in spite of several NCFs being available, if unidirectional preforms are to be used and stacked to form a laminate, a direct solution to unidirectional *prepreg* tapes arises, a factor that could be paramount for their introduction within the aeronautical industry.

Notwithstanding, despite their potential benefits, there is a clear knowledge gap in the modelling and simulation of aerospace-grade NCFs. Whilst several approaches based on mesoscale representative volume elements and macro-mechanics have been proposed, remarkably sparse work has been done on assessing the applicability of commonly used mesoscale ply-by-ply discretization techniques in predicting the resistance of representative unidirectional NCF laminates. In addition, no material card has been defined for these materials. As a result, these factors all together comprise the motivation inherent to the present thesis.

1.3 Thesis objectives

Owing to the aforesaid, this thesis aims to assist the technological development of modelling and simulation strategies of unidirectional non-crimp fabric laminates. Focus is placed on ascertaining critical material parameters by means of numerical methodologies and ascertaining the ability of a state-of-the-art damage model in predicting the failure load of such materials under various loading conditions. Thereby, our objectives comprise:

- an accurate description of the current state-of-the-art pertaining to both the non-crimp fabric technology and the numerical modelling of damage in composite laminates. Concerning the former, we aim to review key factors, including the rationality underlying their emergence as a feasible and interesting solution, as well as their manufacturing and mechanical

performance. On the other hand, we aim to comprehensively describe the significance of numerical modelling of damage in composite laminates within the aeronautical sector. Thus, we aim to analyse the damage mechanisms that must be captured, the importance of the selected damage scale, the standard approaches employed in mesoscale modelling and, lastly, the strategies commonly used in the numerical modelling of non-crimp fabric composites.

- a thorough analysis of the intricacies pertaining to the composite damage model herein employed, including intra- and interlaminar damage representation.
- the development of finite element models pertaining to representative coupons and loading conditions, i.e., double-edge notched, plain strength and open-hole (for both tension and compression), and low velocity impact specimens.
- ascertaining the material card, i.e., by means of standard inverse identification techniques resorting to double-edge notched coupons, determining the computational parameters governing the shape of the longitudinal tensile and compressive, and in-plane shear cohesive laws.
- assessing the validity of the proposed approach for the material system in study with respect to the composite damage model, modelling strategy and ascertained computational parameters by means of representative coupons, namely un-notched and open-hole specimens (in tension and compression).
- conducting a preliminary assessment of the validity of an alternative modelling strategy for the prediction of the low velocity impact response.

1.4 Thesis layout

The structure of the present thesis was delineated keeping in mind the aforementioned objectives. To this purpose, five fundamental parts were constructed, thus creating a coherent progression of the presented ideas and discussions.

In Part II, the state-of-art and literature review[1] is provided in two distinct chapters:

- In chapter 2, the intricacies of non-crimp fabric composites are explored. A brief background on their emergence as a feasible solution for the aerospace industry is initially given for a more thorough understanding of the underlying rationality behind the extensive research on this reinforcement. Subsequently, we thoroughly delve into their manufacturing, ranging from preforming to liquid composite moulding. Lastly, based on a plethora of distinct works reported in literature, their mechanical performance is analysed not merely keeping in mind comparisons to the industrial standards when it comes to composite materials, but also the effects of their inherent governing parameters on the mechanical performance.
- In chapter 3, a comprehensive overview of the prevalent numerical modelling techniques applied in the prediction of damage onset and evolution in composite materials is provided. A brief background on its significance within the aeronautical sector is presented, which is followed by a description of the damage mechanisms in such materials. The implications pertaining to the damage scale in the representation or simulation of damage within composite materials are subsequently discussed. Thereafter, noteworthy aspects pertaining to the basic theories behind cohesive zone models are explored. Lastly, given its pivotal role within this

[1] The present part and corresponding chapter, i.e., Part I and chapter 1, are herein not included given their solely introductory nature.

work, we meticulously review the continuum damage mechanics approach, its application to composite materials and how it correlates to NCF composites.

In Part III, the numerical model herein employed is analysed in two distinct chapters:

- In chapter 4, the composite damage model is comprehensively reviewed. We commence with a succinct introduction of the background and specifics inherent to the model. Subsequently, we delve into the intralaminar continuum damage mechanics framework, including the constitutive and damage laws, the effect of through-thickness stresses and the *in-situ* strengths. Lastly, we thoroughly analyse the distinct interlaminar cohesive zone models used. For plain strength, open-hole and double edge-notched specimens, the interlaminar damage model is explored with respect to the constitutive model, mode-dependent penalty stiffness and damage evolution law. Concerning the low velocity impact models, considerations regarding the penalty stiffness and stable time increment parameters are presented.
- In chapter 5, the finite element framework employed in the analysis of a carbon-fibre reinforced non-crimp fabric laminate is examined. Initially, a brief introduction into the intricacies of the finite element analyses conducted is given, including the importance of parametric scripting and considerations regarding mesoscale models. Subsequently, the models of the plain strength, open-hole and double-edge notched tests (both in tension and compression) are described, given the similarity between the adopted methodologies. Lastly, we meticulously scrutinise the approach used for the low velocity impact simulations.

In Part IV, the results obtained are presented and discussed in three distinct chapters[2]:

- In chapter 6, the results pertaining to the material card identification process are explored. Initially, the methodology used is described for the double-edge notched tension tests, prior to delving into the solution obtained for the double-edge notched compression coupons. Subsequently, the ascertained material card is showcased.
- In chapter 7, the numerical results obtained for the validation specimens are analysed. We commence by delving into the plain tension and plain compression coupons, wherein both the estimated strength values and the damage evolution history are reported. Lastly, the numerical results for open-hole tension and compression tests are compared against those expected with respect to the hole size effects and off-axis loading.
- In chapter 8, the results attained with respect to the low velocity impact tests are presented. To begin with, the penalty stiffness sensitivity study conducted is reported, prior to analysing the results pertaining to each of the assessed impact energies. To conclude the chapter, remarks concerning the limitations observed are discussed, including potential modelling strategies to mitigate them.

Finally, in Part V, comprised of a single chapter, i.e., chapter 9, the main conclusions regarding the work carried out during this thesis are presented. The main aspects to retain from the state-of-the-art, the numerical methodology adopted and the corresponding results are noted. Lastly, given that the present thesis is just a first step in the understanding of modelling and simulation strategies of unidirectional non-crimp fabric laminates, future work that needs to be carried out in light of the derived conclusions is explored.

[2]It should be noted that focus is given to the numerical results. As such, the experimental results are solely used in validating resistance values and no curves are shown.

Part II

State-of-art and literature review

Chapter 2

Non-crimp fabric composites

In this chapter, we seek to comprehensively describe and explore the intricacies of non-crimp fabric composites. We commence by briefly providing background on their emergence as a feasible and interesting solution for material systems within the aerospace industry. Subsequently, we present detailed insights into their definition and traits, followed by a discussion of their manufacturing methods. Lastly, we meticulously review their mechanical performance.

2.1 Background & overview

The history of advanced composite materials, ACMs, comprising fibrous reinforcements bonded within a polymeric resin, can be traced back to the 1930s when the glass fibre-reinforced plastic industry first began to emerge [4]. Subsequent advancements in ACMs eventually led to their introduction within military aircrafts in the 1960s prior to their extension into civil aircraft applications in the early 1980s [3, 4, 10]. Over the decades that followed, as a result of constant innovations and improvements, as well as a relentless pursuit for weight reduction by Original Equipment Manufacturers, OEMs, [2, 4, 11] these materials gained substantial prominence within the aeronautical sector. Indeed, having been witness to a notable surge in their usage (Figure 2.1), ACMs, particularly carbon-fibre reinforced epoxy laminates [4, 11], nowadays shape the landscape of aerospace materials [12], comprising the primary choice for the design of load bearing structures [13], i.e., primary (whose integrity is vital for safety) and secondary structural components [2], such as wings, fuselage sections and tail surfaces. The Airbus A350 XWB and the Boeing 787 Dreamliner entail prime examples of the traction gained by advanced composites, seeing as, within these modern aicrafts, ACMs constitute around 50% of their weight [2, 4, 10, 12]. The shift from conventional isotropic engineering materials to composite ones is attributed to their mechanical properties [4] that, albeit extremely different relative to their traditional metallic counterparts [3], are especially appealing to OEMs aiming at performance and saving [2], i.e.:

- Superior specific properties, namely strength-to-weight and stiffness-to-weight ratios [14]. As a result, significant weight reductions (10 to 30% [2]) are achieved without compromising flight safety [1], which in turn entails in fuel savings (and decrease in carbon dioxide emissions [11]), increased payload, and/or extended range, ultimately improving the overall performance [2–4].

[1] Seeing as ACMs boast exceptional static strength and stiffness values [2, 4, 7, 11].

- Excellent fatigue resistance, enhancing the lifetime of a given component. As a consequence, considerable savings in their long-term cost are achieved [2–4].
- Outstanding corrosion resistance, requiring fewer inspections and thereby aiding in minimising maintenance costs [2, 3].

Moreover, in contrast to metallic structures, composite components allow for fewer rivets and joints, resulting in enhanced aircraft reliability and reduced susceptibility to fatigue cracks induced by stress concentrations associated with such features [4]. Overall, their exceptional properties ultimately make ACMs ideal for structures wherein weight is a critical design variable, providing high strength and stiffness, high-volume production and the ability to manufacture complex shapes in smaller amounts of time, whilst additionally reducing the number of parts and, consequently, assembly times [2–4, 11, 14].

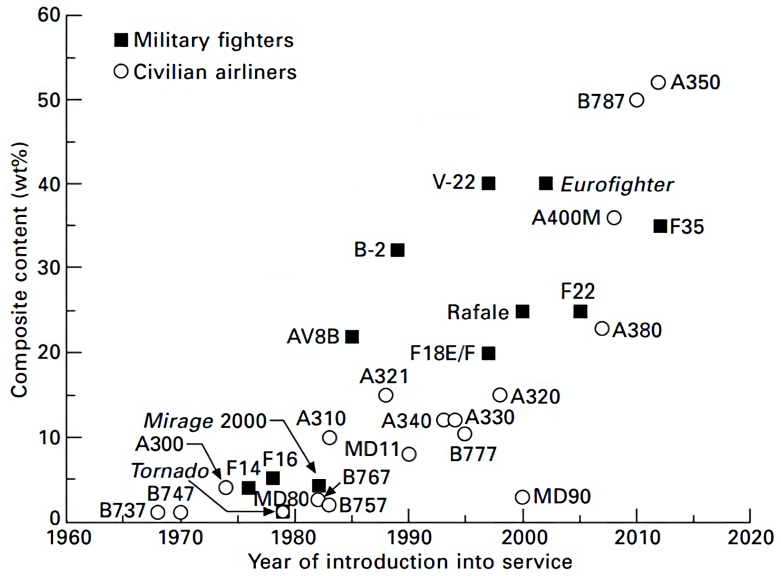


Figure 2.1: Timeline of composite material usage in aircrafts [10].

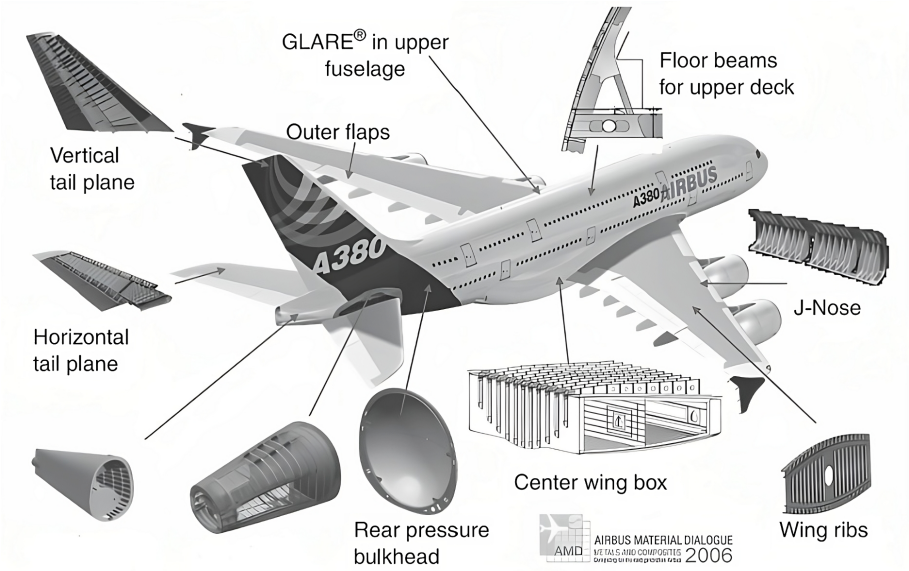


Figure 2.2: Usage of composite materials on the Airbus A380 [15].

Within the aeronautical sector, the production of carbon fibre-reinforced polymer, CFRP, laminates [2] traditionally relies on the use of unidirectional fibre *prepreg* tapes, UDPTs, that are arranged in a specific lay-up (refer to Figure 2.3) in a mould and subsequently cured (heat and pressure are applied) in an autoclave to ensure excellent compaction and consolidation [4, 7, 10, 16]. These tapes comprise a two-part thin sheet (around 0.125 mm thick [16, 17]) of unidirectional and uniformly distributed carbon fibre tows impregnated into a partially cured resin (semisolid state, i.e., rigid enough to preclude its flow as a liquid, yet sufficiently soft to provide pliability and flexibility) [10, 18, 19]. Having been successful and widespread within the aerospace industry [11], OEMs lean on this process for the construction of CFRP laminates [10]. This is attributed to the high-quality of the finished products, boasting exceptional in-plane elastic properties (strength and stiffness), in virtue of the accurate control and ability to achieve high fibre volume content, leading to a remarkable volume fraction of well aligned fibres [4, 7, 10].

Notwithstanding its merits, the above-stated process is nonetheless extremely expensive, representing a significant expense in the production of CFRP structures [11]. Prepreg materials, besides boasting short storage lives and low deposition rates [20], mandate storage at low temperatures (about –20 °C [10]) to arrest cross-linking processes within the epoxy resin and, thus, prevent further curing that would occur at ambient temperatures, contributing to an augmented cost [4, 7, 10, 11]. Moreover, the laminar nature of the final products and their orthotropic properties stemming from the in-plane orientation of the fibres entail poor interlaminar fracture toughness, thereby rendering them susceptible to impact damage, i.e., delamination that severely impairs their post-impact mechanical performance [18, 20]. In addition, such damage often manifests itself internally within the material, hindering visual detection and, thus, mandating intricate and expensive inspection methods [4].

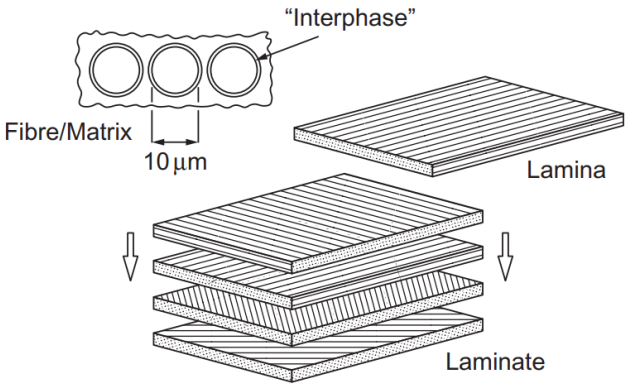


Figure 2.3: Schematic of the inter-phase around a fibre, a UDPT (lamina), and laminae stacked in different orientations to form a laminate [16].

Given the expensive nature of prepreg laminates, as the aerospace industry seeks to provide more structural parts for larger transport aircrafts composed by CFRP, the focus and requirements for aeronautical materials have thereby shifted from prioritising maximum performance (and consequently weight reduction) at any expense to material systems that are more cost-conscious [11, 20, 21]. Within the realm of potential alternatives, textile fabric reinforcements have, in recent years, arisen as a promising solution for primary structural components [22]. In spite of, for an extensive period of time, having been primarily confined to low profile, low-cost applications, many of the available textile reinforcements (woven, braided, knitted or stitched) have developed into mature technologies capable of competing with the conventional prepreg method [16]. As a result,

[2]Henceforth, the term CFRP is employed as a replacement for ACM, owing to its widespread employment.

there has been a growing interest in the use of dry fabric preforms that offer versatile and complex geometries, coupled with manufacturing based on resin infiltration and consolidation techniques, i.e, liquid composite moulding, LCM, methods [7, 11]. Such approach, as opposed to prepreg laminates, encompasses the infiltration of the dry preform with a fluent resin. Amidst the impregnation, the fibres are held in place by the textile structure of the preform [7]. Consequently, LCM processes present remarkable potential for reduced manufacturing costs (by avoiding the expensive autoclave hardening [11]), enhanced processability and deposition rates, and uncomplicated handling and storage, which render them extremely appealing to OEMs [7, 10, 11, 16, 21, 22]. In addition, textile reinforcements have been found to enhance out-of-plane properties and provide higher impact resistance, which aligns with the growing demands within the aerospace industry [22].

Woven reinforcements, in virtue of their status as the most widely used preforms [10, 16], comprised the initial focus of textile-based research initiatives. Such fabrics comprise fibres organised along two mutually perpendicular directions, i.e., the warp (weaving direction) and weft directions. The fibres are woven according to a predetermined pattern, with each warp tow alternately crossing over and under each intersecting weft tow, with the weave of the fabric (plain, twill or satin) being determined by the manner in which the warp and weft yarns intersect [2, 10]. Woven architectures boast a plethora of attractive properties for OEMs in comparison with non-woven counterparts, i.e., great stability in both the warp and weft directions, the highest yarn packing density in relation to fabric thickness, excellent drapeability (enabling the design of complex shapes with no gaps), reduced manufacturing costs (with superior deposition rates[3] and ease of handling) [16]. Moreover, woven laminates have been found to significantly enhance impact damage resistance, with increases of over 30% in compressive strength after a 7J impact event in comparison to equivalent UD prepreg materials having been recorded [23]. Notwithstanding, these advantages come at the expense of mechanical performance [16]. Weaving inevitably yields periodic out-of-plane waviness of the fibre tows, entailing in a high degree of crimp, a vital parameter in the field of textile reinforcements [10, 24]. Crimp may be defined as the percentage difference between the total and projected length of a fibre when contained within a textile. As a consequence of this attribute, only a small portion of fibres within a bundle will be perfectly oriented, whilst the majority of the tow boasts nonzero out-of-plane orientation (refer to Figure 2.4) [24]. Given that maximum structural performance is attained with absolutely straight fibres (the case of UDPTs) [10], the high degree of waviness within a woven composite significantly impairs its in-plane mechanical properties (i.e., stiffness and strength) as compared to those of equivalent UDPT composites (e.g., 23% reduction in tensile strength has been recorded [23]) [16, 24].



Figure 2.4: Out-of-plane crimp of the fibre tows in a woven fabric [18].

[3]Woven reinforcements comprise bi-axial fabrics, thereby the lay-up of a single woven ply effectively corresponds to two non-woven plies [16].

Ultimately, the challenge to achieve a reinforcement capable of reconciling the dichotomy between high in-plane performance of unidirectional straight fibres (characteristic of UDPTs) with appealing attributes such as improved impact resistance, reduced manufacturing costs, enhanced drapeability and ease of handling (offered by woven preforms) gave way to a distinct advanced textile reinforcement category, the non-crimp fabrics, NCFs [25]. Lomov et al. [15] define non-crimp fabrics as "drawn parallel oriented layers of reinforcing threads or tows, which are positioned by means of an additional fixation material", i.e., NCFs entail one to several laminae composed by unidirectional fibre tows stacked in varying orientations with respect to the warp direction and held in place via through-thickness knitting or stitching with a secondary fixation yarn (refer to Figure 2.5) [10, 11, 14, 20, 25]. In recent years, a plethora of NCF systems encompassing distinct manufacturing processes and bonding solutions have been developed and proposed as reliable textile reinforcements [22, 25], as depicted in Figure 2.6.

In contrast to woven systems, NCF based laminates lack gross crimp, which is attributed to the fact that the fibre tows are not forced to interlace with one another to produce a weave, instead being arranged in a more optimal configuration [10, 11, 14]. Notwithstanding, they inevitably possess a degree of in-plane waviness as a consequence of the knitting process [11, 24]. Amidst the stitching process, small local defects (termed openings and/or channels) are introduced within each layer when the machine penetrates them and the stitching yarn pushes the fibres aside, slightly distorting them (and thereby inducing some in-plane crimp) [24]. Such areas further give rise to concerns regarding the development of resin-rich zones within the composite itself that have been found to be associated with damage initiation and propagation during loading [24, 26]. Additionally, the needle piercing process may cause damage to the fibres and entail in performance drops of the material [24].

In spite of the potential drawbacks, channels and openings in NCFs have, nonetheless, been observed to be beneficial as well. Having higher degrees of stitching and, consequently, more openings and/or channels have been found to significantly enhance the permeability of the preforms [24, 26–28]. Moreover, open spaces within the textile facilitate the shear process, thereby allowing for greater fabric deformations, ultimately contributing to the remarkable drapeability of most NCFs that enable the manufacturing of complex shapes with ease [16, 24]. In addition, despite the small degree of crimp that is inevitably introduced and the associated reduction in the performance of NCF based laminates, their in-plane elastic and strength properties remain comparable to those of unidirectional reinforcements and are aligned with the requirements set by the aeronautical industry [11, 22]. Equally important, the presence of through-thickness reinforcement in the form of knitting or stitching has been observed to not compromise/significantly enhance the impact resistance of these materials [11, 20–22]. As a result, when combined with the potential for low-cost fabrication routes, these characteristics align with the growing demands set by OEMs, with NCFs having already been introduced over prepreg laminates in some applications. For instance, CFRP laminates produced with multi-axial warp-knitting[4] NCFs are employed in the production of the Airbus A380 rear pressure bulkhead [15, 16]. Furthermore, by relying on unidirectional NCFs[5], the orientation of each ply may be individually adjusted in contrast to bi-, tri- and multi-axial NCFs or woven fabrics [29]. In spite of coming at the expense of production times, the adoption of such manufacturing process represents a direct alternative for UDPTs that could be swiftly integrated within the sector to reap the numerous benefits offered by NCFs.

[4]Herein, it should be noted that warp-knitting is the most widespread fixation method.
[5]The laminate taken as reference for this work is comprised of unidirectional NCF layers, hence their importance.

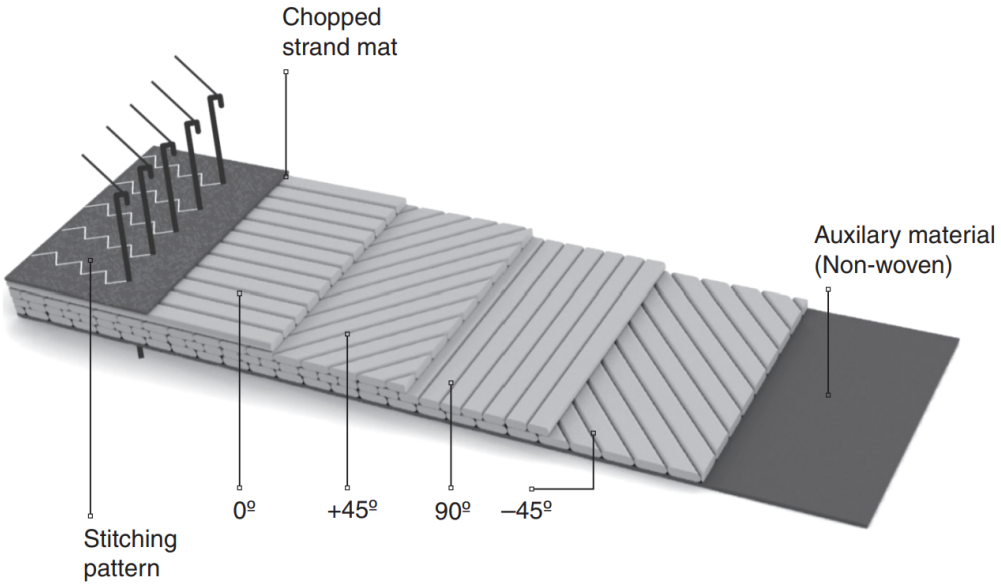


Figure 2.5: Non-crimp fabric schematic [15].

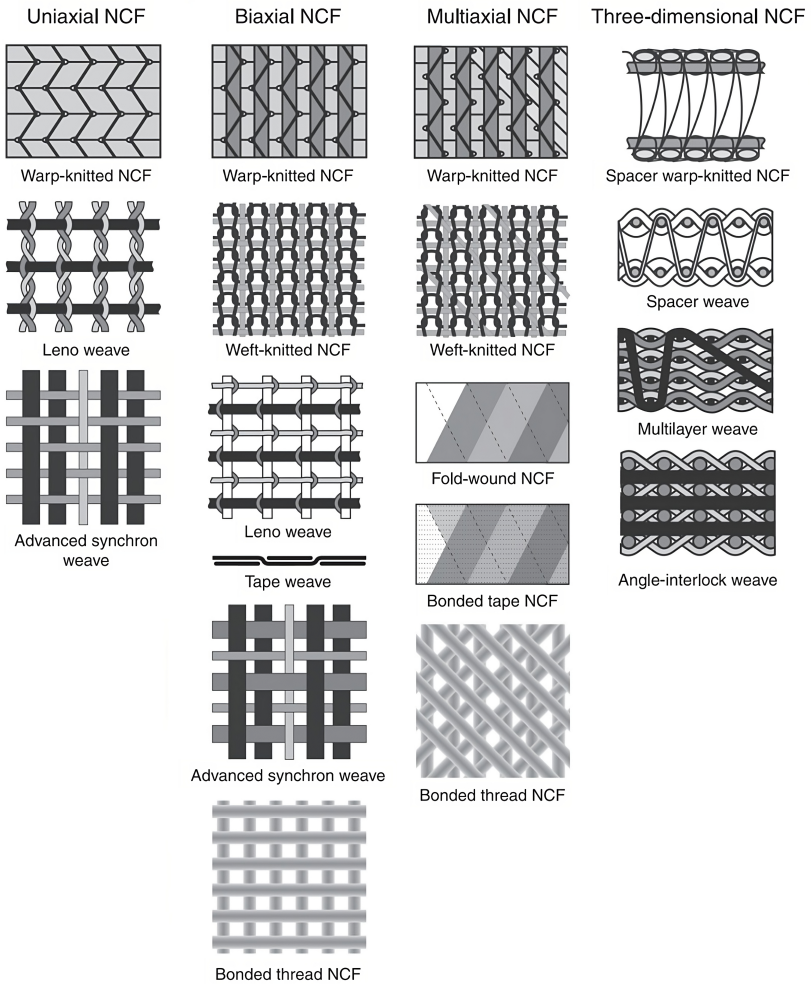


Figure 2.6: Overview of different non-crimp fabric preforms [15].

2.2 Manufacturing

In light of the above stated, a pivotal advantage of NCF based laminates lies within the prospect of leveraging low-cost manufacturing processes based on liquid composite moulding, LCM, methods [11, 22, 25]. LCM processes entail resin infiltration and consolidation techniques [7] wherein the empty interstitial spaces between the fibres within a dry lay-up or preform are infused with a fluent resin [30–32]. As a result, this technology can be broken down into two primary phases, namely preforming and moulding[6] (comprising impregnation, consolidation, and curing) that do not occur simultaneously [18, 25, 30]. The segmentation of the manufacturing process further aids in reducing its complexity and, as a result, enhancing the quality of the final product [25].

2.2.1 Preforming

The preforming phase consists in the manufacturing of NCF preforms aligned with the desired shape by forcing the flat textile reinforcement into a specified geometry [25, 30]. Dry preforms further offer an array of benefits, namely the elimination of cold storage areas, shelf-life constraints and labour-intensive hand lay-up processes, as well as the minimisation of wastage (expensive nesting and cutting-out procedures are not required). When compared to prepregs, cost savings ranging from 25% to 40% [33] have been reported with such materials, which, given that up to 50% of an autoclave component cost may be allocated the raw material, is particularly noteworthy [31].

Amongst the various methods shown in Figure 2.6 for the construction of NCF preforms, warp-knitting has emerged as the most widespread technique, whereby knitting loops are formed to bind the reinforcing layers together in the production direction [15, 25]. Warp-knitted NCFs impart considerable flexibility with respect to both fibre layer setup and orientation, with the technology being highly productive in comparison to alternative methods. Moreover, warp-knitting may be categorised into course-wise and non-course-wise fixation based on the means by which the weft yarn is inserted during the knitting process. Whereas for the former, a single knitting loop binds every warp and weft fibre bundle, the stitch length for the latter is independent of the position of the thread [15]. Overall, in spite of potentially inducing fibre damage or movement[7], non-course-wise weft insertion is commonly used for uni-, bi- and multi-axial NCFs (the use of course-wise techniques has not yet gained widespread acceptance) employing a similar machine technology between them (depicted in Figure 2.7) [15].

In the context of this automated manufacturing process, whose roots stem from the textile industry [18], the fibre layers are initially created by cutting the tows to the desired length, followed by their placement side by side in a predetermined orientation. Subsequently, the laminae are stitched with a secondary fixation yarn. This is achieved by means of a row of compound parallel needles (assembled within a continuous needle bar) that move in unison amidst the loop formation. As the stack of layers advances within the conveyor system, the needle heads penetrate the fabric forming consecutive stitching yarn loops [15, 18].

[6] Albeit preforming encompasses a necessary step within LCM methods, henceforth LCM will be used when referring to the moulding phase for simplicity.

[7] To mitigate this, pillar threads (0° direction) are fixed together in the warp-knitting module by at least two knitting heads [15].

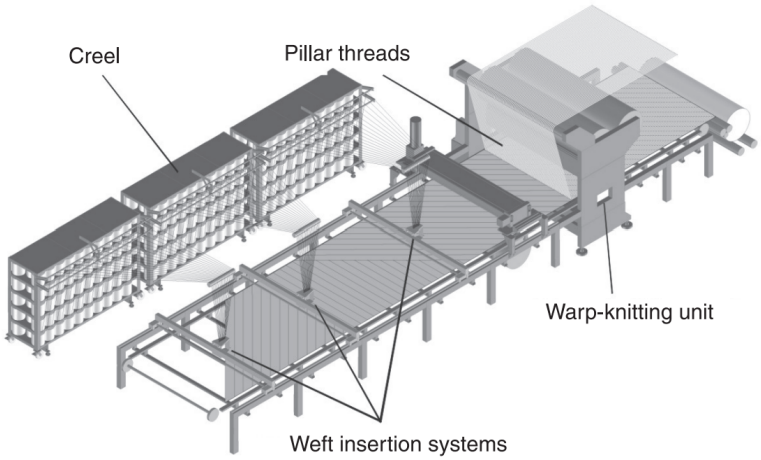


Figure 2.7: Non-course-wise multi-axial warp-knitting machine [15].

Furthermore, it is crucial to note the importance of the preforming process in determining the quality of the resulting NCF laminate. Aside from the textile product itself and the moulding method used, the quality of the final component is "decisively defined by the quality of the preform" [15] (refer to Figure 2.8) that is, e.g., subjected to various parameters related to the fibre and knitting process (including material, type, density, and tension). For instance, different stitching patterns (e.g., tricot, tricot-chain and chain stitching) may, as a consequence, be considered, based on the required properties and configurations for the NCF preform. Thereby, apart from the manufacturing process, it is worth emphasising the difference between fixation/positioning and structural stitches, as each can significantly impact the performance of the resulting fabric [15, 18]. Pertaining to the former, stitch type and length greatly influence the drapeability (measure of the ability of a textile to conform to complex shapes without losing its integrity) and stability (degree of resistance against relative motion of fibres) [18]. The primary function of these stitches is to hold the textile structure in place amidst resin infusion and are not designed to withstand structural loads [21]. Thermoplastics (e.g., nylon) are commonly used in non-structural NCF preforms [14]. With respect to the latter, the potential applications of NCF based laminates may impose considerable structural demands on the seams [15]. The fixation yarn is thereby not merely responsible for ensuring integrity [of the fabric], but is also aimed at creating a 3D reinforcement [18] to enhance the structural response. As a result, fibre yarns such as aramid or glass, in virtue of their superior strength and high performance are typically employed in structural NCF preforms [14, 15, 18].

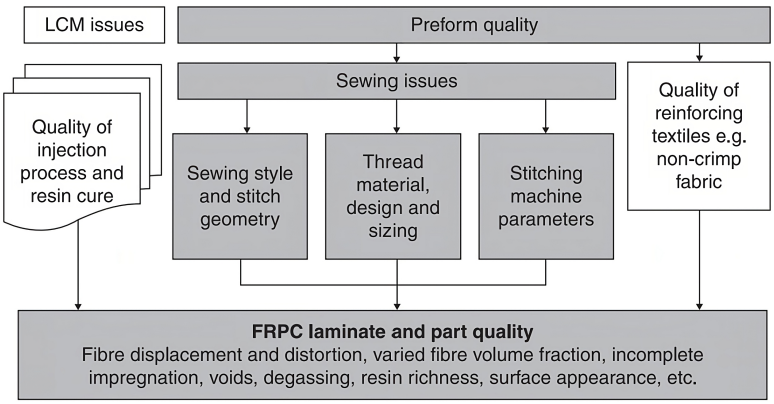


Figure 2.8: Factors influencing the quality of an NCF laminate [15].

2.2.2 Liquid composite moulding processes

Subsequent to preforming, NCF laminates are manufactured by means of moulding processes. Often termed as "out-of-autoclave processes" [31], LCM technologies are inherently cost-effective by eliminating the need for expensive autoclave curing methods, whilst still providing complex composite products of remarkable quality and performance [11, 16, 30–32]. The first step of LCM technology involves impregnation, wherein the preform is placed within the cavity of a closed mould and a fluent resin (driven by a predetermined injection pressure [30]) is infused into it. By virtue of relying on a liquid polymeric material, the viscosity of a given matrix comprises a vital parameter within the landscape of LCM. Common thermoplastic resins employed in aircraft structural components (e.g., PEEK) boast exceedingly high viscosity (10^2 to 10^6 Pa.s [32]), thereby requiring high injection pressures (raising the cost) and potentially inducing movement of the preform resulting in resin-rich areas and diminishing the mechanical performance of the constituent [32]. Ergo, thermoset polymers, in light of their low viscosity (0.1 to 0.5 Pa.s [32]), are typically used. Impregnation is followed by curing of the resin that may commence during or after the former. Once this process is complete, the composite part may be de-moulded (final step in the manufacturing procedure) [30, 32].

The choice of an adequate LCM technique is of the utmost importance in the production of NCF based laminates. The moulding process employed can profoundly affect their degree of crimp and distortion at the mesoscale [18]. Amongst the available methods, three primary types are distinguished, namely resin transfer moulding, RTM, vacuum-assisted resin transfer moulding, VARTM, and resin film infusion, RFI, [30] and comprehensively described in the following sections.

2.2.2.1 Resin transfer moulding

Resin transfer moulding, RTM, (depicted in Figure 2.9) entails a LCM method that, in light of recent technological advancements, has emerged as a reliable manufacturing solution for composite structural components of moderate size (under 3 m [10]) within the aerospace industry, being applied in, e.g., the production of rudders for the Boeing 757 and 777 [31, 34]. Within this process, the dry preforms are placed, stacked (aligned with the predetermined lay-up) and draped within a closed, clamped and matching[8] mould whose cavity corresponds to the shape of the final product [31, 32, 34, 35]. A liquid resin (commonly thermoset to facilitate the flow through the open spaces of the fabric [10, 31, 32]) is then injected into the tool by means of one or more inlets under a positive pressure (in the order of 700 kPa [35]) to guarantee optimal infusion and saturation. Once resin overflows from the vent ports, injection is halted, vent ports are closed and the curing process commences via heating of the mould [31, 32]. Upon hardening, the mould is opened and the component removed for finishing [10, 31, 32, 34].

RTM offers a multitude of advantages pertaining to both the quality of the final component and the cost of the process [31]. With respect to the former, mechanical performance akin to prepreg laminates is achievable in virtue of accurate control of the fibre volume fraction (typically 55 to 70% [10, 31, 32]). In addition, components procured by means of RTM boast great surface finish, diminished part variability and commendable dimensional tolerances. Concerning the latter, the necessity for an autoclave is circumvented by incorporating heat transfer into the mould die and the use of economical dry, bulk materials (devoid of special handling requirements and with extended shelf life) promote cost savings. Further benefits include near-net moulded components (minimising finishing process and scrap/wastage), minimal training costs and low health risks [for operators] [30, 31, 35].

[8] The mould encompasses two separate halves [30].

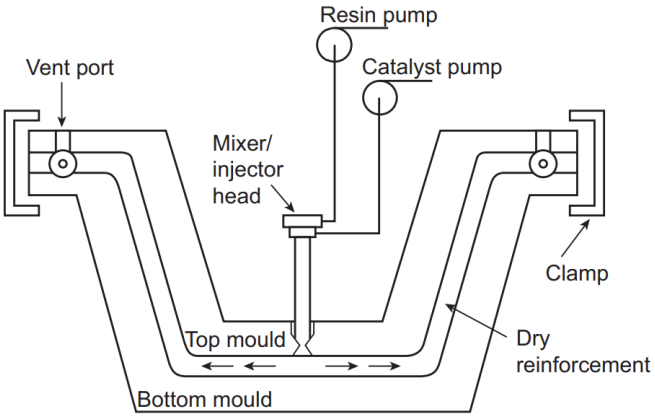


Figure 2.9: Schematic of RTM [31].

Notwithstanding, RTM entails certain drawbacks, namely difficulties in implementing unidirectional layups (potentially compromising structural performance), substantial initial tooling expenditures [34] and limited flexibility in modifying them to accommodate design changes. It is further imperative to ensure adequate rigidity within the mould to counteract deflections that may introduce thickness variations in the laminate. Such necessity commonly entails in increased thermal mass, augmenting cycle times for the curing process [31]. Moreover, minimising the occurrence of voids encompasses one of the most pressing challenges within RTM technology [10]. As a result, stringent control of process parameters during resin injection is mandatory to attain high quality products (e.g., 0 to 2% void content is possible with RTM) [31, 34].

2.2.2.2 Vacuum-assisted resin transfer moulding

Vacuum-assisted resin transfer moulding, VARTM, (depicted in Figure 2.10) comprises a closed-mould process capable of merging the benefits inherent to RTM (i.e., quality, repeatability and handling) with the flexibility intrinsic to open-mould hand lay-up, being widely used in the production of large CFRP structures within the aerospace industry [32]. In the context of this technique, a dry preform is placed and draped into an open rigid tool and subsequently closed and sealed in a flexible vacuum bag. The pivotal difference between VARTM and the traditional RTM lies in the use of a vacuum-pump system to both evacuate air from the cavity (placing it in a state of low pressure and compressing the preform) and draw in the liquid resin into the fabric (by means of the pressure differential) [10, 31, 32, 34]. Similarly to RTM, the polymeric material flows and penetrates the empty spaces between the fibre tows until the mould is filled, at which point the infusion process is halted and the curing process is commenced via heating [10]. Upon hardening, the laminate is de-moulded [32].

VARTM has, in recent years, garnered considerable prominence attributable to enabling the production of cost-effective, large and complex structures of exceptional quality [31, 32]. The use of a single rigid mould promotes cost savings over RTM [34], whilst additionally facilitating its material selection and design [of the mould] that may be effortlessly modified for distinct geometries [32]. Additionally, VARTM requires less expensive consumables, i.e., bagging materials and distribution media [31]. Nevertheless, they may not be reusable, thereby requiring new components for each individual process. The likelihood of air leakage (potentially inducing dry spots and incomplete infusion) is not merely elevated, but also contingent upon the skill and experience of the operator, as well as the quality of the aforementioned consumables. The injection pressure is further limited to the differential between the environment and vacuum, which is considerably

lower than that exerted during RTM methods and may hinder the compaction of air voids within the final component [32]. Moreover, the degree of fabric compaction is highly dependent upon the pressure differential (that is itself small) across the membrane (given its flexibility), ultimately restricting the fibre volume fraction of the laminate to within 40 to 50% [31, 32].

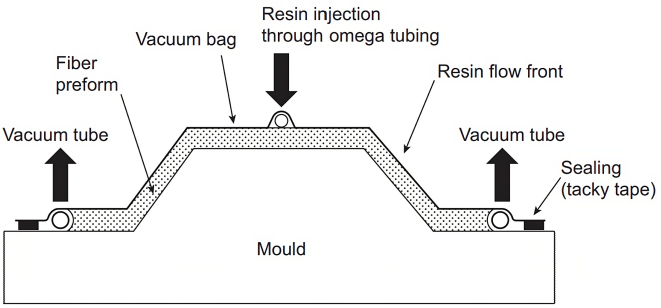


Figure 2.10: Schematic of VARTM [31].

2.2.2.3 Resin film infusion

Resin film infusion, RFI, (depicted in Figure 2.11), similarly to VARTM, entails a robust vacuum-based solution for the production of large CFRP structures for the aeronautical sector (e.g., stiffened panels or rib-type structures) [10]. In fact, it is employed in the manufacturing of the aforementioned rear pressure bulk head of the Airbus A380 [30, 34]. The process, once more, involves an open mould wherein the layers of dry fabric are placed and draped in the shape of the final product [10, 31]. However, in contrast to the previously discussed techniques whereby a liquid resin is injected into the mould, when it comes to RFI procedures, solid thin sheets of B-staged cured polymeric material (condition akin to that of prepregs [10]) are positioned at the top, bottom and/or between the preform layers. The assembly is subsequently sealed within a vacuum bag prior to air extraction with a vacuum pump. The tool is then heated and pressed, causing the resin film(s) to melt. Within this stage, accurate control of the temperature is pivotal to lower the viscosity of the resin and guarantee adequate flow into the fabric under the applied pressure. Upon completion of the infusion process, the temperature and pressure parameters are further raised to start the curing process. Once the laminate has hardened, it can be de-moulded [10, 30, 31]. RFI not merely offers a cost-effective method of producing damage tolerant textile composites [18] with less expensive mould technology (relative to RTM), but also circumvents the drawbacks inherent to VARTM with respect to the fibre volume fraction, being able to attain high fractions of up to 65% [30, 31].

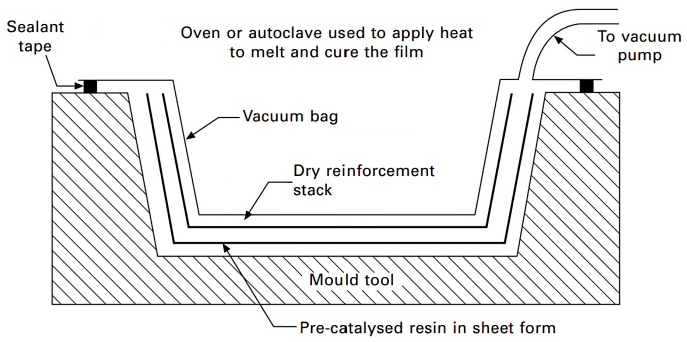


Figure 2.11: Schematic of RFI [10].

2.3 Mechanical performance

2.3.1 In-plane properties

As previously mentioned, broadly speaking, the in-plane properties of NCF based composites tend to be marginally inferior when compared with equivalent UDPT laminates owing to the inevitable degree of crimp introduced by the presence of the stitching yarns [11, 14, 18]. In fact, in an early series of experimental tests conducted by Dexter & Hasko [36] including plain strength and open hole (both in tension and compression) configurations, a slight drop in the in-plane mechanical performance of multi-axial carbon/epoxy NCFs was recorded in comparison with UDPT laminates. Specifically, reductions in the average tensile strength ranging from 10 to 30% were observed, whereas in compression the decrease was about 25%. Both were attributed to potential fibre misalignment or damage (induced amidst the stitching process) and gaps (i.e., resin-rich zones) between tows. Notwithstanding, when observing the open hole strengths of the knitted fabric laminates, the authors found a comparable performance between the NCF and UDPT laminates.

Similar conclusions were derived by Bibo et al. [17] for quasi-isotropic glass fibre reinforced NCF laminates, whose average tensile and compressive moduli were found to be respectively reduced by 20 and 30%. However, as highlighted by the authors, a difference of 6% in the fibre volume fraction was additionally noted. Accordingly, this posed a challenge in such comparisons. To mitigate it, these properties were charted as a function of volume fraction and the reduction observed was less pronounced. Naturally, corresponding strength drops were found and attributed to the smaller fibre volume fraction and the subtle changes in laminate architecture, inevitably inducing some degree of crimping and local stress concentrations. Moreover, tri-axial carbon/epoxy fabrics were evaluated and, whilst no significant differences were observed in the tensile and compressive moduli, a notable drop from 950 to 620 MPa in the average tensile strength was recorded in virtue of the fracture mode. Whilst in UDPT laminates, delamination can occur during deformation, decoupling the shearing $\pm 45°$ plies from the $0°$ plies, the same is not feasible for the stitched layers in virtue of the adopted tri-axial configuration[9], thereby promoting premature failure in the $0°$ plies. Still, the presence of through-thickness stitches was found to improve the tensile strength when the loading orientation was altered to $90°$. In this scenario, stitching acts to hold the transverse fibre bundles together, increasing the maximum possible deformation. Furthermore, within the same study, both the glass- and carbon-fibre reinforced laminates were compared with equivalent 8-harness satin-weave composites, wherein the differences in performance were abundantly clear, with NCF based composites boasting remarkably higher in-plane properties.

Arteiro et al. [37] also conducted tensile and compressive tests in both un-notched and notched thin-ply bi-axial NCF specimens pertaining to two distinct lay-ups. It was shown that laminates pertaining to smaller relative ply orientations and without ply *blocking* entailed a brittle failure mode dominated by fibre breakage. A linear behaviour until final failure was particularly evident for such configurations, indicating that unrecoverable damage mechanisms (e.g., transverse cracking and delamination) are mitigated. This leads to stronger un-notched laminates and delays first-ply-failure until just before complete failure, although it is stated it may increase notch sensitivity. Conversely, laminates with larger relative ply orientations and ply *blocking* displayed a pull-out failure mode. Despite resulting in lower in-plane strengths, this failure mode reduced stress concentrations near notches and open-holes due to stress redistribution, yielding laminates

[9]This concern is thereby not expected for, e.g., bi-axial or unidirectional NCFs, hence the negligible differences mentioned.

with lower notch sensitivity. Furthermore, as opposed to what is commonly observed in UDPT materials, no delamination or transverse cracking were detected on the straight free-edges. Regarding size effects and notch sensitivity, no significant differences were found between NCF and UDPT laminates under tension. Notwithstanding, the same was not identified under compressive loads, with the thin-ply laminates exhibiting a slightly inferior notched response. Instead, a superior bearing performance compared to typical aerospace CFRP laminates was recorded and attributed to their ability to delay damage mechanisms such as delamination, fibre kinking, matrix cracking, and through-the-thickness shear cracking.

With respect to the aforementioned inferior notch behaviour, in a more recent study by Arteiro et al. [38], the authors further argue that a strategy based on the combination of standard grade 0° plies and thin transverse and off-axis plies is capable of improving the structural response of NCF laminates. It was demonstrated that, in spite of the tensile and compressive un-notched strengths of laminates with dispersed and blocked 0° plies being essentially insensitive to the thickness [of that ply], materials with blocked plies exhibited an enhanced response across a wide range of coupon sizes pertaining to centre-notched configurations, owing to higher stress relaxations in the vicinity of the notch tip, yielding larger longitudinal split cracks in such plies. As expected by the authors, this ultimately blunted the notch and reduced local stress concentrations. The bearing response in bolted joints further displayed improvements, which were attributed to the increased stability of the thicker blocked plies in the region confined by the bolt/washer assembly, effectively delaying the onset and propagation of localised compressive damage.

Building upon the previous point, Furtado et al. [39] conducted an experimental study on the effect of: ply thickness; ply-level hybridisation; and type of ply architecture on the damage mechanisms that dominate failure and strength of multi-directional laminates manufactured with carbon fibre UDPTs, NCFs and spread-tow fabrics, STFs. Concerning ply thickness, it was observed that, particularly for laminates manufactured from UDPTs and NCFs, the overall performance of the material improved as the ply thickness decreased (except for notched configurations, wherein a more brittle behaviour was observed) owing to the suppression of premature damage in regions where stress concentrations exist. Selective ply-hybridisation, on the other hand, yielded mixed results. When combining intermediate-grade 0° plies with thin off-axis plies, no discernible effects were recorded. Nonetheless, for high-grade 0° plies, a noticeable improvement in strength was found, although it was accompanied by a heightened sensitivity to loading direction in the presence of stress concentrations. Moreover, when compared with equivalently graded UDPT laminates, both spread-tow, non-crimp and textile fabrics exhibited no exceptional vulnerability to early failure, regardless of the presence or absence of geometric discontinuities.

Additionally, extensive research has also been dedicated to investigating various other aspects of non-crimp reinforcements [11]. For instance, Hogg et al. [40] sought out to assess the mechanical properties of bi- and quadri-axial NCFs depending on the fabric weight and it was determined that, as the aerial weight increased, laminate properties conversely decreased. On the other hand, Beier et al. [41] demonstrated that, whereas stiffness properties remain largely unaffected, the tensile and compressive strengths of carbon/epoxy NCF laminates manufactured by VARTM is significantly dependent on the stitching parameters as a result of pronounced localised fibre waviness. This was further identified in a later study conducted by Vallons et al. [42], wherein slightly different stitching patterns yielded considerable effects on the properties of quasi-UD glass fibre NCFs. An asymmetrical stitching pattern developed by the authors was compared with industrial standards and was found to have a considerable impact on the void content and on the thickness of the laminates. Owing to the presence of an additional stitching line for the industrial standard, the attained laminates were 3% smaller which, given that both fabrics boasted the same areal density,

resulted in a higher fibre volume fraction. Accordingly, the measured tensile strength was 7.7% higher, a difference that persisted even after normalising the results to account for the same fibre volume fraction. This suggests that the influence of the stitching pattern on the behaviour of the composites extends beyond merely affecting this parameter. Lastly, the degree of waviness naturally encompasses another factor of paramount importance in the in-plane performance of NCF laminates, with reductions from 750 to 400 MPa recorded by Wilhelmsson et al. [43] for specimens with low-out-of-plane waviness ($\theta_{max} \approx 4.5°$) and high out-of-plane waviness ($\theta_{max} \approx 8°$).

2.3.2 Out-of-plane properties

With respect to the out-of-plane properties, given the criticality of delamination as a failure mechanism in composite laminates, it is crucial to comprehensively analyse parameters such as the Interlaminar Shear Strength, ILSS, and Mode I Fracture Toughness, which are known to largely govern the delamination response of CFRP materials [18]. When compared with their traditional prepreg counterparts, whilst some authors state that non-crimp composites exhibit superior interlaminar fracture toughness due to the presence of through-thickness stitches [14], results reported in literature are moderately contradictory [18]. In fact, significant improvements have been recorded by both Bibo et al. [17] and Dransfield et al. [44] for carbon-fibre reinforced NCFs of ∼22% in the ILSS and of up to 15 times in the Mode I Fracture Toughness respectively. However, in the same study by Bibo et al. [17], a reduction of ∼27% in the ILSS of glass-fibre reinforced laminates was also noted. Focusing on the experimental campaign by Bibo et al. [17], the authors attribute the decrease pertaining to the ILSS of glass-fibre laminates to either inherent features in the fabric yielding voids, defects at the blanket boundaries, or to the resin itself (let us not forget that the ILSS is a resin-dominated property). On the other hand, the results observed for the tri-axial carbon-fibre NCFs were deemed as "surprising" [17], with the authors speculating about possible deterioration in the properties of the resin in the UDPTs before processing. Such assumptions are marginally reinforced in a study conducted by Godbehere et al. [45], wherein a reduction of approximately 20% of the ILSS of carbon fibre/epoxy NCF composites compared with equivalent UDPT composites was found. Nonetheless, interestingly, in a more recent work by Bhudolia et al. [46], the presence of fixation polyester stitches yielded a 26.5% higher critical energy release rate during Mode I Fracture Toughness, with the stitch-stitch interaction within a bi-angle ply playing a significant role in reducing the delamination extent. Moreover, in juxtaposition to common aerospace-grade woven composites, Beier et al. [41] noted that the ILSS of NCF materials is 17% lower. The substantial difference is attributed to damaged areas located around the individual stitches. Notwithstanding, reductions are to be expected given the nature of the woven reinforcement, boasting a certain degree of fibres aligned with the thickness direction, ultimately leading to an enhanced ability by the material to absorb out-of-plane stresses [41]. In summary, while the findings manifest significant contradictions, there is nevertheless a universal consensus that the interlaminar NCF properties align with the stringent requisites of the aerospace industry.

Furthermore, there have naturally been strategies proposed to enhance the interlaminar properties of such materials as well. For instance, Quan et al. [47] proved that increases of 273 and 206% in respectively the Mode I and Mode II fracture energies of carbon/epoxy NCF laminates are feasible by inter-laying hybrid meltable/non-meltable thermoplastic veils. Similar conclusions were drawn by García-Rodríguez et al. [48], wherein interleaving heavy micro-fibre veils enhanced the mode-I initiation and propagation interlaminar fracture toughness by respectively 101 and 43%. Nonetheless, such optimisation came at the expense of in-plane properties, with reductions of up

to 9% in the average compressive strength having been found.

Beyond the interlaminar properties, understanding the behaviour of such materials under impact further embodies a critical factor in their application within the aeronautical industry [14]. In the aforementioned experimental campaign conducted by Dexter & Hasko [36], carbon-fibre reinforced NCF laminates were shown to possess enhanced damage tolerance over their traditional UDPT counterparts. This was particularly noticeable in the superior compression after impact, CAI, strengths attained (improvements ranged from 45 to 80%).

Bibo et al. [20] were also amongst the foremost authors to investigate the CAI response of carbon/epoxy NCFs compared to UDPTs. It was found that, in spite of the same fracture mechanisms (i.e., shear/transverse and delamination fractures) being present, the intricate nature of the cracking pattern in the NCF was directly influenced by the more complex reinforcement architecture. As opposed to the expected mode II driven planar cracks (observed in UDPT), delamination fracture was often diverted around tows and the presence of a through-the-thickness stitching yarn seemed to limit the amount of damage by decreasing the "cone" angle compared to UDPT laminates. Nonetheless, despite the distinct cracking patterns and damages observed, the CAI strength showed negligible differences between the NCF and UDPT when considered as a function of the delamination damage content. Still, the authors point out that, given the weaker undamaged compressive strength inherent to NCFs, the data suggests that the textile laminates performed better than their unidirectional counterparts, suggesting a superior resistance to damage propagation under such scenarios.

Furthermore, in a more recent study by Sasikumar et al. [21], the impact and CAI response of NCFs was juxtaposed with that of equivalent woven fabrics for two distinct ply thicknesses (i.e., thin and intermediate ply grades for both fabrics). Experimental results revealed that the latter undoubtedly boasted a superior impact damage resistance, namely in the 50% less dissipated energy, and reduced dent depth and projected damage area over the NCFs. Notwithstanding, NCFs actually exhibited on average 20% higher CAI strengths over the woven fabrics, i.e., superior damage tolerance. With respect to ply thickness, it was observed that intermediate-grade plies not merely displayed improved damage resistance (50% less dissipated energy), but also boasted enhanced CAI strengths (20% higher) over their thin-ply NCF counterparts. Such results agree with previous findings by García-Rodríguez et al. [48] within a study aimed at evaluating the effect of ply thickness on the low-velocity impact, LVI, resistance, tolerance and damage sequence. It was shown that, although both ply grades exhibit a common qualitative trend in the progression of damage mechanisms, thin-ply laminates were able to postpone the initiation and decrease the spread of matrix cracks and delaminations. However, the suppression of energy dissipation (by 25 and 55% for impacts at 10 and 14J) ultimately promoted premature fibre fracture, consequently reducing the load-carrying capability (CAI strength) by 27% following an impact at 14J.

Lastly, Mendikute et al. [49] focused on the comparison between various LCM variants, particularly pertaining to their effect on void generation and subsequent impact properties. For this purpose, bi-axial NCF laminates were manufactured by means of four distinct LCM methods, namely VARTM with controlled modified capillary number (0.58 ± 0.18 %[10]), RTM with controlled modified capillary number (1.35 ± 0.28 %), uncontrolled RTM (2.44 ± 0.14 %), and wet compression moulding, WCM (4.34 ± 0.31 %). The presence of voids was shown to substantially reduce the impact response, evident in the 9.57% reduction in dissipated energy for the highest void content. Nonetheless, interestingly, post-impact residual properties were observed to only be slightly affected by increasing the void content. Following an impact at 20 Joules, specimens with

[10]Void content measured.

high and low void levels respectively retained 45.8 and 49.1% of their initial stiffness. As result, the impact of void content on the residual properties is notably less than its effect on the properties observed after the initial impact. The author attribute this to the generation of damage within the specimen amidst the initial imapct, wherein the influence of this inflicted damage could supersede the effect of the voids.

Chapter 3

Numerical modelling of damage in composite materials

In this chapter, we aim to thoroughly delineate the intricacies of modelling and simulation of damage in composite materials. To commence, we briefly provide background on its significance and challenges within the aeronautical industry. Subsequently, we delve into their damage mechanisms and highlight the importance of the damage scale. Thereafter, noteworthy aspects pertaining to the basic theories behind cohesive zone models, CZMs, are discussed. Lastly, given its pivotal role within this work, we meticulously review the continuum damage mechanics, CDM, approach, its application to composite materials and the manner in which it correlates to NCF composites.

3.1 Introduction

As ACMs gain substantial prominence within the realm of aeronautical engineering, namely in the domain of primary structural components, adequate design and substantiation procedures (a subject of continued evolution [7]) are pivotal to ensure optimal performance and safety [50] given their inherently complex damage behaviour (in comparison to their metallic counterparts) [51]. As a result, the standard within the field, with respect to the introduction of novel material systems, is the formulation of meticulously planned test programs. These programs employ a sequence of steps termed the *building block approach* (Figure 3.1) to assess their behaviour under various conditions by means of a synergy between experimental work and analysis [3, 7, 8, 52–54]. Such methodology involves the testing of numerous smaller, less expensive specimens representing structural details under simple loading scenarios to generate design allowables (that account for the variability associated with curing/consolidation procedures, geometrical features and defects) [8, 54–56]. This confers a profound understanding of the structural response at incipient stages, thereby facilitating early risk assessments and enabling a gradual progression in complexity within the design process of structures commonly upheld to strict certification and safety requirements [7, 8]. The main drawback associated with this technique resides in its costly and time-consuming nature. Solely relying on testing is prohibitively expensive and can substantially delay the introduction of new materials and the conception of novel structures, factors that are of paramount importance for the competitive edge of OEMs within the aeronautical industry [7, 8, 57]. Consequently, the development of accurate analytical and numerical models to aid, or potentially supplant, exclusive experimental campaigns to determine design parameters emerges as a matter of utmost signifi-

cance [3, 8]. Indeed, in the absence of reliable and computationally efficient analysis tools, the design process will have to rely on costly matrices of mechanical tests based on a large number of test specimens and empirical knockdown factors, undermining the benefits of advanced composite laminates [3, 9, 58, 59].

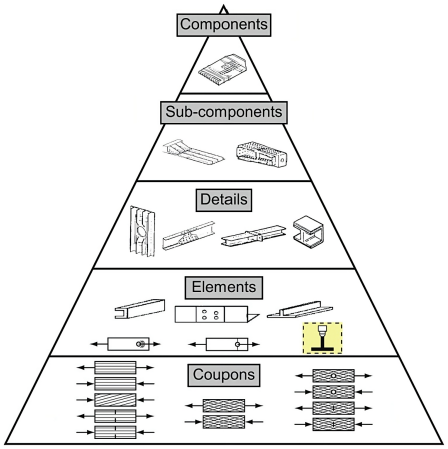


Figure 3.1: Building-block approach test pyramid [57].

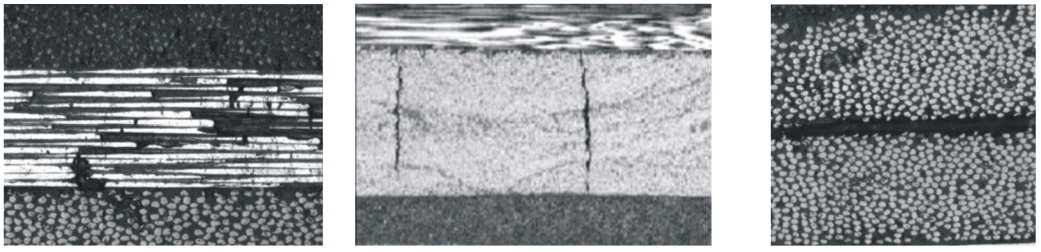
The prospects of enhancing design and certification methodologies by means of high-fidelity models capable of reducing expenditures and expediting time-to-market of innovative materials and structural concepts and potentially streamlining virtual certification are thereby well acknowledged [3, 55, 60]. In fact, this has been the focus of various research endeavours over the course of recent decades aimed at refining methods for failure prediction (from damage onset and evolution to ultimate failure), gaining deeper comprehension into their behaviour, and devising robust analytical formulations [53, 60]. Notwithstanding, such methods, whether based on analytical or numerical principles, are commonly not robust in their ability to provide accurate results under every set of conditions, thereby currently requiring further validation to ensure the precise representation of the structural response under general loading conditions for a wide range of materials and laminate lay-ups [3, 57, 60]. The development of tools capable of capturing such thermo-mechanical response is thus especially pivotal to quantify the fracture resistance and ascertain the residual strength and life of ACMs, facilitating their design and implementation into novel applications by means of a framework capable of describing damage onset and evolution up to and including rupture, ultimately the objective of damage mechanics (the area of study concerned with quantitative descriptions of the physical phenomena that irreversibly alter a material when it is subjected to loads) [1, 3, 61, 62].

The main challenge in developing such an efficient numerical model resides in the means by which the micro-structural changes of the material should be scrutinised to establish correlations between them and the ensuing material response [3, 61, 63]. The aforementioned intricate damage response of ACMs entails stiffness and stress losses more prevalent than in metals due to their complex damage mechanisms [3, 51]. As a result, damage onset and evolution (as well as ascertaining the intensity of each mechanism) must be taken into account within the formulation of a robust and reliable damage model, leading to the definition of *progressive damage models* [3, 63–65]. Nonetheless, even for composite laminates (most comprehensively researched and understood composite materials), accurately defining the onset and propagation of damage, including ultimate fracture, remains a significant challenge in the realm of modern mechanics of composite materials [64]. As a result, in spite of outstanding advancements yielding several successful analytical and numerical solutions, a lack of confidence persists with regard to such methods with their use still not being

widespread due to not being implemented in commercially available software and/or having not gained adequate validation and acceptance for a given material system [8, 53]. Furthermore, given the diversity of the proposed approaches, care must be exerted in ascertaining the conditions for which a particular model remains valid, i.e., assessing when it ceases to be adequate, which, in light of their complexity, is often not trivial [3, 65].

3.2 Damage mechanisms in composite materials

"Often an ill-defined term" [5] with respect to composite materials, macroscopic fracture/failure in CFRP structures is inherently more intricate in regard to their traditional (metallic) counterparts [9, 51]. Prior to rupture, these heterogeneous, laminated materials commonly manifest multiple local failures at lower length-scales (discrete damage events), namely fibre breakage, pullout or kinking/buckling (fibre-dominated modes), matrix cracking and fibre/matrix de-bonding (matrix-dominated modes), and delamination between plies (detachment between two adjoining layers), that grow and accumulate (damage evolution) throughout the loading process [3, 5, 9, 51, 63, 66, 67]. Matrix-dominated damage mechanisms customarily act as first-ply failure, FPF, modes that may yield complete structural collapse even in the absence of any fibre breakage (e.g., for sufficiently thick plies). On the other hand, fibre-dominated mechanisms generally induce ultimate failure, i.e., last-ply failure, LPF, in a catastrophic manner [9]. These various mechanisms (Figure 3.2) may be broadly classified into intralaminar and interlaminar damage, with the former pertaining to the distinct underlying micro-mechanical failure modes (i.e., fibre fracture/buckling, matrix cracking and fibre/matrix de-bonding and pull-out) and the latter referring to the inter-facial separation between plies [3, 7, 65, 66].



(a) Fibre fracture **(b)** Matrix transverse crack **(c)** Delamination

Figure 3.2: Damage mechanisms in laminated composites [65].

Moreover, the primary failure mechanics exhibited under tension and compression loading conditions are markedly distinct. Tensile failure is primarily attributed to matrix cracking and fibre breakage that, as a function of the layup, may further involve delamination. Conversely, when subjected to compressive loads, kink-band formation, along with delamination and off-axis matrix cracking, plays a pivotal role in the fracture process. This phenomenon arises in the form of matrix cracking or yielding accompanied by fibre rotation in plies whose reinforcement is oriented in the loading direction [3, 7, 54, 66]. Nonetheless, damage onset and evolution in CFRP laminates is not merely dependent on the loading scenario [66, 67]. In virtue of having two distinct constituents (fibres and matrix), as well as the resulting anisotropy in both stiffness and strength, damage mechanisms in composite materials manifest at different levels and interact under complex combinations yielding an inter-connected multi-scale failure behaviour [3, 9, 65]. Whilst engagement between damage modes often promotes an enhanced energy absorption capability amidst progressive damage growth, i.e., superior behaviour under severe loading conditions, these combinations are highly dependent on the characteristics of the constituents and laminate design (i.e., stacking

sequence and ply thickness) and may either lead to a reduction in local stress concentrations or the precipitation of a structural collapse [3, 65–67]. Accordingly, the idealisation of the individual [constituent] responses and their interplay remains an extremely complex task as the full details that induce failure are not fully understood, with modelling approaches, in spite of their interaction, simulating interlaminar and intralaminar damage modes separately, given the intricate nature of damage onset and evolution [65, 66].

3.3 Damage scale

Damage onset and evolution in composite materials comprises an intricate multi-scale event in nature. Commonly, as above-stated, it originates at the microscale in the form of matrix cracks that are followed by small-scale delamination at the layer interfaces. Subsequent load increases promote matrix crack growth into mesoscale cracks and delamination, ultimately leading to macroscale cracks and fibre breakage [66]. Accordingly, reliable damage models capable of accurately predicting these physical phenomena are strongly reliant on the scale (or resolution) at which the damage mechanisms under consideration are modelled [3, 7, 65, 68]. An adequate definition of the modelling scale is of particular significance within the realm of composite materials, wherein the in-plane dimensions exceed the length scale at which delamination, matrix cracking, and fibre-matrix debonding occur by one to several orders of magnitude. In fact, the identification, characterisation and formulation of the governing physical principles of damage evolution is highly dependent on the scale of the idealisation of the damage process that may span from molecular dynamics to structural mechanics (including the intermediate micro- and mesoscales) [3, 65, 68]. Currently, damage models and simulation approaches typically target the response of the material/structure at one of these scales (depicted in Figure 3.3) [66].

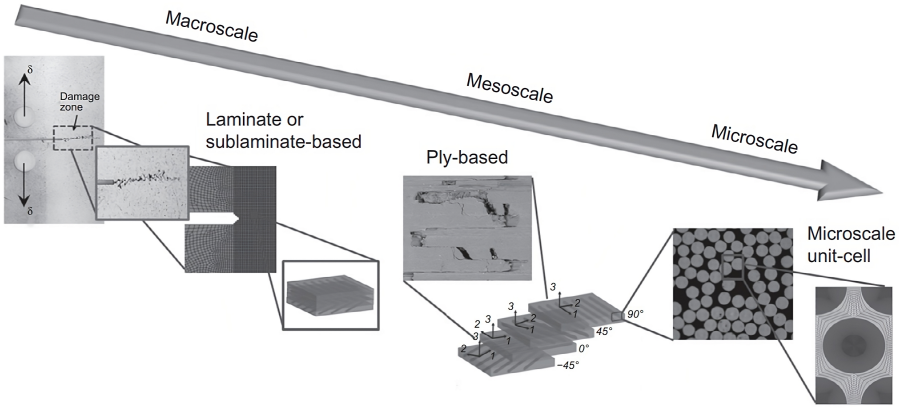


Figure 3.3: Schematic representation of the various scales involved in damage modelling [66].

Micromechanical scale models, commonly extending up to a few hundred microns, embody the smallest scale of damage idealisation in composite materials [3, 65, 69, 70]. At this scale, predictions for the properties of the individual laminae, encompassing not merely elastic constants but also strength properties under a variety of loading conditions, are attained via experimental data on the properties of fibres and matrix materials (regarded as homogeneous solids) [1, 3, 9, 54, 70, 71]. In contradiction to the macroscale, wherein the distinct matrix damage mechanisms are omitted (i.e., aggregated into a single macroscopic parameter, the interlaminar fracture toughness), interlaminar crack propagation, at this level, involves an intricate interplay of energy-dissipating phenomena, including matrix cracking and plasticity, fibre-matrix de-bonding, and crack branching and migration [3, 65, 72, 73]. Accordingly, idealisations at such lower structural scales boast enhanced

resolution and kinematic freedom, being able to recreate a diverse range of damage mechanisms by means of numerical simulations of deformation and failure pertaining to a Representative Volume Element, RVE, of the microstructure. Specifically, micromechanical models excel in capturing the response of individual constituents (fibres and matrix), as well as their interfacial interactions, via separate and distinct damage initiation and evolution laws (allocated to each component) that typically hinge upon a reduction of the material stiffness [3, 9, 65, 70, 73]. Consequently, as opposed to a *hard discontinuity* whereby voids are represented as displacement discontinuities within the model (akin to classical computational fracture mechanics), fracture is seen as a band of localised volumetric stiffness reduction, i.e., a *soft discontinuity* [3, 9, 65]. If successfully implemented, computational micromechanics hold the potential of enabling the designer to anticipate the ramifications of material alterations prior to the availability of experimental lamina test data [1, 3] and assess the influence of the geometry and spatial distribution of the various phases (e.g., fibre volume fraction and clustering), the effect of micro-mechanical defects (e.g., voids and micro-cracks) induced during the curing process and the addition of new constituents (e.g., thermoplastic particles or doping agents) in the mechanical performance [3, 9, 74]. Despite their considerably higher computational cost, the refinement of modelling techniques, coupled with the relentless advancement of computational power, has allowed computational micromechanics to emerge as a reliable tool for analysing the mechanical response of composite materials, with microscale models having been proven to successfully ascertain the properties and damage onset of undamaged material configurations [9, 69, 70]. Nonetheless, they lack in predicting damage evolution, localisation and ultimate failure in composite materials, seeing as the RVEs assumed for ascertaining the response of the virgin materials do not correlate with those pertaining to the extensively damaged arrangement [9, 69]. Moreover, such models entail an additional set of calculations, thereby enhancing the risk of inaccuracies in the predicted lamina properties, and, owing to computational constraints, are generally limited to two-dimensional (2D) representations, thus embodying domains considerably smaller than the ply thickness [3, 9, 65].

As previously mentioned, the damage onset and evolution in composite materials (ultimately culminating in macroscopic fracture) arises from the intricate combination of discrete damage events manifesting across distinct length scales [3, 5, 9, 51, 63, 66, 67]. Accordingly the interplay of the above-stated mechanics at the microscale yields irreversible nonlinearities, i.e., plasticity, damage, and fracture. At the ply level, these nonlinearities, owing to the morphology of CFRP systems, manifest as matrix-dominated intralaminar fracture parallel to the fibre direction, either as transverse or split cracking, and fibre-dominated intralaminar fracture perpendicular to the fibres [70]. In scrutinising the damage evolution and ultimate failure of representative composite laminates employed in actual coupons and structures, a fine description of discrete damage events through computational micromechanics inevitably yields intractable, prohibitively complex models that, in virtue of the currently available computational power, cannot be solved within the time frames demanded by the aeronautical industry, thereby rendering them inapt [9, 70]. As a result, *mesomechanical models* predicated on a ply-by-ply discretization, wherein laminate layers are regarded as the fundamental homogeneous building blocks and imperfections and variabilities inherent to lower scales are neglected, become more suitable in ascertaining the damage and failure of the bulk laminate [1, 3, 9, 69, 70]. Each layer is characterised by its orthotropic material properties, which may be derived by means of experimental programs (characterisation tests at the lamina level) or from micromechanical models employing the properties of the constituents [1, 9, 70]. Such models are further split into two distinct approaches, i.e., the continuum damage mechanics, CDM, and the discrete damage mechanics, DDM, approach, both offering several computational advantages in comparison to micromechanical models [65]. Within these models, phenomenological failure criteria based upon the homogenised stress (or strain) state at the ply

level emerge as the most appropriate approach to accurately capture the onset of the various discrete mesoscale damage modes. Nevertheless, solely few criteria adequately address the crucial aspects of the failure process inherent to laminated composites, i.e., increase of apparent shear strength upon the application of moderate transverse compression values, the ramifications of ply thickness on the strengths of individual plies (*in-situ* effect), the detrimental impact of in-plane shear stresses attributed to fibre misalignment under longitudinal compressive failure by fibre kinking, and the capacity to predict failure under hydrostatic pressure [9, 65, 70]. These failure criteria are employed in conjunction with material degradation solutions to attenuate the material properties associated with a specific mode of failure. Moreover, to address micromechanical effects such as fibre/matrix de-bonding, select mesomechanical methodologies undertake concurrent analyses on idealised unit-cell models representative of typical fibre distribution patterns within the matrix. In addition, the analysis of delamination failure mechanisms is performed at the mesoscale level, commonly represented as a discontinuity between plies, typically modelled employing either cohesive elements or nonlinear springs [3, 7, 65].

Composite damage idealisations predominantly entail CDM models at the mesoscale level, representing one of the most widespread approaches for assessing damage onset and evolution in structural components [65]. Formulated within the framework of the thermodynamics of irreversible processes and devoid of any calibration (thereby potentially offering a truly predictive methodology), continuum strategies with respect to fracture perceive crack initiation and growth as the ultimate ramifications of a gradual, local loss of material integrity [3, 59, 75]. CDM models postulate that, within the homogeneous orthotropic (for laminates) plies, intralaminar damage modes (e.g., fibre fracture/kinking and delamination) are defined as a reduction in the corresponding stiffness, wherein a set of continuous damage variables and interacting activation functions, which explicitly illustrate the local loss of material integrity, is employed to either directly or indirectly capture the density and/or redistribution of microscopic defects associated with damage [3, 7, 65, 75]. Consequently, in contradistinction to the hard discontinuities implemented in DDM approaches, localised damage entails a soft discontinuity [3, 65]. Redistribution of stresses within the laminate culminates in the concentration of deformation and consequent damage growth within a relatively diminutive region in front of the crack tip (process zone) that dictates the direction and rate at which the crack propagates (standard continuum mechanics theory, rather than discrete fracture criteria [75]). Nonetheless, the CDM approach may lack adequate resolution to capture significant damage interactions at the micromechanical scale, given its diffuse representation. Specifically, CDM models encounter difficulty in predicting the accurate propagation of matrix cracks parallel to the fibres, and the damage models for intralaminar damage may not interact appropriately with the delamination models [3, 65].

On the other hand, within DDM mesoscale approaches, plies are represented at the mesoscale level, i.e., assumed, once more, to boast homogeneous orthotropic properties; however, displacement discontinuities (e.g., cracks), as opposed to CDM models, correspond to zero-thickness cohesive process zones. In alternative, embedded discontinuity models (e.g., the extended finite element method, X-FEM) enable the introduction of cracks and delaminations in locations that are independent of mesh orientation and obviating the necessity for re-meshing [3, 65, 76]. Moreover, DDM models may be employed in the representation of intricate matrix cracks and delaminations by means of a single simple cohesive law [3, 65]. Nonetheless, intralaminar damage, within multidirectional laminates, typically forms in a more widely spread and diffused pattern, thus CDM approaches offer a more reliable physical representation of intralaminar damage in comparison to the discrete models [69].

Despite offering a comprehensive representation of the initiation and propagation of the var-

ious damage mechanisms transpiring at the ply level, as well as their interactions, the level of discretization required by mesoscale approaches (each and every layer must be modelled and simulated) often yields prohibitively expensive computational models. As a minimal element size is commonly required to guarantee numerical objectivity and accurate physical representation of the damage mechanisms, this computational cost further escalates rapidly with increasing number of plies and dimension of the structure [9, 69]. Moreover, within a multi-directional laminate, neighbouring plies generally provide structural support to the damaged layers, introducing alternative load paths. As a result, the individual plies exhibit a distinct behaviour than the one captured by the standard test methods suggested for the characterisation of unidirectional laminates. Consequently, ply-based approaches are unsuitable for preliminary design and optimisation of composite structures, or for large-scale numerical simulations in the absence of global-local coupling analyses on account of high computational costs and the assumption of independent behaviour of the layers. Under such circumstances, *macromechanical models* formulated at the laminate level not merely become imperative, but also present themselves as the only feasible solution, given their less intricate nature that aids in markedly reducing the computational effort [9, 69]. Within structural-level damage models, the basic building block is the laminate, assumed as homogeneous, with the effects of constituent materials solely manifesting by means of averaged apparent properties of the composite material, a hypothesis that allows designers to ascertain stress patterns and stress concentration (i.e., critical) regions within a component [1, 9]. Cracks are portrayed as hard discontinuities and predicting their propagation may be based on a strain-softening law or a criterion pertaining to the critical energy release rate. Notwithstanding, structural-level crack propagation criteria are strongly linked with the material system and laminate configuration. As a result, these criteria must be determined for each novel material system and laminate stacking sequence, with a new set of properties adequately determined by means of either direct experimental programs or virtual testing employing mesoscale models and experimental data at the ply level [3, 9]. Additionally, macroscale semi-empirical fracture models fail to address the characteristics of the crack-tip damage zone and the intricate interactions between micro and macro-failures associated with the crack-extension process. Instead, the crack-tip damage zone is represented as an "effective" notch-tip damage region assumed to grow in a self-similar manner, which, in numerous instances, is nonetheless not observed. Moreover, the scarce resolution with respect to the damage mechanisms frequently renders structural-level damage models imprecise following a brief propagation of damage [3, 65].

Alternatively, in light of the multi-scale nature of damage and failure in CFRP laminates, *multi-scale* approaches have been proposed, wherein the diverse aspects of the bulk structural problem at various levels of complexity, each marked by a well-defined length-scale are addressed [69]. Multi-scale models can be classified into two categories: hierarchical and concurrent. With respect to the former, homogenisation is employed to transfer the predicted material behaviour from a lower to a higher scale, i.e., the different levels at which analyses are conducted are interconnected through length scale transitions, wherein the structural response at a given level is homogenised to attain mechanical properties pertaining to the next higher level [1, 3, 69]. Although hierarchical multi-scale models are typically reliable at predicting the elastic response of materials with complex microscale architectures, they encounter a fundamental issue regarding damage and failure prediction, seeing as homogenisation ceases to be valid due to localisation of strain. Consequently, hierarchical multi-scale models cannot objectively predict the fracture energy, size of the fracture process zone, or size effects [69]. Conversely, within concurrent multi-scale models, as the name advocates, two distinct levels are simultaneously present in the model and connected by matching the boundary conditions at both scales, usually invoking periodicity to reduce the computational cost; ultimately being devoid of homogenisation to bridge the scales [3, 7, 69]. In undamaged regions, a

macro-model with effective homogenised behaviour is utilised, while in damaged areas, the model resolution is augmented, and meso/micro features are explicitly accounted for. Amongst their shortcomings, concurrent multi-scale damage models are plagued by high computational costs and difficulties in characterising small-scale (microscale) models [69]. Still, multi-scale analyses can be performed by leveraging the most favourable attributes of each level of analysis [1, 3]. For instance, in a hierarchical multi-scale approach, analyses on unit cells at the micro-scale can determine the stiffness and strengths of the unidirectional fibre bundle by means of homogenisation techniques, with mesomechanical models subsequently being capable of evaluating the fibre architecture, providing stiffness and strength parameters for macro-scale computations [1, 3, 7, 9]. Notwithstanding, the reliability and accuracy of such frameworks are naturally dependent on the effectiveness of the damage models available for each length-scale [9].

3.4 Cohesive zone models

As previously stated, failure in laminated fibre-reinforced composites arises from the development of intralaminar and/or interlaminar (delamination) damage mechanisms that largely depend on factors such as loading, geometric configuration, and stacking sequences. Notwithstanding, delamination, in particular, embodies a prominent damage mode in these materials, owing to their inherently poor interlaminar strengths, capable of significantly compromising their structural integrity. Nonetheless, its detection during inspection does not constitute a trivial matter, thereby complicating maintenance operations in composite structures. As a result, the anticipation of delamination onset and growth is naturally a paramount concern [77, 78].

Although methodologies based in *Linear Elastic Fracture Mechanics*, LEFM, have demonstrated significant effectiveness in assessing its progression (for scenarios where other material non-linearities can be disregarded), their application is predicated on the existence of an initial crack. Moreover, challenges persist when implementing these techniques within the framework of finite element codes, i.e., the computation of fracture parameters (e.g. stress intensity factors or energy release rates) requires nodal variables and topological information from the nodes both ahead of and behind the crack front. Although this calculation can be performed without substantial effort in the case of a stationary crack, it becomes increasingly intricate and laborious when dealing with scenarios of progressive crack propagation [78]. An alternative approach to the numerical simulation of delamination can be defined the context of *Damage Mechanics* in the form of **Cohesive Zone Models**, CZMs, that boast remarkable efficacy in the simulation of nonlinear progressive failure analyses where both ply damage and delaminations are considered [3, 79]. Thereby, it is deemed to be the most feasible strategy when analysing large three-dimensional (3D) structures with multiple delamination onsets and propagation fronts, being nowadays widely used to model interlaminar damage [3, 77, 78, 80, 81].

The origin of CZMs can be traced back to the early 1960s, crediting specifically the work of Dugdale [82] and Barenblatt [83]. Dugdale's [82] pioneering concept proposed that stresses in the material are bounded by the yield stress and that a thin plastic zone is generated in front of the notch. On the other hand, Barenblatt [83] incorporated the idea of cohesive forces on a molecular scale, facilitating the solution of the equilibrium problem in elastic bodies manifesting cracks [78, 80, 84]. The key novelty in both models laid within the inclusion of a *fracture process zone*, FPZ, designated as the cohesive zone, wherein in cohesive tractions act on the separating surfaces. Hillerborg et al. [85] subsequently transposed the concept of the CZM into a finite element framework. This approach portrayed a micro-cracked FPZ capable of stress transfer until complete separation was achieved [84]. The CZM concept, depicted in Figure 3.4, thus embodies

the FPZ (damaged material) by means of a fictitious crack (dashed line) able to transfer cohesive forces from one face to another. These tractions are governed by a *cohesive law* relating them with the *crack opening displacements*, CODs, and whose underlying area comprises the fracture energy [80].

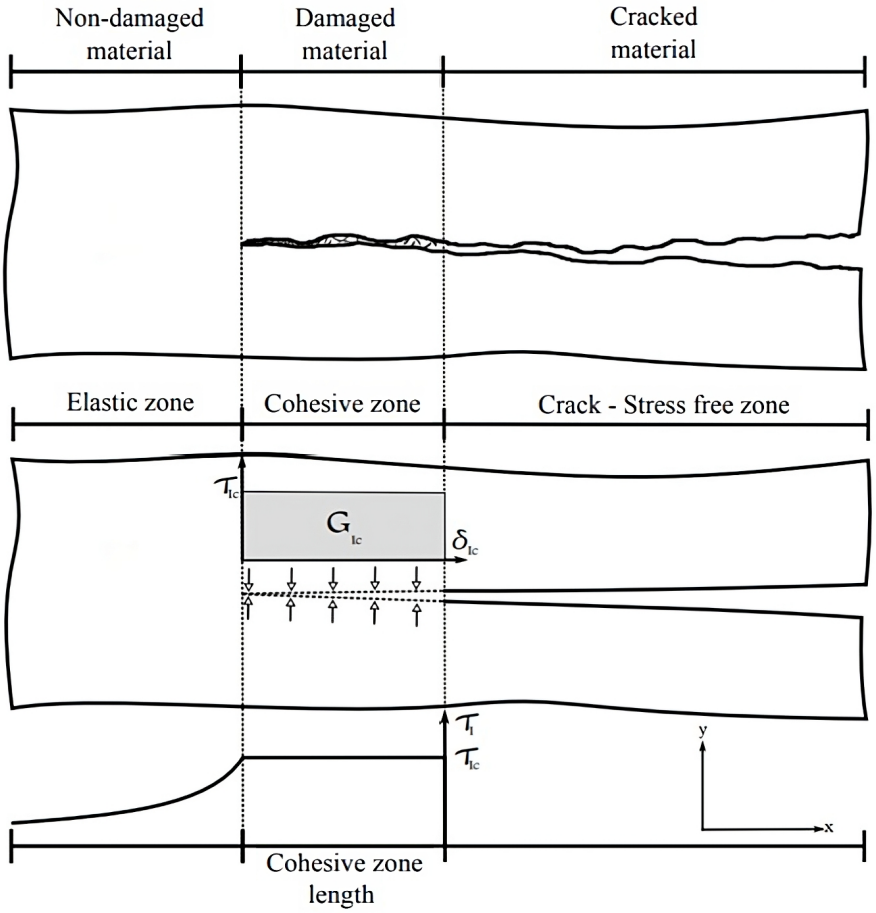


Figure 3.4: Top: FPZ of a quasi-brittle material. Middle: CZM concept. Bottom: stress distribution along the crack path for a constant cohesive law under pure mode I loading [80].

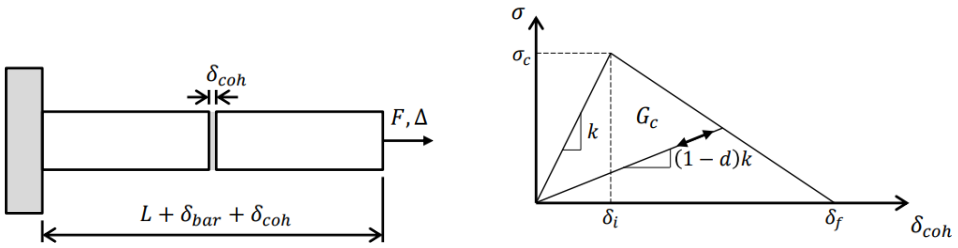
CZMs are based on accurate kinematic descriptions of the fracture process [77], employing strong discontinuities in the displacement field [3, 65]. These models are generally implemented in cohesive (decohesion) elements [78] that resort to failure criteria combining attributes of strength-based analysis to predict the onset of the softening process, along with fracture mechanics, contributing to the prediction of damage propagation [3]. Cohesive elements can be broadly categorised into two principal groups: continuous interface elements and point cohesive (decohesion) elements. With respect to the former, there are several sub-types that include zero-thickness volumetric elements connecting solid elements, finite-thickness volumetric elements connecting shell elements, and line elements. Conversely, the latter are identical to nonlinear spring elements connecting nodes [3, 86].

As stated, CZMs are governed by a so-called *cohesive interfacial law* (or *traction-separation law*) that establishes phenomenological mechanical relations between the cohesive tractions, σ, and the interfacial separations, δ, dictating the softening behaviour and influencing the development of the FPZ [81]. This law defines the interfacial behaviour in such a manner that, as the interfacial separation increases, the tractions across the interface reach a peak value, subsequently decreasing and

vanishing upon complete decohesion (stiffness and strength fully degraded) [3, 65, 81]. Thereby, by incorporating the characterisation of both damage onset and evolution, CZMs uphold the predictive criteria vital in achieving a comprehensive representation of fracture in a continuum. For a more thorough understanding of the cohesive law, let us consider a quasi-brittle bar of length, L, and cross-section, A, (Figure 3.5a) wherein, to model its fracture behaviour, a cohesive interface is introduced; an example that effectively demonstrates these principles. The opening of the crack is assumed to follow the softening law depicted in Figure 3.5b. From the figure, we conclude that the initial crack response is linear elastic and that the closing forces relate to the interfacial displacement jump, δ_{coh}, by means of a high *penalty stiffness*, k. If the COD exceeds the critical value, δ_i, these forces undergo a linear softening response such that the area under the traction-displacement curve equals the fracture toughness, G_c. Ultimately, complete separation occurs when the COD exceeds δ_f. Thereby, such laws are termed *bi-linear cohesive laws* defined as:

$$\sigma = \begin{cases} k\delta, & \delta < \delta_i \\ (1-d)k\delta, & \delta_i \leq \delta < \delta_f \end{cases} \tag{3.1}$$

where d pertains to the damage variable dependent on the displacement jump, i.e., as a consequence of increasing damage, the load-carrying ability of the material is reduced, which is accounted for by means of this parameter [3, 65].



(a) Elastic bar with a cohesive crack **(b)** Bilinear cohesive law

Figure 3.5: Quasi-brittle bar of length L and cross-section A with a cohesive interface [65].

Nonetheless, in the realm of composite materials, the fracture process often involves multiple physical phenomena, each exerting its influence at distinct CODs. Whereas some act in the vicinity of the crack tip (small CODs), others operate at higher displacement jumps, thereby extending further into the crack growth response. As a result, the determination of initiation strength, fracture toughness, and shape parameters typically require experimental characterisation and vary depending on the three opening modes: mode I (in the normal direction), shear mode II (in-plane direction), mode III (out-of-plane direction) and mixed-mode [81]. Nonetheless, direct experimental measurements of such variables pose practical challenges [87], and, alternatively, analytical or semi-analytical calculations through inverse methods have been employed to derive them as well [88, 89]. Ultimately, several laws have been proposed to model interlaminar damage in composite materials, with the primary differences amongst them being the onset and evolution criteria under mixed-mode conditions, and the considered idealised shape (that dictates damage evolution) ranging from bi-linear [77, 78] to trapezoidal [90] or exponential [91] profiles [80, 81]. However, it is worth noting that these simplified shapes may exhibit limited accuracy, particularly when confronted with a substantial FPZ arising from plastic deformation or fibre bridging/friction effects [81]. In such scenarios, the softening law may exhibit a peak at low displacements to capture the tip process zone, combined with a prolonged tail at higher CODs to represent bridging effects in the crack wake. Consequently, to model this intricate behaviour, multi-linear softening laws [92, 93]

have been proposed, combining two or more bi-linear cohesive laws as depicted in Figure 3.6 [3, 65]. Such models have additionally proven to provide not merely a more precise estimation of the process zone length, but also a more accurate representation of experimentally determined R-curves [3, 65, 92].

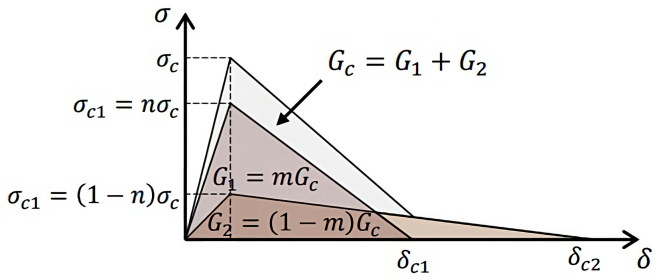


Figure 3.6: Tri-linear cohesive law obtained by superposing two bi-linear laws [65].

Moreover, in structural applications involving composites, crack/delamination growth often arises under mixed-mode loading conditions. Thereby, a constitutive model capable of accurately describing the damage development under mixed-mode fracture is paramount in assuring an excellent performance of a CZM [3, 77]. A mixed-mode cohesive law is typically represented within a single three-dimensional (3D) map by incorporating the bi-linear material responses in pure mode I and pure mode II on normal planes (refer to Figure 3.7). Amidst mixed-mode loading conditions, damage onset is given by a COD equal to δ^0 and complete fracture is attained at δ^F. As a result, cohesive tractions, σ, for mode I and mode II are respectively governed by the reduced curves $O - N^M - \delta_I^{FM}$ and $O - S^M - \delta_{II}^{FM}$, with the area under each one amounting to the fracture energies under mixed-mode.

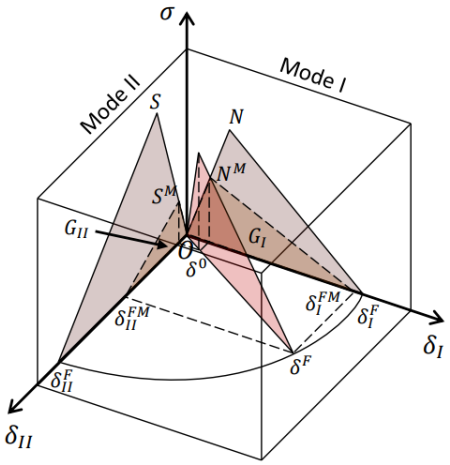


Figure 3.7: Mixed-mode cohesive law [65].

Turon et al. [78], in an early mixed-mode CZM, devised a thermodynamically consistent damage model incorporating an onset criteria predicated upon the damage propagation principle [80], i.e., the Benzeggagh and Kenane criterion [94]. The model dictated that the initial strength, σ_c, and the critical value of the energy release rate, G_c, (respectively initiation and progression criteria) were defined as a function of a mixed-mode parameter, B,

$$B = \frac{G_{II}}{G_T} = \left(\frac{\delta_{II}}{\delta}\right)^2 = 1 - \left(\frac{\delta_I}{\delta}\right)^2 \tag{3.2}$$

where $G_T = G_I + G_{II}, \delta_I$ and δ_{II} embody the CODs in mode I and II, respectively, and δ pertains to the total mixed-mode relative displacement $\left(\delta = \sqrt{\delta_I^2 + \delta_{II}^2}\right)$. On the other hand, σ_c and G_c are computed by

$$\sigma_c^2 = N^2 + \left(S^2 - N^2\right) B^\eta \tag{3.3}$$

$$G_c = G_I + \left(G_{II} - G_I\right) B^\eta \tag{3.4}$$

where N and S comprise the ply transverse tensile and shear strengths, respectively; G_I and G_{II} pertain to respectively the mode I and II critical energy release rate values; and the parameter η is derived by applying a least squares fit to the experimental data obtained, e.g., from mixed-mode bending, MMB, tests at different mode ratios [3, 78].

Notwithstanding, certain challenges in accurately predicting crack propagation under mixed-mode conditions persisted, as argued by Dávila et al. [65]. These were primarily associated with the mode ratio [between mode I and II loading] that is rarely constant during the fracture process, even for MMB specimens, whose mode ratio, within a LEFM framework, is constant amidst propagation. Experimental observations concluded that the CODs pertaining to damage onset are predominantly governed by mode I, whereas, prior to complete separation, the displacement jumps primarily occur in mode II [3]. Consequently, in a subsequent CZM, Turon et al. [95] aimed at addressing such drawbacks. It was initially observed that, when delamination growth occurs under pure mode I or II loading, no effect of the interface strength on the energy dissipated took place. However, in the event that the mixed-mode ratio varied with damage evolution, the mixed-mode interface strength and fracture toughness of the material were found to fluctuate according to Equations 3.3 and 3.4. Thereby, it was mandatory to ensure that the time derivative of the damaged area remained non-negative to avoid predicting material healing [3, 95]. In light of such restriction, a relation between interlaminar strengths and fracture toughness was defined as:

$$\tau_0 = \sigma_0 \sqrt{\frac{G_{IIc}}{G_{Ic}}} \tag{3.5}$$

where τ_0 corresponds to the interlaminar shear strength and σ_0 to the peel strength. Turon et al [95] further demonstrated that the load-displacement curves attained by computing τ_0 according to Equation 3.5 are independent of the specified interlaminar strengths, whilst additionally agreeing with the LEFM solution for any given mixed-mode ratio. However, Equation 3.5 is solely valid for problems where the FPZ is small enough for LEFM principles to be applicable, i.e., crack growth is only driven by the fracture toughness and the interlaminar strengths do not affect the dissipated energy [77]. For tougher materials exhibiting non-negligible FPZs ahead of the crack tip, as observed by Sørensen et al. [96] and confirmed by Harper et al. [97], such assumptions do not hold true as the interlaminar strengths severely affect the numerical results. Both the strength and shape of the cohesive law define the global response, and, consequently, modifying the interlaminar strengths would not be appropriate [3, 95]. An alternative solution proposed by the authors [95] was predicated upon adjusting the penalty stiffness based on the measured interlaminar strengths yielding a relation between the mode I, K_I, and shear mode interface stiffness, K_{shear}:

$$K_{shear} = K_I \frac{G_{Ic}}{G_{IIc}} \left(\frac{\tau_{shear}^0}{\tau_I^0}\right)^2 \tag{3.6}$$

where τ_{shear}^0 and τ_I^0 are the shear mode and mode I interlaminar shear strengths, respectively. Although the implementation of distinct penalty stiffness for mode I and shear mode loading was

initially disregarded[1], a more recent work by Turon et al. [77] has provided an updated version of the CZM addressing this limitation. Within the novel formulation, interlaminar strengths and fracture toughness parameters were experimentally measured and used in a CZM to analyse delamination in two distinct specimens, one with an initial crack and another without any initial crack. With respect to the former (wherein LEFM principles hold true), accurate energy dissipation was proven, regardless of the specific selection of model parameters. Concerning the latter, delamination failure was once more correctly estimated, upholding the performance of the revised CZM. Moreover, the study highlighted the influence of interface strengths and the mixed-mode interaction parameter on the predicted failure load. It was concluded that the varying failure loads attained underscore the importance of precise experimental characterisation of these parameters. It further emphasised the necessity for a robust formulation that ensures correct energy dissipation under diverse mixed-mode loading conditions [77].

Lastly, some consideration regarding *size effects* in composite materials are noteworthy. In the case of notch-ductile components, the ability to bear loads is primarily determined by strength properties, whereas in notch-brittle components, it is predominantly dictated by the fracture toughness. For materials falling within the intermediate range, both variables naturally play significant roles. Notably, cohesive laws, being defined in terms of strength and fracture toughness, G_c, boast the capacity to accurately represent both crack onset and material softening, thereby enabling them to effectively encompass the entire spectrum of material responses [3, 65].

3.5 Continuum damage mechanics

3.5.1 Continuum mechanics approach

The primary objective of damage mechanics is to predict the behaviour of a material, or more specifically, its response in the presence of damage initiating at some stress state and propagating as the applied loads increase the stresses in the material [1]. It has been well established that, within the realm of material science, all materials inevitably exhibit irreversible nonlinearities (manifesting themselves as plasticity, damage, and fracture). To put them into context, let us consider a positive definite constitutive tangent relationship (relating strain increments to stress components), a response recognised as hardening (refer to Figure 3.8). Hardening is seen as a macroscopic, distributed and irreversible material response that not only smears the stress concentrations, but also effectively eliminates any singularities; and arises from mechanisms (e.g., plasticity and distributed damage) acting at the micro-structural level. Moreover, distinct nonlinearities can be discerned through a comparative analysis of the unloading paths versus the loading paths. For instance, whereas unloading path A in Figure 3.8 embodies a linear elastic behaviour, path B, in spite of maintaining the same slope as path A, displays an additional strain offset, i.e., the material has undergone plastic deformation. Unloading path C, on the other hand, takes this one step further, diverging from the original one both in terms of slope and offset, suggesting the emergence of additional nonlinearities, e.g., cracking. Furthermore, a distinct behaviour from those previously analysed may also be denoted, particularly for the scenario wherein the constitutive tangential stiffness is non-positive definite (path D). This is indicative of a response classified as **softening**, typified by the formation and coalescence of voids and micro-cracks, conducting to damage localised along a fracture surface and elastic unloading adjacent to it [3, 65].

[1]The use different penalty stiffness values required the re-formulation of the constitutive model and was deemed out of scope.

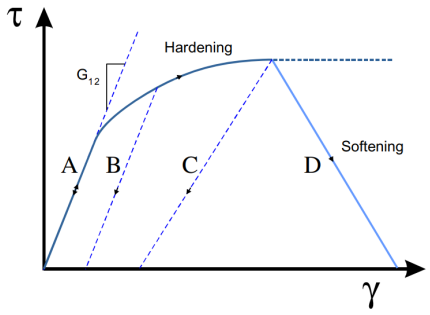


Figure 3.8: Typical shear stress–strain response exhibiting multiple nonlinearities [65].

Naturally, an extensive array of models have been proposed to accurately capture the nonlinearities inherent to various materials. Hardening of composite materials can be precisely depicted with local constitutive models, i.e., models essentially described by differential equations (lacking the notion of characteristic length) wherein the stress components at any specific point is uniquely reliant upon the history of the deformation gradient up to that very point; an assumption predicated upon the implicit supposition that the material exhibits continuum behaviour at any arbitrarily small scale [3, 65].

As an alternative approach, the constitutive response of a material may be approximated by means of a spatially periodic RVE to accurately capture the micromechanical response of the individual constituents, as well as the interactions between them [3, 65, 98]. Furthermore, simplifications with respect to the degree of complexity of the system are often made, i.e., by considering a 2D (assuming plane-strain conditions) approximation of the 3D continuum. It is further postulated that each RVE deforms in a repetitive manner, and, as a result, periodic boundary conditions are imposed to ensure compatibility conditions along the boundaries pertaining to the deformation field. Balancing the need to reflect stochastic fluctuations of material properties at the desired scale and computational efficiency requirements, the RVE size is another crucial consideration. It should ideally be as large as feasible, yet computational constraints mandate it being as small as possible. Notwithstanding, even with a substantial RVE size, if the analysis involves highly nonlinear responses promoting localised damage, the periodicity of the boundary conditions and, as a result, the efficacy of the RVE representation itself become questionable [3, 65].

Such concerns may, nonetheless, be circumvented by means of considering an alternative approach that has demonstrated superior effectiveness, namely the *crack band theory* devised by Bažant and Oh [99]. Before the introduction of this theory, the idea of representing cracking within a continuum through strain softening was met with considerable debate and it was often argued that materials with a non-positive definite tangential moduli tensor did not exist [65]. However, this methodology has proven its ability to enforce the objectivity of the solution subsequent to reaching the maximum strength of a material [1]. Initially applied to concrete that exhibits a gradual strain-softening due to micro-cracking, this fracture theory is predicated on the hypothesis that this type of fracture can be modelled as a broad, smeared band of parallel micro-cracks, rather than a singular line crack. The material thereby undergoes progressive micro-cracking in tandem with a strain-softening nonlinear behaviour. From a computational standpoint, the crack is modelled by altering the matrix isotropic elastic moduli to orthotropic ones. Such point in the deformation history, wherein the tangential stiffness of the constitutive model loses its positive definite properties, indicates the formation of discontinuities. This change effectively reduces the stiffness in the direction perpendicular to the cracks within the band, which is readily implemented within a finite element, FE, program [1, 3, 65, 99]. Bažant and Oh [99] further postulate that the

post-peak response may be adjusted using a characteristic element length. This methodology ensures that the computed energy dissipated due to the fracture process remains constant and equivalent to the product of the fracture energy, G_c, and the crack surface area, A [3, 65, 99]. In addition, given that damage localises within a single FE layer, the problem manifests itself by a strong sensitivity of the solution to the size of the FEs. Thereby, there exists a maximum FE size, L_e^{Max}, for the simulation of a crack band in order to avoid snap-back in the constitutive model (i.e., preventing $\varepsilon_f < \varepsilon_i$, as illustrated in Figure 3.9) that may be expressed as:

$$L_e^{Max} = \frac{2EG_c}{\sigma_c^2} \tag{3.7}$$

where E, G_c and σ_c respectively comprise the Young's modulus, fracture energy and strength for a given damage mechanism [65, 99, 100]. It should be noted that the implications of Equation 3.7 bear significant weight, i.e., employing an element size larger than L_e^{Max} (for some composites, this value may be a fraction of a millimetre) leads to an overestimation of the critical Energy Release Rate, ERR. Consequently, seeing as utilising such fine meshes becomes computationally unfeasible, a potential workaround involves the artificial reduction of strength to maintain the correct value of G_c. However, it is important to note that such approach should be reserved for problems where the solution is anticipated to be dependent on fracture, not strength [65]. Additionally, the crack band theory further requires *a priori* knowledge of the crack path for an adequate mesh definition, seeing as cracking and damage tend to grow parallel to its orientation. In instances where a well-defined path does not exist, e.g, when the FPZ significantly rotates during the passage of the fracture front or the damage pattern is highly diffuse, the applicability of the crack band theory is limited [3, 99].

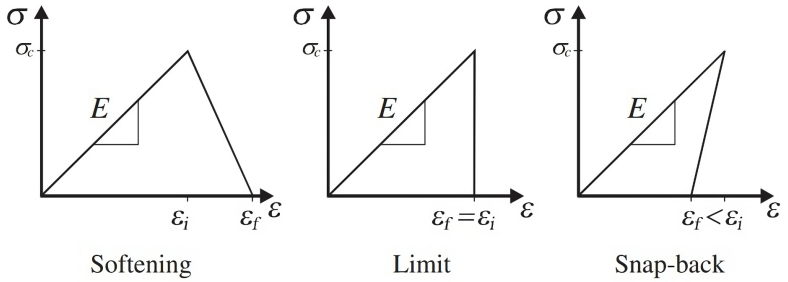


Figure 3.9: Snap-back at constitutive level [65].

Moreover, within the framework of CDM, non-local methodologies also present feasible solutions to mesh sensitivity issues, helping to maintain the objectivity of numerical responses. Many of these techniques incorporate spatial interaction terms that exert a smearing effect on the deformation fields and thus deter localisation in a plane. A comparable smearing effect may also be achieved by means of a computationally simpler technique resorting to rate-dependent (viscous) properties. Material properties pivotal for crack smearing, or strain softening, are selected such that the width of a localising diffuse crack band in a continuum matches the characteristic length, which is associated with the material response [3, 65].

Notwithstanding, Germain et al. [101] postulate that, whilst classical non-local models may be adequately equipped to describe the response of a single layer or a bulk composite, certain unresolved questions persist regarding the representation of damage onset and evolution in composite laminates, specifically the inter-layer interactions. As a result, a non-local model was devised by the authors operating on the assumption that damage remains confined within each layer, i.e.,

non-local damage variables must be defined for each individual layer. The authors, thus, identified two sets of nodal damage variables at the nodes located at the interfaces between two layers. Furthermore, in an effort to account for anisotropic damage evolution, an internal length was defined for each material direction and damage variable. In addition, over the last few decades, a plethora of other CDM models have been devised and applied to composite materials, as will be discussed in subsequent sections.

3.5.2 Idealisation of damage modes in composite materials

The intricate damage mechanisms inherent to advanced FRP further introduce challenges in the numerical modelling of failure within these materials. Whereas some intralaminar modes, e.g., transverse matrix cracking (Figure 3.2b) and delamination (Figure 3.2c) occur in easily identifiable fracture planes (parallel to the fibre direction), others (e.g., fibre failure) prove to be more challenging to idealise. Consequently, representing intralaminar damage by means of kinematic descriptions based on strong discontinuities is rendered a formidable task, in light of the aforementioned complexities. From a computational standpoint, a more feasible strategy involves the use of failure criteria rooted in the homogenised stress or strain state, thereby idealising the failure mechanisms [3, 65].

Naturally, numerous failure criteria have been proposed to predict the onset of matrix cracking and fibre fracture, some which were delineated in the worldwide failure exercise, WWFE, [102–106] which effectively evaluated the status at the time of available theoretical methods for predicting material failure in fibre-reinforced polymer composites [3, 61, 65, 107]. It was ascertained that, owing to an incomplete understanding of the damage mechanisms and challenges in developing tractable models of failure modes, only few criteria were able to satisfactorily represent several pertinent aspects of the failure process in laminated composites. Nonetheless, some of the noted limitations, including the effect of ply thickness (*in-situ* effect), fibre misalignment in compression, and the effect of shear non-linearity on fibre kinking and in-situ strength were subsequently addressed [3, 65]. Phenomenological, physically based, and interactive failure criteria, especially the *LaRC03 criteria* [61, 107], proposed corrections [108, 109] and their general 3D extensions (*LaRC04 criteria*) [63], contrarily to criteria based on curve-fitting, are based on a physical model for each failure mechanism. Thereby, such models are capable of accurately predicting matrix and fibre failure without requiring curve-fitting parameters and without any restrictions regarding loading combinations, being able to not merely establish when failure occurs, but also describing the post-failure behaviour of a given composite structure [3, 61, 63, 107, 109]. In fact, as will be discussed in the following section, such approximations of the LaRC03-04 criteria [107] (with some slight modifications) are still nowadays employed with great success in the simulation of failure within composite laminates [8].

Notwithstanding, pertaining to three dimensional failure criteria for fibre reinforced laminates, it is worth noting the works by Catalanotti et al. [110] and Camanho et al. [66]. Concerning the former, it aimed at addressing shortcomings of other three-dimensional interaction criteria at the time to predict matrix failure under general stress states, given that reasonable estimations were only attained for transverse compression if some relations between the material strengths were satisfied. The authors state that, when accounting for *in-situ* strengths, such relations are not always satisfied, yielding wrong predictions of both the first ply failure load and fracture angle. The proposed failure criteria was able to overcome such obstacles, accurately estimating the fracture angle for both simple and multi-axial stress states. Nevertheless, for loading scenarios pertaining to high hydrostatic pressures, the quality of these predictions was found to be degraded. With respect to the three dimensional invariant-based failure criteria for FRP proposed within the

latter [66], a 3D kinking model (Figure 3.10) relying on an invariant failure criterion was devised to predict longitudinal compressive (kinking) failure. This model assumed that fibre kinking arises from local micro-structural imperfections that initiate a kink band when local matrix cracking occurs in the vicinity of the misaligned, micro-buckled fibres. These local micro-structural flaws are embodied in the model as an initial fibre misalignment, leading to shearing stresses between fibres that create an instability. The attained results exhibited great correlation with experimental data for transverse failure modes, failure under off-axis loading and for the impact of superposed hydrostatic pressure on failure behavior of different FRPs.

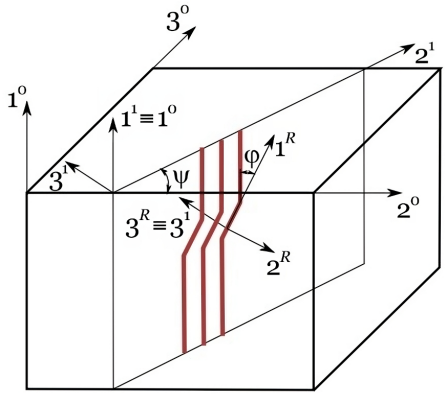


Figure 3.10: 3D kinking model [111].

In addition, focusing on the aforementioned effect of the ply thickness, it is reasonable to postulate that the existence of defects within a ply span its entire thickness. Furthermore, cracking of the ply can be assumed to occur when the loads (in the fibre direction) it is subjected to exceeds those required to propagate a slit crack (refer to Figure 3.11), a mechanism termed as *tunnelling*. This stress corresponds to the above stated *in-situ strength*. Moreover, in multi-directional laminates, cracks progressively accumulate in the transverse plies during the loading process. As the load on an individual transverse ply escalates, new cracks abruptly nucleate. Initially, this takes place at somewhat random locations and then evolves towards a progressively more uniform crack spacing. Upon reaching a certain load level, the crack density arrives at a saturation value, triggering a different event such as delamination or fibre failure in an adjacent ply. In particular, as the density of cracks in each ply of the laminate amplifies, intricate networks of cracks evolve, which have the potential to connect through the laminate's thickness, thereby inducing delaminations [3, 65].

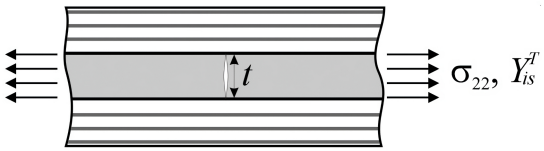


Figure 3.11: *In-situ* strength determined from the propagation of a slit crack in a ply [65].

3.5.3 CDM models applied to composite materials

CDM models for composite materials can be traced back to Ladevèze & LeDantec [112] and Matzenmiller et al. [113], that built upon previous work by Kachanov [114] and Lemaître et al. [115]. To accurately predict the ultimate strength of composite materials, as extensively

reported, it is crucial to have a precise numerical representation of all damage modes and their interactions. Thereby, in existing CDM models, a clear differentiation is made between distinct damage mechanisms, particularly between fibre and matrix failure, and a gradual softening of the material response is included, with internal damage variables delineating this behaviour for each corresponding damage mode [1, 3, 65]. Notwithstanding, these type of responses commonly do not include a characteristic length, prompt strain localisation along a surface known as the failure surface and induce a singularity of the damage rate at the crack tip [3, 65]. Thereby, such models exhibit a pathological mesh sensitivity (with respect to element size) in numerical computations [1, 65]. Without a characteristic length, such analyses would predict failure to occur with zero energy dissipation as the element size approaches zero. To resolve these localisation instabilities, damage rate singularities and lack of objectivity, a characteristic length must thereby be introduced within the constitutive model [3, 65]. Continuous representation of cracks makes CDM and related models particularly suitable for numerical simulations. In fact, CDM formulations can be implemented in nonlinear FE codes with relative ease, without necessitating special discretization and remeshing techniques [3].

Moreover, the evolution of intralaminar damage in laminated composites can be represented by softening laws defined by a maximum traction and a critical energy release rate that dictate the evolution of damage in terms of the fracture energy dissipated in each damage mode. When a damage activation function, F_M, of a specific type of damage mechanism, M, is satisfied, the associated damage variable, d_M, assumes a positive, non-zero value less than or equal to one, and the ply compliance tensor, H, is affected by the presence of damage. Furthermore, it is necessary to define the evolution laws for the damage variables, d_M, which need to assure that the computed energy dissipated is independent of the refinement of the mesh [3, 65].

Within the realm of CDM models, Maimí et al. [52, 100, 116] were amongst the foremost authors to devise a comprehensive methodology capable of accurately predicting the initiation and evolution of intralaminar damage mechanisms (and eventual failure) within composite laminates. Within the model, strain-softening constitutive laws were employed to simulate localised intralaminar damage modes based on four possible fracture planes (associated with fibre tensile fracture and kinking, and matrix cracking) situated at 0 and 53° relative to the ply thickness direction, predicted using a simplified version of the LaRC04 failure criteria [63, 107]. Damage evolution was depicted using exponential laws, which were employed to describe the cohesive response of all failure modes of the ply, except for the longitudinal tension damage evolution law. Furthermore, to account for ply thickness effects on the initiation of transverse matrix cracking, the aforementioned in-situ strengths were resorted to within the failure criteria. The proposed model also demonstrated its ability to handle complex load histories, including the effects of crack-closure during tension-compression load reversals, thereby dealing effectively with the unilaterality of damage. In addition, in order to ensure mesh-independent solutions and preserve the objectivity of the numerical solution, a modified version of the crack band model was utilised for the regularisation of the energy dissipated for each corresponding damage mechanism. The authors further proposed a viscous model to mitigate convergence difficulties associated with strain-softening constitutive models. The model was implemented into an Abaqus®`VUMAT` subroutine and was validated against experimental results on open-hole specimens [100]. The FE model employed 4-node shell elements (S4 elements) with one integration point along the ply thickness and maximum and mean errors of 10.5 and 4.2% were obtained.

The above-stated model was subsequently used in a study by Camanho et al. [59] aimed at accurately predicting the strength and size effects of notched laminates, whilst additionally comparing a plethora of methodologies. It was concluded that fibre-based failure criteria not only

were unable of encompassing hole size effects, but also constantly under-predicted the strength of the notched CFRP laminates (with errors as high as 49.1%). LEFM theory, on the other hand, accurately predicted size effects for specimens with hole diameters between 6 and 10 mm, yet the authors further state that it should not be employed for coupons whose hole diameters are either less than 2 mm or exceedingly large (i.e., with failure stresses tending to a constant value). Furthermore, in spite of simpler approaches, e.g., point stress and inherent flaw models (that do not require complex FE implementations) being able to provide reasonable solutions, their accuracy is largely reliant upon the measurement of the characteristic distance and length of the inherent flaw for each lay-up and stacking sequence. Conversely, the CDM model proposed by Maimí et al. [52, 100, 116] entailed in precise estimations of the size effects and final failure loads, whilst also providing information concerning the integrity of the material during the loading history, a paramount factor. Moreover, the model only requires properties measured at the ply level and fracture energies that are measured using both standard test methods and novel compact tension/compression methodologies, thereby addressing limitations with other approaches. Lastly, the authors note that the FE-based CDM model may further be applied to arbitrary configurations where analytical solutions could not be developed.

Bessa [117] was also amongst the authors that employed the CDM model devised by Maimí et al. [52, 100, 116] to ascertain the strength and failure modes of open-hole specimens subjected to tensile and compressive loads, and coupons subjected to off-axis loading. In addition, the author incorporated a CZM proposed by González et al. [118] in an attempt to more accurately capture delamination with the composite material. Concerning the open-hole tensile tests, maximum and mean errors of 11.5 and 5.0% were obtained, with these values increasing to 16.5 and 11.6% for compressive loading scenarios. Thereby, the author states that the CDM methodology is suited for the aforementioned analyses, yet also emphasises the need for supplementary numerical studies to corroborate its appropriateness for simulations involving off-axis tests. It is further noted that the precision in predicting open-hole compressive strength could potentially be augmented, given that it is largely contingent upon the longitudinal compressive fracture energy (whose measurement was met with several challenges). Moreover, the model displayed a considerable computational demand, suggesting that this was a noteworthy aspect to be considered in future iterations.

Building upon the CDM model by Maimí et al. [52, 100, 116], Lopes et al. [119] extended the plane stress formulation into 3D scenarios. Combining it with the CZM proposed by Turon et al. [78], an impact CDM/CZM model able to predict both intralaminar and interlaminar damage mechanisms (i.e., capture the progressive failure behaviour of fibres, matrix, and interfaces between plies) was thus developed. This impact approach was then incorporated into an explicit FE framework to ascertain the response of composite laminates under LVIs. The results attained from these simulations displayed the model's robust ability to accurately predict several critical parameters. These include the dynamics of the impact, the footprint resulting from the impact, the location and size of delaminations, matrix cracks, and fibre damage. Furthermore, the model effectively quantifies the energy dissipated through various processes such as delamination, intralaminar damage, and friction. Similar results were observed in a work by González [120, 121] into the analysis of LVI and CAI events. Once more, the CZM proposed by Turon et al. [78] was employed. However, as opposed to the previous studies, no modifications to the CDM model proposed by Maimí et al. [52, 100, 116] were made. It was observed that the simulations exhibited a closer correlation with experimental data when a lesser number of plies (and consequently interfaces) were considered. A higher number of layers, besides significantly increasing the computational effort, exhibited a reduced correlation with experimental results attributed to the plethora of contact constraints posed by the cohesive elements. Notwithstanding, as stated by the author, the modelling approach was

able to effectively describe the various phenomena occurring during the impact and CAI tests. This detailed understanding is not feasibly attained through physical testing or non-destructive inspections, thereby emphasising the invaluable contribution of this modelling approach to the aeronautical sector.

Additionally, in a more recent study by Lopes et al. [122], the extended formulation of the CDM model was revisited, yet delamination was modelled by means of a cohesive zone surface behaviour coupled with a penalty surface contact algorithm, i.e., the fracture behaviour is lumped into a zero-thickness region. The foremost goal with such approach was to simplify the modelling processing and decrease the total number of elements. Notwithstanding, the cohesive interaction was stated by the authors as more expensive in terms of computational cost per iteration. Once more, the use of ply-by-ply meshes that are aligned with the material directions, and accounting for ply-to-ply cohesive contact behaviour enabled the accurate capture of phenomena such as delamination, matrix cracking, and fibre breakage across a range of impact energies. Furthermore, it facilitated reliable predictions related to specimen perforation. This methodology was further explored by González et al. [123] for the virtual testing of LVI and subsequent CAI on polymer-based composite structures, with a marginal difference. In spite of cohesive surfaces also being incorporated to analyse delamination, each ply was described in the through-the-thickness direction by means of conventional shell elements (as opposed to solid ones) located at the mid-plane, as illustrated in Figure 3.12, and by the CDM model devised by Maimí et al. [52, 100, 116]. Surface elements are placed on the bottom and top faces of the ply, and are connected to them via rigid Tie connectors that facilitate the transfer of kinematics from the shell to the surface elements. Thereby, the latter can be understood as sheets of nodes that move in accordance with the displacements and rotations of the ply, without storing elastic energy. The foremost advantage with the use of S4R elements is readily identifiable from a computational standpoint. By eliminating the FE thickness inherent to 3D solid or continuum shell elements, the authors expected significant reductions of the computational cost, without significant losses of accuracy. Indeed, the predictions concerning the evolution of impact load and displacement exhibited remarkable correlation with experimental data. However, the evaluation of the dissipated energy and the projected delamination area indicated an underestimation of the interlaminar damage mechanism. The authors attributed this to a limited interaction between interlaminar and intralaminar damage mechanisms. Furthermore, it was observed that the majority of the predicted CAI maximum loads exceeded the experimental results.

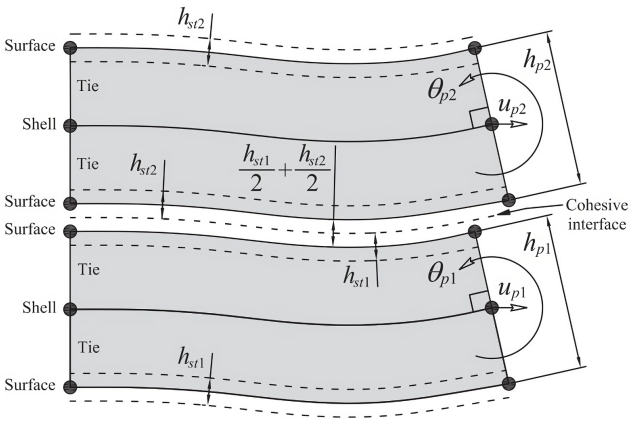


Figure 3.12: FE modelling strategy based on the use of conventional shell elements, wherein h_p refers to the ply thickness [123].

Ultimately, the aforementioned studies laid down the foundation for Soto et al. [80, 124] to develop "A methodology to simulate low velocity impact and compression after impact in large composite stiffened panels"[2]. Initially, a numerical benchmark was performed at the coupon level to ascertain the most efficient modelling methodology in predicting both the LVI and CAI responses. Thereby, focus was given on comparing the computational efficiency and accuracy of various FE types (i.e. solid, continuum shell and conventional shell[3]) and cohesive interaction technologies (i.e. cohesive elements and cohesive surfaces). It was observed that the elasticity domain and delamination threshold were accurately represented across all scenarios, exhibiting relative discrepancies under 5%. Conventional shell elements did, however, display a stiffer response due to their inability to account for out-of-plane compliance. The maximum displacement further yielded notable predictions (of within 3% of the experimental data), whereas more significant disparities were noted in the estimation of the maximum force (by ∼10% for all models). Further dissimilarities emerged pertaining to the dissipated energy and projected delamination area, with the analysis being more heavily influenced by the selection of the element type rather than the chosen cohesive interaction technique. For instance, conventional shell elements under-predicted the former by roughly 27.3%, whereas this value improved to 15.8% for solid elements. This was attributed by the authors to the fact that conventional shell elements do not account for out-of-plane stresses, a factor of considerable significance for thicker plies. Furthermore, continuum shell elements encountered numerical challenges that prematurely ended simulations, regardless of the cohesive interaction technique. Concerning delamination, S4R elements overestimated the projection by 25% and 14% for respectively, cohesive surfaces and zero-thickness elements. Solid elements, on the other hand, exhibited a better correlation with experimental results, demonstrating a mere 3% discrepancy. It should be noted, however, that conventional shell elements in conjunction with a cohesive surface were capable of predicting the largest delamination, which may be explained by their ability to accurately capture bending with a single element per ply and the enhanced capability of cohesive surfaces to capture large deformations relative to cohesive elements. In regard to the CAI simulations, all strategies accurately predicted the experimental CAI stiffness and strength. Additionally, pertaining to the computational effort, conventional shell elements with zero-thickness cohesive elements were faster by 1.54 times than when used with cohesive surfaces. Similar conclusions were derived for solid elements that, when combined with zero-thickness cohesive elements were faster by 1.3 times. More significant variations were nonetheless observed depending on the FE type, with S4R elements outpacing 3D solid elements by up to 3.3 times. Another aspect of paramount importance noted by the authors was the element deletion criterion. Excessive element distortion issues, that may significantly compromise the accuracy and robustness of the numerical models, are common in finite element analyses, FEA, involving severe damage. To mitigate this, the matrix damage variables were thereby limited so as to ensure that the matrix never had a residual matrix stiffness lower than 100 MPa. Having compared the different methodologies, conventional shell elements with zero-thickness cohesive elements was the selected modelling approach, given that it provided a good balance between accuracy and computational efficiency. Notwithstanding, the impact prediction obtained was not in agreement with the experimental test with respect to the projected delamination area and force-displacement response after skin perforation. Still, the predicted damage was accurate enough to yield reasonably good CAI estimations.

The previous strategy was later employed by Sasikumar et al. [125] within a study aimed at improving the CAI strength of thin laminates resorting to ply-thickness hybridisation in a virtual testing based approach. To this purpose, various hybrid laminate configurations (incorporating

[2]This is the methodology herein employed for LVI tests, thus, in this section, we mainly consider the obtained results, with more details being provided in the following sections.

[3]Intralaminar damage is once more described by the CDM model proposed by Maimí et al. [52, 100, 116].

intermediate and thick grade plies) were assessed so as to ascertain the optimal impact damage tolerant materials. The FE model was initially calibrated based on the impact and CAI experimental results of a baseline laminate, composed entirely of intermediate plies. Subsequently, it was employed to optimise symmetric ply hybrid laminates. Through the virtual testing of symmetric laminates, under impact (8.9 and 10.5 J) and CAI conditions, optimal laminates were identified. These were able to improve the CAI strength by 31% compared to the baseline. Further enhancement was observed in unsymmetrical laminates, which showed a 40% improvement over the baseline and a 10% improvement over the optimal symmetric hybrid laminate. Furthermore, one of the optimal symmetric hybrid laminates inferred by means of virtual testing was experimentally tested and the predicted increase in CAI strength was remarkably confirmed.

Despite the notable success of the CDM model developed by Maimí et al. [52, 100, 116] across various loading scenarios, as extensively reported thus far, in a more recent work, Furtado et al. [8] introduced a revision of this model. Whereas the original model was capable of accurately predicting the onset and accumulation of intralaminar damage mechanisms, it was devised assuming that the out-of-plane stresses are too small to promote damage. Thereby, damage is activated only by the in-plane components of the stress tensor, an hypothesis that does not correlate well for scenarios wherein the triaxiality of the stress components cannot be neglected. To address this, the authors proposed modifications to the constitutive law (to account for the distinct Young's moduli in longitudinal tension and compression) and incorporated a bi-linear softening law for longitudinal compression more suitable to represent kinking failure (following experimental findings by Moran et al. [126]). Furthermore, the damage activation function for longitudinal compression was updated based on the aforementioned 3D failure criteria proposed by Camanho et al. [111], thus accounting for the impact of through-thickness stresses. Engineering solutions were introduced as well to capture the impact of pressure on longitudinal compression and in-plane shear fracture toughness. In addition, the CZM model proposed by Turon et al. [77] was modified with a frictional cohesive law to deliver a more accurate representation of delamination propagation and load-bearing capacity in scenarios where the effect of through-thickness pressure is significant. The modified approach underwent rigorous validation for various material systems and test specimens of escalating complexity, i.e., from un-notched tension and compression, open-hole tension and compression, to filled-hole compression. The attained predictions exhibited a remarkable agreement with experimental data across all cases, often situating themselves within the standard error and with a maximum relative error of 13%.

The previous CDM model was subsequently employed by Arteiro et al. [57] in estimating edge impact and compression after edge impact, CAEI, in CFRP laminates. A slightly different modelling methodology than that previously described [80, 124] was employed, with 8-node C3D8R 3D brick elements with reduced integration being preferred to model each ply, given the complex stress state that arises from an edge impact event. Delamination between plies, on the other hand, was modelled using the cohesive surface interactions available in Abaqus®. The obtained results exhibited good correlation with experimental data, not only in the estimation of the size and shape of damage, but also in the residual strength predictions of dispersed- and blocked-ply CFRP laminates subjected to CAEI. Crucially, the model was further able to reliably capture the effects of stacking sequence variations, aligning well with experimental observations. Notwithstanding, the authors state that the exceedingly high computational times required, ranging from hours to days depending on model size, remain prohibitive for applications in conceptual design or structural optimisation. As a result, research is still need with the aim of reducing the computational demands of such models and broadening their industrial applicability.

3.6 Numerical modelling of NCF composites

Numerical modelling of NCF composites may be categorised pertaining to the two distinct strategies mainly employed in their representation, namely macro- and meso-mechanics approaches [127]. Concerning the former, as previously mentioned, the material is assumed to be comprised of homogenised layers of different orientations, assuming evenly distributed fibre tows. The mechanical properties at the layer level are often derived from the rule of mixtures, ROM, or multi-scale methodologies [128, 129]. The internal architecture of the composite, specifically fibre undulation, is commonly incorporated into the model via two primary mechanisms. First, it can be represented as a local coordinate system at an elemental level. Alternatively, the undulation may be characterised as a sinusoidal function, predicated on the assumption of periodicity in fibre waviness [127]. In regards to the latter, the individual constituents of the NCF composite are depicted within a FE framework resorting to RVEs, an approach that considers the inherent heterogeneity of NCF laminates. Furthermore, whilst several models [13, 130–135] have demonstrated success in accurately forecasting the stiffness, strength, and ultimate failure mechanisms of these materials, this approach poses a significant computational challenge, rendering it unfeasible for application to larger-scale structural components.

Furthermore, it is worth noting some of the distinct failure criteria that have been proposed for NCF composites, each with its own unique limitations. While many have been developed for UDPTs (refer to subsection 3.5.2), less research has been devoted to their development specifically for NCF composites. Indeed, predicting failure in such materials is particularly challenging due to the different damage mechanisms that occur until failure onset (e.g., fibre kinking and matrix failure) [127]. Edgren et al. [136] proposed a model predicated upon the hypotheses of a linear interaction between the longitudinal compressive and shear stresses to predict the strength of an individual layer. Although the constitutive model demonstrated significant alignment with experimental results for quasi-isotropic NCF composites, it necessitated a substantial quantity of input data for each layer within the configuration. On the other hand, Wilhelmsson et al. [137] put forward a defect severity model to estimate the longitudinal compressive strength of UD NCF laminates, with its 2D FE implementation being able to not only accurately predict the compressive strength, but also precisely capture the emergence of kink-bands. Molker & Wilhelmsson [138] introduced a physically-based orthotropic criterion for the transverse failure of UD NCF composites. This model followed a meso-micromechanical approach and successfully estimated the orthotropic strength behaviour, differentiating between intra and inter-bundle failures. Lastly, Shipsha et al. [139] assessed the impact of the stacking sequence on the strength and failure mechanisms for a variety of cross-ply NCF lay-ups under compression. The authors further presented a failure criterion for intralaminar fibre kinking and interlaminar damage, yet with discrepancies of up to 25% in relation to the experimental data.

Notwithstanding, it should be noted that such models hinge on distinct methodologies than the ply-by-ply discretisation adopted in the previously mentioned CDM models and in the present work. Still, Yin & Iannuci [140] did assess the CAI behaviour of bi-axial NCFs at the mesoscale by stacking homogenised plies together. Furthermore, a similar methodology to that of Soto et al. [80, 124] was employed, wherein a shell element formulation was used in conjunction with cohesive surfaces (to assess delamination) and intralaminar damage was described by means of the CDM model developed by Maimí et al. [52, 100, 116]. The authors observed that the predicted CAI strength exhibited a remarkable correlation with experimental data. Nonetheless, the implementation of such methodologies to NCF materials is clearly scarce, thus representing a knowledge gap within the literature. As such, aligned with the stated objectives of our work, we aim to understand

the applicability of commonly used methodologies for UDPTs to NCF laminates and ultimately address some shortcomings.

Part III

Numerical model

Chapter 4

Composite damage model

In the present chapter, our objective is to comprehensively describe the composite damage model herein employed and implemented into a `Fortran` material user-defined subroutine `VUMAT` tailored for the commercial explicit finite element solver Abaqus/Explicit. We commence with a succinct introduction of the background and specifics inherent to the model. Thereafter, we delve into the intricacies of the intralaminar CDM framework. Lastly, we thoroughly analyse the distinct interlaminar CZMs employed.

4.1 Introduction

The composite damage model herein adopted coincides with the most recent revision by Furtado et al. [8] into the intralaminar CDM framework initially proposed by Maimí et al. [52, 100, 116], and into the interlaminar CZMs developed by Turon et al. [77] and Alfano et al. [141]. The foremost purpose of the revised framework, as postulated by Furtado et al. [8], was to enhance the predictive prowess of the damage model with respect to damage onset and evolution under general loading conditions, whilst preserving the original complexity so as not to exacerbate the computational cost (thereby rendering it compatible with industrial prerequisites).

The continuum damage model for the plies furnishes a means for the accurate prediction of onset and accumulation of the different intralaminar (within the ply itself) damage mechanisms in laminated composites [8]. The formulation of the CDM model is based on the definition of a potential (the complementary free energy density) within the framework of the thermodynamics of irreversible processes, as a function of damage variables associated with each intralaminar failure mode, as shown in Figure 4.1. Furthermore, damage onset and progression are modelled via damage activation, i.e., the conditions that initiate inelastic response, and damage evolution functions respectively. As opposed to the original framework proposed by Maimí et al. [52, 100, 116], the revised formulation [8] incorporates uncoupled longitudinal tensile and compressive elastic behaviours, accounting for different stiffness values in tension and in compression parallel to the direction of the fibres, with damage accumulation in both scenarios being modelled via bi-linear softening laws. In addition, Maimí et al. [52, 100, 116] solely considered the in-plane stress components of the stress tensor as a factor in damage onset, neglecting the potential contribution of out-of-plane elements (assumed as too small to promote damage). Such assumption, nonetheless, does not hold true for loading scenarios wherein the triaxiality of the stress state cannot be neglected. To surmount this shortcoming, the 3D invariant based failure criterion for fibre kinking proposed by Camanho et al. [111] was thus included to capture the hydrostatic pressure effects on

the shear response of the polymer matrix via the definition of an artificial in-plane shear strength, S_L^{ef}. Such criterion further allows for the scaling of the fracture toughness for longitudinal compression $\mathcal{G}_{1-}$, and the longitudinal compressive strength ratio at the inflection point f_{XC}, as a function of the applied hydrostatic pressure [8].

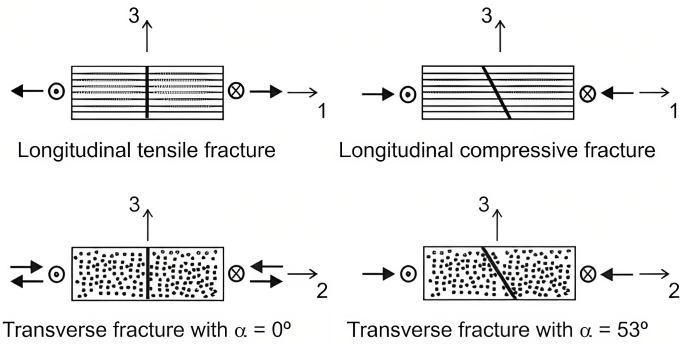


Figure 4.1: Composite intralaminar damage modes [52].

Moreover, an effective fracture toughness for in-plane shear is defined to account for the effect of transverse compressive stresses on the fracture toughness associated with in-plane shear fracture $\mathcal{G}_6$, given that experimental evidence has reported an increase in the mode II fracture toughness when the cracking faces are compressed against each other. Finally, an energy regularisation approach based on the fracture energy associated with each failure mechanism and based on the characteristic length of the finite elements is used to ensure mesh independent results after damage onset [99]. Lastly, one of the primary advantages of the CDM model herein employed lies within the determination of the required material properties that can be achieved via standard experimental tests [8].

Notwithstanding, accurate simulation of failure within composite laminates further requires the prediction of delamination onset and propagation. To this purpose, Furtado et al. [8] noted the limitations with such estimations. The authors state that the majority of formulations are developed for pure mode I and II loading, and subsequently extended for mixed-mode loading, thereby being poorly validated for such conditions. Secondly, within such definitions, friction effects were commonly not accounted for. Whilst some engineering solutions are noted, to address such shortcomings, the CZM proposed by Turon et al. [77] including a mode-dependent penalty stiffness was combined with the coulomb friction law postulated by Catalanotti et al. [142] within a user-defined material subroutine to assess delamination onset and propagation. However, it should be noted that such approach is herein solely employed for plain strength, open-hole and double-edge notched models. For LVI simulations, aligned with the methodology proposed by Soto et al. [80, 124], built-in Abaqus/explicit cohesive surfaces are used to ascertain delamination growth. Accordingly, the relevant aspects for each solution are comprehensively described in subsequent sections.

4.2 Intralaminar damage model

4.2.1 Constitutive law

The intralaminar CDM model, aligned with the above-stated, is rooted in the definition of the constitutive equation, formulated within the thermodynamics of irreversible processes framework as a function of damage variables, each associated with the various intralaminar failure modes

depicted in Figure 4.1. To postulate the constitutive law, a scalar function (positive definite and zero at the origin with respect to the free variables, i.e., the stress components [143]) equating to the complementary free energy density in the ply must be established [52]. This function, accounting for the distinct longitudinal Young's moduli in tension and compression [8], is expressed by[1]:

$$\mathcal{G} = \frac{\langle \sigma_{11} \rangle^2}{2\,(1-d_1)\,E_1} + \frac{\langle -\sigma_{11} \rangle^2}{2\,(1-d_1)\,E_{1c}} - \nu_{12}\sigma_{22}\left(\frac{\langle \sigma_{11} \rangle}{E_1} + \frac{\langle -\sigma_{11} \rangle}{E_{1c}}\right) + \frac{\sigma_{22}^2}{2\,(1-d_2)\,E_2} + \frac{\sigma_{12}^2}{2\,(1-d_6)\,G_{12}} + (\alpha_{11}\sigma_{11} + \alpha_{22}\sigma_{22})\,\Delta T + (\beta_{11}\sigma_{11} + \beta_{22}\sigma_{22})\,\Delta M \quad (4.1)$$

where σ_{ij} (i,j = 1,2) represent the stress components[2]; d_i (i = 1,2,6) correspond to the scalar damage variables[3]; E_1 and E_{1c} are, respectively, the longitudinal tensile and compressive Young's moduli; E_2 comprises the transverse Young's modulus; G_{12} denotes the shear modulus; ν_{12} is the in-plane Poisson's ratio; α_{ii} (i = 1,2) encompass the coefficients of thermal expansion; β_{ii} (i = 1,2) are the coefficients of hygroscopic expansion; ΔT and ΔM are, respectively, the temperature and moisture content variations; and $\langle \bullet \rangle$ stands for the Macaulay brackets, which return the argument $\bullet$ if positive, and zero otherwise [8].

The definition of the ply complementary free energy density (Equation 4.1) serves as the foundation for establishing the relation between the stress and strain tensors [57]; achieved by ensuring the thermodynamic irreversibility of the damage process, i.e., the rate of change of the complementary free energy, $\dot{\mathcal{G}}$, minus the external work supplied to the solid at constant strains, $\dot{\sigma} : \epsilon$, must not be negative [52]:

$$\dot{\mathcal{G}} - \dot{\sigma} : \varepsilon \geq 0 \quad (4.2)$$

Equation 4.2 embodies the positiveness of the dissipated energy that must be satisfied by any constitutive model [52, 143]. Expanding it in terms of the stress tensor and damage variables [52] yields:

$$\left(\frac{\partial \mathcal{G}}{\partial \sigma} - \varepsilon\right) : \dot{\sigma} + \frac{\partial \mathcal{G}}{\partial d_1}\dot{d}_1 + \frac{\partial \mathcal{G}}{\partial d_2}\dot{d}_2 + \frac{\partial \mathcal{G}}{\partial d_6}\dot{d}_6 \geq 0 \quad (4.3)$$

To guarantee that the dissipated energy is positive, considering that the stress components constitute free variables and, thus, can fluctuate without restrictions, the term in parenthesis must be equal to zero [52]. Consequently, the strain tensor correlates to the derivative of the complementary free energy density in relation to the stress tensor:

$$\epsilon = \frac{d\mathcal{G}}{d\sigma} = \mathbf{H} : \sigma + \alpha \Delta T + \beta \Delta M \quad (4.4)$$

Moreover, if negligible temperature and moisture variations are to be assumed[4], the expression reduces to:

$$\epsilon = \frac{d\mathcal{G}}{d\sigma} = \mathbf{H} : \sigma \quad (4.5)$$

[1] It should be noted that subscripts 1 and 2 respectively correlate to the longitudinal (fibre) and transverse directions.

[2] σ corresponds to the average stress tensor over a representative volume assumed to be considerably larger than the diameter of a fibre [52].

[3] Associated with longitudinal, transverse and shear damage modes respectively.

[4] The case with our analysis.

where $\mathbf{H}$ denotes the lamina compliance tensor [8], which, in Voigt notation [52], reads:

$$\mathbf{H} = \frac{\partial^2 \mathcal{G}}{\partial \sigma^2} = \begin{bmatrix} \frac{1}{(1-d_1)|\sigma_{11}|}\left(\frac{\langle\sigma_{11}\rangle}{E_1} + \frac{\langle-\sigma_{11}\rangle}{E_{1c}}\right) & -\frac{\nu_{12}}{|\sigma_{11}|}\left(\frac{\langle\sigma_{11}\rangle}{E_1} + \frac{\langle-\sigma_{11}\rangle}{E_{1c}}\right) & 0 \\ -\frac{\nu_{12}}{|\sigma_{11}|}\left(\frac{\langle\sigma_{11}\rangle}{E_1} + \frac{\langle-\sigma_{11}\rangle}{E_{1c}}\right) & \frac{1}{(1-d_2)E_2} & 0 \\ 0 & 0 & \frac{1}{(1-d_6)G_{12}} \end{bmatrix} \tag{4.6}$$

To account for the unilateral effect [52], i.e., the closure of longitudinal and transverse cracks under load reversal, four damage variables associated with longitudinal (d_{1+} and d_{1-}) and transverse (d_{2+} and d_{2-}) damage are further assumed to delineate the d_1 and d_2 parameters [8, 52] as follows:

$$d_1 = d_{1+}\frac{\langle\sigma_{11}\rangle}{|\sigma_{11}|} + d_{1-}\frac{\langle-\sigma_{11}\rangle}{|\sigma_{11}|} \tag{4.7}$$

$$d_2 = d_{2+}\frac{\langle\sigma_{22}\rangle}{|\sigma_{22}|} + d_{2-}\frac{\langle-\sigma_{22}\rangle}{|\sigma_{22}|} \tag{4.8}$$

wherein it is readily apparent that the model tracks damage caused by tension (d_+) and compression (d_-) separately. As a result, a damage mode may be deemed either active or passive contingent upon the corresponding normal stress [52]. Concerning shear damage, given it is predominately a consequence of transverse cracks not prone to the closure effect (i.e., do not close under shear stress), a sole damage variable is attributed, d_6 [8, 52].

4.2.2 Damage laws

Beyond the formulation of the constitutive law, the comprehensive definition of the constitutive model mandates the appropriate characterisation of the damage activation and evolution functions (i.e., damage laws), which govern damage propagation [57]. The determination of the domain pertaining to elastic response under complex stress states constitutes an indispensable component of an accurate damage model. The model herein adopted thereby postulates a linear elastic domain enclosed by four surfaces, wherein each of them pertains to one intralaminar failure mechanism (as per Figure 4.1), i.e., longitudinal tensile failure (F_{1+}), longitudinal compressive failure (F_{1-}), transverse failure wherein the crack plane stands perpendicular to the mid-plane of the laminate (F_{2+}) and transverse failure wherein the crack plane does not stand perpendicular to the mid-plane of the laminate (F_{2-}) [8, 52]. These surfaces are materialised by respective damage activation functions stemming from physically-based failure criteria [8, 57] and computed as:

$$F_{1+} = \phi_{1+} - r_{1+} \leq 0 \tag{4.9}$$

$$F_{1-} = \phi_{1-} - r_{1-} \leq 0 \tag{4.10}$$

$$F_{2+} = \phi_{2+} - r_{2+} \leq 0 \tag{4.11}$$

$$F_{2-} = \phi_{2-} - r_{2-} \leq 0 \tag{4.12}$$

where ϕ_i (i= 1+, 1-, 2+, 2-) denote the loading functions[5], established in terms of the strain tensor and based on an approximation of the LaRC03-04 failure criteria [8, 107]; and r_i (i= 1+, 1-, 2+, 2-) correspond to the elastic domain thresholds that take an initial value of 1 for an undamaged material configuration, increasing with damage evolution, which is expressed by the Kuhn-Tucker conditions:

[5] Although the full details regarding their definition and physical meaning lie outside the scope of this work, the interested reader is directed to References [52, 100, 116] for a more comprehensive understanding.

$$\dot{r}_i \geq 0; \;\; F_i \leq 0; \;\; \dot{r}_i F_i = 0 \tag{4.13}$$

Disregarding viscous effects, the damage activation functions must always be non-positive. As the damage activation function F_i is negative, the material exhibits linear elastic response; however, in the event that a criterion is activated by the strain state, $F_i = 0$, the gradient $\dot{\phi}_i$ must be assessed. Should it be negative, the state corresponds to one of unloading or neutral loading. Conversely, for a positive gradient, there is damage evolution and the *consistency condition* has to be satisfied [52]:

$$\dot{F}_i = \dot{\phi}_i - \dot{r}_i = 0 \tag{4.14}$$

Moreover, two key attributes inherent to the model are worth highlighting. First, the threshold values for damage are not static, i.e., they are dependent on the damage variables. Second, the loading functions are intimately tied to the strain tensor. Under these conditions, it is feasible to carry out an explicit integration of the constitutive model. In addition, within the formulation of the constitutive model, the relation between active and inactive elastic domains must further be defined. Whilst the evolution of an active domain has already been characterised by the consistency condition, it is equally necessary to specify how an inactive one progresses if other damage modes are engaged. To this purpose, it is postulated that the longitudinal and transverse domains are not coupled, yet compressive and tensile damage are [52].

Commencing with transverse loading conditions, damage (i.e., matrix cracking) may exhibit varied orientations depending on the load nature, i.e., tension, shear, or compression-dominated. Furthermore, under load response, transverse cracks (perpendicular to the mid-plane of the ply) do not influence the compression response. As a result, the elastic domain and the compressive damage variable, d_{2-}, remain unaffected by r_{2+}. Conversely, cracks induced by high compressive transverse stresses commonly situate themselves on a fracture plane at an angle of $\alpha_0 = 53°$ and bear the same effect as cracks perpendicular to the mid-plane when the loading conditions are reversed from compression to tension. Thereby, the evolution of the transverse tensile elastic domain threshold, r_{2+}, is governed by both mechanisms [52]. Given these considerations, it may thus be expressed as:

$$\text{Tension loading:} \quad \dot{r}_{2+} = \dot{\phi}_{2+} \quad \text{and} \quad \dot{r}_{2-} = 0 \tag{4.15}$$

$$\text{Compression loading:} \quad \dot{r}_{2-} = \dot{\phi}_{2-} \quad \text{and} \quad \dot{r}_{2+} = \begin{cases} \dot{\phi}_{2-} & \text{if} \quad r_{2+} \leq r_{2-} \\ 0 & \text{if} \quad r_{2+} > r_{2-} \end{cases} \tag{4.16}$$

Integrating these expressions then yields:

$$r_{2+} = \max\left\{1, \max\left\{\phi^s_{2-}\right\}, \max\left\{\phi^s_{2+}\right\}\right\} \tag{4.17}$$

$$r_{2-} = \max\left\{1, \max\left\{\phi^s_{2-}\right\}\right\} \tag{4.18}$$

On the other hand, under longitudinal loading conditions, tensile fracture occurs in a plane perpendicular to the fibre direction. Consequently, if the load was to be reversed, compressive forces act to close the crack surfaces, thereby allowing for load transfer. Furthermore, in spite of any broken or misaligned fibres not carrying any additional loads (i.e., the compressive stiffness is dependent on the amount of longitudinal damage), the elastic domain, within the model, is postulated to remain unchanged. Conversely, amidst longitudinal compression, a kink band forms, comprised of damaged material (i.e., broken fibres and matrix cracks). However, this damage

does not align in a unique plane of orientation. Furthermore, under load reversal, compression generated cracks open, resulting in an increase in the elastic domain threshold [52]. Given these considerations, it may thus be expressed as:

$$\text{Tension loading:} \quad \dot{r}_{1+} = \dot{\phi}_{1+} \quad \text{and} \quad \dot{r}_{1-} = 0 \tag{4.19}$$

$$\text{Compression loading:} \quad \dot{r}_{1-} = \dot{\phi}_{1-} \quad \text{and} \quad \dot{r}_{1+} = \begin{cases} \dot{\phi}_{1-} & \text{if} \quad r_{1+} \leq r_{1-} \\ 0 & \text{if} \quad r_{1+} > r_{1-} \end{cases} \tag{4.20}$$

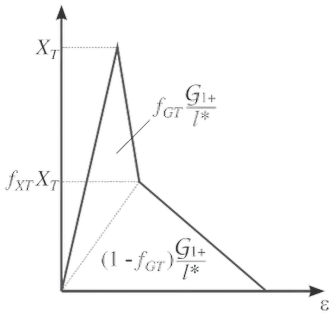
Integrating these expressions then yields:

$$r_{1+} = \max\left\{1, \max\left\{\phi^s_{1-}\right\}, \max\left\{\phi^s_{1+}\right\}\right\} \tag{4.21}$$

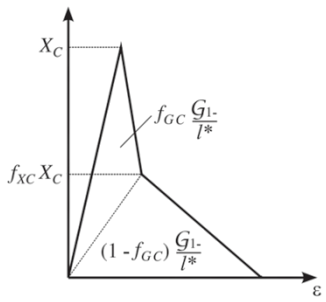
$$r_{1-} = \max\left\{1, \max\left\{\phi^s_{1-}\right\}\right\} \tag{4.22}$$

Lastly, for the complete definition of the damage laws, the stress-strain response of the material must be defined. To this purpose, different stress-strain relations pertaining to the aforementioned softening behaviour are considered for each corresponding damage mechanism to accurately capture the mechanical response of a UD lamina before and after initiation of the different failure modes [8]. Such responses are depicted in Figure 4.2, wherein:

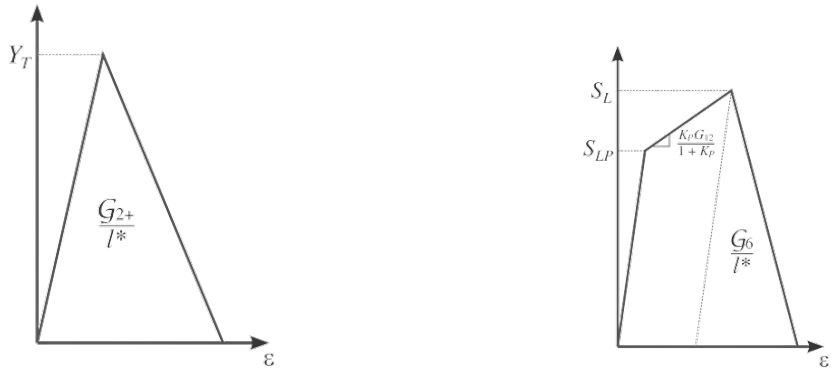
- Under longitudinal tensile loading, an initial linear-elastic response is assumed, followed by a bi-linear softening law after damage initiation (Figure 4.2a).
- Based on experimental findings by Moran et al. [126], the stress-strain response under longitudinal compression proposed by Furtado et al. [8] entails an initial linear-elastic response (preceding kink band formation) followed by linear softening, corresponding to the propagation of a kink band, until reaching a plateau, corresponding to kink band broadening at constant stress. Nonetheless, as will be discussed in subsequent sections, within the context of this work, a softening response akin to that of longitudinal tension was assumed (Figure 4.2b).
- Under transverse tensile/compressive loads, an initial linear-elastic response is assumed, followed by a linear softening behaviour (Figure 4.2c).
- Under in-plane shear, a nonlinear elasto-plastic response is assumed, wherein a reduced slope in the stress-strain curve is adopted to account for the inelastic response induced by plastic deformation, followed by a linear softening law (Figure 4.2d).



(a)



(b)



(c) **(d)**

Figure 4.2: Uniaxial response in: **a)** longitudinal tension, **b)** longitudinal compression, **c)** transverse tension/compression, **d)** in-plane shear (adapted from [8]).

Accordingly, the damage evolution laws herein employed lead to strain softening once an activation criterion is satisfied. Nonetheless, it should be noted that softening constitutive equations may yield physically implausible responses. Whereas for a material exhibiting a positive definite tangent stiffness tensor, there is an initial stage of damage (diffuse damage) and the numerical solution is independent of the numerical discretization, for composite materials, whose tangent stiffness tensor is not positive definite, damage localises in a narrow band, and the numerical solution depends upon the discretization. As a result, decreasing the element size in the localised zone decreases the computed energy dissipated and the structural response is not objective because it does not converge to a unique solution with mesh refinement [100].

To account for such mesh dependency [of the numerical solution] and guarantee correct energy dissipation during damage propagation, an energy regularisation approach is used. Within such solution, the slopes of the softening laws are determined as a function of the fracture toughness and as a function of the characteristic length of the FEs following the crack band model [8, 99]:

$$g_i = \frac{\mathcal{G}_i}{l^*} \tag{4.23}$$

where g_i comprises the energy dissipated per unit volume, $\mathcal{G}_i$ entails the fracture toughness and l^* consists of the characteristic length.

4.2.3 Effect of through-thickness stresses

As previously mentioned, the foremost goal with the revised intralaminar damage model was accounting for test cases wherein the triaxiality of the stress state is not negligible. To this purpose, the damage activation function pertaining to longitudinal compression was modified to include the aforementioned 3D invariant-based failure criterion for fibre kinking (Figure 4.3) proposed by Camanho et al. [111] used to define an artificial in-plane shear strength S_L^{ef} (Figure 4.4) representing the effect of hydrostatic pressure on the shear response of the matrix. This parameter is computed by means of imposing that, at failure, the two-dimensional activation function proposed by Maimí et al. [100] (left-hand side of the equation) equals that derived from the 3D invariant-based failure criterion [111] (right-hand side of the equation) [8]:

$$\frac{\left\langle \left|\widetilde{\sigma}_{12}^R\right| + \eta^L \widetilde{\sigma}_{22}^R \right\rangle}{S_L} = \alpha_1 I_1 + \alpha_2 I_2 + \alpha_3 I_3 + \alpha_{32} I_3^2 \tag{4.24}$$

and solving for the in-plane shear strength, S_L.

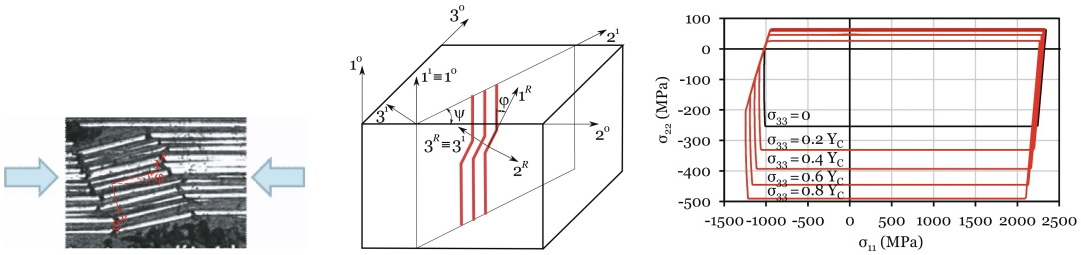


Figure 4.3: Fibre kinking kinematics and effect of through-thickness stresses predicted by a 3D invariant-based failure criterion [8].

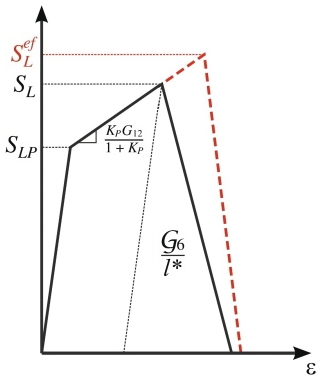


Figure 4.4: Effect of hydrostatic pressure on the longitudinal in-plane shear response [8].

In addition, the 3D invariant-based failure criterion included within the CDM model is used to scale the fracture toughness for longitudinal compression, $\mathcal{G}_{1-}$, as well as the longitudinal compressive strength ratio at the inflection point, f_{XC}, depending on the hydrostatic pressure. Concerning the former, it is scaled proportionally to the increase of longitudinal compressive strength [8]:

$$\mathcal{G}_{1-}^{ef} = \mathcal{G}_{1-} \left| \frac{\bar{\sigma}_{11}}{X_C} \right|, \quad \text{if } \left| \frac{\bar{\sigma}_{11}}{X_C} \right| > 1 \tag{4.25}$$

where X_C comprises the UD longitudinal compressive strength and $\bar{\sigma}_{11}$ pertains to the compressive strength predicted by invariant-based failure criterion for multi-axial stress states. On the other hand, with respect to the effective longitudinal compressive strength ratio at the inflection point, f_{XC}^{ef}, this parameter is expressed by:

$$f_{XC}^{ef} = \min\left\{1, f_{XC}\left(1 - f_{fxc}\left\langle -I_3 \right\rangle\right)\right\} \tag{4.26}$$

where $I_3 = \sigma_{22} + \sigma_{33}$ comprises the third invariant of the formulation proposed by Camanho et al. [111] and f_{fxc} constitutes a frictional parameter that needs to be calibrated using the experimental curves from a bearing, filled-hole compression or open-hole compression test.

Lastly, an engineering solution is further incorporated to account for changes in the in-plane shear fracture toughness, experimentally observed to increase under through-thickness compression, thereby also delaying delamination onset. This strengthening effect is thus represented by an effective fracture toughness, G_{IIc}^{ef}, [8]:

$$G_{IIc}^{ef} = G_{IIc}\left(1 - \eta_G \left\langle -\sigma_{33} \right\rangle\right) \tag{4.27}$$

where G_{IIc} pertains to the mode II fracture toughness, η_G comprises a material dependent empirically derived enhancement factor, σ_{33} denoted the through-thickness stress and $\langle x \rangle$ is the Macaulay operator. As stated by the authors [8], it can be postulated that transverse compression stresses, at the ply level, boast similar strengthening effects, given that a similar fracture process occurs for transverse cracking. As a result, the effective fracture toughness for in-plane shear is defined as:

$$\mathcal{G}_6^{ef} = \mathcal{G}_6 \left(1 - \eta_G \langle -\sigma_{22} \rangle\right) \tag{4.28}$$

Ultimately, the resulting effect of this modification is shown in Figure 4.5.

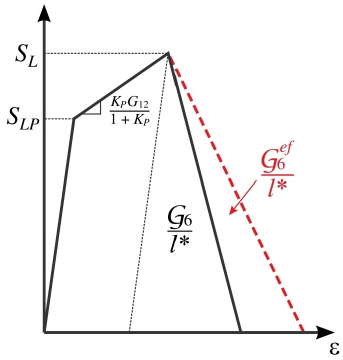


Figure 4.5: Effect of transverse compressive stresses on the longitudinal in-plane shear response [8].

4.2.4 In-situ strengths

Moreover, the accurate prediction of damage initiation and progression in composite laminates is fundamentally reliant on appropriate model formulation, yet an equally significant factor to consider is the accuracy of material properties that constitute the model. It is particularly crucial to recognise that certain ply properties, in light of the aforementioned in-situ effect, comprise *in-situ* strengths, i.e., their value varies with ply thickness when contained within a multi-directional laminate (as illustrated in Figure 4.6) [8]. Within this context, Camanho et al. [144] introduced an analytical model for predicting the *in-situ* transverse and shear strength based on a Fracture Mechanics model to correlate the *in-situ* properties with the fracture toughness of the material [8].

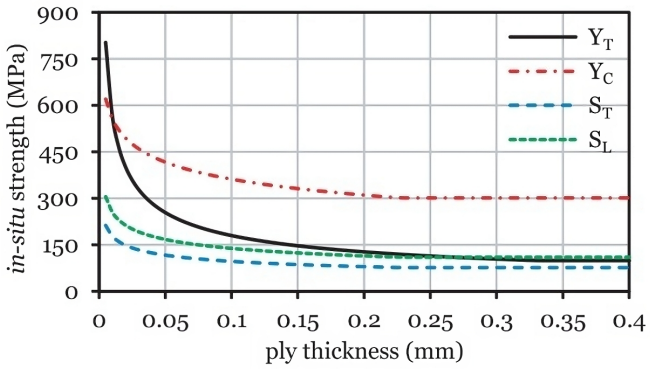


Figure 4.6: Ply *in-situ* strengths: transverse tensile strength, Y_T; transverse compressive strength, Y_C; transverse shear strength, S_T; in-plane longitudinal shear strength, S_L, [57].

In addition, the computation of *in-situ* shear strengths heavily leans on the approximation of the non-linear shear response, commonly achieved by employing either the Tsai-Hahn or Ramberg-Osgood laws. Notwithstanding, distinct methodologies yield different predictions, given that, as they currently are derived, these solutions are largely dependent on the shape of the stress-strain behaviour prior to failure. As a result, adopting contradictory assumptions for the shear behaviour to derive the *in-situ* strengths should be avoided. For the sake of consistency, the *in-situ* strengths must be defined in light of the bi-linear shear response implemented within the model [8].

Within this work, the *in-situ* strengths were computed and implemented. For the sake of completeness, such process is herein presented. According to Camanho et al. [144], three distinct ply configurations must be considered in the calculation of the transverse tensile and in-plane shear strengths, namely thick and thin inner, and thin outer.

Commencing with a **thick embedded ply** within a multi-directional laminate, a slit crack (refer to Figure 4.7) is expected to propagate in the transverse direction, T. Thereby, the mode I and II energy release rates may be expressed by [8]:

$$\mathcal{G}_I(T) = \frac{\pi a_0}{2}\Lambda^o_{22}\sigma^2_{22} \tag{4.29}$$

$$\mathcal{G}_{II}(T) = \frac{\pi a_0}{2}\chi\left(\gamma_{12}\right) \tag{4.30}$$

where $2a_0$ represents the length of the slit crack in the thickness direction, $\chi(\gamma)$ is given by [8]:

$$\chi\left(\gamma_{12}\right) = 2\int_0^{\gamma_{12}} \sigma_{12} d\gamma_{12} \tag{4.31}$$

and Λ^o_{22} is computed by [145]:

$$\Lambda^o_{22} = 2\left(\frac{1}{E_2} - \frac{\nu^2_{12}}{E_1}\right) \tag{4.32}$$

Moreover, Dvorak & Laws [145] postulate that the *in-situ* transverse tensile strength is attained by solving Equation 4.29 for Y^{is}_T:

$$Y^{is}_T = \sqrt{\frac{2\mathcal{G}_{Ic}(T)}{\pi a_0 \Lambda^0_{22}}} \tag{4.33}$$

With respect to the in-situ shear strength, the shear response of a composite laminate implemented in the present CDM model may be approximated as [8]:

$$\sigma_{12} = \begin{cases} G_{12}\gamma_{12}, & \gamma_{12} \leq S_{LP}/G_{12} \\ K_1\gamma_{12} + K_2, & \gamma_{12} > S_{LP}/G_{12} \end{cases} \tag{4.34}$$

where $K_1 = \frac{K_p G_{12}}{1+K_p}$, $K_2 = S_{LP}\left(1 - \frac{K_p}{1+K_p}\right)$, G_{12} comprises the in-plane shear modulus, S_{LP} defines the shear stress corresponding to the onset of plastic flow and K_p pertains to the shear incremental stiffness under plastic flow. The mode II fracture toughness is then attained by substituting Equation 4.34 in Equation 4.30 [8]:

$$\mathcal{G}_{IIc}(T) = \pi a_0 \left[\int_0^{\frac{S_{LP}}{G_{12}}} G_{12}\gamma_{12} d\gamma_{12} + \int_{\frac{S_{LP}}{G_{12}}}^{\gamma_{12}^{is}} \left(K_1\gamma_{12} + K_2\right) d\gamma_{12} \right] = \\ = \pi a_0 \left[\left(\gamma_{12}^{is}\right)^2 \frac{K_1}{2} + \gamma_{12}^{is} K_2 - \frac{S_{LP}^2}{2G_{12}(1+K_p)} \right] \quad (4.35)$$

In addition, Dvorak & Laws [145] further proposed that the *in-situ* strength of a thick embedded ply can be correlated to that of a UD thick ply, seeing as a UD laminate can be seen as a special case of a thick ply with unconstrained outer surfaces. Thereby, employing the classical solutions for stress intensity factors of surface cracks in unidirectional laminates, the mode I and II fracture toughness may be computed as [8]:

$$\mathcal{G}_{Ic}(T) = 1.12^2 \pi a_0 \Lambda_{22}^0 \left(Y^T\right)^2 \quad (4.36)$$

and

$$\mathcal{G}_{IIc}(T) = 2\pi a_0 \left[\gamma_L^2 \frac{K_1}{2} + \gamma_L K_2 - \frac{S_{LP}^2}{2G_{12}(1+K_p)} \right] \quad (4.37)$$

where $\gamma_L = \frac{S_L - K_2}{K_1}$. Furthermore, combining Equation 4.33 and Equation 4.36, the transverse tensile *in-situ* strength for a thick ply is taken as [8]:

$$Y_T^{is} = 1.12\sqrt{2} Y_T \quad (4.38)$$

and combining Equation 4.35 and Equation 4.37, the in-plane shear strength is attained by solving the following equation for γ_{12}^{is} [8]:

$$\left(\gamma_{12}^{\text{is}}\right)^2 \frac{K_1}{2} + \gamma_{12}^{is} K_2 = \gamma_L^2 K_1 + 2\gamma_L K_2 - \frac{S_{LP}^2}{2G_{12}(1+K_p)} \quad (4.39)$$

Ultimately, knowing γ_{12}^{is}, the in-plane shear strength is obtained by solving the second member of Equation 4.34 for σ_{12} [8]:

$$S_L^{is} = \sqrt{2S_L^2 - S_{LP}K_2} \quad (4.40)$$

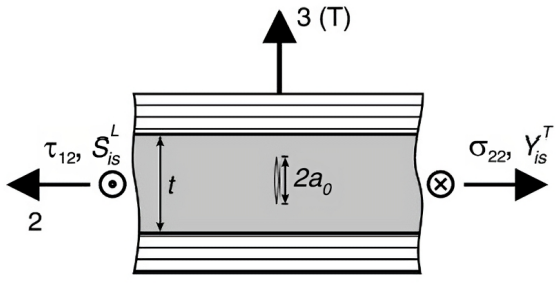


Figure 4.7: Thick embedded ply [8].

On the other hand, considering a **thin embedded ply**, a slit crack (Figure 4.8) is likely to grow in the longitudinal direction, L, since it already extended through the ply thickness, Therefore, the mode I and II energy release rates are expressedasby [8]:

$$\mathcal{G}_{Ic}(L) = \frac{\pi t}{8}\Lambda_{22}^{0}\sigma_{22}^{2} \tag{4.41}$$

$$\mathcal{G}_{IIc}(L) = \frac{\pi t}{8}\chi\left(\gamma_{12}\right) \tag{4.42}$$

The *in-situ* transverse tensile strength is thus computed by solving Equation 4.41 for Y_T^{is} [8]:

$$Y_T^{is} = \sqrt{\frac{8\mathcal{G}_{Ic}}{\pi t \Lambda_{22}^{0}}} \tag{4.43}$$

Furthermore, substituting Equation 4.31 in Equation 4.42 yields:

$$\mathcal{G}_{IIc} = \frac{\pi t}{4}\left[\left(\gamma_{12}^{is}\right)^{2}\frac{K_1}{2} + \gamma_{12}^{is}K_2 - \frac{S_{LP}^{2}}{2G_{12}(1+K_p)}\right] \tag{4.44}$$

Solving the previous equation for γ_{12}^{is}, the in-plane shear strength can be obtained by solving the second member of Equation 4.34 for σ_{12} [8]:

$$S_L^{is} = \sqrt{\frac{8\mathcal{G}_{IIc}K_1}{\pi t} + S_{LP}K_2} \tag{4.45}$$

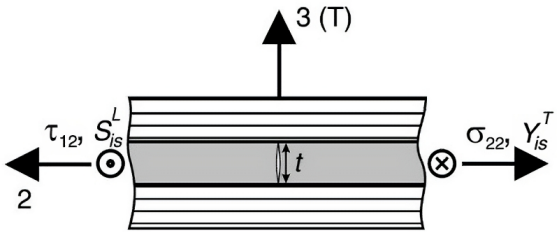


Figure 4.8: Thin embedded ply [8].

Lastly, a **thin outer ply** comprises a special case of the thin ply for which the energy release rate is larger, seeing as the slit crack is closer to the surface of the laminate (Figure 4.9). As a result, the mode I and II energy release rates read:

$$\mathcal{G}_{Ic} = 1.22^{2}\frac{\pi t}{4}\Lambda_{22}^{o}\sigma_{22}^{2} \tag{4.46}$$

$$\mathcal{G}_{IIc} = \frac{\pi t}{4}\chi\left(\gamma_{12}\right) \tag{4.47}$$

Once more, the *in-situ* transverse tensile strength is computed by solving Equation 4.46 for Y_T^{is} [8]:

$$Y_T^{is} = 1.78\sqrt{\frac{\mathcal{G}_{Ic}}{\pi t \Lambda_{22}^{0}}} \tag{4.48}$$

Moreover, substituting Equation 4.31 in Equation 4.47 yields:

$$\mathcal{G}_{IIc} = \frac{\pi t}{2}\left(\left(\gamma_{12}^{is}\right)^2 \frac{K_1}{2} + \gamma_{12}^{is} K_2 - \frac{S_{LP}^2}{2G_{12}(1+K_p)}\right) \tag{4.49}$$

Solving the previous equation for γ_{12}^{is}, the in-plane shear strength can be obtained by solving the second member of Equation 4.34 for σ_{12} [8]:

$$S_L^{is} = \sqrt{\frac{4\mathcal{G}_{IIc}K_1}{\pi t} + S_{LP}K_2} \tag{4.50}$$

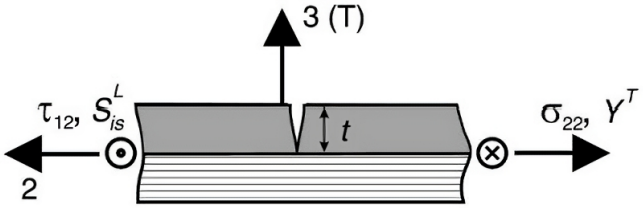


Figure 4.9: Thin outer ply [8].

Although not mentioned up to this point, the *in-situ* transverse compressive strength, Y_C^{is}, is computed by imposing that the slope of the $\sigma_{22} - \sigma_{12}$ failure envelope for $\sigma_{22} = 0$, η_L, is equal to that of the envelope obtained with the in situ properties (refer to Figure 4.10). Furthermore, for consistency, the derivation of the *in-situ* strength is predicated upon the LaRC03-04 failure criterion and the coefficient of longitudinal influence η_L, in spite of being possible to determine it experimentally, it may also be estimated in the absence of bi-axial test data by [8]:

$$\eta_L = \frac{-S_L^{UD}\cos\left(2\alpha_0\right)}{Y_C^{UD}\cos^2\left(\alpha_0\right)} \tag{4.51}$$

with the *in-situ* transverse compressive strength Y_C^{is}, in turn, being taken as:

$$\eta_L = \eta_{L,is} \Leftrightarrow Y_C^{is} = \frac{S_L^{is} Y_C^{UD}}{S_L^{UD}} \tag{4.52}$$

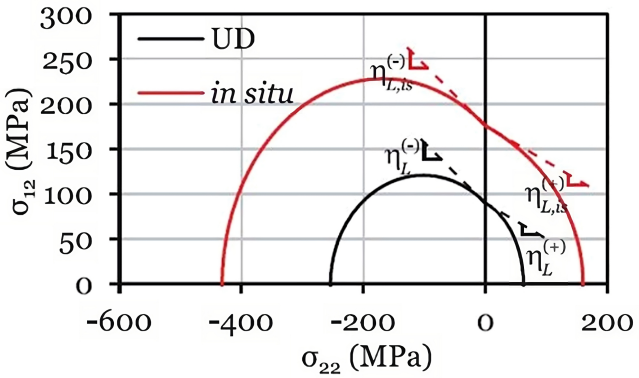


Figure 4.10: $\sigma_{22} - \sigma_{12}$ failure envelope [8].

In summary, the general algorithm for the computation of *in-situ* strengths consists of the following [8]:

- For an **embedded** ply:
  - the *in-situ* transverse tensile strength is taken as the maximum between those pertaining to thin and thick embedded plies:

$$Y_T^{is} = \max\left\{\sqrt{\frac{8\mathcal{G}_{Ic}}{\pi t\Lambda_{22}^0}},\quad 1.12\sqrt{2}Y_T^{UD}\right\} \tag{4.53}$$

  - the *in-situ* in-plane shear strength is taken as the maximum between those pertaining to thin and thick embedded plies:

$$S_L^{is} = \max\left\{\sqrt{\frac{8\mathcal{G}_{IIc}K_1}{\pi t} + S_{LP}K_2},\quad \sqrt{2S_L^2 - S_{LP}K_2}\right\} \tag{4.54}$$

  - the *in-situ* transverse compressive strength is given by:

$$Y_C^{is} = \frac{S_L^{is}Y_C^{UD}}{S_L^{UD}} \tag{4.55}$$

- For an **outer** ply:
  - the *in-situ* transverse tensile strength is taken as the maximum between:

$$Y_T^{is} = \max\left\{1.78\sqrt{\frac{\mathcal{G}_{Ic}}{\pi t\Lambda_{22}^0}},\quad Y_T^{UD}\right\} \tag{4.56}$$

  - the *in-situ* in-plane shear strength is taken as the maximum between those pertaining to a thin outer and a UD ply:

$$S_L^{is} = \max\left\{\sqrt{\frac{4\mathcal{G}_{IIc}K_1}{\pi t} + S_{LP}K_2},\quad S_L^{UD}\right\} \tag{4.57}$$

  - the *in-situ* transverse compressive strength is given by:

$$Y_C^{is} = \frac{S_L^{is}Y_C^{UD}}{S_L^{UD}} \tag{4.58}$$

4.3 Interlaminar damage model

4.3.1 Plain strength, open-hole & double edge-notched tests

4.3.1.1 Constitutive model

As previously stated, the methodology herein employed [8] for the CZMs of the plain strength, open-hole & double edge-notched tests is based on the approach introduced by Alfano et al. [141] aimed at combining interface damage with friction. For this purpose, a linear elastic behaviour is initially considered prior to a damage evolution phase governed by the law proposed by Crisfield et al. [146], along with the Coulomb friction function postulated by Catalanotti et al. [142]. The CZM devised by Alfano et al. [141] dictates that the homogenised interfacial stress over the representative element area, τ, is expressed by:

$$\tau = (1-d)\begin{bmatrix} K_{sh} & 0 & 0 \\ 0 & K_{sh} & 0 \\ 0 & 0 & K_n \end{bmatrix}\begin{bmatrix} \Delta_1 \\ \Delta_2 \\ \Delta_n \end{bmatrix} + d\begin{bmatrix} K_{sh} & 0 & 0 \\ 0 & K_{sh} & 0 \\ 0 & 0 & K_n \end{bmatrix}\begin{bmatrix} \Delta_1 - \Delta_1^{di} \\ \Delta_2 - \Delta_2^{di} \\ -\langle -\Delta_n \rangle \end{bmatrix} \tag{4.59}$$

where d denoted the damage variable; $\mathbf{K}$ represents the stiffness matrix; Δ pertains to the relative displacement vector and Δ^{di} comprises the inelastic sliding displacement [8]. The friction law engineered by Catalanotti et al. [142] is then introduced:

$$\phi = \mu\tau_n^d + \tau_{sh}^d \tag{4.60}$$

where τ_{sh}^d is computed as:

$$\tau_{sh}^d = \sqrt{\left(\tau_1^d\right)^2 + \left(\tau_2^d\right)^2} \tag{4.61}$$

ultimately yielding the non-associative correlation governing the evolution of Δ^{di}:

$$\dot{\Delta}^{di} = \dot{\lambda}\begin{bmatrix} \frac{\partial\phi}{\partial\tau_1^d} \\ \frac{\partial\phi}{\partial\tau_2^d} \\ 0 \end{bmatrix} = \dot{\lambda}\begin{bmatrix} \frac{\tau_1^d}{\tau_{sh}^d} \\ \frac{\tau_2^d}{\tau_{sh}^d} \\ 0 \end{bmatrix} \tag{4.62}$$

wherein the Kuhn-Tucker conditions: $\dot{\lambda} \geq 0, \phi(\tau) \leq 0$ and $\dot{\lambda}\phi(\tau) = 0$ must be fulfilled [8].

4.3.1.2 Mode dependent penalty stiffness

Beyond the formulation of the constitutive law, the comprehensive definition of the penalty stiffness is of the utmost importance in assuring the performance of CZMs. However, the majority of formulations provided in literature are primarily developed for pure mode loading and subsequently extended to account for mixed-mode loading conditions. As a result, their validation for such scenarios is often inadequate. In light of the aforesaid (refer to section 3.4), in a previous work, Turon et al. [78] assumed that the shear and normal penalty stiffness were equal ($K_n = K_{sh}$) and, thereby, a relation was imposed wherein the shear strengths do not embody fully independent material properties, instead being computed as a function of the mode I and mode II fracture toughness and the normal strength [8, 78]:

$$\tau_{sh}^0 = \tau_n^0\sqrt{\frac{\mathcal{G}_{IIc}}{\mathcal{G}_{Ic}}} \tag{4.63}$$

Notwithstanding, it is pivotal to note that the interface stiffness (K_n and K_{sh}) embody parameters that ensure a stiff connection between the crack surfaces before crack propagation, whereas the fracture toughness ($\mathcal{G}_{Ic}$ and $\mathcal{G}_{IIc}$) and interlaminar strengths (τ_n^0 and τ_{sh}^0) are properties that can be experimentally determined [8]. As a result, it was, in the same work, highlighted by the authors [78] that, so as to avoid erroneous calculation of the energy dissipation, and guarantee accurate predicitions of delamination, a dependent interface stiffness, $K_n \neq K_{sh}$, should be employed as opposed of the dependent shear strength, $\tau_{sh}^0 = f\left(\tau_n^0, \mathcal{G}_{Ic}, \mathcal{G}_{IIc}\right)$ [8, 78]:

$$\frac{K_{sh}}{K_n} = \frac{\mathcal{G}_{Ic}}{\mathcal{G}_{IIc}}\left(\frac{\tau_{sh}^0}{\tau_n^0}\right)^2 \tag{4.64}$$

This solution and the corresponding reformulation of the CZM were introduced in the most recent work by Turon et al. [77], wherein the mixed-mode tractions were defined as a function of the Euclidean norm of the individual tractions along the 1, 2, and 3 directions, considering various penalty stiffness values [8, 77]. The mixed-norm of the displacement jump, λ, is thereby redefined as:

$$\lambda = \frac{K_{sh}\Delta_{sh}^2 + K_n\Delta_n^2 - K_n\left\langle-\Delta_n\right\rangle^2}{\sqrt{K_{sh}^2\Delta_{sh}^2 + K_n^2\Delta_n^2 - K_n^2\left\langle-\Delta_n\right\rangle^2}} \tag{4.65}$$

4.3.1.3 Damage evolution law

The final step in the definition of the CZM encompasses the formulation of the damage activation and evolution functions. Beginning with the former, in accordance with Turon et al. [77], it is postulated as

$$F(\Delta) = H(\Delta) - r_d \leq 0 \tag{4.66}$$

where $H(\Delta)$ represents a monotonic loading function, and r_d comprises the threshold function [8, 77]. Both are respectively expressed as:

$$H(\Delta) = \min\left(\frac{\lambda - \Delta^0}{\Delta^f - \Delta^0}, 1\right) \tag{4.67}$$

$$r_d = \max\left(1, \max_s[H(\Delta)]\right) \quad 0 < s < t \quad \forall t \tag{4.68}$$

where Δ^0 and Δ^f respectively embody the displacement jumps pertaining to delamination onset and propagation under mixed-mode conditions [8, 77]. For their definition, the Benzeggagh and Kennane criterion [94] is employed as follows:

$$\Delta^0 = \sqrt{\frac{K_n\left(\Delta_n^0\right)^2 + \left[K_{sh}\left(\Delta_{sh}^0\right)^2 - K_n\left(\Delta_n^0\right)^2\right]\beta^\eta}{K_\beta}} \tag{4.69}$$

$$\Delta^f = \frac{K_n\Delta_n^0\Delta_n^f + \left[K_{sh}\Delta_{sh}^0\Delta_{sh}^f - K_n\Delta_n^0\Delta_n^f\right]\beta^\eta}{K_\beta\Delta^0} \tag{4.70}$$

where K_β represents a mode-dependent interfacial stiffness [8, 77], expressed as:

$$K_\beta = K_n(1-\beta) + \beta K_{sh} \tag{4.71}$$

and β pertains to the local mixed mode ratio defined as:

$$\beta = \frac{K_{sh}\Delta_{sh}^2}{K_{sh}\Delta_{sh}^2 + K_n\left\langle -\Delta_n\right\rangle^2} \tag{4.72}$$

Lastly, the damage variable, d, is computed as:

$$d = \frac{r_d\Delta^f}{r_d\Delta^f + (1 - r_d)\, r_d\Delta^0} \tag{4.73}$$

4.3.2 Low velocity impact tests

On the other hand, for the LVI simulations, a **built-in** Abaqus/explicit CZM based on cohesive surfaces is herein used for the interlaminar damage model. With respect to damage evolution, this parameter is governed by the shape of the cohesive law, herein assumed as linear. Furthermore, damage propagation further satisfies the Benzeggagh Kenane criterion [94], with a quadratic traction criterion being employed to assess damage onset [80, 124].

Moreover, considerations regarding the density of the cohesive interactions are noteworthy. Since the boundary-value problem is solved by the explicit dynamics procedure as a wave propagation one, a bounded solution is attained when the time increment for the simulation, Δt, is below the Stable Time Increment, STI. This parameter embodies the stability limit, i.e. the minimum

time required for a dilatation wave to move across any element with the model and, for a continuum FE, is given by [80, 124]:

$$\Delta t_{elem} \leq l^* \alpha \sqrt{\frac{\rho}{E}} \tag{4.74}$$

where ρ pertains to the material density, E denotes the maximum component of the constitutive tensor and $\alpha = \sqrt{1+\zeta^2} - \zeta$ wherein ζ comprises the critical damping fraction preventing FEs from ringing/collapsing for the highest element frequency. In addition, the STI for a zero-thickness cohesive element is expressed by [80, 124]:

$$\Delta t_{int}^{coh} \leq \sqrt{\frac{\bar{\rho}}{K_{coh}}} \tag{4.75}$$

where $\bar{\rho}$ and K_{coh} respectively pertain to the surface density and penalty stiffness values of the zero-thickness cohesive elements. Such equation is further applicable to Abaqus/Explicit surface elements. Notwithstanding, cohesive surfaces cannot be used with conventional shell elements in a straightforward manner when multiple plies are stacked over each other in light of a poor kinematic description. Whilst surface elements allow for a sheet of nodes without structural behaviour to be created, thereby making it possible to employ conventional shell elements with cohesive surfaces, their mass[6] must be defined, seeing as, within a dynamic system, all the nodes require inertia and mass terms, thereby rendering their definition akin to that of zero-thickness cohesive elements. Furthermore, the STI of a contacting surface is controlled by [80, 124]:

$$\Delta t_{int}^{con} \leq \sqrt{\frac{\rho h_{elem}}{K_n}} \tag{4.76}$$

where $\bar{\rho}$ pertains to the material density, h_{elem} denotes the element thickness to which the contacting surface belongs and K_n comprises the normal contact penalty stiffness value [80, 124]. Moreover, the computational time is primarily dictated by the STI, i.e., $\Delta t_{min} = \min(\Delta t_{elem}, \Delta t_{int}^{coh}, \Delta t_{int}^{con})$, however the interaction, Δt_{int}^{coh} and Δt_{int}^{con}, and element, Δt_{elem}, STIs are generally not the same. Focusing on the aforementioned mass definition, the surface density, $\bar{\rho}$, a numerical parameter, specified for the surface elements may be used to reduce the difference between the STIs and thereby reduce the simulation time by means of distributing the mass of the laminate throughout the elements. In regards to a surface element, this property may be expressed by [80, 124]:

$$\bar{\rho}_{sfm} = \frac{f_{sfm} \rho h_{lam}}{2(n_{int}+1)} \tag{4.77}$$

where h_{lam} comprises the laminate thickness, n_{int} denotes the number of interfaces modelled and f_{sfm} constitutes the optimum mass distribution factor (ranging between 0 and 1). Furthermore, when using conventional shell elements, their density must be altered to preserve the overall mass of the system [80, 124], i.e.,:

$$\rho_{mod} = \rho(1 - f_{sfm}) \tag{4.78}$$

Seeing as the STI inherent to the model, when combining shell elements with cohesive surfaces, may be controlled by the contact STI, Δt_{int}^{con}, the optimum mass distribution factor, f_{sfm}, may be obtained by equalling the STI expressions [80, 124]:

[6] This value should theoretically be zero, given that such elements do not possess any volume.

$$\frac{\Delta t_{int}^{con}}{\Delta t_{int}^{coh}} \simeq 1 \tag{4.79}$$

Notwithstanding, considering Equation 4.75, the STI is further affected by the contact penalty stiffness value, K_n, and, as a result, f_{sfm} must in fact be taken as the minimum between [80, 124]:

$$f_{sfm} = \min\left(\frac{2(n_{int}+1)K_n(l^*\alpha)^2}{2(n_{int}+1)K_n(l^*\alpha)^2 + Eh_{lam}}, \frac{2(n_{int}+1)h_{elem}^{min}}{2(n_{int}+1)h_{elem}^{min} + h_{lam}}\right) \tag{4.80}$$

where E comprises the maximum component of the constitutive tensor and h_{elem}^{min} denotes the minimum element thickness modelled [80, 124].

Lastly, the CZM requires the definition of a cohesive penalty stiffness value. As the material is perfectly bonded prior to crack nucleation, this parameter should ideally be as large as feasible so as to not contribute to the global compliance of the structure. To this purpose, some authors recommend defining it as the ratio between the interface elastic modulus and the interface thickness, whereas others recommend it to be $K_{coh} \geq \frac{50E_{22}}{t}$. The aforementioned definitions lead to penalty stiffness values in the order of 5×10^5 to 1×10^6, which have been used to attain accurate predictions. In addition, this parameter must have the same value for mode I and II to avoid incurring in changes in the local mode ratio under mixed-mode damage evolution unless a consistent formulation is used. Notwithstanding, in explicit simulations, the penalty stiffness does not only affect the accuracy, but also, as above-stated, the computational performance through the STI (refer to Equation 4.75).

Delving further into the intricacies of this parameter for a more comprehensive understanding, it may be seen as a series of springs for which the equivalent stiffness is:

$$\frac{1}{E_{eq}^{coh}} = \sum_{n=1}^{n_{plies}} \frac{h_i}{E_i} + \sum_{n=1}^{n_{int}} \frac{1}{K_i} \tag{4.81}$$

and the value E_{eq}^{coh} should equal the equivalent stiffness of the system without cohesive elements, E_{eq}, (Figure 4.11) [80, 124], i.e.,

$$\frac{1}{E_{eq}} = \sum_{n=1}^{n_{plies}} \frac{h_i}{E_i} \tag{4.82}$$

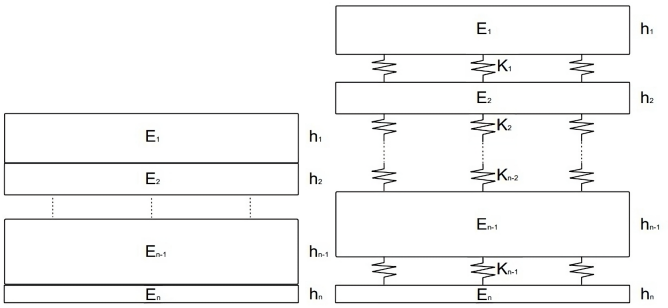


Figure 4.11: System without (left) and with (right) cohesive elements [80, 124].

Thereby, the penalty stiffness not merely depends on the loading conditions, but also on the number of interfaces considered and the elastic properties of the surrounding plies. As a result,

challenges are posed in defining a closed-form expression to estimate the penalty stiffness that takes into account all of these factors. Consequently, such value is commonly derived through a sensitivity analysis on the elastic regime to choose the minimum one for which convergence to the same elastic response is achieved, thus not affecting the compliance of the model whilst also mitigating the detrimental effect on the STI [80, 124].

Chapter 5

Finite element model

Within the present chapter, we seek to comprehensively describe the FE framework employed in the analysis of a CFRP NCF laminate. To this purpose, we commence by providing a brief introduction into the intricacies of the finite element analyses, FEAs, conducted. Subsequently, the models of the plain strength, open-hole and double-edge notched tests (both in tension and compression) are described, given the similarity between the adopted methodologies. Lastly, we meticulously examine the approach used for the low velocity impact simulations.

5.1 Introduction

To mitigate the extensive experimental campaigns required within the *building block approach* to determine design parameters, the accurate numerical prediction of damage onset and evolution by means of FEAs emerges as a matter of utmost significance [3, 8]. As a result, aligned with the foremost objective of the present thesis of characterising vital material parameters and assessing the validity of standard modelling approaches for UDPT laminates, FEAs were conducted on representative unidirectional NCF coupons, including un-notched, open-hole, double-edge notched and low velocity impact simulations.

The FEAs were conducted on the explicit commercial FE code Abaqus®/Explicit and parametric `Python` scripts were employed within the model generation phase. This approach reveals itself of the utmost importance, by allowing the expedited definition of the necessary FE models with remarkable flexibility. Various geometries, lay-ups and materials can be attained by means of simple modifications to the governing parameters, i.e., width, length, hole diameter and notch length and radius for the geometry, the number of plies and ply angles for the stacking sequence, and the ply material properties for the material system [3].

Lastly, all the necessary models were defined at the mesoscale, i.e., predicated upon a ply-by-ply discretization, wherein laminate layers are regarded as the fundamental homogeneous building blocks and imperfections and variabilities inherent to lower scales are neglected, thereby becoming more suitable in ascertaining the damage and failure of the bulk laminate [1, 3, 9, 69, 70].

5.2 Plain strength, open-hole and double-edge notched models

Starting with the geometries of the plain strength, open-hole and double-edge notched models, the necessary parameters for their definition include width, w, hole diameter, d, and notch length, a and notch tip radius. It should be noted that the radius is maintained at a constant 0.5 mm for all coupons. The remaining values align themselves with those employed in the corresponding benchmark experimental tests and are compiled in Tables 5.1 through 5.3 considering the various specimens required.

Table 5.1: Geometry of the plain strength models.

	Plain tension/compression
w [mm]	25.0

Table 5.2: Geometries of the open-hole models.

	Open-hole tension		Open-hole compression	
Specimen	# 1	# 2	# 1	# 2
w [mm]	36.0	72.0	36.0	18.0
d [mm]	6.0	12.0	6.0	3.0

Table 5.3: Geometries of the double-edge notched models.

	Double-edge notched tension				Double-edge notched compression				
Specimen	# 1	# 2	# 3	# 4	# 1	# 2	# 3	# 4	# 5
w [mm]	5.0	10.0	20.0	25.0	5.0	7.5	10.0	12.5	15.0
a [mm]	3.0	6.0	12.0	15.0	3.0	4.5	6.0	7.5	9.0

Furthermore, the laminate is clamped on one end, while at the opposite side a displacement is imposed on all boundary nodes by means of defining an appropriate smooth step amplitude. Notwithstanding, the imposition of such boundary conditions, BCs, raises concerns pertaining to the un-notched models. In this case, stress singularities may develop in regions close to the BCs, promoting early failure and yielding spurious results[1]. To mitigate this, two linear elastic regions are included in both the upper and bottom sides of the specimen and are connected to the laminate by means of tie constraints to ensure accurate kinematic description. Moreover, given the symmetry of the double-edge notched models, only half of the specimen is represented (i.e., the experimental width parameter corresponds to $2w$) to significantly reduce the computational cost. Thereby, a symmetry BC must also be introduced.

On the other hand, with respect to the material system studied herein, distinct stacking sequences are considered. Concerning the plain strength models, solely the baseline centre-symmetric (i.e., the mid-plane axis runs through the centre of the mid-ply [125]) laminate composed of 13 intermediate grade plies (nominal thickness of 0.143 mm) is analysed. The corresponding lay-up is $[45/\text{-}45/0/45/\text{-}45/90/0]_{\$}$ and the total nominal thickness amounts to 1.86 mm. In regards

[1] This is usually not a concern in open-hole and double-edge notched models, seeing as the presence of a hole/notch already leads to a stress concentration, thereby promoting failure in the vicinity of the feature.

to the open-hole cases, so as to ascertain the sensitivity of the model to off-axis loading conditions, three additional stacking sequences are assessed, corresponding to 30, 60 and 90° off-axis tension/compression (refer to Table 5.4). Lastly, pertaining to the double-edge notched models, cross-ply centre-symmetric laminates (illustrated in Table 5.5) are adopted, yet with a distinct number of plies (and corresponding thickness), i.e., a 15 ply (2.15 mm thick) and a 31 ply (4.43 mm thick) laminates are defined for, respectively, tension and compression.

Table 5.4: Lay-ups for the open-hole models.

	Lay-up
0° off-axis	$[45/-45/0/45/-45/90/0]_{\$}$
30° off-axis	$[75/-15/30/75/-15/-60/30]_{\$}$
60° off-axis	$[-75/15/60/-15/15/-30/60]_{\$}$
90° off-axis	$[-45/45/90/-45/45/0/90]_{\$}$

Table 5.5: Lay-ups for the double-edge notched models.

	Lay-up
DENT	$[90/0/90/0/90/0/90/0]_{\$}$
DENC	$[90/0/90/0/90/0/90/0/90/0/90/0/90/0/90/0]_{\$}$

Lastly, with respect to the mesh, one 8-node linear brick element with reduced integration (C3D8R) per ply thickness is adopted for the plies, whereas the interface is represented with 0.01 mm thick COH3D8 user-defined cohesive elements. Additionally, concerning the former, since the elements have only one integration point, it is possible for them to distort in such a way that the strains calculated at the integration point are all zero, which, in turn, leads to uncontrolled distortion of the mesh, i.e., hourglassing. So as to avoid this, *enhanced* hourglassing control is selected. As for the mesh sizes, making use of Equation 3.7, the maximum element size may be computed for each damage mechanism. These values are reported in Table 5.6 and, in light of them, a mesh of 0.25 × 0.25 × t is defined for the un-notched models, with the parameters increasing to 0.5 × 0.5 × t mm^3 for both open-hole and double-edge notched simulations. These values were selected in order to attain reasonably fine meshes without significantly enhancing the computational demand.

Table 5.6: Maximum element sizes for each damage mechanism.

Damage mechanism	L_e^{Max} [mm]
X_T	17.5
X_C	18.2
Y_T	7.6
Y_C	3.2
S_L	5.9

Ultimately, the definition of the plain strength, open-hole and double-edge notched is comprehensively illustrated in Figures 5.1 to 5.3.

5.2. Plain strength, open-hole and double-edge notched models

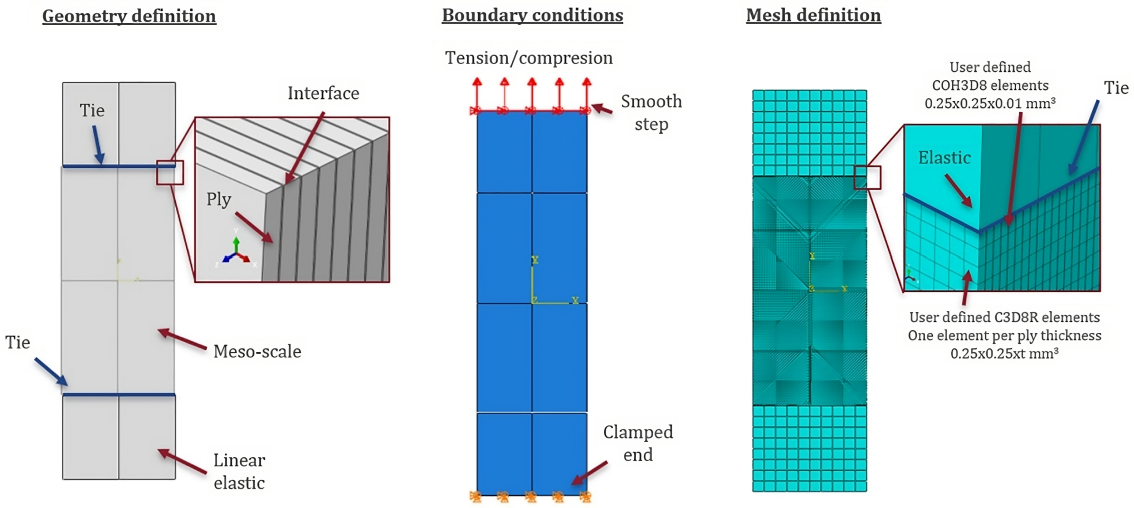


Figure 5.1: Finite element models for plain tension and compression [8].

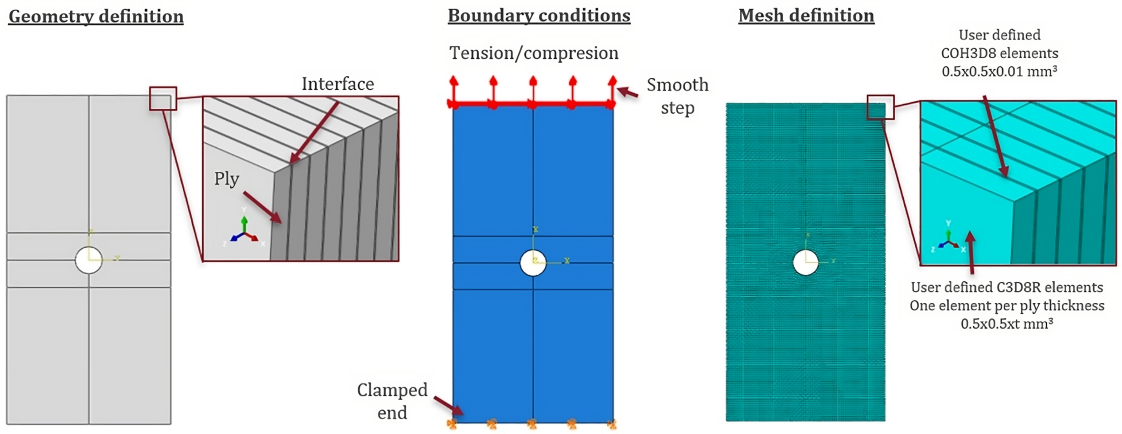


Figure 5.2: Finite element models for open-hole tension and compression [8].

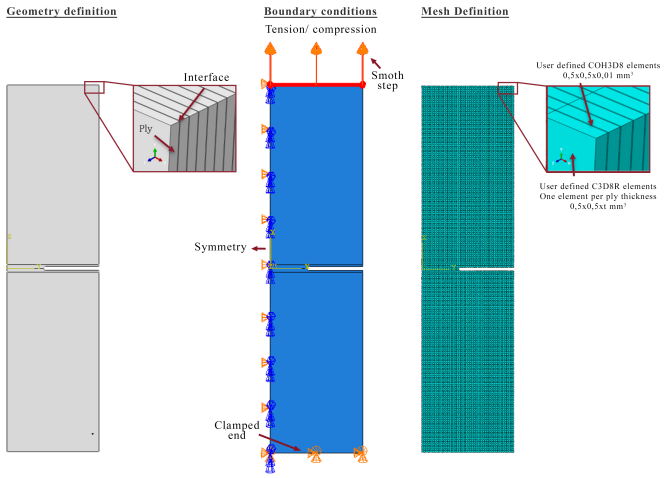


Figure 5.3: Finite element models for double-edge notched tension and compression (adapted from Furtado et al. [8]).

5.3 Low velocity impact models

The FE model herein specified for the LVI simulations is aimed at reproducing the ASTM D7136 [147] test standard. As previously mentioned, the composite laminate is defined at the mesoscale, wherein every ply (as an homogenised material) and every interface (susceptible to delamination) are represented, as it has been demonstrated to boast accurate predictions for such conditions [80, 124]. Commencing with the geometry adopted, rectangular specimens of 100 × 150 mm^2 are considered. A rectangular support for the plate of 125 × 75 mm^2 is further represented, along with four cylindrical clamps (ϕ = 14 mm) to restrain the coupon and emulate the rubber clamps commonly used in these experimental tests to restrain the composite component. Lastly, an hemispherical impactor of ϕ = 16 mm and m = 2 kg are modelled as well (as illustrated in Figure 5.4).

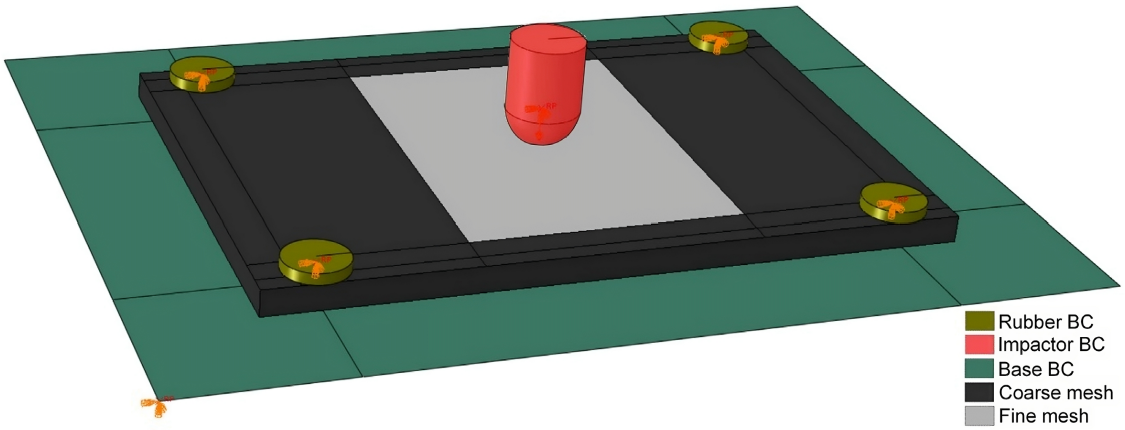


Figure 5.4: Numerical model and BCs considered for the LVI simulations [80, 124].

Concerning the BCs, all the inherent degrees of freedom for both the support and clamps are fixed in order to avoid any movement within these components. On the other hand, for the impactor, naturally, a vertical downwards (out-of-plane direction for the plate) velocity is initially imposed, whose value is contingent upon the considered impact energy. Within our work, the considered scenarios encompass impacts of 6.7, 13.4 and 20.1 J. In addition, for these simulations, contact and friction parameters must be specified. To this purpose, aligned with the methodology proposed by Soto et al. [80, 124], built-in Abaqus/Explicit algorithms are employed. With respect to the former, the contact penalty method is selected, wherein the contact stiffness value, K_n, is adjusted to equal the penalty stiffness inherent to the cohesive elements, K_{coh}, in order to, as stated, control the STI. As for the latter, the Coulomb friction model is resorted to, with the friction coefficients being set to 0.1 (between both the plies, and the impactor and the plate). Furthermore, the placement of surface elements at interfacial locations necessitates the definition of tie constraints (Figure 5.5) to establish a link between them and the plies, thereby ensuring an accurate kinematic description to assess delamination. The discretization method used is surface-to-surface, with the master one always being assigned to the plies [80, 124].

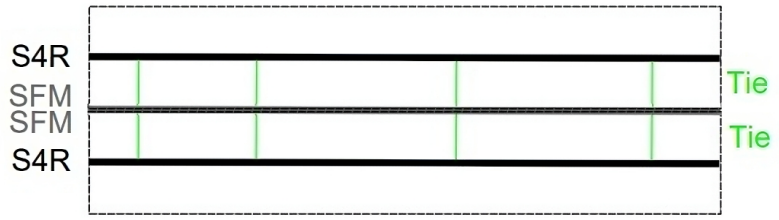


Figure 5.5: Modelling strategy pertaining to conventional shell elements linked to surface elements [80, 124].

In regards to the numerical discretization, the impactor, support and clamps are all modelled by means of rigid elements (R3D4), however distinct mesh sizes are specified, namely 0.5, 2.5 and 1 mm for each respective component. Conversely, conventional shell elements with reduced integration (S4R) are assigned to the composite plies (represented at the mid-plane, without offset) and, in addition, a refined region (of 90 $\times$ 90 mm^2) is also defined. This aids in guaranteeing correct energy dissipation, yet is only allocated to the vicinity of the impact site in order to reduce the computational effort. As a result, two distinct element sizes are defined[2], i.e., 1.0 and 5.0 mm for respectively the refined and un-refined zones. Moreover, as previously mentioned, surface elements are attributed to interfacial locations [80, 124]. With respect to the material system, the lay-up considered comprises the aforesaid centre-symmetric sequence, i.e., $[45/\text{-}45/0/45/\text{-}45/90/0]_{\$}$.

[2]Keeping in mind the maximum element sizes computed within the preceding section.

Part IV

Results & discussion

Chapter 6

Material card identification

In this chapter, we aim to thoroughly present the results pertaining to the material card identification process. As previously mentioned, the methodology herein employed was an inverse one resorting to double-edge notched models. To this purpose, we commence by providing and discussing the results attained for these specimens in tension. Subsequently, we comprehensively describe the solution obtained for the double-edge notched compression tests. Lastly, the ascertained material card properties are showcased.

6.1 Double-edge notched tension

6.1.1 Size effect law

Starting with the double-edge notched tension, DENT, specimens, our primary goal with these simulations was ascertaining (by means of an iterative procedure[1]) the optimal, according to the experimentally determined size effect law, longitudinal tensile stress at the inflection point and the fraction of the longitudinal tensile fracture toughness dissipated up to that point. These variables are respectively governed by the computational parameters f_{XT} and f_{GT} that dictate the shape of the cohesive law (refer to Figure 4.2a).

To this purpose, our initial iteration, i.e., $f_{XT} = 0.4$ and $f_{GT} = 0.1$ (refer to Figure 6.1), was based on the values employed by Furtado et al. [8]. However, it should be noted that the amount of energy dissipated in the first portion of the bi-linear law was lowered (from 0.3-0.52 to 0.1), seeing as the longitudinal fracture toughness pertaining to the material in study was remarkably high. As a result, it was initially expected that an exceedingly high f_{GT} would yield a poor correlation with the experimental results, particularly for larger specimens, whose resistance is mainly dominated by the fracture toughness of the material. Notwithstanding, the obtained predictions immediately exhibited strong disparities in relation to the experimental results for the smaller coupons. As shown in Table 6.1, the numerical results for the two smallest models were significantly above the 10% threshold considered ideal in the aeronautical industry. Although only two specimens were analysed, if we were to consider a linear progression as illustrated in Figure 6.2a, it is clear to see that the difference between the experimental and numerical results would inevitably grow. Thereby, this cohesive law was disregarded.

[1] It should be noted that only the most significant iterations are shown herein.

6.1. Double-edge notched tension

Table 6.1: Numerical predictions for iteration 1 of the DENT models.

	Experimental results		Numerical results	
w [mm]	σ_{max}^{exp} [MPa]	STDV [MPa]	σ_{max}^{num} [MPa]	Relative error [%]
5	386.5	24.6	306.8	-20.62
10	322.0	20.7	268.45	-16.63

In our second iteration, in an attempt to overcome the limitations described above, the parameter f_{GT} was augmented to 0.42 to more accurately estimate the resistance values of the larger coupons. In addition, although the influence of this parameter is reduced for the smaller specimens, it inevitably affects the estimated values. Consequently, to mitigate any potential severe overestimation that could occur by increasing the fraction of the longitudinal tensile fracture toughness dissipated up to the inflection point, f_{XT} was conversely lowered to 0.3 (refer to Figure 6.1). With these alterations, we were able to obtain remarkably more accurate numerical predictions for the smaller coupons, evidenced by relative errors significantly below 10% (as depicted in Table 6.2). Nonetheless, concerns arose with respect to the strength prediction for the biggest specimen and with the slope of the size effect law shown in Figure 6.2b. As the resistance of larger coupons is mainly governed by the fracture toughness, considerably increasing f_{GT} yielded exceedingly high predictions, ultimately resulting in an inaccurate representation of the size effect.

Table 6.2: Numerical predictions for iteration 2 of the DENT models.

	Experimental results		Numerical results	
w [mm]	σ_{max}^{exp} [MPa]	STDV [MPa]	σ_{max}^{num} [MPa]	Relative error [%]
5	386.5	24.6	381.95	-1.18
10	322.0	20.7	330.90	+2.76
20	259.0	7.8	280.42	+8.27
25	235.2	8.0	268.21	+14.04

Considering the above results, wherein the resistance values laid within the ideal threshold for the smaller specimens, for our third iteration, modifications were exclusively made to f_{GT}, with the objective of augmenting the slope of the size effect curve. By decreasing f_{GT} to 0.3, whilst keeping f_{XT} unaltered (refer to Figure 6.1), it was expected that the strength predictions for the larger specimen would significantly decrease, thereby increasing the slope. Accordingly, as depicted in Table 6.3 and Figure 6.2c, the resistance values were kept below the ideal threshold and the slope increased, ultimately falling within the 10% threshold (relative error of -5.77%).

Table 6.3: Numerical predictions for iteration 3 of the DENT models.

	Experimental results		Numerical results	
w [mm]	σ_{max}^{exp} [MPa]	STDV [MPa]	σ_{max}^{num} [MPa]	Relative error [%]
5	386.5	24.6	361.97	-6.35
10	322.0	20.7	297.36	-7.65
20	259.0	7.8	249.4	-3.71
25	235.2	8.0	231.99	-1.36

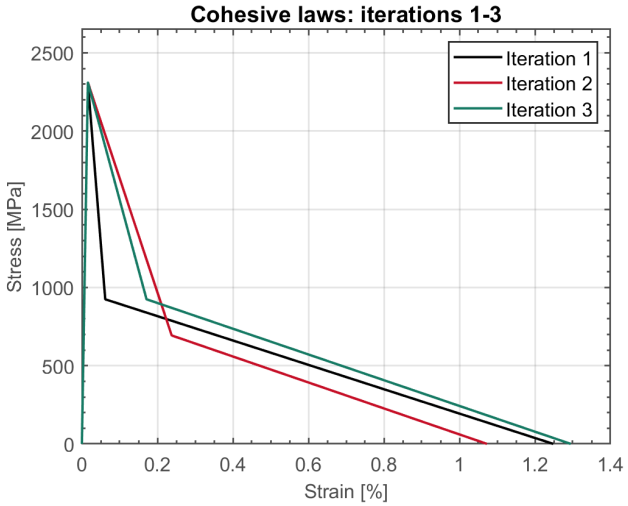
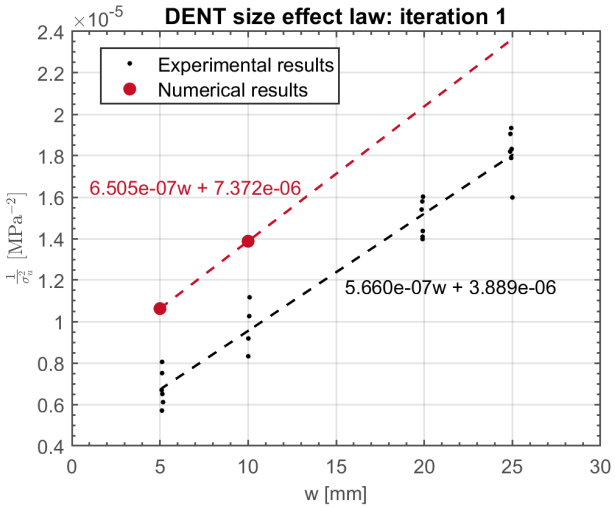
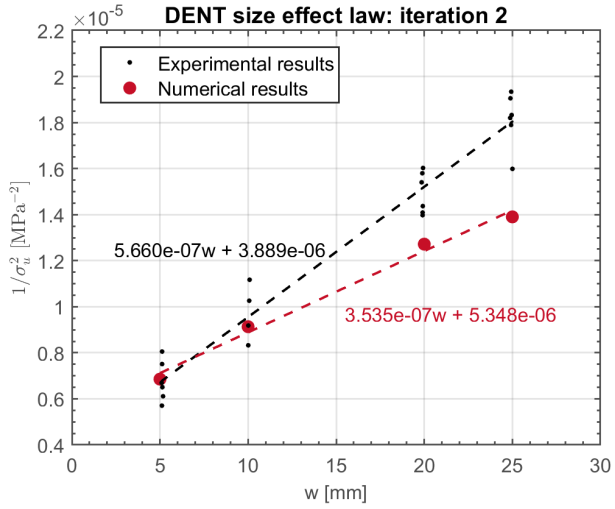


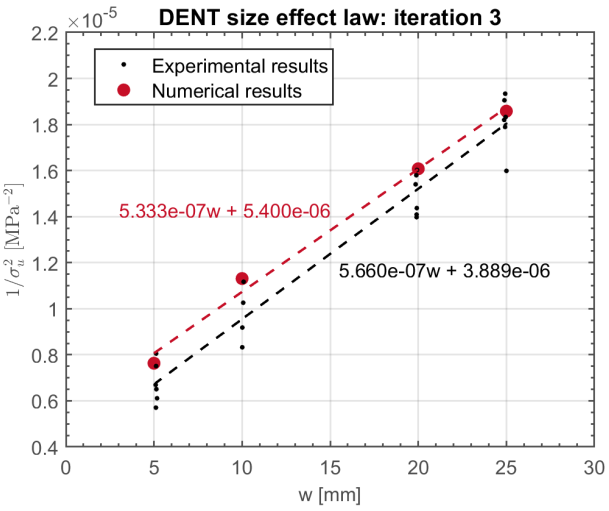
Figure 6.1: Tensile bi-linear cohesive laws: iterations 1-3.



(a)



(b)



(c)

Figure 6.2: DENT numerical size effect laws: **a)** iteration 1, **b)** iteration 2 **c)** iteration 3.

Nevertheless, as will be discussed in subsequent chapters, when initially applying these parameters to off-axis open-hole loading conditions, inaccurate results were recorded. Although this is not a direct consequence of the ascertained computational parameters, premature failure was observed in these specimens due to inadequate delamination and in-plane shear responses. Concerning the former, given that 30 and 60° plies are highly susceptible to delamination, it was postulated that, as opposed to the commonly employed initiation values for the mode I and II fracture toughness (respectively 0.388 and 2.141 N/mm), the propagation ones (respectively 0.843 and 2.381 N/mm) would delay the onset of interlaminar damage, thus postponing failure. On the other hand, concerning the latter, it was theorised that augmenting the elastic domain and consequently delaying damage initiation (as shown in Figure 6.3), i.e., a cohesive law akin to the highest experimental shear resistance curves would yield more accurate results. Accordingly, such effects were noted.

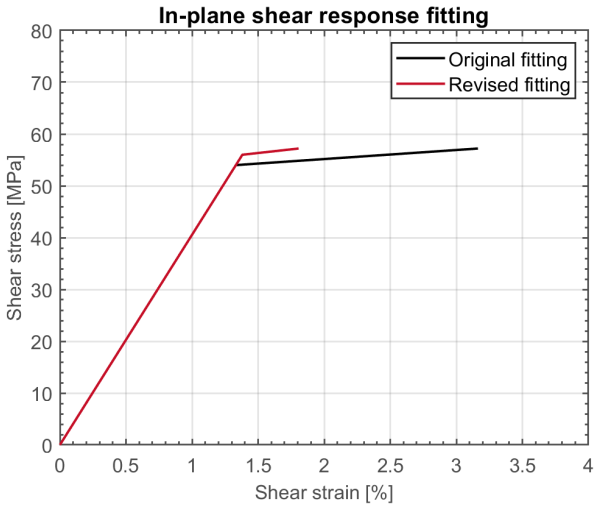


Figure 6.3: In-plane shear response fitting.

Notwithstanding, given that these changes were initially assessed for open-hole coupons, it was necessary to guarantee that they would not compromise the results stated above, thereby requiring

additional iterations. In fact, for these parameters, the cohesive law used for iteration 3 (shown in Figure 6.1) did not prove to be adequate. Interestingly, the alterations made significantly decreased the numerical predictions for the larger specimens (refer to Table 6.4) and, although these values still remained below the 10% threshold, the size effect was no longer precisely captured, clearly evidenced by the increased slope in Figure 6.4 exhibiting a relative error of 21.51%.

Table 6.4: Revised numerical predictions for iteration 3 of the DENT models.

	Experimental results		Numerical results	
w [mm]	σ_{max}^{exp} [MPa]	STDV [MPa]	σ_{max}^{num} [MPa]	Relative error [%]
5	386.5	24.6	368.88	-4.56
10	322.0	20.7	294.78	-8.45
20	259.0	7.8	236.71	-8.61
25	235.2	8.0	216.3	-8.04

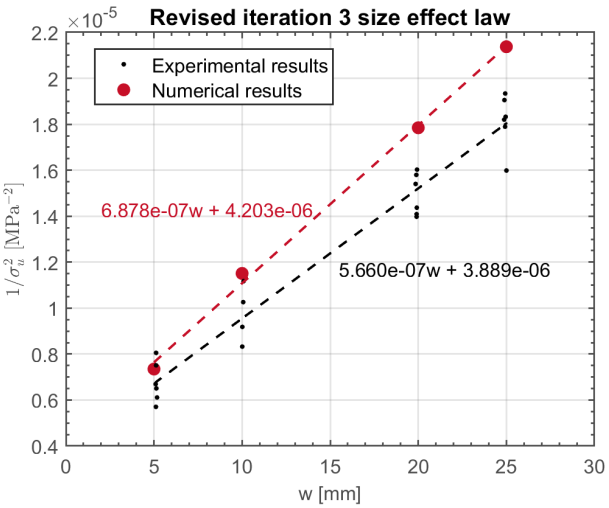
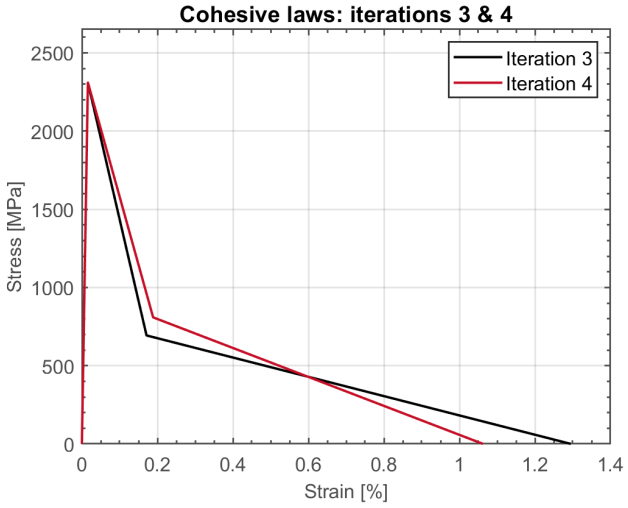
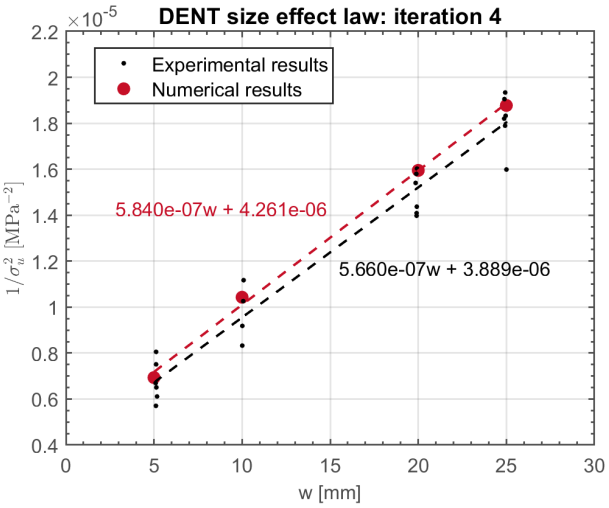


Figure 6.4: Revised size effect law for iteration 3 of the DENT models.

As a result, a similar methodology to iteration 3 was employed, wherein the f_{GT} parameter was augmented to 0.33 for iteration 4. However, analysing the numerical prediction for the second smallest specimen, it was also theorised that f_{XC} should be increased to mitigate the significant drop observed. Consequently, this variable was increased to 0.35, with the attained cohesive law shown in Figure 6.5a. Accordingly, as depicted in Table 6.5 and Figure 6.5b, the predicted resistance values fell below the ideal threshold and the slope decreased, ultimately both falling within the admissible relative error (relative error of +3.18% for the latter).



(a) Tensile bi-linear cohesive laws: iterations 3 & 4



(b) Size effect law

Figure 6.5: Numerical results for iteration 4 of the DENT models.

Table 6.5: Numerical predictions for iteration 4 of the DENT models.

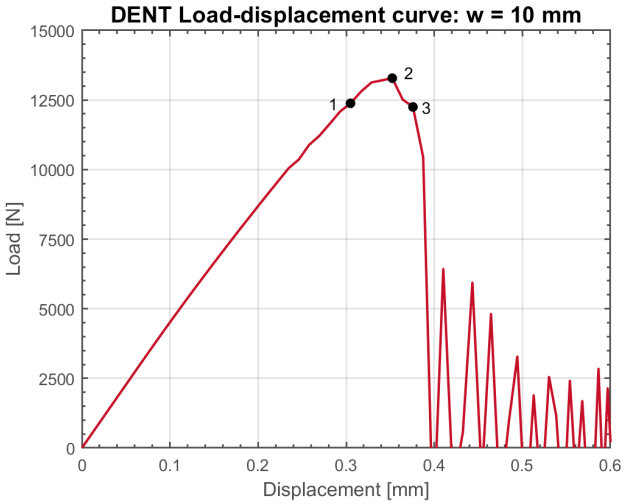
	Experimental results		Numerical results	
w [mm]	σ_{max}^{exp} [MPa]	STDV [MPa]	σ_{max}^{num} [MPa]	Relative error [%]
5	386.5	24.6	379.78	-1.74
10	322.0	20.7	309.65	-3.84
20	259.0	7.8	250.4	-3.32
25	235.2	8.0	230.79	-1.88

6.1.2 Damage onset & evolution history

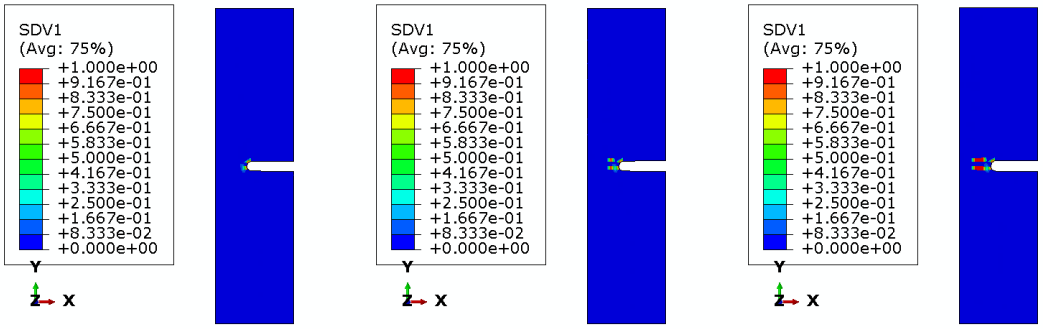
Beyond the numerical predictions themselves, one of the primary advantages of the employed CDM model is also being able to provide the entire damage onset and evolution history. Thereby, it becomes relevant to analyse its initiation and progression, which, within the scope of the DENT tests, is presented for the w = 10 mm coupon that presents general features across the considered

sizes. To this purpose, we refer to Figure 6.6, wherein the load-displacement curve and the evolution of the damage variables for distinct points along the curve are given.

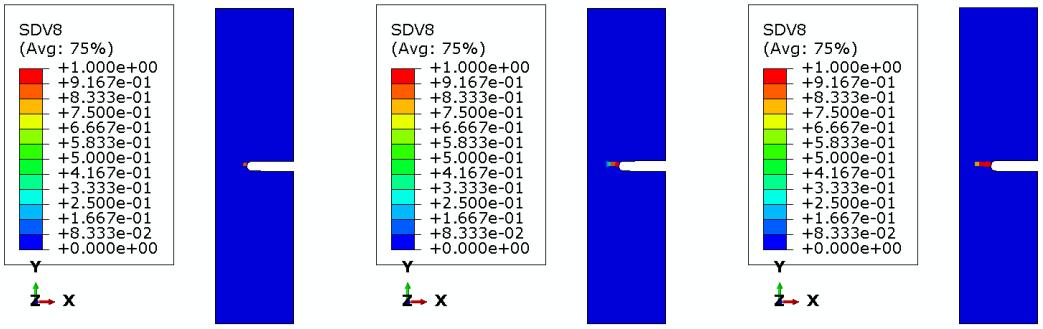
As expected, both inter- and interlaminar damage nucleates around the notch tip as depicted in Figures 6.6b, 6.6e, 6.6k and 6.6h. Its presence inherently introduces localised stress concentrations, which are accurately predicted by the phenomenological model. Furthermore, as the applied load increases, transverse matrix cracks grow across the width of the specimen as illustrated in Figure 6.6l, as a result of fibre breakage in the embedded 0° plies (refer to Figure 6.6f), with the damage being confined to an area near the notch. Such localised damage ultimately induces catastrophic failure, as per Figure 6.6g.



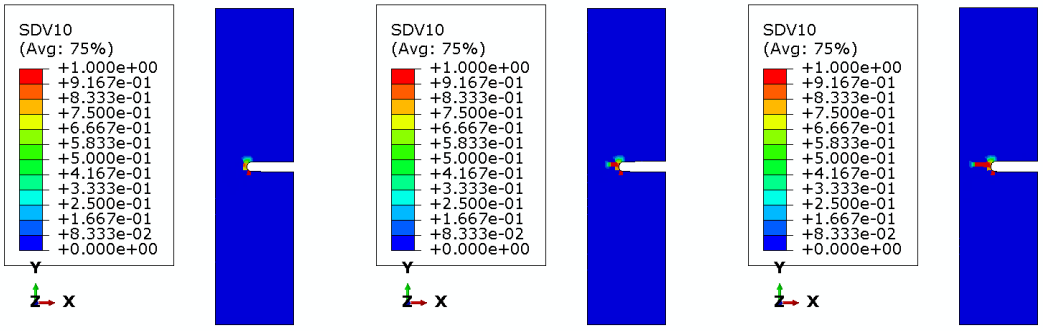
(a) Load-displacement curve



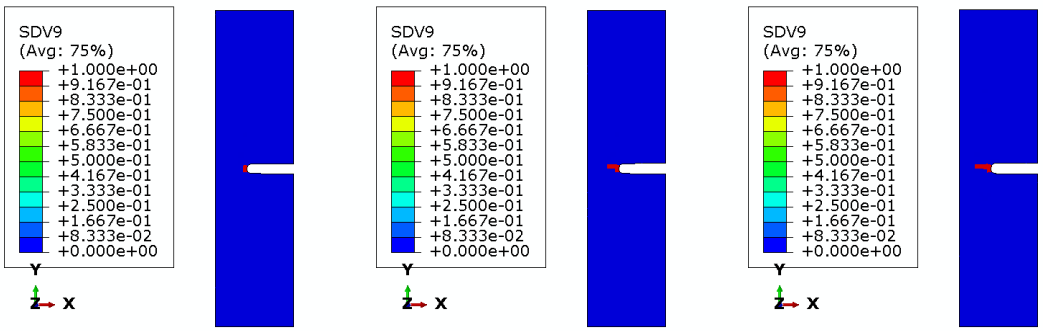
(b) Point 1: interface damage **(c)** Point 2: interface damage **(d)** Point 3: interface damage



(e) Point 1: longitudinal damage **(f)** Point 2: longitudinal damage **(g)** Point 3: longitudinal damage



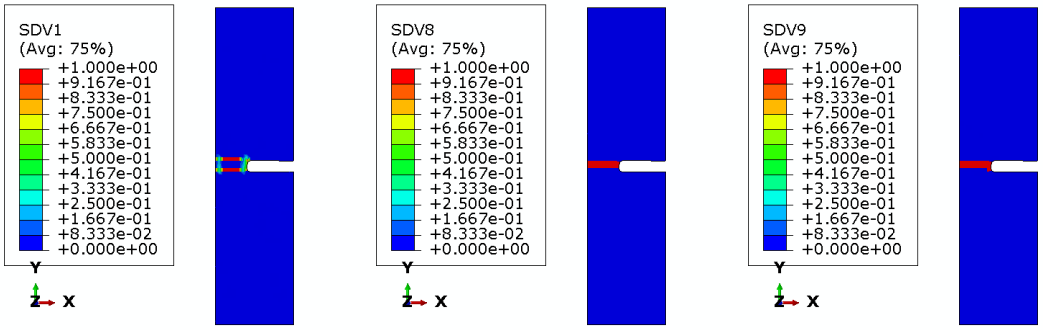
(h) Point 1: shear damage **(i)** Point 2: shear damage **(j)** Point 3: shear damage



(k) Point 1: transverse matrix damage **(l)** Point 2: transverse matrix damage **(m)** Point 3: transverse matrix damage

Figure 6.6: Damage onset and evolution history for the w = 10 mm DENT test.

Lastly, it should be noted that, in spite of inter- and intralaminar damage growth exhibiting a fairly similar evolution up to failure, as is anticipated for tensile loads, intralaminar modes, i.e., fibre breakage and matrix cracking play a more pronounced role. This is most evident by analysing the *post-mortem* specimen, i.e., after catastrophic failure, shown in Figure 6.7.



(a) Interface damage **(b)** Longitudinal damage **(c)** Transverse matrix damage

Figure 6.7: *Post-mortem* for the w = 10 mm DENT test.

6.2 Double-edge notched compression

6.2.1 Size effect law

As previously mentioned, the stress-strain response under longitudinal compression proposed by Furtado et al. [8] entails an initial linear-elastic response (preceding kink band formation) followed by a linear softening, corresponding to the propagation of a kink band, until reaching a

plateau, corresponding to kink band broadening at constant stress. Consequently, with respect to the double-edge notched compression, DENC, specimens, our initial goal simply comprised ascertaining the optimal longitudinal compressive stress at the inflection point, dictated by the computational parameter f_{XC}, capable of satisfying the experimentally determined size effect law. Once more, our initial iteration was based on the value employed by Furtado et al. [8], i.e., $f_{XC} = 0.2$ as shown in the longitudinal compression cohesive law depicted in Figure 6.8. Furthermore, it should be noted that, throughout the iterative procedure, only two specimens (the smallest and the second largest) are mainly considered. These coupons provide a representative understanding of the size effect, whilst not significantly increasing the computational cost (for the larger specimen), with the remaining ones thus being used for validation purposes.

Concerning the obtained strength predictions pertaining to the first iteration, strong disparities in relation to the experimental results were observed, particularly for the larger specimen (refer to Table 6.6). In addition, the size-effect was also incorrectly captured as illustrated in Figure 6.10a by the slope of the numerical curve, whose relative error to the experimental one slightly exceeds 10% (-11.30% in relative error). Thereby, this cohesive law was disregarded.

Table 6.6: Numerical predictions for iteration 1 of the DENC models.

	Experimental results		Numerical results	
w [mm]	σ_{max}^{exp} [MPa]	STDV [MPa]	σ_{max}^{num} [MPa]	Relative error [%]
5	148.8	3.1	184.77	+24.17
12.5	120.2	3.5	174.4	+45.09

In light of the poor strength predictions attained, two distinct strategies were subsequently employed for the second iteration in an attempt to overcome the overestimation, namely reducing the maximum longitudinal compression strength, X_C, and lowering the inflection point by decreasing f_{XC}. Beginning with the first, it should be noted that the resistance value $X_C = 890.7$ MPa initially adopted was inversely derived from a cross-ply specimen, seeing as this comprises the preferred method for its determination within the aeronautical industry. Nonetheless, a significant difference was registered between the maximum compressive strength for the mentioned multi-directional laminate and that pertaining to a unidirectional coupon (890.7 MPa vs. 676.0 MPa respectively). As such, it was theorised that adopting the lesser strength value (refer to Figure 6.8 for the corresponding cohesive law) would shift the size effect curve to within an acceptable threshold. Indeed, such effects were clearly noted in the numerical results obtained for the smaller specimen as shown in Table 6.7, wherein a relative error of merely 2.35% was recorded. Nonetheless, in regards to the larger specimen, it was clear that adopting the reduced strength value only yielded negligible differences, which in turn resulted in an inadequate representation of the size effects, as depicted in Figure 6.10b. These results are nonetheless easily explained by analysing the proposed cohesive law illustrated in Figure 6.9. For this stress-strain response, it is postulated that the entire longitudinal compression fracture toughness is dissipated prior to reaching the constant stress plateau. Thus, seeing as the resistance of larger specimens is largely governed by this energy, which was preserved between the iterations, it is observed that the resistance value does not play a significant role in such predictions. On the other hand, the behaviour of smaller specimens is significantly more dominated by the resistance value, hence the observed differences. In addition, these effects were further confirmed when increasing the inflection point to 0.75 (cohesive law depicted in Figure 6.8), wherein greater changes in terms of the numerical prediction were observed for the smaller specimen (refer to Table 6.8). In fact, these effects are also noticeable in the size effect law obtained (shown in Figure 6.10c), whose slope is under the 10% relative error threshold

(8.41%). However, given the poor correlation between the numerical and experimental resistance values, this cohesive law was dismissed.

Table 6.7: Numerical predictions for iteration 2 of the DENC models.

	Experimental results		Numerical results	
w [mm]	σ_{max}^{exp} [MPa]	STDV [MPa]	σ_{max}^{num} [MPa]	Relative error [%]
5	148.8	3.1	152.3	+2.35
12.5	120.2	3.5	141.68	+17.87

Table 6.8: Numerical predictions for iteration 3 of the DENC models.

	Experimental results		Numerical results	
w [mm]	σ_{max}^{exp} [MPa]	STDV [MPa]	σ_{max}^{num} [MPa]	Relative error [%]
5	148.8	3.1	163.41	+9.82
12.5	120.2	3.5	150.21	+24.97

Alternatively, for iteration 4, as mentioned, the inflection point was simply lowered by decreasing f_{XC} to 0.01, with the resulting cohesive law resembling a linear softening response (refer to Figure 6.8). As expected, the repercussions of such change were most noticeable for the smaller specimen as depicted in Table 6.9. In turn, improvements in the representation of the size effects were also observed as illustrated in Figure 6.10d, with this value, in fact, being within -7.16% of the experimental one. Still, the numerical predictions with respect to the strength values fell outside the ideal 10% threshold, deeming the cohesive law unacceptable.

Table 6.9: Numerical predictions for iteration 4 of the DENC models.

	Experimental results		Numerical results	
w [mm]	σ_{max}^{exp} [MPa]	STDV [MPa]	σ_{max}^{num} [MPa]	Relative error [%]
5	148.8	3.1	181.5	+21.96
12.5	120.2	3.5	172.34	+43.37

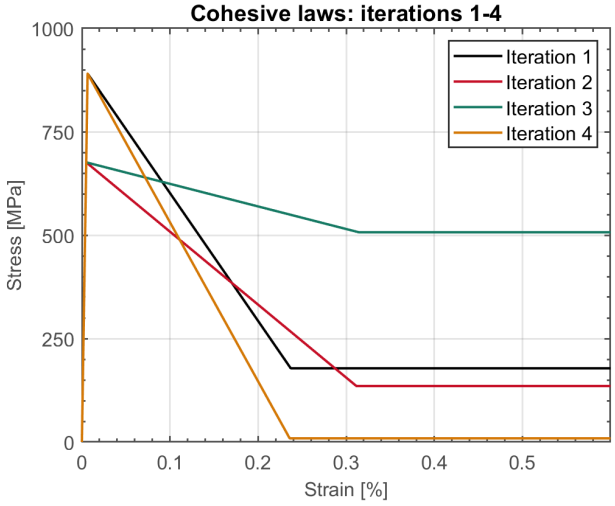


Figure 6.8: Compressive plateau cohesive laws: iterations 1-4.

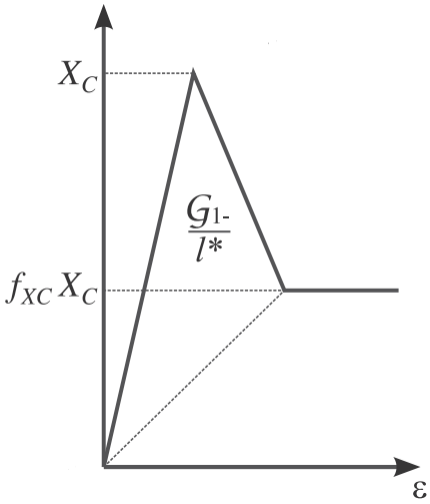
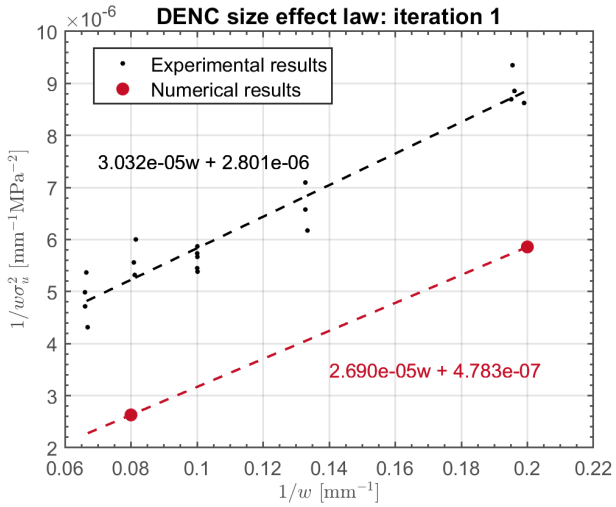
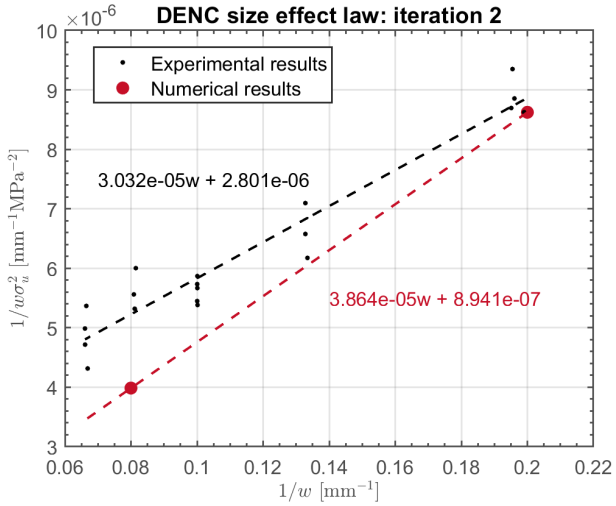


Figure 6.9: Originally proposed longitudinal compression cohesive law [8].

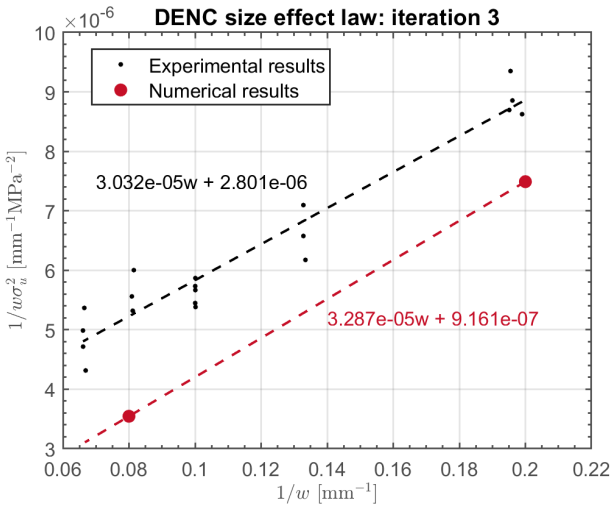


(a)

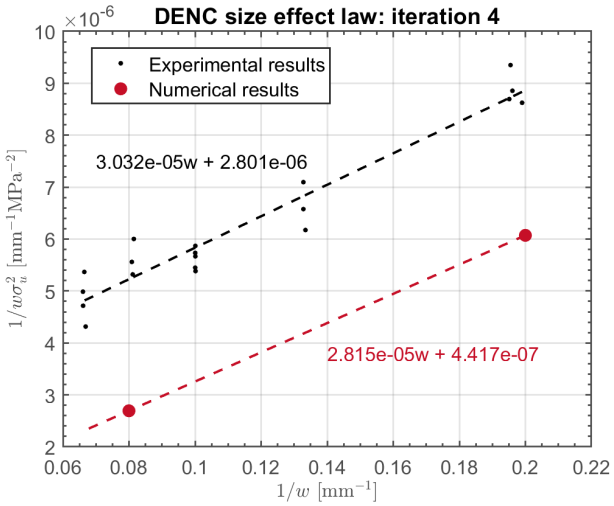


(b)

6.2. Double-edge notched compression



(c)



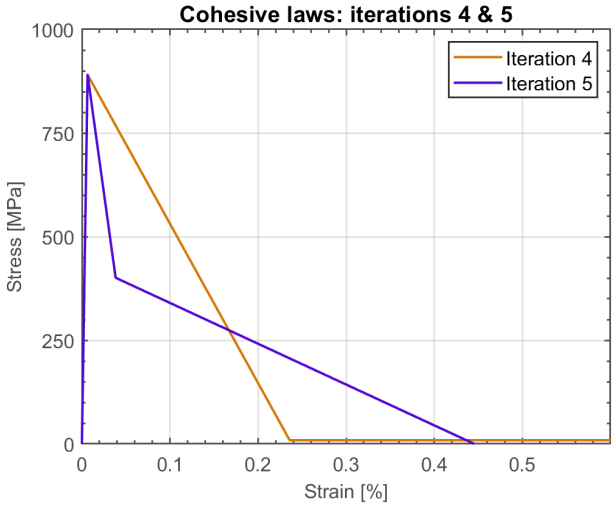
(d)

Figure 6.10: DENC numerical size effect laws: **a)** iteration 1, **b)** iteration 2 **c)** iteration 3, **d)** iteration 4.

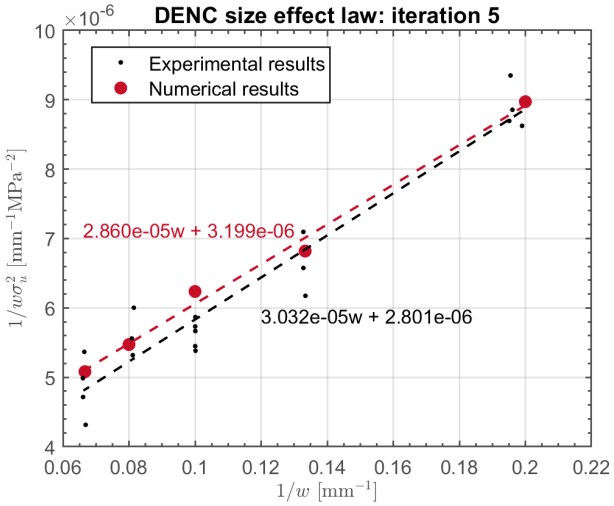
In addition, the consideration of a linear softening law effectively constitutes a lower bound for the strength values and a maximum one for the slope of the size effect law. Thereby, the longitudinal compression cohesive law proposed by Furtado et al. [8] was deemed inadequate to represent the size effects for our material system. As a result, it was theorised that, by means of adopting a bi-linear softening law as per Figure 4.2b, greater control of the slope for the first portion of the stress-strain response and of the corresponding dissipated fracture toughness could be achieved, ultimately improving our predictions. In fact, these expected effects correlated well with the observed results[2]. By considering the bi-linear softening law shaped by $f_{XC} = 0.45$ and f_{GC} [3] $= 0.15$ shown in Figure 6.11a, we were able to attain strength predictions remarkably below 10% (refer to Table 6.10), whilst also accurately representing the size effect law as illustrated in Figure 6.11b by the -5.67% relative error between the slope of the curves.

[2]Notwithstanding, although several cohesive laws were tested, for the sake of simplicity, only the final result is herein displayed.

[3]This computational parameter was introduced as a consequence of considering a bi-linear softening law. Its meaning is similar to that of the previously mentioned f_{GT}.



(a) Compressive bi-linear vs. plateau cohesive laws



(b) Size effect law

Figure 6.11: Numerical results for iteration 5 of the DENC models.

Table 6.10: Numerical predictions for iteration 5 of the DENC models.

	Experimental results		Numerical results	
w [mm]	σ_{max}^{exp} [MPa]	STDV [MPa]	σ_{max}^{num} [MPa]	Relative error [%]
5	148.8	3.1	149.30	+0.34
7.5	142.0	5.1	139.83	-1.53
10	133.5	2.4	126.62	-5.16
12.5	120.2	3.5	120.91	+0.59
15	117.3	5.6	114.54	-2.35

Furthermore, in light of the aforementioned changes (to the delamination and in-plane shear responses), it was once more necessary to guarantee that such alterations would not compromise the results stated above, thereby requiring additional iterations. Nonetheless, as opposed to the DENT tests, the bi-linear cohesive law shown in Figure 6.11a proved to be capable of accurately

capturing both the strength values and the size effect. As depicted in Table 6.11, the numerical predictions are well below the 10% threshold and, as per Figure 6.12, the slope of the numerical size effect law was even improved, exhibiting a relative error of -3.59%.

Table 6.11: Revised numerical predictions for iteration 5 of the DENC models.

	Experimental results		Numerical results	
w [mm]	σ_{max}^{exp} [MPa]	STDV [MPa]	σ_{max}^{num} [MPa]	Relative error [%]
5	148.8	3.1	151.38	+1.73
7.5	142.0	5.1	139.96	-1.44
10	133.5	2.4	130.74	-2.07
12.5	120.2	3.5	123.46	+2.71
15	117.3	5.6	117.79	+0.42

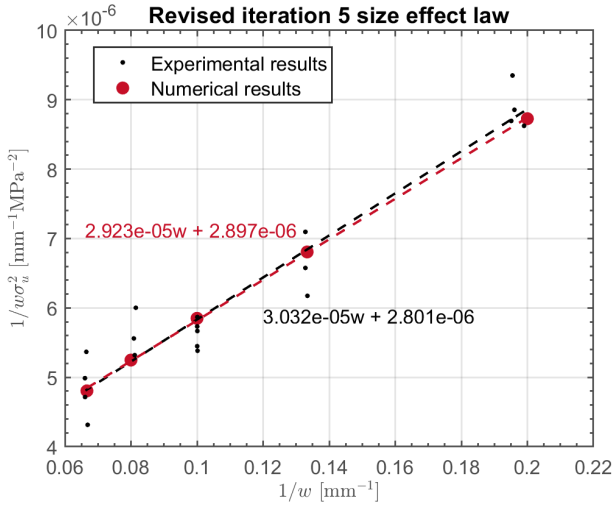
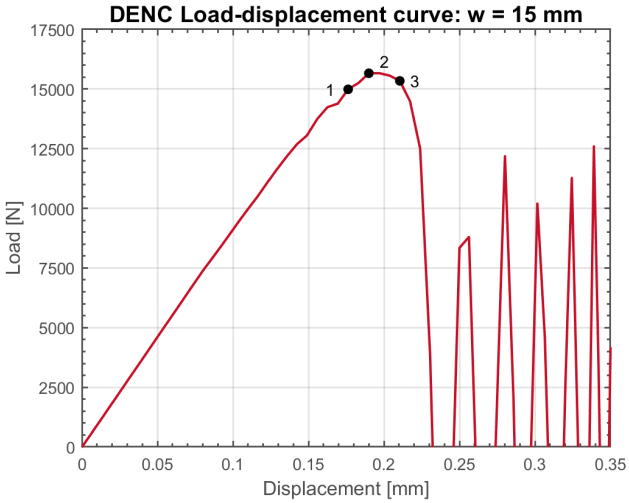


Figure 6.12: Revised size effect law for iteration 5 of the DENC models.

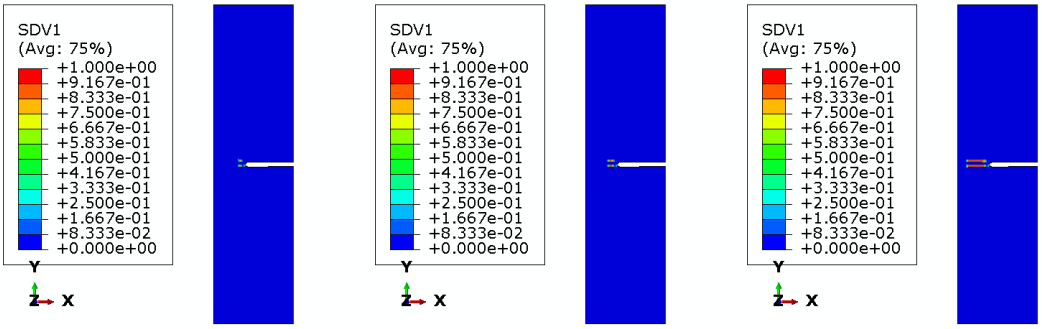
6.2.2 Damage onset & evolution history

Similarly to the DENT models, given the nature of the CDM model, it also becomes relevant to analyse the initiation and progression of damage, which, within the scope of the DENC tests, is presented for the w = 15 mm coupon that presents general features across the considered sizes. To this purpose, we refer to Figure 6.13, wherein the load-displacement curve and the evolution of the damage variables for distinct points along the curve are given.

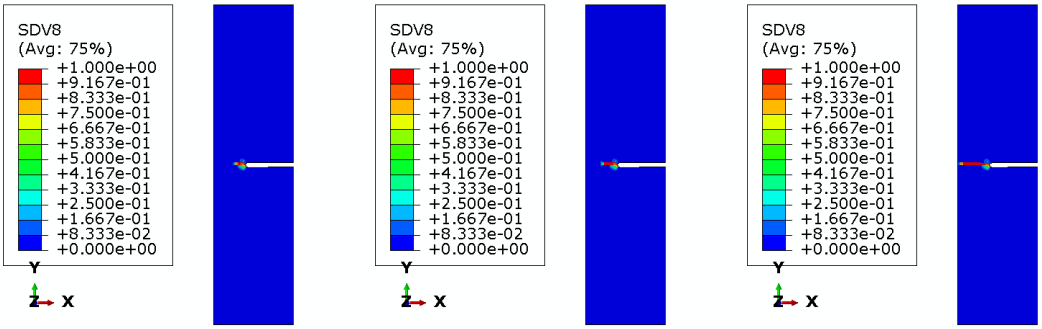
Regarding the damage mechanisms for the DENC simulations, similar conclusions to that pertaining to the DENT models may be derived. Once more, in light of the stress concentrations introduced by the notch, both inter- and intralaminar damage mechanisms nucleate from its vicinity and extend across the width of the laminate whilst remaining near such feature (refer to e.g., Figures 6.13e to 6.13g for the longitudinal fibre damage). Furthermore, catastrophic failure again occurs as a result of localised damage within the embedded 0° plies. Nonetheless, analysing Figures 6.13b to 6.13d, we infer that delamination growth now occurs in a much more unstable manner than what was previously reported.



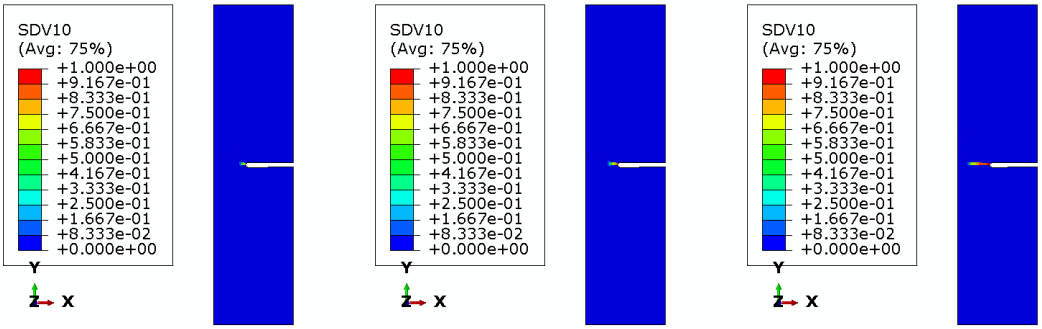
(a) Load-displacement curve



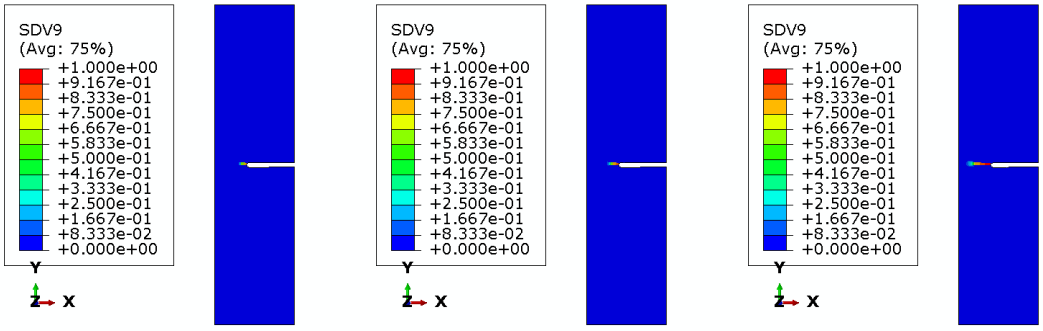
(b) Point 1: interface damage **(c)** Point 2: interface damage **(d)** Point 3: interface damage



(e) Point 1: longitudinal damage **(f)** Point 2: longitudinal damage **(g)** Point 3: longitudinal damage



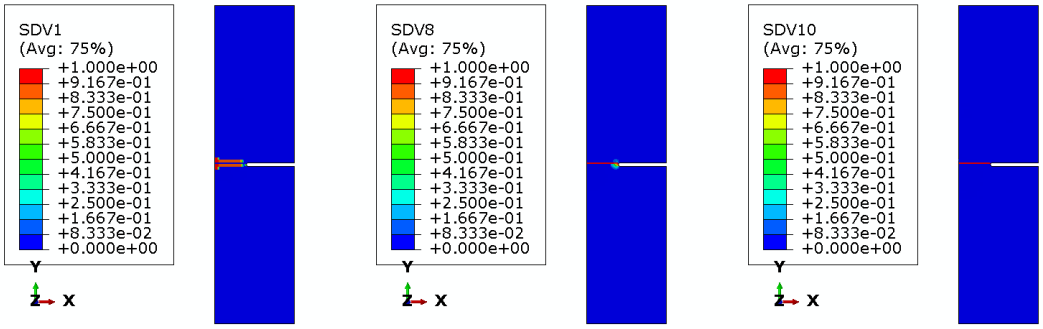
(h) Point 1: shear damage **(i)** Point 2: shear damage **(j)** Point 3: shear damage



(k) Point 1: transverse matrix damage **(l)** Point 2: transverse matrix damage **(m)** Point 3: transverse matrix damage

Figure 6.13: Damage onset and evolution history for the w = 15 mm DENC test.

This effect is further corroborated by means of inspecting the *post-mortem* specimen displayed in Figure 6.14. It is clear that, in the case of compressive loads, delamination plays a more prominent role. Although intralaminar damage mechanisms are still present to a significant degree, delamination evolves in a much more unstable manner and even propagates to the edge of the specimen, inducing a small fraction of free-edge delamination. Moreover, as such effects are to be anticipated for compressive loads, it is reasonable to infer that the damage onset and evolution observed for both the DENT and DENC tests affirm the validity of the modelling approach herein employed.



(a) Interface damage **(b)** Longitudinal damage **(c)** Transverse damage

Figure 6.14: *Post-mortem* for the w = 15 mm DENC test.

6.3 Material card

Lastly, the ascertained material card[4] is summarised in Tables 6.12 to 6.21 (including the ply *in-situ* strengths) wherein the penalty stiffness, K, and friction coefficient, μ, parameters correspond to the recommended ones by Furtado et al. [8]. Furthermore, it should be noted that for the low velocity impact simulations, the penalty stiffness value was altered to 2.5×10^4 following a penalty stiffness sensitivity study, as suggested by Soto et al. [80, 124], and the surface density was computed to be 1.70064×10^{-10} due to STI concerns. It is also worth noting that, whilst for the double-edge notched, un-notched and open-hole simulations, all the required damage variables are set to 1, for low velocity impact tests, in light of element deletion criterion concerns, the maximum value for the damage variables are specified as $d_1 = 0.99$, $d_2 = 0.98$ and $d_6 = 0.98$.

[4]The determined parameters are presented in bold. The remaining properties are determined via experimental tests.

Table 6.12: Ply elastic properties.

Elastic		
E_1	[MPa]	145900
E_{1c}	[MPa]	137909
E_2	[MPa]	7427
G_{12}	[MPa]	4055
ν_{12}	-	0.312

Table 6.13: Ply strength properties.

Strength		
X_T	[MPa]	2311
$\mathbf{f_{XT}}$	-	0.35
X_C	[MPa]	890.7
$\mathbf{f_{XC}}$	-	0.45
Y_T	[MPa]	40.45
Y_C	[MPa]	134.7
Y_{BT}	[MPa]	25.079
Y_{BC}	[MPa]	319.23
S_L	[MPa]	57.2
$\mathbf{S_{LP}}$	[MPa]	56
$\mathbf{K_p}$	[MPa]	0.075

Table 6.14: Ply fracture toughness properties.

Fracture		
$\mathcal{G}_{2+}$	$[\mathrm{kJ/m^2}]$	0.843
$\mathcal{G}_{2-}$	$[\mathrm{kJ/m^2}]$	3.956
$\mathcal{G}_6$	$[\mathrm{kJ/m^2}]$	2.381
$\mathcal{G}_{1+}$	$[\mathrm{kJ/m^2}]$	320.6
$\mathbf{f_{GT}}$	-	0.33
$\mathcal{G}_{1-}$	$[\mathrm{kJ/m^2}]$	52.5
$\mathbf{f_{GC}}$	-	0.15

Table 6.15: Ply geometrical parameters.

Geometrical		
α_0	[rad]	0.925
t	[mm]	0.143

Table 6.16: Ply friction parameters.

Friction		
η_G	$[\mathrm{MPa^{-1}}]$	0.0245
f_{fxc}	$[\mathrm{MPa^{-1}}]$	0.01

Table 6.17: Ply *in-situ* properties.

	Y_T^{is} [MPa]	Y_C^{is} [MPa]	S_L^{is} [MPa]
Outer plies	148.957	222.345	94.4182
Embedded plies	236.693	287.571	122.116

Table 6.18: Interlaminar penalty stiffness.

Elastic		
K_n	$[\mathrm{N/mm^3}]$	10^6

Table 6.19: Interlaminar strength properties.

Strength		
τ_N	[MPa]	40.45
τ_{sh}	[MPa]	57.2

Table 6.20: Interlaminar fracture toughness properties.

Fracture		
$\mathcal{G}_{Ic}$	$[\mathrm{kJ/m^2}]$	0.843
$\mathcal{G}_{IIc}$	$[\mathrm{kJ/m^2}]$	2.381
η_{B-K}	-	3.2

Table 6.21: Interlaminar friction parameters.

Friction		
μ	-	0.1

Chapter 7

Plain strength & open-hole tests

In this section, we seek to comprehensively present and discuss the numerical results obtained for the validation specimens. To this purpose, we commence with plain tension and plain compression coupons, wherein both the estimated strength values and the damage evolution history are reported. Lastly, we contrast the numerical results for open-hole tension and compression tests against those expected with respect to the hole size effects and off-axis loading.

7.1 Plain tension

7.1.1 Numerical prediction

Commencing with the numerical predictions for the plain tension, PT, test, we refer to Table 7.1 for the attained value. Overall, our result (693.2 MPa) agrees with the expected maximum strength (682.8 MPa), not merely falling within the 10% relative error threshold (+1.52%) commonly employed in the aeronautical industry [8] but also being considerably below the upper bound imposed by the standard deviation, STDV. Moreover, in light of the validation objective of this simulation, it is thus reasonable to infer that the obtained numerical prediction affirms the validity of the adopted approach for, at least, the resistance of the un-noteched laminate.

Table 7.1: Numerical prediction obtained for the PT test.

Experimental results		Numerical results	
σ_{max}^{exp} [MPa]	STDV [MPa]	σ_{max}^{num} [MPa]	Relative error [%]
682.8	29.9	693.2	+1.52

In addition, for a more comprehensive interpretation, we further highlight Figure 7.1, wherein the numerical prediction obtained is plotted against the reference experimental result for the PT test. It should be noted that both values are represented as normalised parameters derived with respect to the experimental one (i.e., for the numerical result: $\sigma_{max}^{num}/\sigma_{max}^{exp}$). Furthermore, the normalised standard deviation, STDV_{norm}, obtained in a similar manner, is also included.

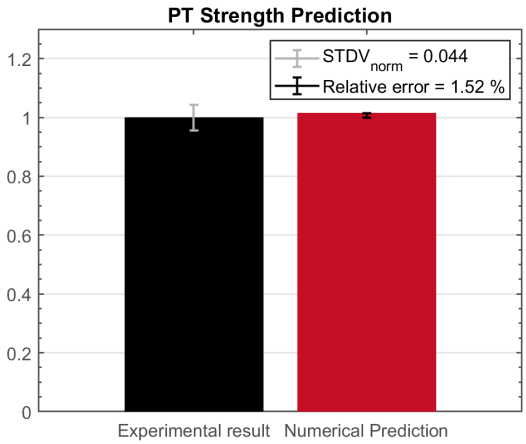


Figure 7.1: Normalised numerical prediction obtained for the PT test.

7.1.2 Damage onset & evolution history

Besides the numerical prediction in terms of the resistance value, in order to effectively ascertain the validity of the proposed approach, considerations regarding the initiation and progression of damage throughout the loading history further comprise a matter of the utmost importance. Initially analysing solely the load-displacement curve depicted in Figure 7.2, concerns immediately arise. A highly non-linear behaviour is identified that does not agree with the experimental findings. Notwithstanding, although this factor may at first seem to undermine the methodology herein adopted, it may, in fact, be easily explained by a myriad of distinct factors. To begin with, comparing the longitudinal tensile curve ascertained in the preceding section with the originally proposed one (as illustrated in Figure 7.3a), it is clearly noticeable that the damage evolution for the first portion of the curve is much more pronounced for the initial parameters. In turn, as depicted in Figure 7.3b, this translates into a linear behaviour up to ultimate failure, i.e., no permanent damage or generalised plastic deformation develops before the coupon breaks. Secondly, we recall the alterations made to the mode I and II fracture toughness values[1], as well as to the in-plane shear stress-strain response aimed at postponing damage onset and whose effects appear to be more prevalent.

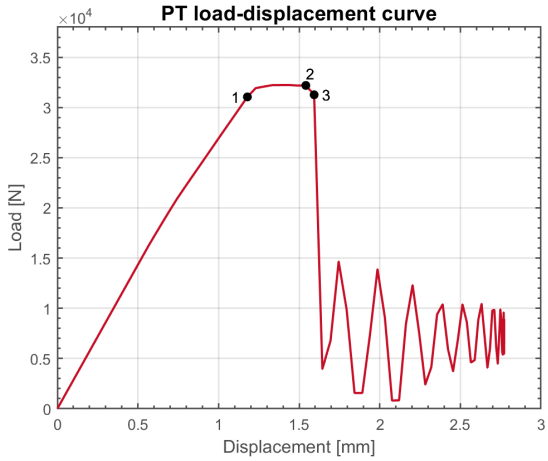
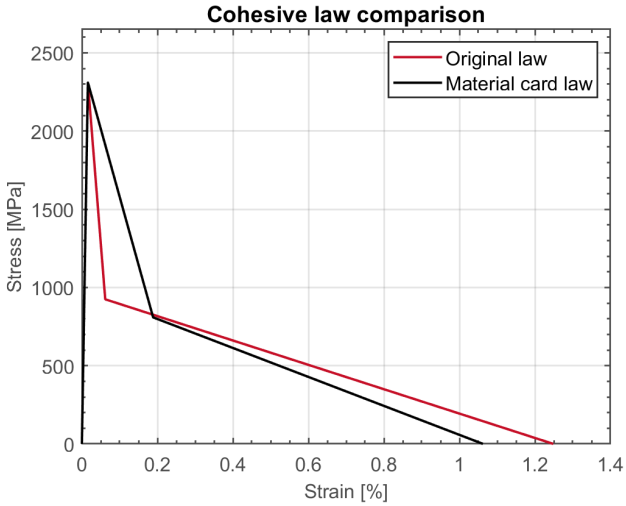
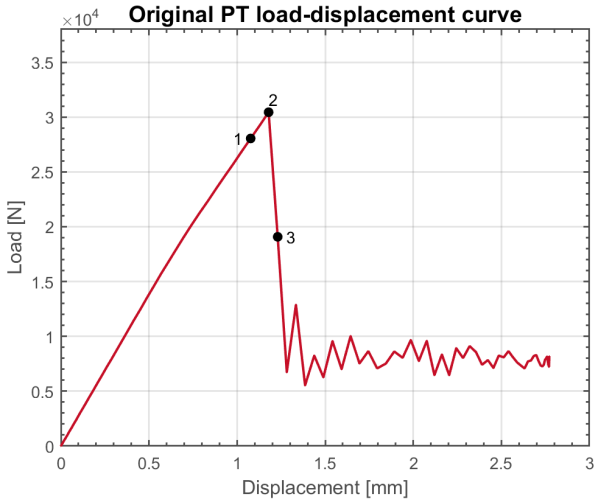


Figure 7.2: PT load-displacement curve.

[1]The load-displacement curve obtained for the initial parameters does not take into account such changes.



(a) Cohesive law comparison



(b) PT L-D curve: original cohesive law

Figure 7.3: Comparison between the material card and original bi-linear cohesive laws and corresponding PT load-displacement curve.

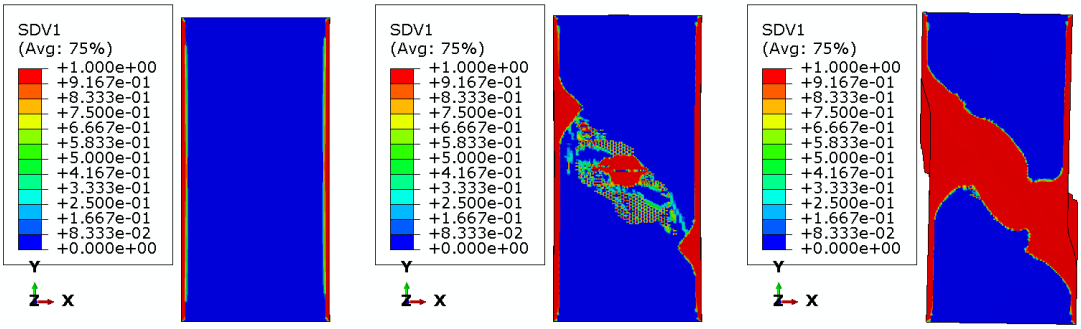
In fact, examining the progression of the damage variables throughout the loading history for both cohesive laws, the repercussions of such changes become most evident. Beginning with the evolution of damage for the material card parameters depicted in Figure 7.4, we identify that both inter- and intralaminar damage mechanisms nucleate prior to reaching the ultimate failure load as shown in Figures 7.4a, 7.4d and 7.4g. Furthermore, as the applied load increases, it becomes clearly noticeable that damages extends across a 45° orientation relative to the fibre direction (Figures 7.4b, 7.4e and 7.4h), which becomes even more clear just after catastrophic failure. Although, given the nature of the CDM model employed, i.e., predicting damage arising from damage concentrations and treating each ply as an homogenised medium, the micro-mechanisms underlying the formation of damage may not be effectively ascertained, conclusions may still be derived regarding the failure mode. The laminate in study boasts a considerably higher fraction of layers oriented at $\pm$ 45° in relation to 0° ones and, thus, may be considered as a *softer* material. As a result, it may be postulated that, as these layers tend to deform and rotate under shear mechanisms, stress concentrations are induced, promoting inter- and intralaminar damage mechanisms in critical layers. For instance, as shown in Figure 7.4a, we observe the onset of free-edge delamination

between a -45 and a 90° ply, suggesting higher interlaminar stress concentrations as a consequence of such mechanisms. These stress concentrations, as shear damage activates and rapidly evolves, further propagate to the embedded 0° plies, promoting longitudinal fibre damage as shown in Figure 7.4e, which, in turn, yields catastrophic failure as per Figure 7.4f. The shear effect in the ± 45° laminae is further identified in the 90° ones in the form of transverse matrix damage as shown in Figure 7.4k, however this does not constitute the ultimate failure mode.

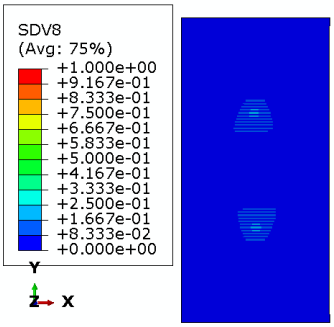
As for the original parameters, reviewing the damage evolution depicted in Figure 7.5, comparable conclusions may be drawn. Damage primarily arises as a result of stress concentrations induced by deformation in the ± 45° laminae, which is evidenced by its 45° orientation in Figures 7.5b, 7.5e, 7.5h and 7.5k. The foremost difference lies within no damage nucleation prior to the ultimate load point, as depicted in Figures 7.5a, 7.5d, 7.5g and 7.5j. Consequently, as previously stipulated, failure occurs in a much more abrupt and catastrophic manner.

Overall, we may thus conclude that the alterations made to the cohesive law and to the in-plane shear response dictate the changes observed in the damage evolution. The reduced slope for the ascertained material card parameters, in conjunction with the postponing of shear damage, allow for longitudinal fibre damage to nucleate and evolve more slowly, and for the ± 45° plies to rotate to a higher extent prior to the activation of shear damage (resulting in the non-linear plateau). Once it is activated, stress concentrations in the 0° plies are rapidly induced, leading to catastrophic failure. Thereby, the observed non-linear behaviour does not appear to undermine the validity of the employed inter- and intralaminar damage models, seeing as the changes in the damage evolution perfectly align themselves with the aforementioned alterations made.

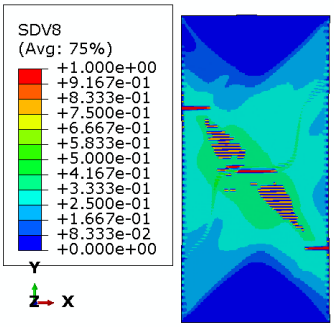
Furthermore, similar fracture surfaces and ultimate failure mechanisms (i.e., localised damage in the 0° plies) are observed between the two cohesive laws, once more, reaffirming the validity of our approach. Still, the original bi-linear softening law appears to correlate better with experimental findings, yet was discarded in virtue of not agreeing with the size effects pertaining to the DENT models. As a result, this may, in turn, suggest that revisions into the standard approach in the determination of the cohesive law parameters, i.e., DENT and DENC models may be required.



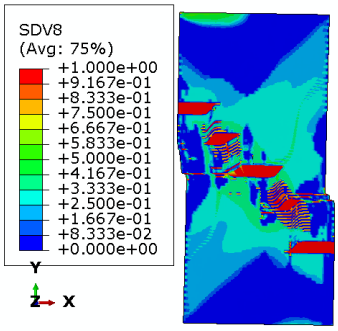
(a) Point 1: interface damage **(b)** Point 2: interface damage **(c)** Point 3: interface damage



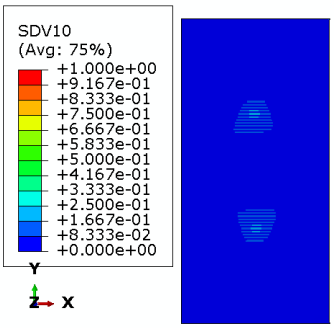
(d) Point 1: longitudinal fibre damage



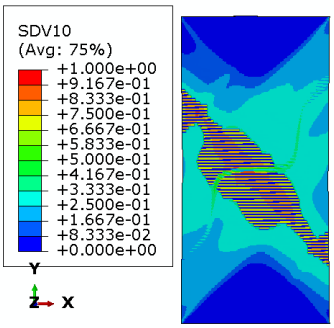
(e) Point 2: longitudinal fibre damage



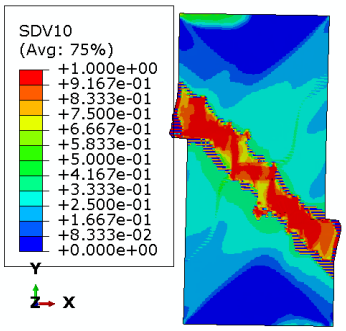
(f) Point 3: longitudinal fibre damage



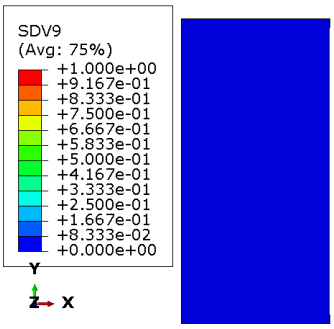
(g) Point 1: shear damage



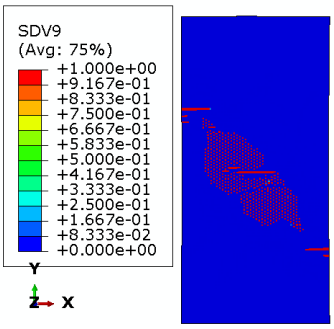
(h) Point 2: shear damage



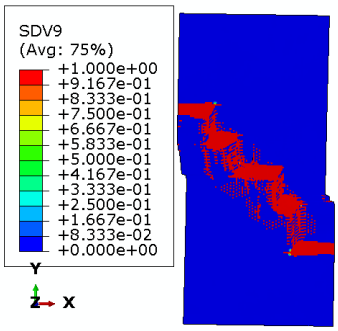
(i) Point 3: shear damage



(j) Point 1: transverse matrix damage

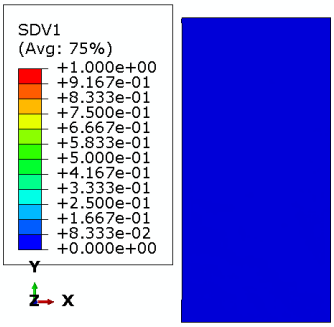


(k) Point 2: transverse matrix damage

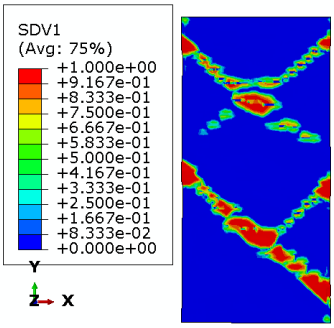


(l) Point 3: transverse matrix damage

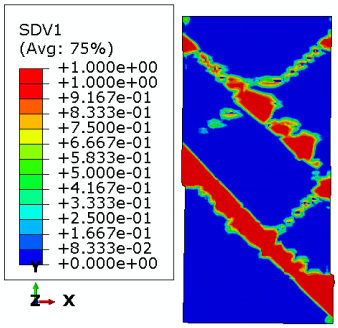
Figure 7.4: Damage evolution for the material card cohesive law.



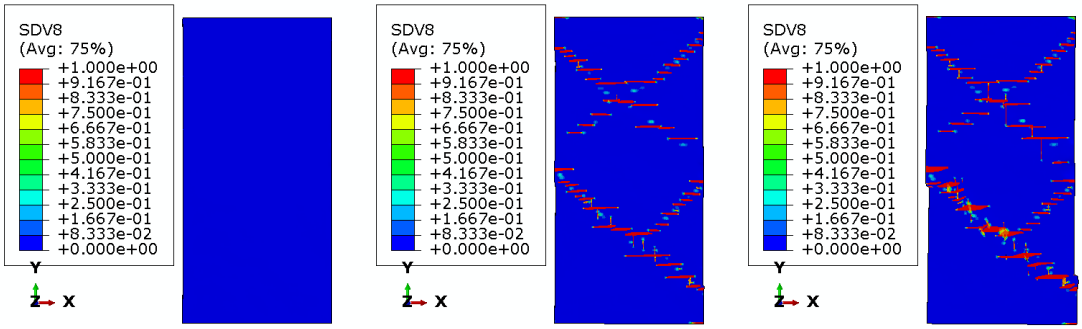
(a) Point 1: interface damage



(b) Point 2: interface damage



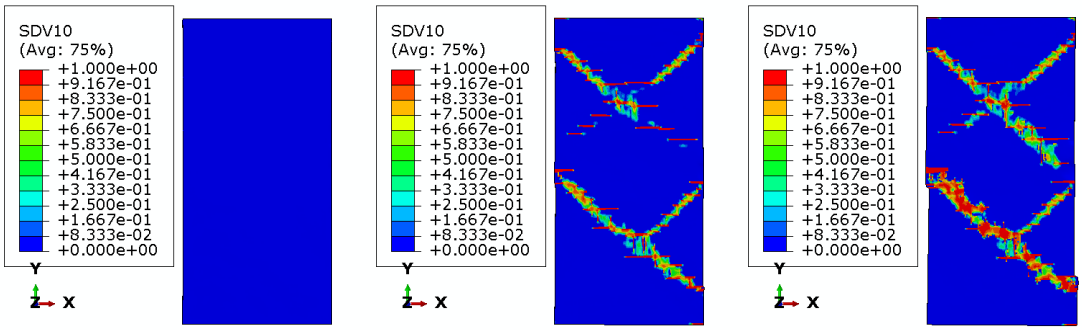
(c) Point 3: interface damage



(d) Point 1: longitudinal fibre damage

(e) Point 2: longitudinal fibre damage

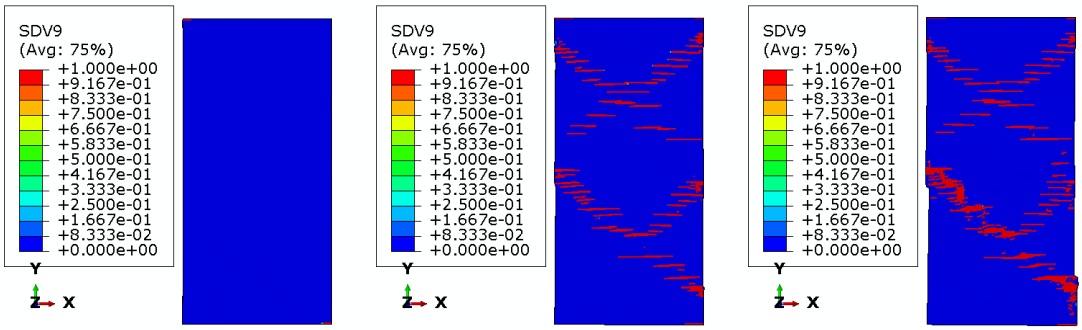
(f) Point 3: longitudinal fibre damage



(g) Point 1: shear damage

(h) Point 2: shear damage

(i) Point 3: shear damage



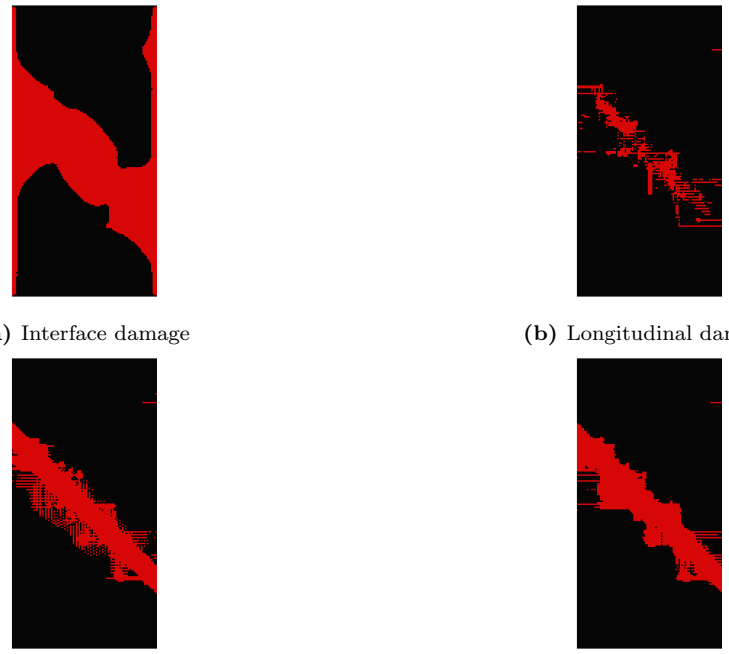
(j) Point 1: transverse matrix damage

(k) Point 2: transverse matrix damage

(l) Point 3: transverse matrix damage

Figure 7.5: Damage evolution for the original cohesive law.

Lastly, we additionally highlight Figure 7.6, wherein the *post-mortem* specimen (pertaining to the ascertained material card parameters) is shown and the final fracture surface oriented at 45° relative to the fibre direction is most clear.



(a) Interface damage **(b)** Longitudinal damage

(c) Transverse damage **(d)** Shear damage

Figure 7.6: *Post-mortem* for the PT test.

7.2 Plain compression

7.2.1 Numerical prediction

Concerning the plain compression, PC, test, the numerical prediction obtained further reinforces the validity of the intra- and interlaminar damage models herein adopted. As depicted in Table 7.2, the maximum compressive strength (383.3 MPa) attained correlates remarkably well with the experimental one (395.1 MPa), as evidenced by the -2.85% relative error achieved. Furthermore, in spite of the numerical result falling outside of the boundaries imposed by the STDV, the difference between the lower bound (of the interval imposed by the STDV) and the numerical prediction is reasonably small and thereby may be neglected.

Table 7.2: Numerical prediction obtained for the PC test.

Experimental results		Numerical results	
σ_{max}^{exp} [MPa]	STDV [MPa]	σ_{max}^{num} [MPa]	Relative error [%]
395.1	8.2	383.8	-2.85

Moreover, similarly to the plain tension models, we refer to Figure 7.7 for the plotted normalised values.

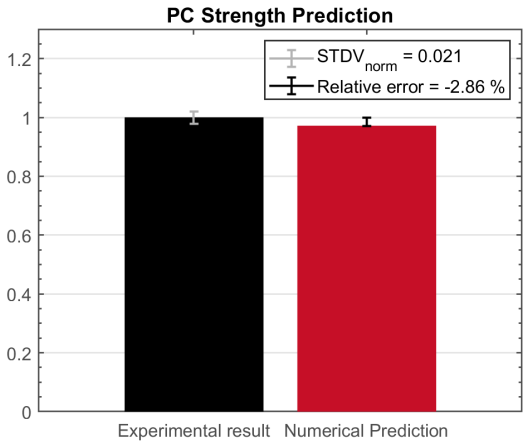
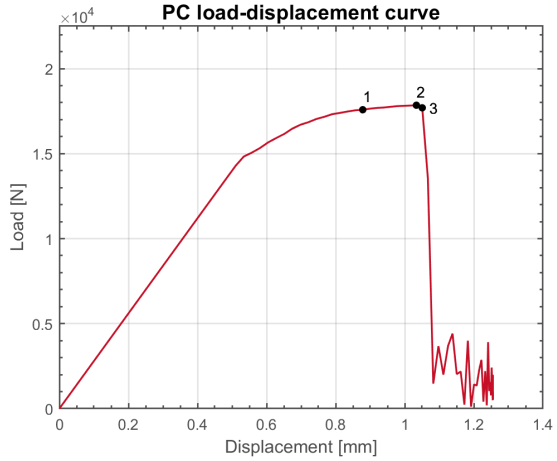


Figure 7.7: Normalised numerical prediction obtained for the PC test.

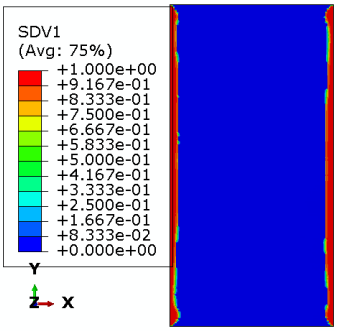
7.2.2 Damage onset & evolution history

Having analysed the numerical prediction for the resistance value, let us evaluate the initiation and progression of damage in order to ascertain the ultimate failure mode. To this purpose, we refer to Figure 7.8, wherein the load-displacement curve and the evolution of the damage variables throughout the loading history are provided.

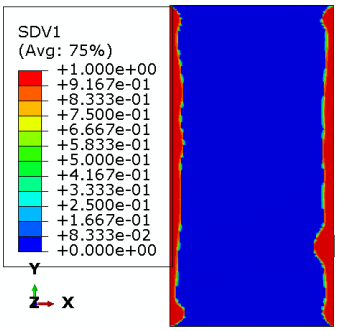
Beginning with the load-displacement curve shown in Figure 7.8a, similarly to the PT tests, a high degree of non-linearity is observed. This effect is also noticeable in the experimental findings, however to a much reduced extent. Still, once more, this may be justified by the alterations made with respect to the cohesive law, mode I and II fracture toughness values and in-plane shear response, thus not constituting a significant concern. Concerning the damage evolution itself (Figure 7.8), it is however identified that the effect of shear deformation in the $\pm$ 45° laminae is much less pronounced in the embedded 0° plies. Longitudinal fibre damage nucleates prior to the ultimate load, yet upon reaching it, is mainly localised across the width of the specimen, as shown in Figure 7.8f. Nonetheless, this is to be expected, seeing as, under compressive loads, the fibres cannot sustain such high stresses, thereby not allowing for shear damage to extensively develop. Such factor may be also corroborated by analysing the interlaminar damage growth. Although free-edge delamination is once more identified between embedded 90 and -45° plies as shown in Figure 7.8b, it does not significantly change up to the ultimate load (refer to Figure 7.8c). In fact, it only extends across the width of the specimen after catastrophic failure and does so in a similar manner to the longitudinal fibre damage seen in Figure 7.8g. Thereby, it is reasonable to infer that delamination occurs as a result of interlaminar stress concentrations induced by fibre damage in the 0° plies. This is also true for transverse matrix damage in the embedded 90° plies, given that no damage nucleates prior to rupture as shown in Figure 7.8l and only a slight amount is present after catastrophic failure (refer to Figure 7.8m) in a similar fashion to the fibre damage. Ultimately, we deduce that catastrophic failure occurs as a result of localised damage within the 0° plies as is expected for PC tests. In addition, analysing the *post-mortem* specimen shown in Figure 7.9, we identify that our material exhibits a net-section failure mode, which may be indicative of a more brittle failure plane. This is to be expected in light of the cohesive law adopted, i.e., by eliminating the constant stress plateau, there is less energy available to be dissipated, ultimately resulting in a more brittle material. Consequently, the attained results reaffirm the validity of our approach.



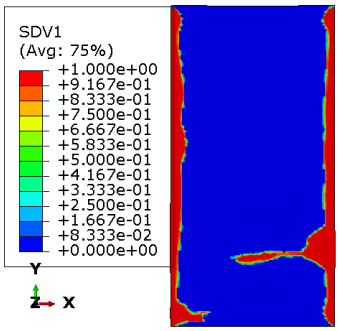
(a) Load-displacement curve



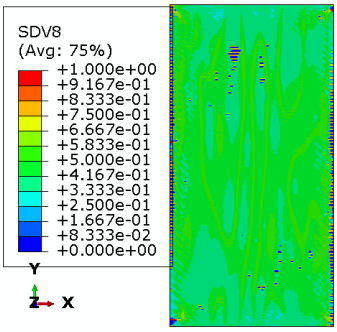
(b) Point 1: interface damage



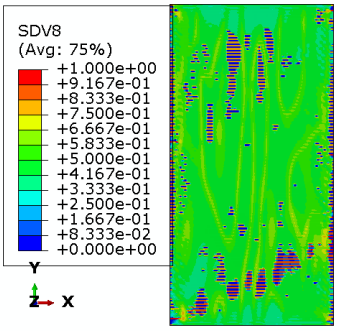
(c) Point 2: interface damage



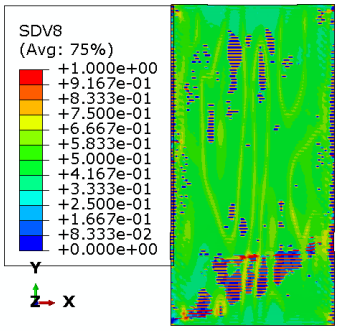
(d) Point 3: interface damage



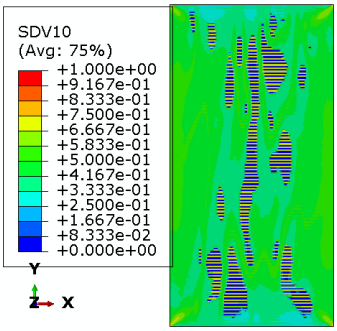
(e) Point 1: longitudinal fibre damage



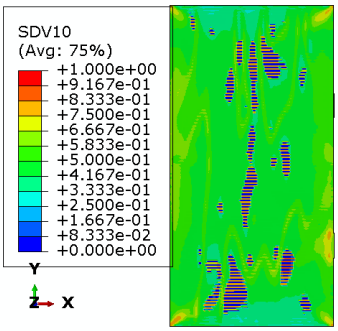
(f) Point 2: longitudinal fibre damage



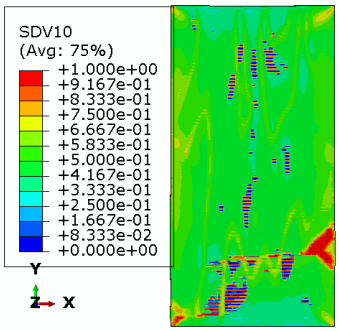
(g) Point 3: longitudinal fibre damage



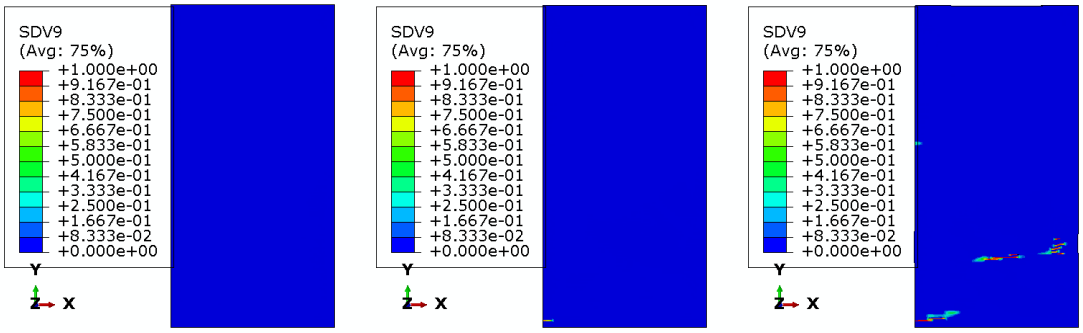
(h) Point 1: shear damage



(i) Point 2: shear damage



(j) Point 3: shear damage

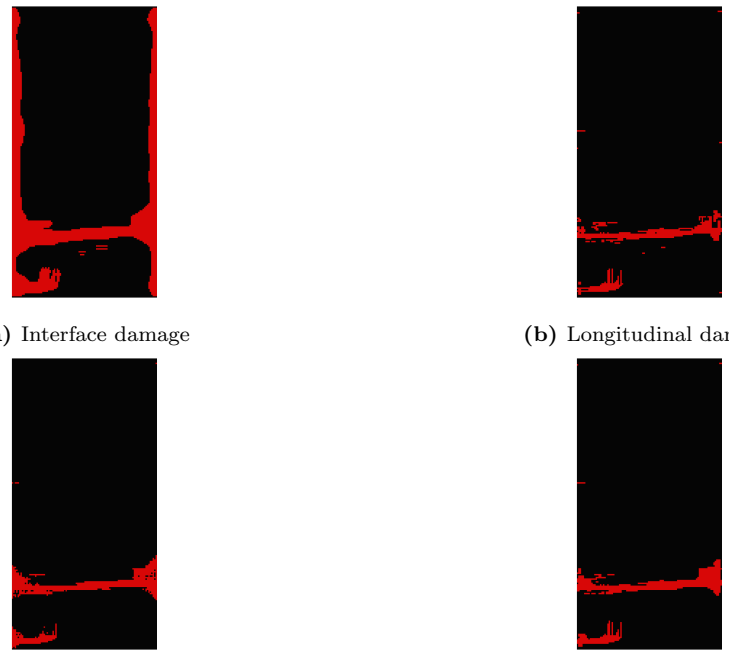


(k) Point 1: transverse matrix damage

(l) Point 2: transverse matrix damage

(m) Point 3: transverse matrix damage

Figure 7.8: Damage onset and evolution history for the PC test.



(a) Interface damage

(b) Longitudinal damage

(c) Transverse damage

(d) Shear damage

Figure 7.9: *Post-mortem* for the PC test.

7.3 Open-hole tension

7.3.1 Size effects

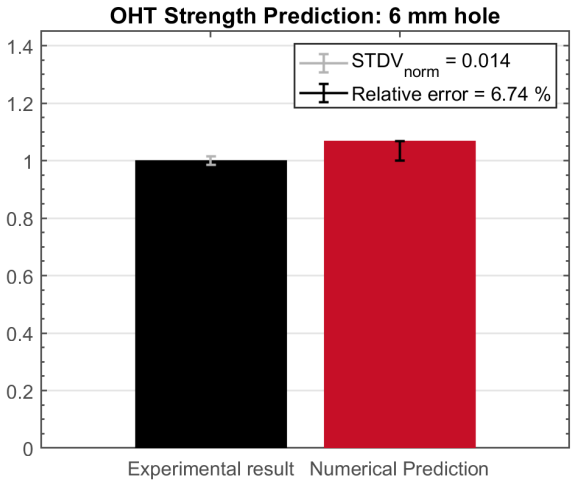
7.3.1.1 Numerical prediction

With respect to the open-hole tension, OHT, tests, let us initially evaluate the numerical predictions obtained pertaining to the hole size effects, recalling that two distinct hole sizes (in diameter) were assessed, namely 6 and 12 mm holes, wherein the diameter-to-width ratio, d/w, was maintained at 1/6, and whose resistance values are shown in Table 7.3. For the baseline specimen, i.e., the smaller one, we identify that the strength value is slightly over-predicted by +6.75% (within the ideal threshold), however falls outside the interval imposed by the STDV. On the other hand, concerning the larger hole, substantially different results were nevertheless observed, i.e., whilst the resistance is also overestimated, the relative error increases tremendously

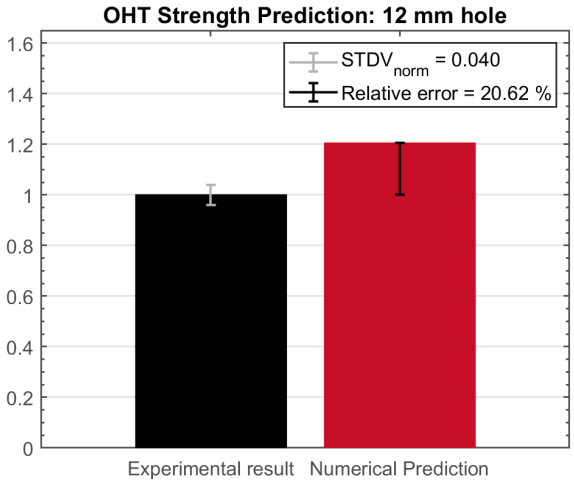
to +20.62%. Similarly to preceding sections, for a more comprehensive understanding, we further highlight Figure 7.10, wherein the normalised plots are included. In addition, it should be noted that, concerning Figure 7.10c, our foremost goal is ascertaining the response of the proposed approach in regard to the baseline specimen. As such, the normalised values (including the STDV) for the larger specimens are obtained with respect to the corresponding baseline value (e.g., for the numerical result: $\sigma_{norm}^{large} = \sigma_{large}^{num}/\sigma_{small}^{num}$). Taking into consideration the results attained, concerns naturally arise, seeing as the CDM model herein employed is seemingly not able to capture the hole size effects, which represents a contradictory conclusion to that derived for the DENT models.

Table 7.3: Numerical predictions obtained for the OHT tests pertaining to the hole size effects.

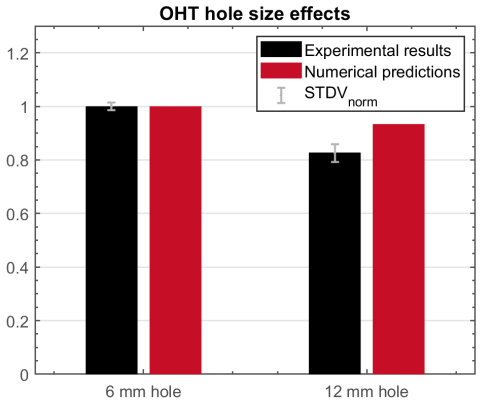
	Experimental results		Numerical results	
d [mm]	σ_{max}^{exp} [MPa]	STDV [MPa]	σ_{max}^{num} [MPa]	Relative error [%]
6	461.4	6.5	492.50	+6.75
12	381.1	15.3	459.7	+20.62



(a) $d = 6$ mm



(b) $d = 12$ mm



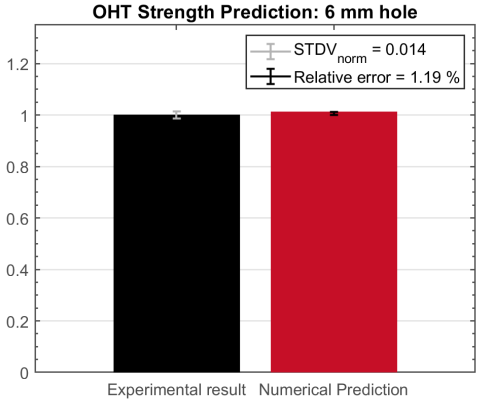
(c) Hole size effect evolution

Figure 7.10: Normalised numerical predictions obtained for the OHT tests pertaining to the hole size effects.

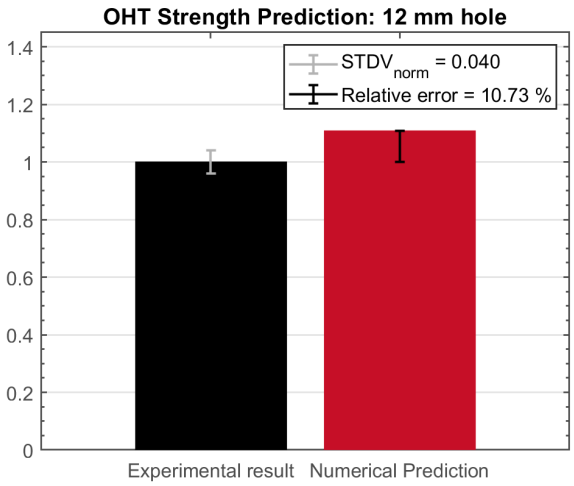
However, if we were to, e.g., revisit the original bi-linear softening law, improvements in the representation of the size effects may be observed as shown in Table 7.4 and Figure 7.11. Thereby, we deduct that, in fact, this may not constitute a limitation inherent to the CDM model. By means of selecting appropriate cohesive laws, pronounced size effects (such as the one in question) can be accurately captured, thus strengthening the validity of our approach. Nonetheless, as previously mentioned, the original cohesive law does not agree with the size effects pertaining to the DENT models. Furthermore, given that DENT tests are considered as the standard methodology in ascertaining these parameters, this cohesive law was not considered as appropriate for the material card. Thereby, this may reflect either necessary revisions to the standard approach in the determination of the cohesive law parameters or poor correlation between the size effects (of the DENT and open-hole specimens) of the provided experimental results.

Table 7.4: Original numerical predictions obtained for the OHT tests pertaining to the hole size effects.

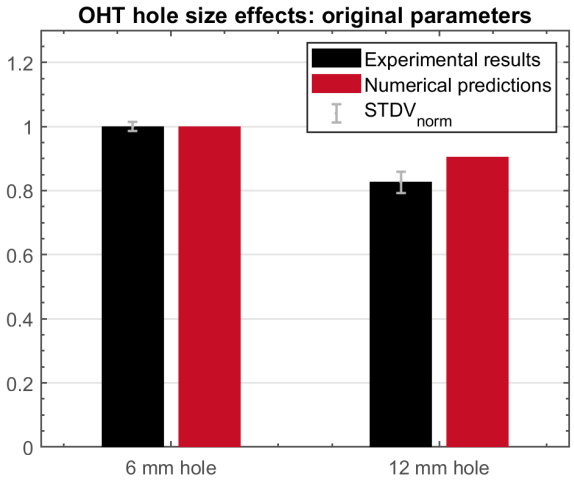
	Experimental results		Numerical results	
d [mm]	σ_{max}^{exp} [MPa]	STDV [MPa]	σ_{max}^{num} [MPa]	Relative error [%]
6	461.4	6.5	466.9	+1.62
12	381.1	15.3	422.0	+10.73



(a) $d = 6$ mm



(b) $d = 12$ mm



(c) Hole size effect evolution

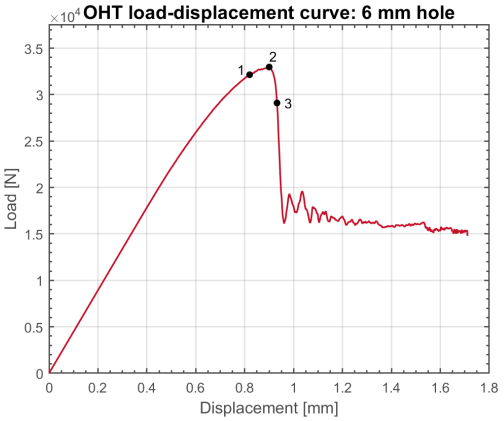
Figure 7.11: Original normalised numerical predictions obtained for the OHT tests pertaining to the hole size effects.

7.3.1.2 Damage onset & evolution history

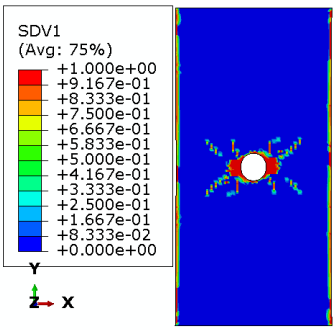
Beyond the numerical prediction, it further becomes paramount to assess the ultimate failure mode, which is ascertained for the baseline coupon ($d = 6$ mm) that presents general features across the considered sizes. To this purpose, we refer to Figure 7.12, wherein the load-displacement curve and the evolution of the damage variables throughout the loading history are provided.

Beginning with the load-displacement curve depicted in Figure 7.12a, aligned with the experimental findings, a linear behaviour up to failure is observed with some slight load drops. The small drops may indicate the development of a FPZ near the hole, resulting in a more extensive damage zone before final failure, yet have a negligible effect on the overall stiffness. Notwithstanding, similarly to the previously described for the PT test, we identify that the shear response plays a major role in the damage evolution history. Concerning interlaminar damage, as shown in Figure 7.12b, both free-edge delamination and delamination in the vicinity of the hole are observed between a -45 and a 90° ply prior to reaching final failure. Although damage near the hole is to be expected in light of the inherent stress concentrations induced, free-edge delamination may be a result of

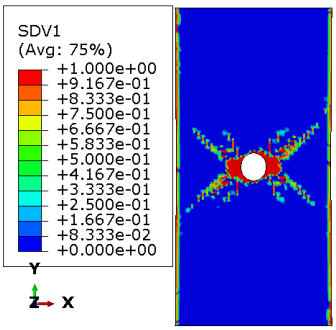
deformation in the -45° lamina, inducing high interlaminar shear concentrations. Furthermore, as the applied load increase and the extent of shear damage accordingly grows, we identify that interlaminar damage evolves at a -45° orientation relative to the fibre direction (Figure 7.12c), with the impact of shear damage in inducing stress concentrations being more noticeable just after catastrophic failure as shown in Figure 7.12d. The shear effect is also evident concerning the intralaminar damage mechanisms. Although fibre damage initially nucleates within the vicinity of the hole (as illustrated in Figure 7.12e, extending perpendicularly to the fibre direction, the inherently softer nature of the laminate induces stress concentrations along a 45° fracture plane. Such concentrations yield both transverse matrix damage (Figure 7.12l) and longitudinal fibre breakage (Figure 7.12f) with the latter ultimately being responsible for catastrophic failure as depicted in Figure 7.12g.



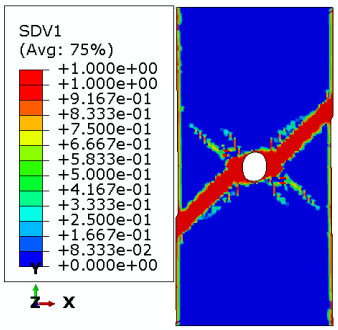
(a) Load-displacement curve



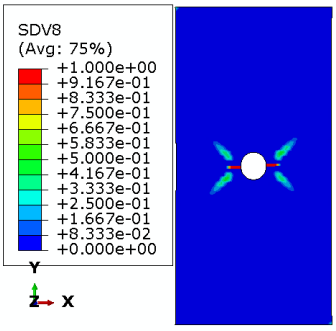
(b) Point 1: interface damage



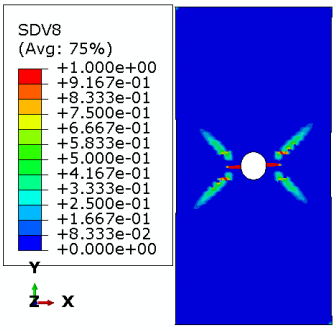
(c) Point 2: interface damage



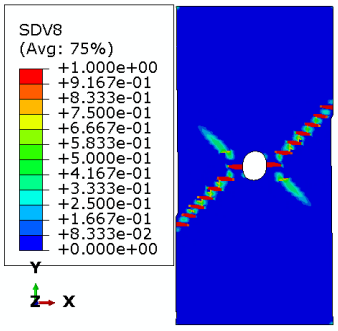
(d) Point 3: interface damage



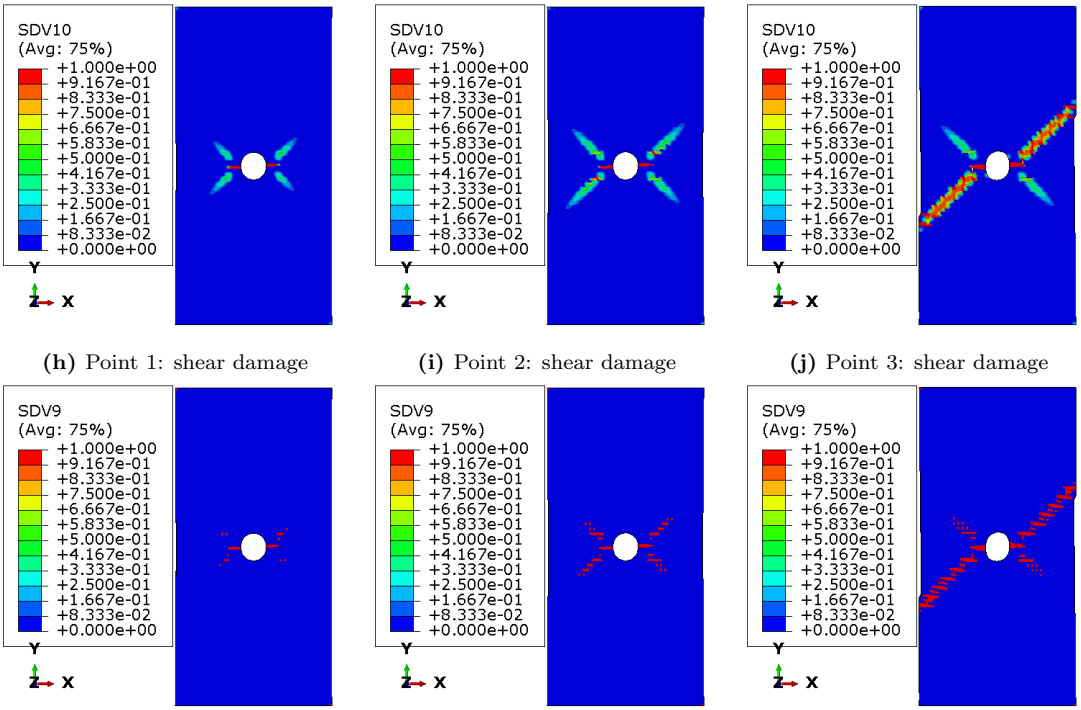
(e) Point 1: longitudinal fibre damage



(f) Point 2: longitudinal fibre damage



(g) Point 3: longitudinal fibre damage



(h) Point 1: shear damage **(i)** Point 2: shear damage **(j)** Point 3: shear damage

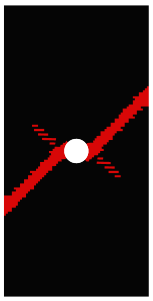
(k) Point 1: transverse matrix damage **(l)** Point 2: transverse matrix damage **(m)** Point 3: transverse matrix damage

Figure 7.12: Damage onset and evolution history for the OHT test.

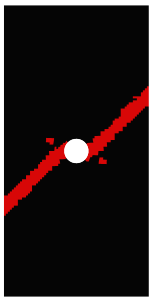
The pressing impact of shear damage mechanisms and the corresponding stress concentrations by them induced are further corroborated by analysing the *post-mortem* specimen shown in Figure 7.13. Whilst localised damage in the form of fibre breakage in the 0° plies comprises the primary cause for catastrophic failure, the -45° fracture surface is abundantly clear. Notwithstanding, this is, as mentioned, to be expected given the changes made to the cohesive law, mode I and II fracture toughness values and the in-plane shear response. Although the elastic domain was augmented and damage was postponed, once it activates, it evolves more rapidly and up to smaller shear strains. As such, it is expected that, as per the PT tests, shear damage evolves in a more pronounced manner, which becomes more significant given the softer nature of the laminate in study.



(a) Interface damage **(b)** Longitudinal damage



(c) Transverse damage



(d) Shear damage

Figure 7.13: *Post-mortem* for the $d = 6$ mm OHT test.

7.3.2 Off-axis loading

7.3.2.1 Numerical prediction

In regard to the off-axis OHT tests, as previously mentioned, two sets of results become relevant, i.e., prior to and after the alterations made to the mode I and II fracture toughness values and the in-plane shear response, seeing as it was in fact with such simulations that inadequate behaviours were originally noticed. Accordingly, our original predictions (i.e., without any changes) are compiled in Table 7.5, wherein we observe that only the estimated values regarding 0 and 90° off-axis loading were within the 10% threshold. Moreover, it is particularly significant to note that the prediction for 60° off-axis loading is below that pertaining to 0° off-axis loading, which does not agree with the experimental findings. On the other hand, following the stated changes, as per Table 7.6, we note that all the values attained boast relative errors below 10%, with the maximum one being -7.24%. Most importantly, significant improvements are also observed with respect to the 60° off-axis loading test, whose estimated value substantially increased and is above the predicted resistance for 0° off-axis loading.

Table 7.5: Original numerical predictions obtained for the OHT off-axis loading tests.

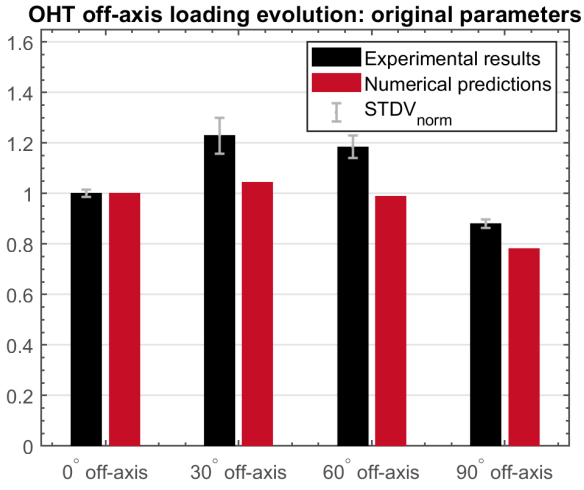
	Experimental results		Numerical results	
	σ_{max}^{exp} [MPa]	STDV [MPa]	σ_{max}^{num} [MPa]	Relative error [%]
0°	461.4	6.5	480.6	+4.17
30°	566.9	32.7	502.4	-11.39
60°	546.5	20.5	475.1	-13.06
90°	406.1	8.1	375.9	-7.43

Table 7.6: Material card numerical predictions obtained for the OHT off-axis loading tests.

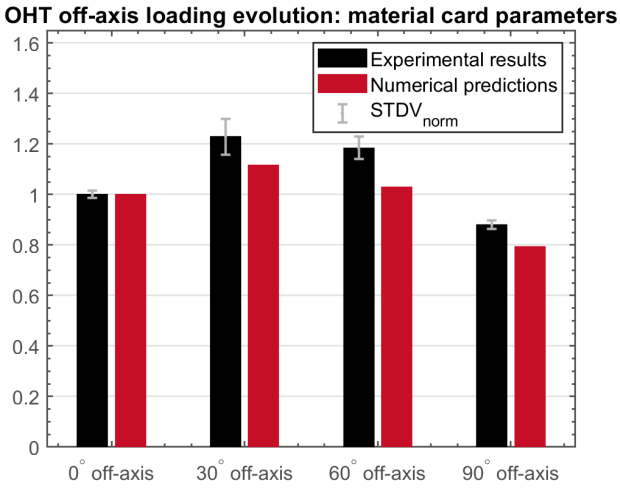
	Experimental results		Numerical results	
	σ_{max}^{exp} [MPa]	STDV [MPa]	σ_{max}^{num} [MPa]	Relative error [%]
0°	461.4	6.5	492.5	+6.75
30°	566.9	32.7	550.3	-2.93
60°	546.5	20.5	506.90	-7.24
90°	406.1	8.1	390.3	-3.90

Moreover, we highlight Figure 7.14, wherein the normalised predictions (derived with respect to 0° off-axis loading) are displayed for both the original and material card parameters and their

evolution is comprehensively provided.



(a) Original parameters

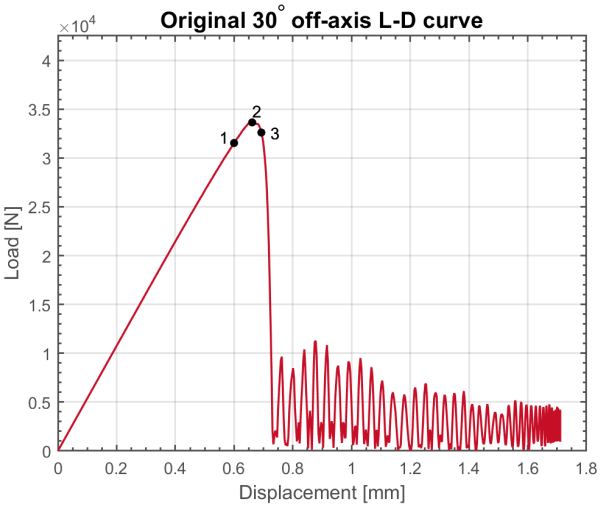


(b) Material card parameters

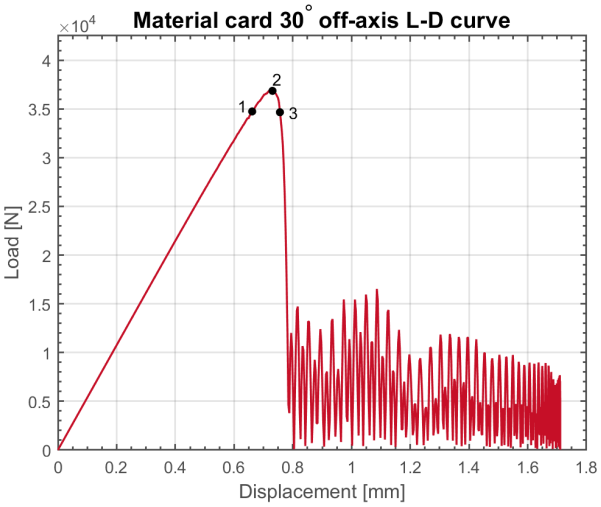
Figure 7.14: OHT off-axis loading evolution.

7.3.2.2 Damage onset & evolution history

Beyond the numerical prediction in terms of the resistance value, it further becomes relevant to assess the initiation and progression of damage throughout the loading history for both the original and material card parameters. This analysis is conducted for the 30° off-axis loaded coupons and we initially refer to Figure 7.15 for the load-displacement curves attained. Simply analysing both plots, it becomes clear that the alterations made significantly postpone damage onset and consequently catastrophic failure. In light of the nature of these tests, this is to be expected, seeing as the laminate lay-up encompasses plies at 30 and 60°, which are particularly susceptible to delamination. Moreover, no lamina is oriented at 0°, effectively rendering the laminate softer and augmenting the impact of the shear response.



(a) Original parameters

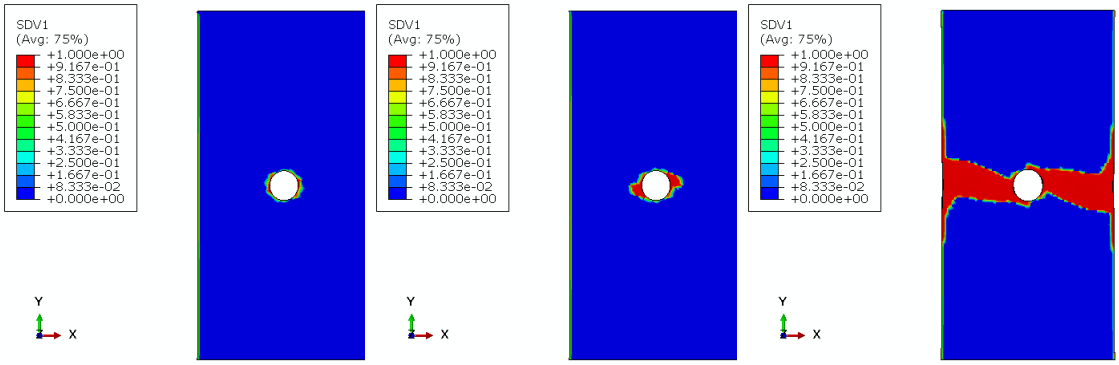


(b) Material card parameters

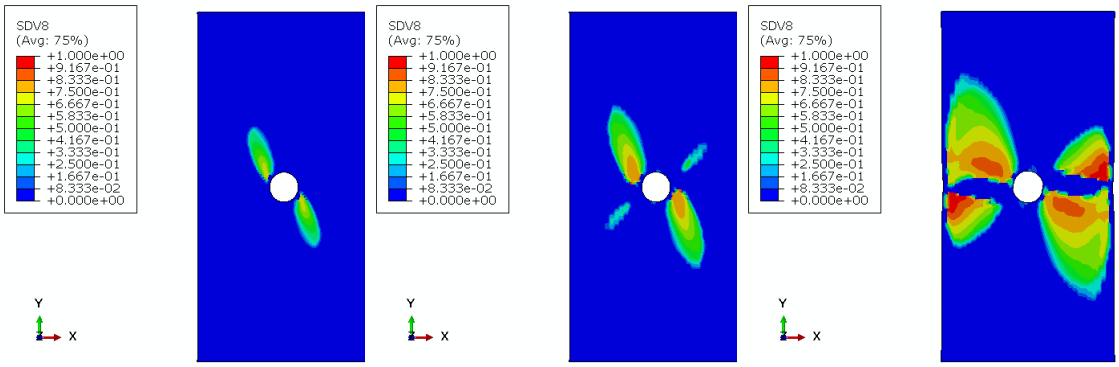
Figure 7.15: Comparison between the OHT 30° off-axis load-displacement curves obtained for the original and material card parameters.

Nonetheless, the postponement of critical damage mechanisms comprised the only expected substantial difference, i.e., by delaying damage onset, no changes in the ultimate failure mode were anticipated. In fact, analysing Figure 7.16 and Figure 7.17, we identify that catastrophic failure emerges as a consequence of extensive shear damage and delamination in the 60° plies for both cases. Furthermore, damage evolves in a similar fashion, nucleating around the hole as expected in light of the inherent stress concentrations introduced by such feature and extending across the width of the specimen up to the ultimate failure load. In addition, although the extent of damage pertaining to this point is quite different for the two scenarios (refer to Figure 7.16h and Figure 7.17h), this factor may be easily explained. For the original in-plane shear response proposed, damage onset took place at a lower stress value, subsequently evolving at a slower rate and up to a higher strain value. As a result, by augmenting the elastic domain and increasing the slope of the non-linear shear response, although damage activates later, it propagates much more rapidly and up to a lower strain value, the reason for which a higher extent of damage is noted for the material card parameters (Figure 7.17h). Accordingly, although the mode I and II fracture toughness values were increased, it may be postulated that the substantially higher amount of

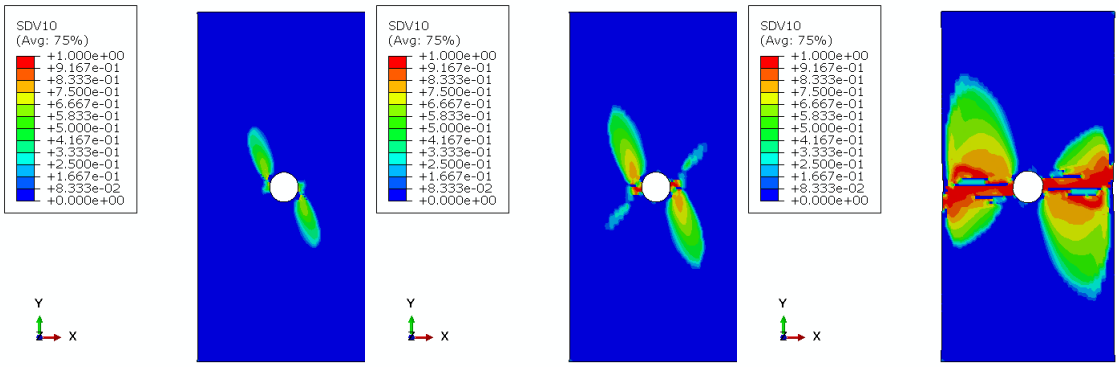
damage may induce considerable interlaminar stress concentrations near the hole, thus increasing the extent of delamination for the revised in-plane shear response (Figure 7.17b) when compared with the original one (Figure 7.16b).



(a) Point 1: interface damage **(b)** Point 2: interface damage **(c)** Point 3: interface damage

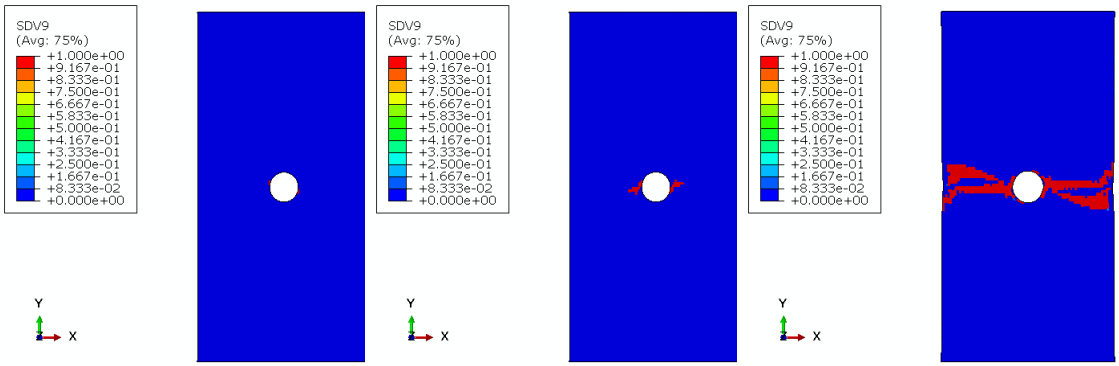


(d) Point 1: longitudinal fibre damage **(e)** Point 2: longitudinal fibre damage **(f)** Point 3: longitudinal fibre damage



(g) Point 1: shear damage **(h)** Point 2: shear damage **(i)** Point 3: shear damage

7.3. Open-hole tension

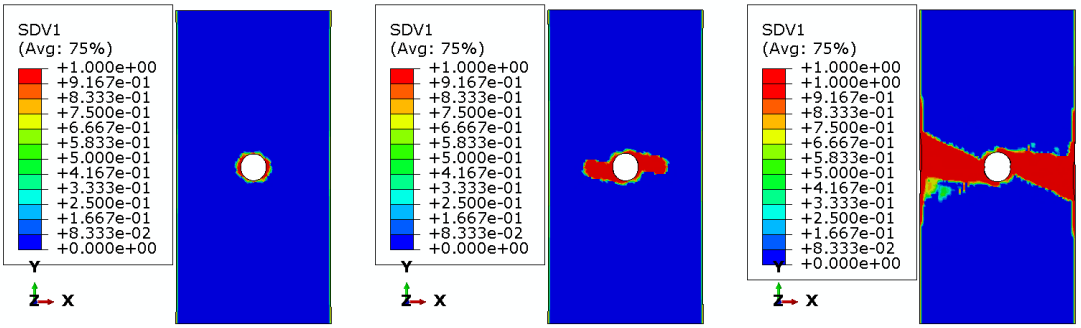


(j) Point 1: transverse matrix damage

(k) Point 2: transverse matrix damage

(l) Point 3: transverse matrix damage

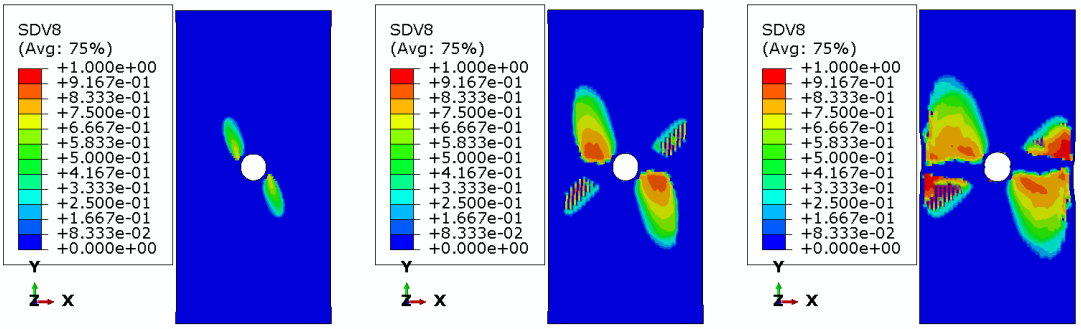
Figure 7.16: OHT 30° off-axis loading damage evolution for the original parameters.



(a) Point 1: interface damage

(b) Point 2: interface damage

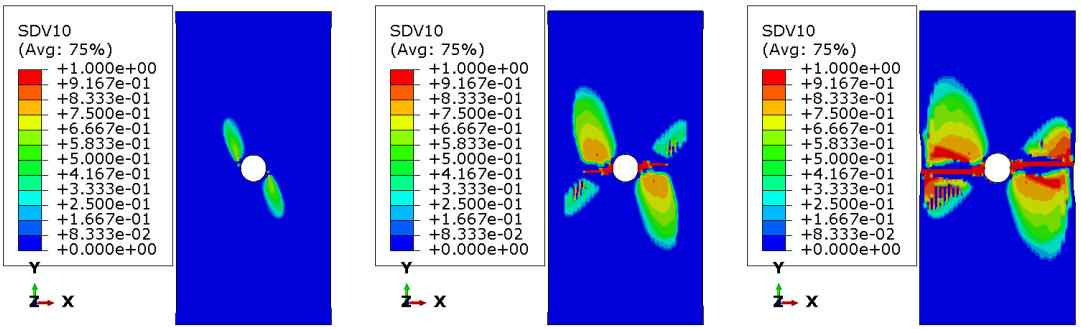
(c) Point 3: interface damage



(d) Point 1: longitudinal fibre damage

(e) Point 2: longitudinal fibre damage

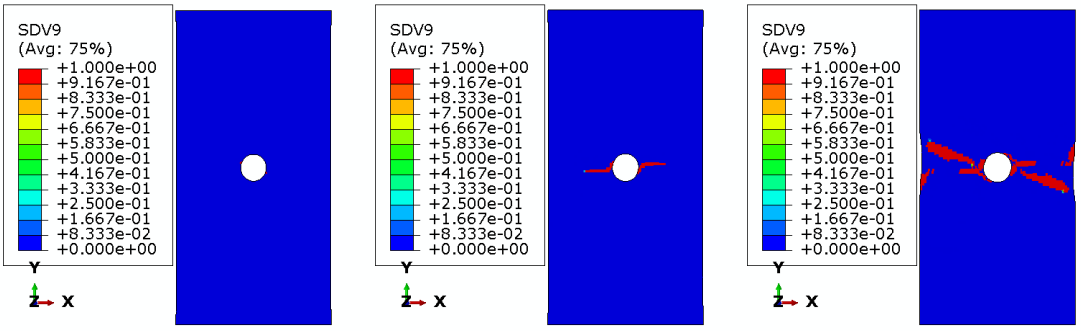
(f) Point 3: longitudinal fibre damage



(g) Point 1: shear damage

(h) Point 2: shear damage

(i) Point 3: shear damage



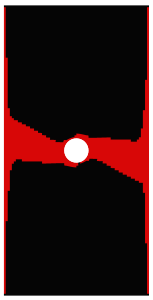
(j) Point 1: transverse matrix damage

(k) Point 2: transverse matrix damage

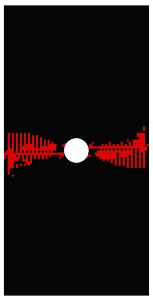
(l) Point 3: transverse matrix damage

Figure 7.17: OHT 30° off-axis loading damage evolution for the material card parameters.

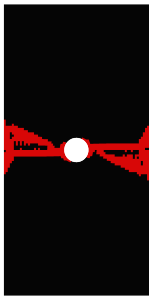
Lastly, we highlight Figure 7.18, wherein the *post-mortem* specimen pertaining to the material card parameters is shown. We identify that the fracture plane is perpendicularly oriented in relation to the fibre direction, with a clean surface dominated by fibre fracture evident, which comes as a result of extensive delamination and shear damage that comprise the paramount fracture mechanisms. As such behaviour is to be expected, the validity of our approach is reaffirmed.



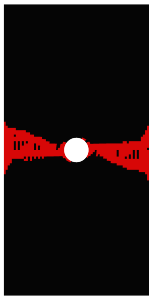
(a) Interface damage



(b) Longitudinal damage



(c) Transverse damage



(d) Shear damage

Figure 7.18: *Post-mortem* for the OHT 30° off-axis loading test: material card parameters.

7.4 Open-hole compression

7.4.1 Size effects

7.4.1.1 Numerical prediction

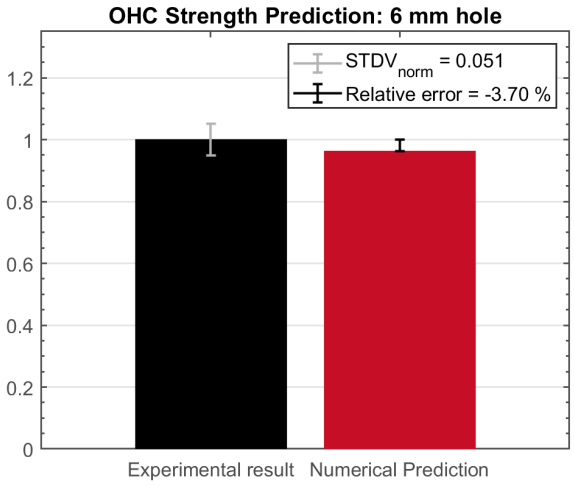
Concerning the numerical predictions obtained for the open-hole compression, OHC, tests, we recall that two distinct hole sizes (in diameter) were assessed, namely 6 and 3 mm holes, wherein the

diameter-to-width ratio, d/w, was maintained at 1/6, and whose resistance values are depicted in Table 7.7. Beginning with the larger specimen, considered as the baseline, the estimated strength is slightly under-predicted, however it is not merely within the ideal 10% threshold (-3.70% in relative error), but also falls inside the bounds imposed by the STDV. On the other hand, in regard to the smaller specimen, significantly distinct results are identified. Whilst there exists some degree of consistency, seeing as the resistance is under-estimated as well, the relative error tremendously increases to -19.94%.

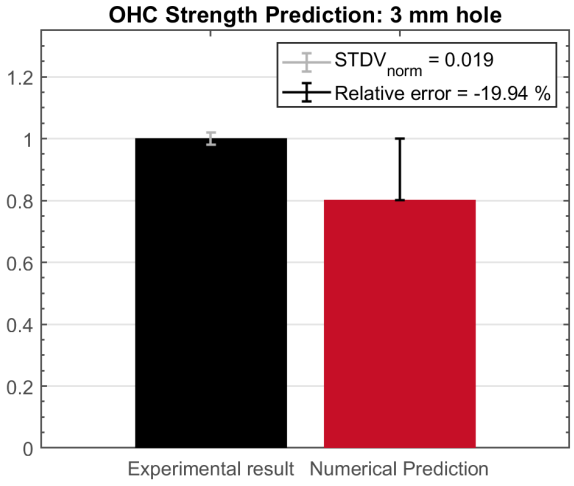
Table 7.7: Numerical predictions for the OHC tests pertaining to the hole size effects.

	Experimental results		Numerical results	
d [mm]	σ_{max}^{exp} [MPa]	STDV [MPa]	σ_{max}^{num} [MPa]	Relative error [%]
6	275.6	14.0	265.4	-3.70
3	378.3	7.3	303.1	-19.94

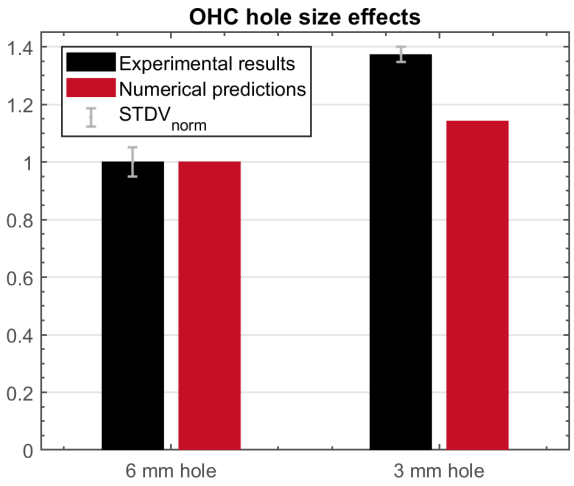
In addition, for the normalised plots, we refer to Figure 7.19.



(a) 6 mm hole



(b) 3 mm hole



(c) Size effect evolution

Figure 7.19: OHC hole size effects: normalised plots.

Furthermore, similarly to the methodology adopted for the OHT tests, several of the previously proposed cohesive laws were revisited. Nonetheless, no improvements were noted and thereby are herein not reported. Overall, as opposed to the previously stated, for compressive loads, the accurate representation of pronounced[2] hole size effects may thus constitute a limitation of the CDM model employed. In fact, this has also been reported by Furtado et al. [8], hence suggesting that future research is needed.

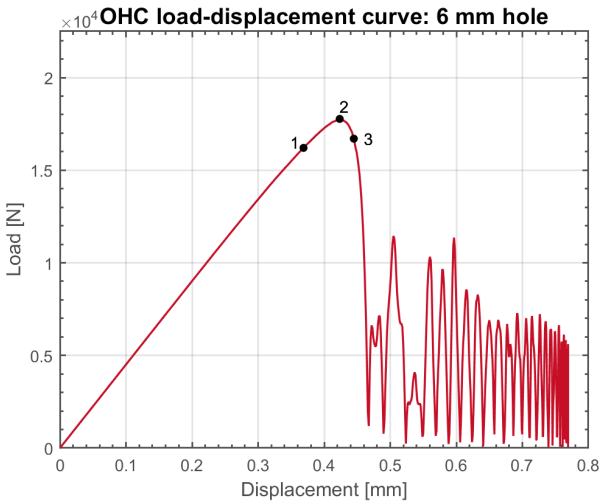
7.4.1.2 Damage onset & evolution history

Having analysed the numerical prediction for the resistance value, let us evaluate the initiation and progression of damage in order to ascertain the ultimate failure mode. Within the context of the size effects pertaining to OHC tests, this is ascertained for the baseline coupon ($d = 6$ mm) that presents general features across the considered sizes. To this purpose, we refer to Figure 7.20, wherein the load-displacement curve and the evolution of the damage variables throughout the loading history are provided.

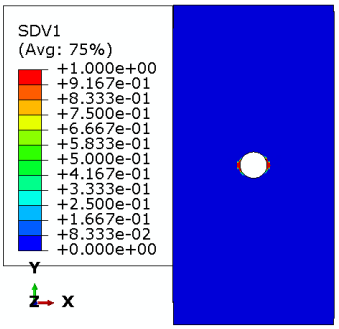
Commencing with the load-displacement curve depicted in Figure 7.20a, similarly to the OHT test, a linear behaviour up to failure is observed, which correlates well with the experimental findings, however, for this case, no load drops are registered. As for the damage evolution, similar conclusions to those derived between the PT and PC simulations may be inferred between the OHT and OHC tests to a larger degree. Whereas some effect of shear deformation in the $\pm$ 45° laminae was still noticeable for the PC models, with respect to the OHC ones, the influence of such mechanisms is much less pronounced. For instance, in terms of interlaminar damage, no free-edge delamination is observed between embedded 90 and -45° plies prior to the ultimate load point as shown in Figure 7.20b. Instead, throughout the entire loading history, interlaminar damage localises near the vicinity of the hole and, even after catastrophic failure, only a small degree of free-edge delamination is observed. Concerning intralaminar damage mechanisms, comparable conclusions may be drawn. Both shear and longitudinal fibre damage nucleate from the vicinity of the hole (Figures 7.20e and 7.20h) and extend across the width of the specimen, with only some degree of sub-critical propagation along a 45° fracture plane as shown in Figures 7.20f and 7.20i.

[2]It should be noted that the experimentally recorded size effects for OHC tests are much more pronounced than those registered for DENC models.

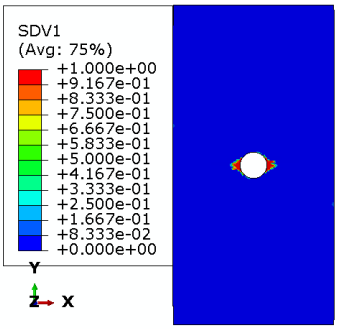
This is also true for transverse matrix damage in the embedded 90° plies. Damage only nucleates closer to the ultimate load point, perhaps as a consequence of stress concentrations induced by more pronounced fibre damage in the 0° laminae, and also propagates perpendicularly to the fibre direction near the hole as depicted in Figures 7.20l and 7.20m.



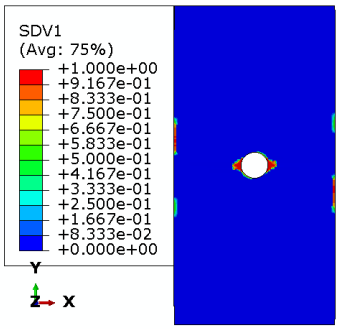
(a) Load-displacement curve



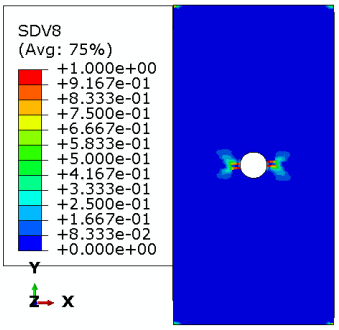
(b) Point 1: interface damage



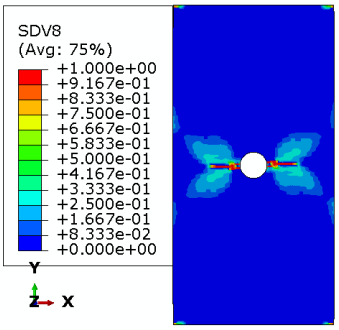
(c) Point 2: interface damage



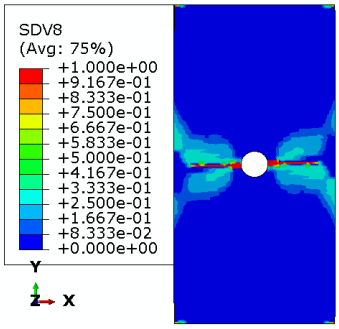
(d) Point 3: interface damage



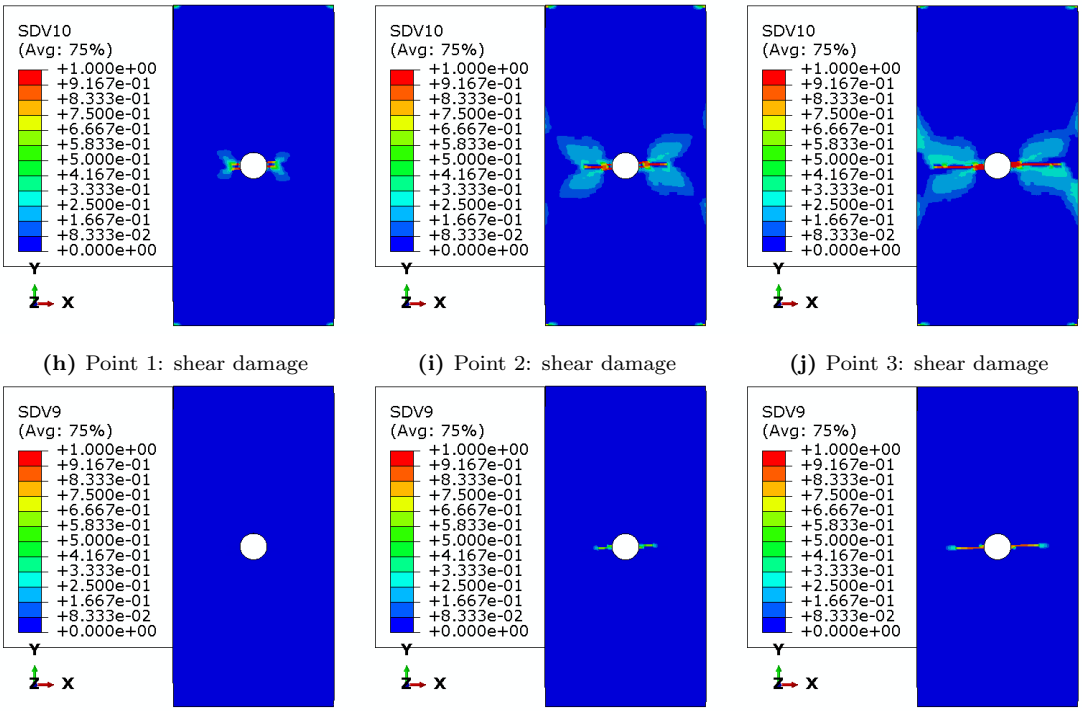
(e) Point 1: longitudinal fibre damage



(f) Point 2: longitudinal fibre damage



(g) Point 3: longitudinal fibre damage



(h) Point 1: shear damage **(i)** Point 2: shear damage **(j)** Point 3: shear damage

(k) Point 1: transverse matrix damage **(l)** Point 2: transverse matrix damage **(m)** Point 3: transverse matrix damage

Figure 7.20: Damage onset and evolution history for the $d = 6$ mm OHC test.

Overall, we thus deduce that catastrophic failure occurs as a result of localised damage within the 0° plies nucleating in the vicinity of the hole owing to the inherent stress concentrations introduced by such feature. Lastly, we highlight Figure 7.21, wherein the *post-mortem* specimen is depicted and a net-section fracture plane is observed, ultimately suggesting that shear mechanisms do not play such a significant role in OHC tests.



(a) Interface damage **(b)** Longitudinal damage



(c) Transverse damage **(d)** Shear damage

Figure 7.21: *Post-mortem* for the $d = 6$ mm OHC test.

7.4.2 Off-axis loading

7.4.2.1 Numerical prediction

Lastly, comparably to its OHT counterpart, with respect to the off-axis OHC tests, the same two sets of results must be assessed. To this purpose, we initially refer to Table 7.8, wherein the predictions pertaining to the original parameters are compiled. From the estimated strength values, it is identified that once more, only the 0 and 90° off-axis resistances are within the 10% threshold. Furthermore, it is now particularly significant to note that the prediction for 60° off-axis loading is below that pertaining to 90° off-axis loading, which does not agree with the experimental findings. On the other hand, following the aforesaid changes, as per Table 7.9, we note that, whilst the predictions for 30 and 60° off-axis loading remain outside the ideal threshold, significant improvements are noted. Most importantly, this becomes more prevalent with respect to the 60° off-axis loading test, whose estimated value substantially increased and is above the predicted resistance for 90° off-axis loading.

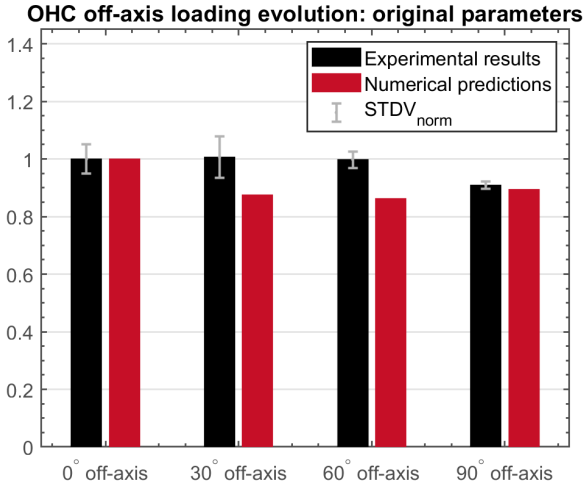
Table 7.8: Original numerical predictions obtained for the OHC off-axis loading tests.

	Experimental results		Numerical results	
	σ_{max}^{exp} [MPa]	STDV [MPa]	σ_{max}^{num} [MPa]	Relative error [%]
0°	275.6	14.0	260.9	-5.32
30°	278.4	19.7	228.1	-18.05
60°	276.0	7.9	225.3	-18.38
90°	251.5	3.3	233.1	-7.30

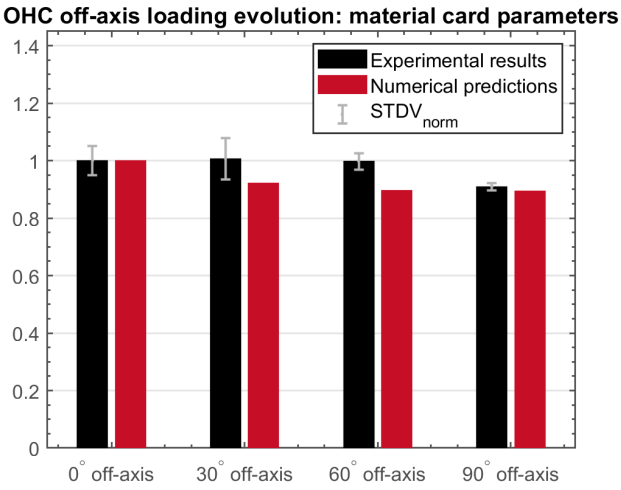
Table 7.9: Material card numerical predictions obtained for the OHC off-axis loading tests.

	Experimental results		Numerical results	
	σ_{max}^{exp} [MPa]	STDV [MPa]	σ_{max}^{num} [MPa]	Relative error [%]
0°	275.6	14.0	265.4	-3.70
30°	278.4	19.7	244.9	-12.02
60°	276.0	7.9	237.7	-13.87
90°	251.5	3.3	235.3	-6.46

Moreover, we highlight Figure 7.22, wherein the normalised predictions (derived with respect to 0° off-axis loading) are displayed for both the original and material card parameters and their evolution is comprehensively provided.



(a) Original parameters



(b) Material card parameters

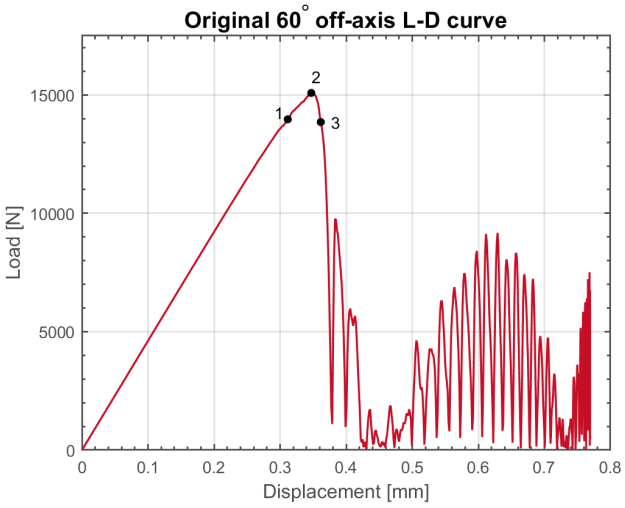
Figure 7.22: OHC off-axis loading evolution.

7.4.2.2 Damage onset & evolution history

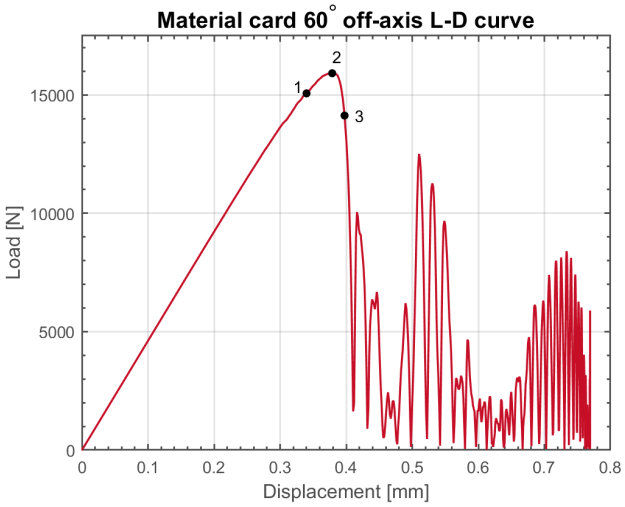
Besides the numerical prediction in terms of the resistance value, similarly to the methodology adopted for the OHT off-axis loading tests, comprehensively examining the initiation and progression of damage throughout the loading history for both the original and material card parameters arises as a matter of the utmost importance. This analysis is conducted for the 60° off-axis loaded coupon and we initially refer to Figure 7.23 for the load-displacement curves attained. Once more, simply by observing both plots, it is clear that damage onset and catastrophic failure are substantially postponed, which is to be expected. For the loading condition in study, the laminate effectively encompasses plies at 30 and 60°, which are particularly susceptible to delamination. Moreover, no lamina is oriented at 0°, effectively rendering the laminate softer and augmenting the impact of the shear response.

Additionally, in a manner akin to the previously stated observations no changes in the fundamental damage mechanisms or the final failure mode are identified between the parameters. A thorough analysis of figures Figure 7.24 and Figure 7.25 reveals that catastrophic failure emerges as a consequence of extensive shear damage and delamination in both instances. Moreover, the

progression of damage demonstrates comparable characteristics, nucleating near the vicinity of the hole in light of the stress concentrations introduced by such feature and extending across the width of the specimen until reaching the maximum failure load. Furthermore, even though the extent of damage related to this point differs significantly between the two scenarios (refer to Figure 7.24h and Figure 7.25h), this factor lies within the previously stated explanation related to the alterations made to the in-plane shear response. In spite of damage activating later, its evolution is more rapid, leading to higher damage extents (Figure 7.25h). The significantly elevated level of damage further promotes considerable interlaminar stress concentrations near the hole, thereby amplifying the extent of delamination (Figure 7.25b) in comparison to the original parameters (Figure 7.24b), even though the values for mode I and II fracture toughness were augmented.

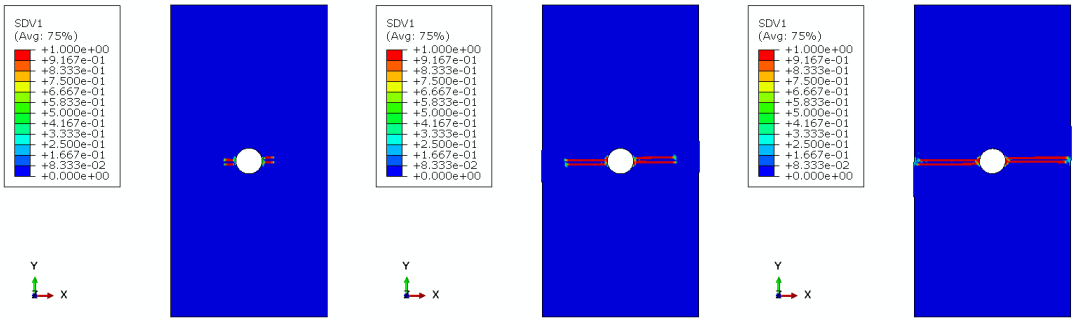


(a) Original parameters

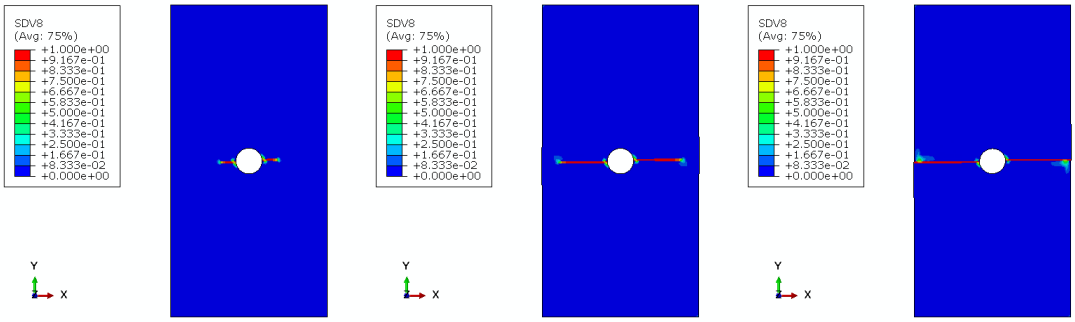


(b) Material card parameters

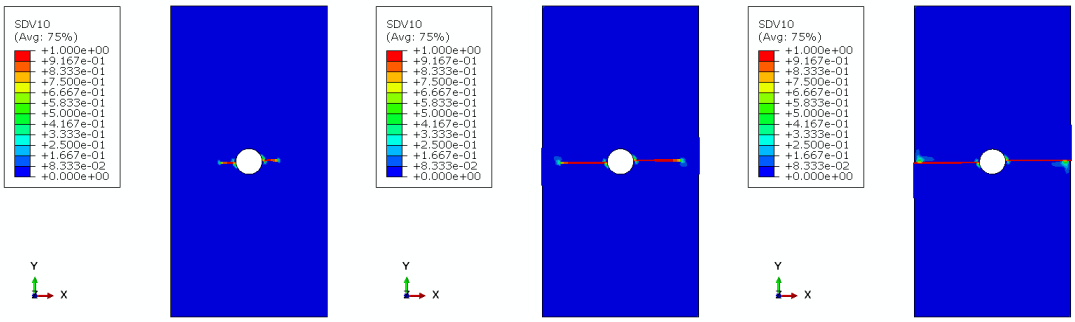
Figure 7.23: Comparison between the OHC 60° off-axis load-displacement curves obtained for the original and material card parameters.



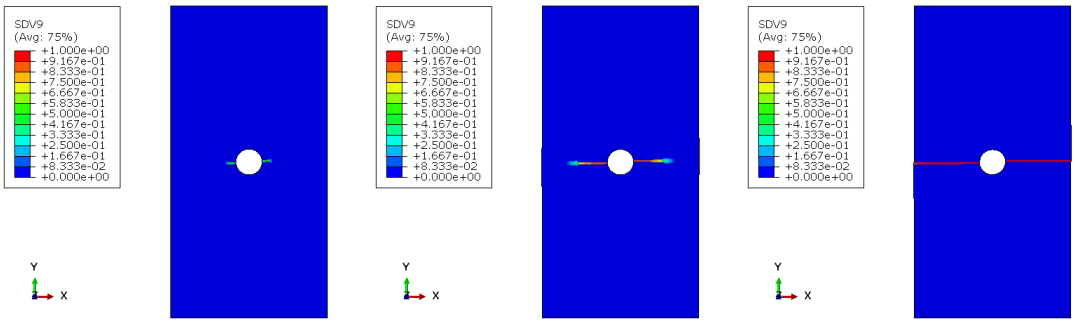
(a) Point 1: interface damage **(b)** Point 2: interface damage **(c)** Point 3: interface damage



(d) Point 1: longitudinal fibre damage **(e)** Point 2: longitudinal fibre damage **(f)** Point 3: longitudinal fibre damage



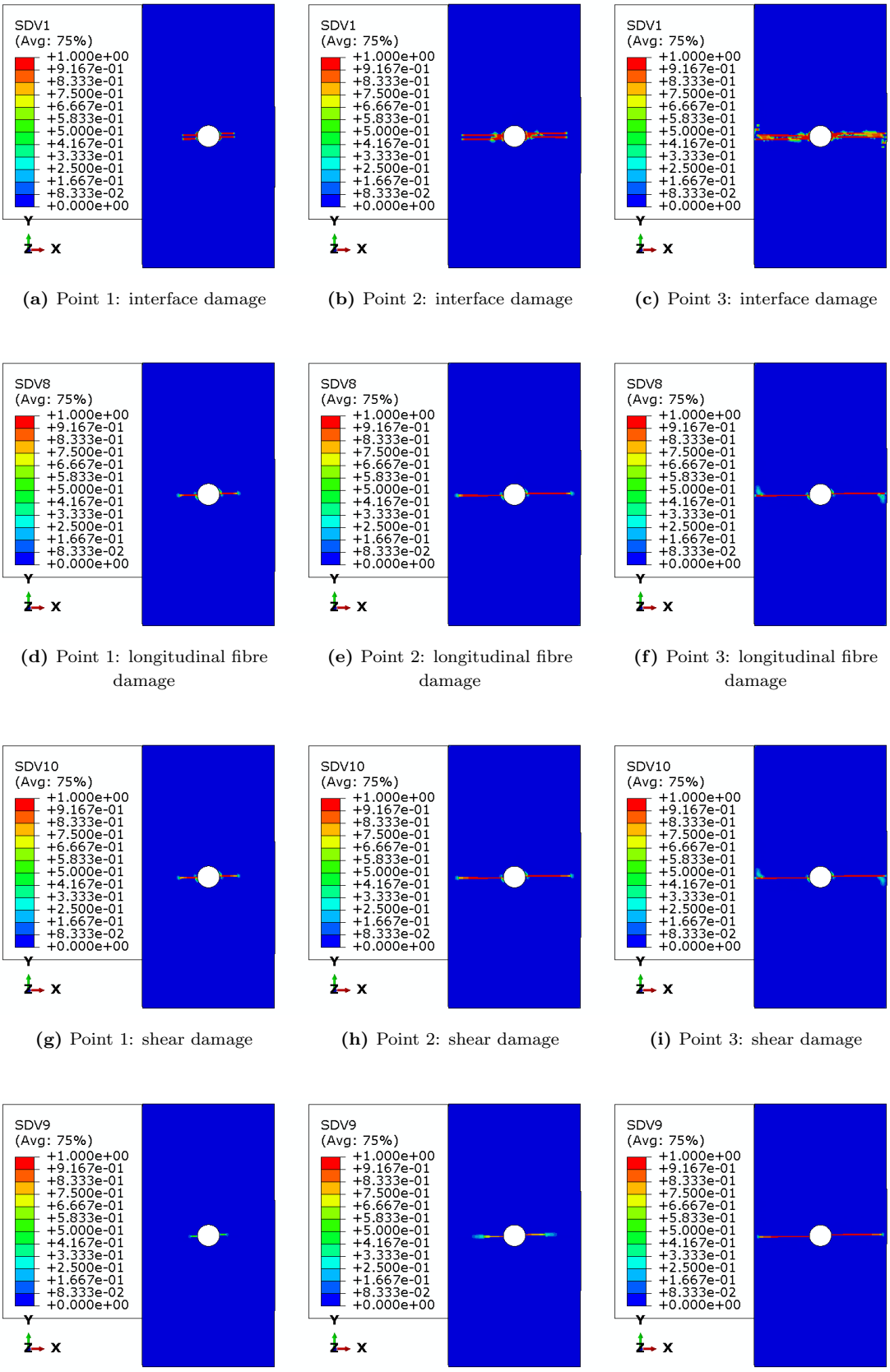
(g) Point 1: shear damage **(h)** Point 2: shear damage **(i)** Point 3: shear damage



(j) Point 1: transverse matrix damage **(k)** Point 2: transverse matrix damage **(l)** Point 3: transverse matrix damage

Figure 7.24: OHC 60° off-axis loading damage evolution for the original parameters.

7.4. Open-hole compression



(a) Point 1: interface damage **(b)** Point 2: interface damage **(c)** Point 3: interface damage

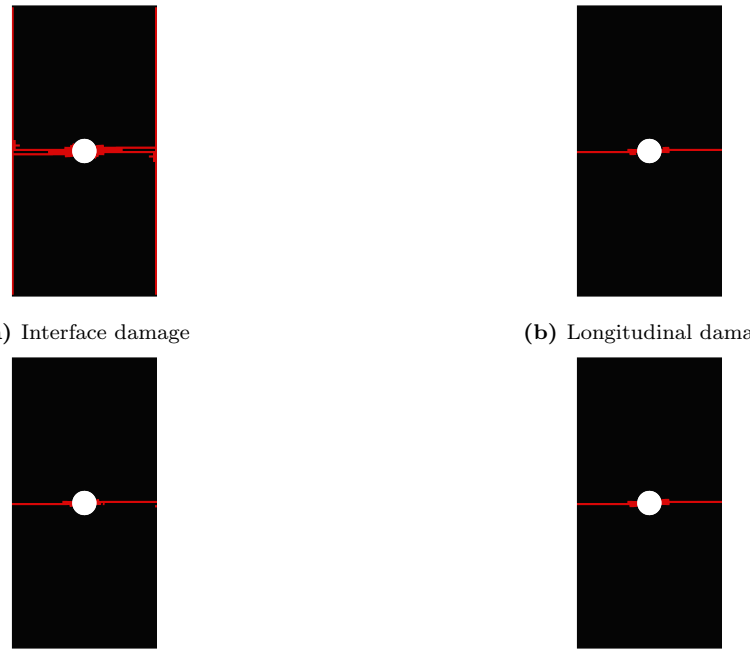
(d) Point 1: longitudinal fibre damage **(e)** Point 2: longitudinal fibre damage **(f)** Point 3: longitudinal fibre damage

(g) Point 1: shear damage **(h)** Point 2: shear damage **(i)** Point 3: shear damage

(j) Point 1: transverse matrix damage **(k)** Point 2: transverse matrix damage **(l)** Point 3: transverse matrix damage

Figure 7.25: OHC 60° off-axis loading damage evolution for the material card parameters.

Lastly, we highlight Figure 7.26, wherein the *post-mortem* specimen pertaining to the material card parameters is shown. We identify that the fracture plane is perpendicularly oriented in relation to the fibre direction, with a clean surface dominated by fibre fracture evident, which comes as a result of extensive delamination and shear damage that comprise the paramount fracture mechanisms. Once more, as such behaviour is to be expected, the validity of our approach is reaffirmed.



(a) Interface damage

(b) Longitudinal damage

(c) Transverse damage

(d) Shear damage

Figure 7.26: *Post-mortem* for the OHC 60° off-axis loading test: material card parameters.

Chapter 8

Low velocity impact tests

In this chapter, we seek to comprehensively explore the results attained with respect to the low velocity impact tests. To this purpose, we start by presenting the conducted penalty stiffness sensitivity study. Subsequently, the results pertaining to each of the assessed impact energies are explored. Lastly, remarks regarding the noted limitations are given, including potential alternatives to address some of the ascertained limitations and future research that must be performed.

8.1 Penalty stiffness sensitivity study

In the context of the low velocity impact simulations, it initially becomes pivotal, as per Soto et al. [80, 124], to conduct a penalty stiffness sensitivity study to ascertain its optimal value. This parameter may significantly compromise the inherent compliance of our system, thereby leading to incorrect elastic response predictions. To mitigate such impact, the penalty stiffness ought to be set as large as feasible, seeing as the material is perfectly bonded prior to crack nucleation. However, it is important to consider that, when dealing with explicit simulations, the influence of penalty stiffness is not restricted to the accuracy, i.e., it additionally affects the computational performance via the STI. Consequently, the determination of the optimal value for this parameter must take into account this factor.

To this purpose, two distinct penalty stiffness values (2.5×10^4 [1] and 1.0×10^5) were analysed for the 13.4J impact energy and, in order to establish the most effective one, the elastic response pertaining to each case was contrasted, as depicted in Figure 8.1. From the obtained results, we infer that augmenting the penalty stiffness value does not yield any substantial discernible differences in the response of the laminate prior to the onset of delamination when compared to the lower one. Conversely, the higher value significantly increases the computational time and, thereby, the smaller penalty stiffness, i.e., 2.5×10^4, was herein adopted for the LVI simulations.

[1] It should be noted that this comprises the recommended value by Soto et al. [80, 124].

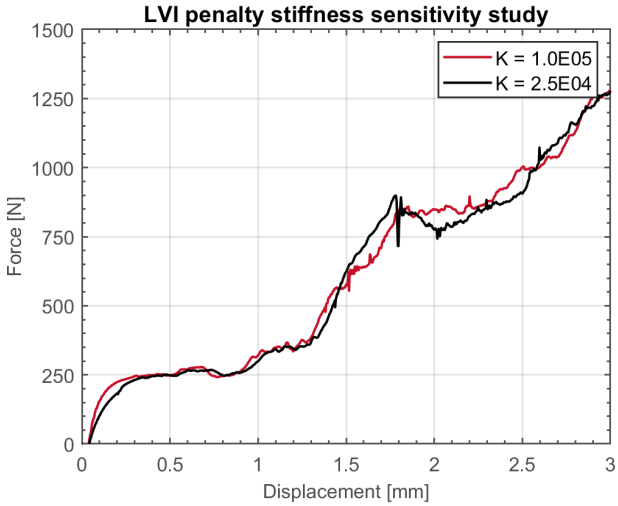


Figure 8.1: LVI penalty stiffness sensitivity study.

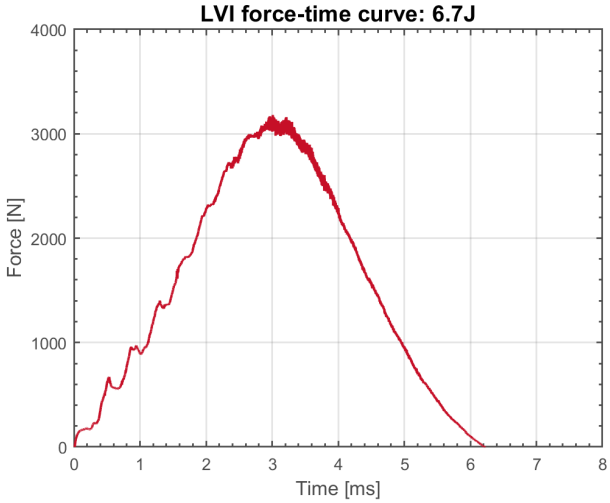
8.2 Impact energy: 6.7J

Concerning the impact results themselves, let us begin with the lowest energy assessed, i.e., 6.7J. To this purpose, we highlight Table 8.1 wherein the maximum values obtained pertaining to the maximum force, F_{max}, the maximum displacement, U_{max}, and the dissipated energy, E_{dis}, are shown and compared with the experimental ones. Reviewing the attained predictions, we infer that, although the estimated force and displacement are within the stipulated 10% threshold, the dissipated energy significantly differs from the experimental result. This discrepancy was also noted by Soto et al. [80, 124], however, within our work, it may come as a consequence of inadequate damage representation, as will be discussed in the following sections.

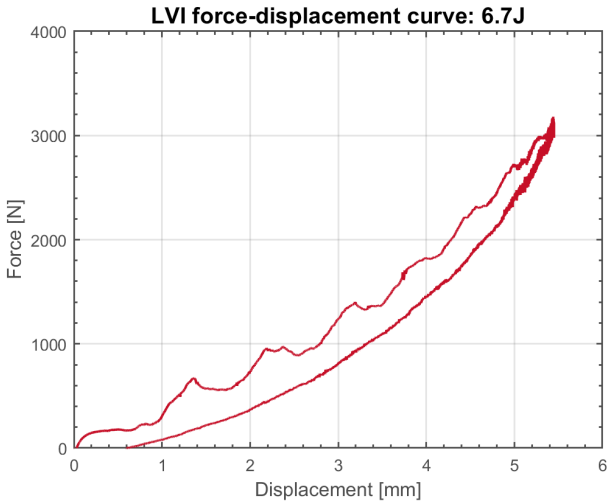
Table 8.1: Numerical predictions obtained for the LVI test: 6.7J impact energy.

	Experimental results	Numerical results (Relative error [%])
F_{max} [N]	3357.29	3179.94 (-5.28)
U_{max} [mm]	5.109	5.45 (+6.69)
E_{dis} [J]	1.36	1.09 (-19.76)

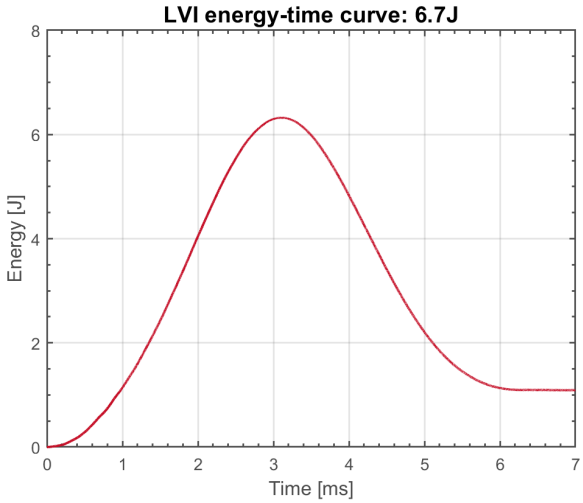
In addition, for a more comprehensive representation of the force-time, force-displacement, and energy-displacement curves, we focus on Figure 8.2. The attained evolution for such variables agrees with the experimental results. No significant amount of damage is expected, which is confirmed by the shapes of Figures 8.2a and 8.2b, wherein no load drops are discernible.



(a) Force-time



(b) Force-displacement



(c) Energy-time

Figure 8.2: Numerical LVI results: 6.7J impact energy.

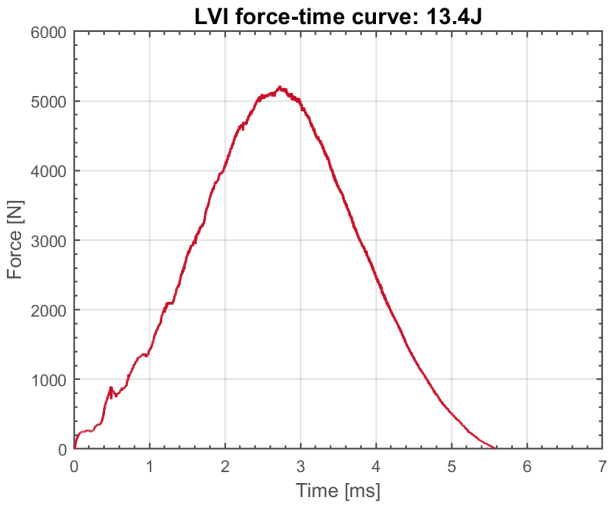
8.3 Impact energy: 13.4J

On the other hand, substantially different conclusions may be inferred for the 13.4J impact. Analysing the attained predictions depicted in Table 8.2, we identify that, whilst the maximum displacement is accurately captured, the relative errors pertaining to the maximum force and dissipated energy significantly increase over the ideal threshold. Such discrepancies, particularly for the former, have also been observed by Soto et al. [80, 124] and thus do not immediately constitute pressing concerns.

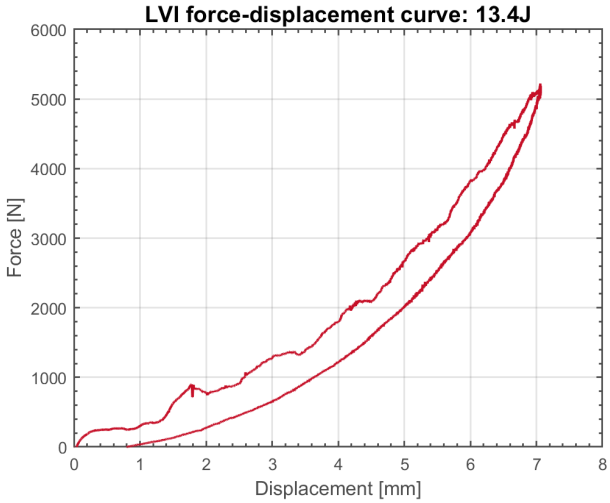
Table 8.2: Numerical predictions obtained for the LVI test: 13.4J impact energy.

	Experimental results	Numerical results (Relative error [%])
F_{max} [N]	4505.82	5222.2 (+15.90)
U_{max} [mm]	6.74	7.07 (+4.83)
E_{dis} [J]	5.788	2.13 (-63.16)

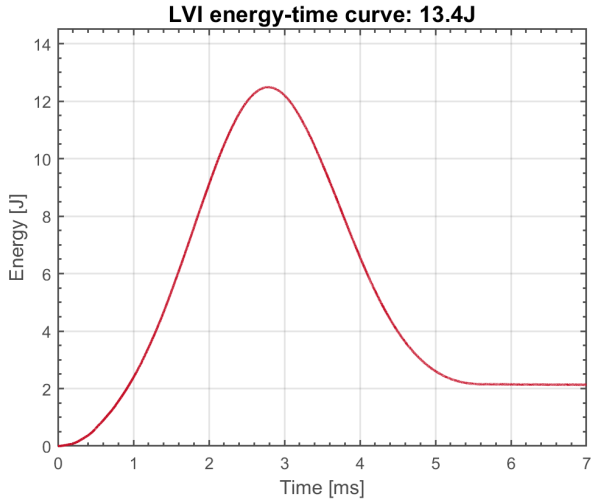
Notwithstanding, analysing the obtained curves illustrated in Figure 8.3, the reason for such differences becomes evident. Whilst, from the experimental findings, the 13.4J impact is within the barely visible impact damage, BVID, range, no load drops are, once more, noted in the force-time and force-displacement history (refer to respectively Figures 8.3a and 8.3b), suggesting that the damage onset and evolution is not accurately captured. Accordingly, the dissipated energy remarkably decreases, seeing as the extent of damage is severely underestimated and, consequently, there is not an adequate amount of energy dissipated in the form of inter- and intralaminar damage mechanisms.



(a) Force-time



(b) Force-displacement



(c) Energy-time

Figure 8.3: Numerical LVI results: 13.4J impact energy.

8.4 Impact energy: 20.1J

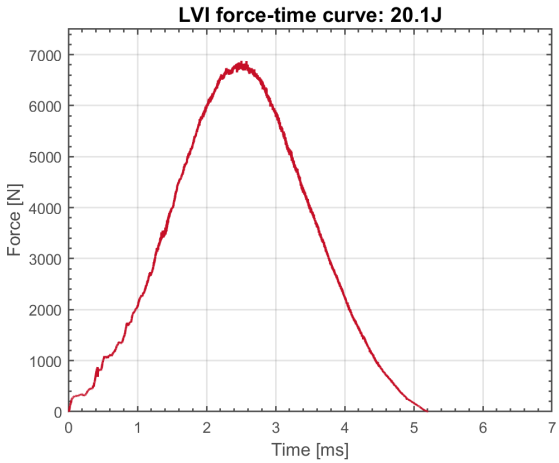
Moreover, increasing the impact energy even further to 20.1J, these findings become abundantly clear. Once more, the maximum force and dissipated energy (refer to Table 8.3) fall outside the admissible threshold, however the relative errors exponentially increased when compared to the 6.7 and 13.4J impacts.

Table 8.3: Numerical predictions obtained for the LVI test: 20.1J impact energy.

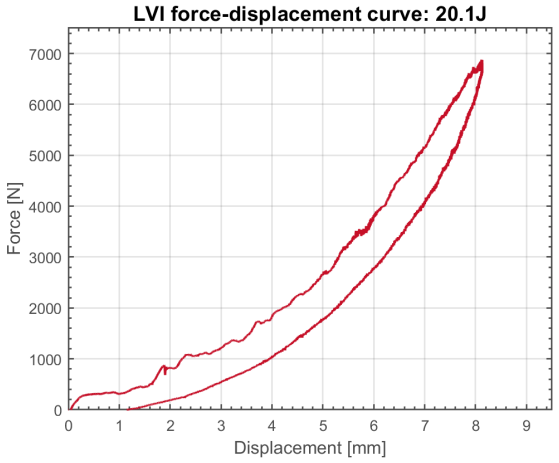
	Experimental results	Numerical results (Relative error [%])
F_{max} [N]	4701.19	6880 (+46.35)
U_{max} [mm]	8.36	8.13 (-2.71)
E_{dis} [J]	13.56	3.60 (-73.47)

In addition, this impact energy, as per the experimental findings, is anticipated to induce a

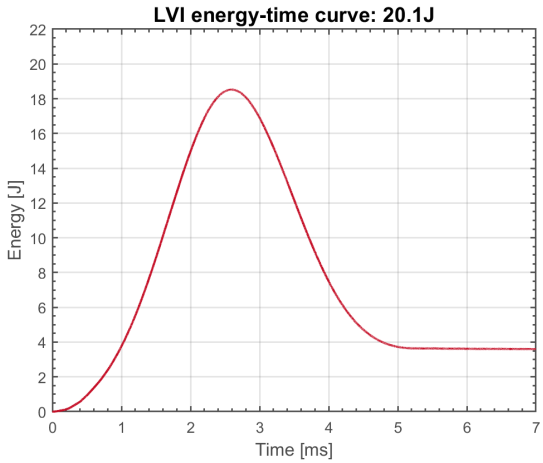
significant amount of visible damage to both the front and back faces of the laminate. Thereby, the experimental curves exhibit significant load drops, which are not identified in Figure 8.4. Overall, the attained numerical results thus suggest that damage onset and evolution within the LVI simulations is not accurately captured.



(a) Force-time



(b) Force-displacement



(c) Energy-time

Figure 8.4: Numerical LVI results: 20.1J impact energy.

Ultimately, the obtained results suggest that the adopted modelling methodology does not constitute a valid approach for the material system in study. Is is postulated that this may be attributed to the nominal thickness of the bulk laminate that is considerably smaller than the one employed by Soto et al. [80, 124] in the validation of this strategy. The use of conventional shell elements does not accurately represent the through-thickness stress components, that may play a key role in the damage onset and evolution of our material. Thereby, it is theorised that future research must be conducted, e.g., resorting to solid elements that do not assume a plane-stress state and that could potentially overcome the observed limitations. Furthermore, although not performed (in light of the poor results), ascertaining the compression after impact behaviour further comprises a matter of the utmost importance.

Part V

Conclusions & future work

Chapter 9

Conclusions and future work

Within the present thesis, a modelling and simulation strategy pertaining to a novel material system of interest, i.e., uni-directional non-crimp fabric laminates, was implemented, in an attempt to understand its validity and ascertain its material card. In this chapter, we thereby aim to present the main conclusions inferred from our work. The main aspects to retain from the state-of-the-art, the numerical methodology adopted and the corresponding results are presented. Lastly, given that the present thesis is just a first step in the understanding of modelling and simulation approaches of unidirectional non-crimp fabric laminates, future work that needs to be carried out in light of the derived conclusions is explored.

9.1 Conclusions

As the paradigm within the aeronautical industry shifts from maximising performance at all costs to more cost-conscious solutions, concerns arise with unidirectional prepreg laminates that comprise the standard composite materials in the sector. These material systems, albeit providing insurmountable in-plane mechanical properties, not merely represent a significant expense in the certification of composite structures, but also boast poor interlaminar fracture toughness, rendering them highly susceptible to impact damage. To mitigate this, extensive research has been devoted to textile fabric reinforcements that present remarkable potential for reduced manufacturing costs and enhanced out-of-plane properties. Whilst woven reinforcements comprised the initial focus of textile-based research initiatives, such systems inherently boast high degrees of crimp, which severely compromises their in-plane performance. As a result, in recent years, non-crimp fabric composites have emerged as an interesting solution. These materials, being defined by several unidirectional laminae stacked in varying orientations and held in place via through-thickness knitting, lack gross crimp. Although a small amount of waviness is inevitably induced by the presence of the stitching yarns resulting in a reduction of the in-plane properties, such differences are negligible, which has been extensively substantiated in the available literature. In addition, non-crimp fabric laminates have been proven to boast superior impact resistance. Thereby, such materials are able to balance the dichotomy between high in-plane performance of unidirectional straight fibres with appealing characteristics such as improved impact resistance, reduced manufacturing costs, enhanced drapeability and ease of handling offered by woven preforms. In addition, if unidirectional non-crimp fabrics are to be stacked, such as the laminate herein studied, a direct alternative to unidirectional prepreg materials is achieved, which could be swiftly integrated within the sector to reap the numerous benefits offered by this reinforcement architecture.

Notwithstanding, their successful introduction further hinges on structural substantiation campaigns, commonly triggered when a novel composite material emerges. These are typically conducted in accordance with a *building-block approach*, wherein numerous small, less expensive specimens are tested and analysed under simple loading scenarios to generate design allowables prior to evaluating the material response for more complex structural details. Testing alone is nevertheless extremely costly and time-consuming and, consequently, the development of accurate analytical and numerical models to aid, or potentially supplant, this methodology is of the utmost importance. To this purpose, knowledge concerning the damage mechanisms that must be captured is paramount, which, for composite materials, are inherently more intricate in regard to their traditional metallic counterparts. Prior to rupture, laminated materials commonly manifest multiple localised failures at lower length-scales that grow and accumulate throughout the loading process, ultimately resulting in catastrophic failure. Accordingly, seeing as damage onset and evolution in composite materials comprises an intricate multi-scale event in nature, an adequate definition of the modelling scale is of particular significance within the realm of composite materials. Whilst smaller scales allow for a more refined description of discrete damage events, the corresponding micromechanical models are prohibitively complex in light of the currently available computational power. As a result, mesomechanical models predicated on a ply-by-ply discretization, wherein laminate layers are regarded as the fundamental homogeneous building blocks and imperfections and variabilities inherent to lower scales are neglected, become more suitable in ascertaining the damage and failure of the bulk laminate. Within a meso-mechanics approach, interlaminar damage is commonly modelled by means of cohesive zone models, which are based on accurate kinematic descriptions of the fracture process and governed by a traction-separation law that dictates delamination onset and complete decohesion. On the other hand, intralaminar damage is typically represented within a continuum damage mechanics framework aimed at predicting the behaviour of a material, or more specifically, its response in the presence of damage initiating at some stress state and propagating as the applied loads increase the stresses in the material. Accordingly, several continuum damage mechanics models resorting to several failure criteria to predict damage onset and evolution have been proposed in the available literature and extensively validated for a myriad of loading conditions and modelling strategies, including un-notched, open-hole, low velocity impact and compression after impact. Whilst this approach has naturally been extended to non-crimp laminates, most of the available models are predicated upon representative volume elements, with only a sparse amount of work being conducted on a ply-by-ply discretization.

Thereby, there is a clear knowledge gap in the available literature pertaining to the mesoscale modelling and simulation of unidirectional non-crimp laminates based on such approaches. To this purpose, our work aimed to assess the validity of commonly used mesoscale modelling strategies for representative coupons, namely un-notched, open-hole and low velocity impact specimens. In addition, to achieve this, seeing as no material card has been reported for these composites, we further sought to ascertain the required computational parameters through the standard methodology, i.e., double-edge notched coupons.

The numerical model herein adopted consisted of a composite damage model implemented within a finite element framework capable of predicting intra- and interlaminar damage mechanisms. The intralaminar continuum mechanics damage model was applied to every specimen and aligned itself with an extensively validated approach furnishing a means to accurately predict longitudinal, transverse and shear mechanisms. The formulation of the model was based on the definition of the complementary free energy density within the framework of the thermodynamics of irreversible processes, as a function of damage variables associated with each intralaminar failure mode. Furthermore, damage onset and progression were modelled via damage activation

and evolution functions respectively. Being predicated upon a previously proposed model, a 3D invariant based failure criterion for fibre kinking and engineering solutions were incorporated to capture the effects of through-thickness stresses. Moreover, to ensure the precision of the material properties, *in-situ* strengths are considered. Concerning the representation of interlaminar damage, two strategies were used. For the un-notched, open-hole and double-edge notched coupons, an interlaminar cohesive zone model predicated upon a mode-dependent penalty stiffness was considered to more accurately capture mixed-mode loading conditions and combined with a coulomb friction law postulated in literature to account for friction effects. Concerning the low velocity impact simulations, built-in Abaqus/Explicit cohesive surfaces were employed, with damage onset and propagation being respectively governed by a quadratic traction criterion and the Benzeggagh Kenane criteria. Furthermore, to attain accurate results without significantly increasing the computational efforts, the penalty stiffness and surface density were determined by means of recommended methods in literature. Furthermore, although a ply-by-ply discretization was used in the finite element models, two modelling approaches were once more considered. For the unnotched, open-hole and double-edge notched coupons, solid elements were considered, whereas for low velocity impact tests, conventional shell elements were selected.

The numerical results pertaining to the material card identification process show a remarkable correlation with the experimental ones. For the double-edge notched tension models, several bilinear cohesive laws were assessed, with the composite damage model accurately capturing the alterations made to the computational parameters that govern the stress-strain response. As expected, changing the inflection point displayed more pronounced effects for the smaller specimens, whereas for the larger ones, this was achieved by varying the portion of dissipated energy in the first part of the softening behaviour. Moreover, for our final iteration, the predicted resistance values and slope of the size effect law were within the standard 10% threshold commonly used in the aeronautical industry. The damage onset and evolution were accurately predicted as well, with damage nucleating within the vicinity of the notch owing to the stress concentrations introduced by such features, prior to its extension across the width of the specimen up until catastrophic failure. On the other hand, concerning the double-edge notched compression tests, it was identified that the originally proposed longitudinal compression plateau cohesive law was not able to accurately capture the experimental results. Seeing as changes could solely be conducted for the inflection point, the estimated strength pertaining to larger specimens did not show significant differences throughout the tested resistance values and inflection point parameters. As a result, although precise representations of the slope of the size effect law were obtained, such softening response was disregarded, seeing as the relative errors associated with the predicted resistance values were above 10%. In light of these results, a bi-linear stress-strain response akin to that for longitudinal tension was postulated, which allows for a larger degree of control over the dissipated fracture toughness and, consequently, over the resistance values for the larger specimens. As expected, with these alterations, we were able to obtain predicted resistance and slope values that were within the ideal threshold. With respect to the damage evolution, damage nucleated near the notch and extended across the width of the specimen up until catastrophic failure. In addition, as expected for compressive loads, delamination was more prominent for these simulations. Overall, the results obtained confirmed the validity of the adopted modelling methodology and a consistent material card was calibrated.

Concerning the validation tests and starting with the plain tension specimen, the numerical strength obtained correlated well with the experimental value. Although discrepancies were noted in the damage evolution, i.e., a non-linear response was observed prior to catastrophic failure, these differences agree with the alterations made to the delamination and in-plane shear response. Given

the softer nature of the laminate studied herein, shear mechanisms play a larger role in inducing stress concentrations in the 0° plies and postponing its onset yielded the non-linear behaviour. This was confirmed by analysing the failure mode of a coupon prior to the aforementioned changes, seeing as, in both cases, fracture mainly propagates along a 45° failure plane, with the primary difference being the rate at which damage evolves. Furthermore, catastrophic failure occurs as a consequence of fibre damage in the 0° plies, which is to be expected for this test, thus corroborating the validity of the modelling approach. For the plain compression tests, both the strength value and damage history were accurately captured. Catastrophic failure arose as a consequence of localised damage within the 0° plies as expected and a net-section fracture plane was identified, suggesting a more brittle behaviour. This may be explained by the cohesive law adopted that, in its essence, allows for less energy dissipation, resulting in a more brittle material. In regard to the open-hole tests, a constant limitation was identified pertaining to the representation of size effects in both tension and compression. Still, whilst improvements were noticed for tensile loads by altering the computational parameters, this effect was more prevalent in compression, seeing as no comparable conclusions could be inferred. The damage onset and evolution history was accurately captured for both cases, with damage nucleating near the hole and extending across the width of the specimen. Furthermore, similarly to what was identified in plain tension/compression tests, shear mechanisms played a more pressing role for open-hole tension coupons, i.e., fibre fracture propagated along a 45° failure plane, whereas in compression, a net-section fracture plane was once more detected. Focusing on off-axis loading, although initially premature failure was detected for 30 and 60°, following alterations to the delamination and in-plane shear response, improvements in the resistance evolution were evident. These changes were aimed at postponing shear damage and delamination that play a more prominent role for such loading conditions. Thereby, no changes in the critical damage mechanisms were expected, which was confirmed by comparing the response prior to and after such changes. The foremost differences laid within the activation of critical shear mechanisms and the rate at which it evolved, evidenced by the higher extent of damage noticed for the ultimate failure load pertaining to the revised responses. However, it should be noted that the values obtained in 30 and 60° off-axis compression still fell outside the 10% threshold. Ultimately, the results obtained affirmed the validity of the adopted modelling methodology.

With respect to the low velocity impact simulations, poor results were nonetheless observed throughout the considered impact energies. Whilst for the smaller energy value tested, the maximum force and displacement are within the admissible threshold, augmenting the impact energy resulted in exponential growth in the relative errors identified. It was noted that, although significant amounts of damage were expected for these simulations, this did not occur. In fact, even for a visible impact damage energy of 20.1J, the evolution of the force-time and force-displacement curves did not exhibit discernible load drops, i.e., no substantial damage nucleated as a result of the impact event. Ultimately, this not only contributed to increasing the maximum force but also to accordingly reduce the amount of dissipated energy. The extent of damage is severely underestimated and, consequently, there is not an adequate amount of energy dissipated in the form of inter- and intralaminar damage mechanisms.

Overall, we were able to ascertain the material card parameters and the results obtained support the validation of the adopted modelling methodology for the in-plane coupons. Notwithstanding, some limitations were identified, which future research should focus on and that are highlighted in the following section.

9.2 Future work

In spite of the significant advancements achieved in the modelling and simulation of unidirectional non-crimp fabric laminates, some work must still be performed to reliably accomplish this task. Focusing on the hole size effects, some limitations in their prediction were noticed for both the tensile and compressive tests. Although improvements were made for the former, no comparable conclusions were inferred for the latter. Although these were accurately captured in the material card identification process, the ascertained computational parameters did not yield accurate hole size effect predictions. Thereby, revisions into the standard methodology to identify the softening laws may be necessary, particularly for the double-edge notched compression tests that, in recent years, have been improved. In addition, although the off-axis tensile response was precisely captured, research is still required to address the shortcoming observed in compression in terms of the resistance values that fell outside the 10% threshold for 30° and 60° off-axis loading. Among the possible solutions, the use of ply-oriented meshes may be attempted.

Lastly, and most importantly, severe limitations were observed for the out-of-plane impact response. Extensive research is thereby required, which may encompass the use of alternative modelling strategies. Within our work, it was postulated that conventional shell elements tied with surface elements may not be able to precisely reproduce the through-thickness response for such thin laminates and, consequently, the use of solid elements, by not assuming a plane stress state, could show great promise. Moreover, in light of the poor results obtained for the low velocity impact simulations, no compression after impact tests were performed. Given the importance of these tests within the aeronautical industry, evaluating their response further comprises a matter of utmost importance that any future research into our material system should focus on.

References

[1] Melro AR. Analytical and numerical modelling of damage and fracture of advanced composites. Ph.D. thesis; University of Porto; 2011.

[2] Gay D. Composite materials: design and applications. CRC press; 2022.

[3] Arteiro A. Technology development and structural mechanics of composites built of spread tow thin-ply technology. Master's thesis; University of Porto; 2012.

[4] Rana S, Fangueiro R. Advanced composite materials for aerospace engineering: processing, properties and applications. Woodhead Publishing; 2016.

[5] Herakovich CT. Mechanics of composites: a historical review. Mechanics Research Communications 2012;41:1–20.

[6] Tsai SW. Theory of Composites Design. Composites Design Group, Department of Aeronautics & Astronautics, Stanford University; 2008.

[7] Camanho PP, Dávila CG, Pinho ST, Remmers JJ. Mechanical response of composites; vol. 10. Springer Science & Business Media; 2008.

[8] Furtado C, Catalanotti G, Arteiro A, Gray P, Wardle B, Camanho P. Simulation of failure in laminated polymer composites: Building-block validation. Composite Structures 2019;226:111168.

[9] Arteiro A, Catalanotti G, Reinoso J, Linde P, Camanho PP. Simulation of the mechanical response of thin-ply composites: from computational micro-mechanics to structural analysis. Archives of Computational Methods in Engineering 2019;26:1445–87.

[10] Mouritz AP. Introduction to aerospace materials. Elsevier; 2012.

[11] Lepore MA, Ferrante L, Sanguigno L, Maligno AR. A non-crimp fabric mechanical characterization for the production of aerospace components. Material Design & Processing Communications 2021;3(5):e222.

[12] Galos J. Thin-ply composite laminates: a review. Composite Structures 2020;236:111920.

[13] Tessitore N, Riccio A. A novel fem model for biaxial non-crimp fabric composite materials under tension. Computers & structures 2006;84(19-20):1200–7.

[14] Baker AA. Composite materials for aircraft structures. AIAA; 2004.

[15] Lomov SV. Non-crimp fabric composites: manufacturing, properties and applications. Elsevier; 2011.

[16] Horrocks AR, Anand SC. Handbook of technical textiles. 2nd ed.; Elsevier; 2016.

[17] Bibo G, Hogg P, Kemp M. Mechanical characterisation of glass-and carbon-fibre-reinforced composites made with non-crimp fabrics. Composites science and technology 1997;57(9-10):1221–41.

[18] Ferreira LMM. Study of the behaviour of non-crimp fabric laminates by 3D finite element model. Ph.D. thesis; Universidad de Sevilla, Escuela Técnica Superior de Arquitectura; 2012.

[19] Suratkar AP. Damage in non-crimp fabric carbon fiber reinforced epoxy composites under various mechanical loading conditions. Ph.D. thesis; University of Western Ontario; 2022.

[20] Bibo G, Hogg P, Backhouse R, Mills A. Carbon-fibre non-crimp fabric laminates for cost-effective damage-tolerant structures. Composites Science and Technology 1998;58(1):129–43.

[21] Sasikumar A, Trias D, Costa J, Blanco N, Orr J, Linde P. Impact and compression after impact response in thin laminates of spread-tow woven and non-crimp fabrics. Composite Structures 2019;215:432–45.

[22] Petriccione A, Annicchiarico D, Antonucci V, Giordano M, Riccio A, Scaramuzzino F, et al. A stiffness volume averaging based approach to model non-crimp fabric reinforced composites. Composites science and technology 2012;72(2):360–9.

[23] Curtis P, Bishop SM. An assessment of the potential of woven carbon fibre-reinforced plastics for high performance applications. Composites 1984;15(4):259–65.

[24] Carvelli V, Lomov SV. Fatigue of textile composites. Elsevier; 2015.

[25] Boisse P. Advances in composites manufacturing and process design. Woodhead Publishing; 2015.

[26] Truong T. The mechanical performance and damage of multiaxial multiply carbon fabric reinforced composites. Department of metallurgy and applied materials science, Faculty of engineering sciences, Katholieke Universiteit Leuven 2005;.

[27] Lundström T. The permeability of non-crimp stitched fabrics. Composites Part A: Applied Science and Manufacturing 2000;31(12):1345–53.

[28] Nordlund M, Lundstrom TS. Numerical study of the local permeability of non-crimp fabrics. Journal of composite materials 2005;39(10):929–47.

[29] Kunze E, Böhm R, Geller S, Gude M. Experimental analysis of process induced draping effects in textile preforms. In: AIP Conference Proceedings. 1; AIP Publishing LLC; 2019, p. 020012.

[30] Bersee HE. Composite aerospace manufacturing processes. Encyclopedia of Aerospace Engineering 2010;.

[31] Irving P, Soutis C. Polymer composites in the aerospace industry. Woodhead Publishing; 2019.

[32] Advani SG, Hsiao KT. Manufacturing techniques for polymer matrix composites (PMCs). Elsevier; 2012.

[33] Scott F, Heath R. Resin transfer moulding for civil aircraft manufacture. SAMPE European 1992;:235–47.

[34] Schwartz M. Innovations in materials manufacturing, fabrication, and environmental safety. CRC press; 2010.

[35] Kuruvilla J, Oksman K, Gejo G, Wilson R, Appukuttan S. Fiber Reinforced Composites: Constituents, Compatibility, Perspectives and Applications. Woodhead Publishing; 2021.

[36] Dexter HB, Hasko GH. Mechanical properties and damage tolerance of multiaxial warp-knit composites. Composites Science and Technology 1996;56(3):367–80.

[37] Arteiro A, Catalanotti G, Xavier J, Camanho P. Notched response of non-crimp fabric thin-ply laminates. Composites Science and Technology 2013;79:97–114.

[38] Arteiro A, Catalanotti G, Xavier J, Linde P, Camanho P. A strategy to improve the structural performance of non-crimp fabric thin-ply laminates. Composite Structures 2018;188:438–49.

[39] Furtado C, Tavares RP, Arteiro A, Xavier J, Linde P, Wardle BL, et al. Effects of ply thickness and architecture on the strength of composite sub-structures. Composite Structures 2021;256:113061.

[40] Hogg P, Ahmadnia A, Guild F. The mechanical properties of non-crimped fabric-based composites. Composites 1993;24(5):423–32.

[41] Beier U, Fischer F, Sandler JK, Altstädt V, Weimer C, Buchs W. Mechanical performance of carbon fibre-reinforced composites based on stitched preforms. Composites Part A: Applied science and manufacturing 2007;38(7):1655–63.

[42] Vallons K, Adolphs G, Lucas P, Lomov SV, Verpoest I. The influence of the stitching pattern on the internal geometry, quasi-static and fatigue mechanical properties of glass fibre non-crimp fabric composites. Composites Part A: Applied Science and Manufacturing 2014;56:272–9.

[43] Wilhelmsson D, Gutkin R, Edgren F, Asp L. An experimental study of fibre waviness and its effects on compressive properties of unidirectional NCF composites. Composites Part A: Applied Science and Manufacturing 2018;107:665–74.

[44] Dransfield KA, Jain LK, Mai YW. On the effects of stitching in CFRPs—I. mode I delamination toughness. Composites Science and Technology 1998;58(6):815–27.

[45] Godbehere A, Irving P. Non crimped fabrics versus prepreg CFRP composites - a comparison of mechanical performance. In: FRC '94 - International Conference on Fibre Reinforced Composites. University of Newcastle upon Tyne; 1994, p. 6–9.

[46] Bhudolia SK, Kam KK, Perrotey P, Joshi SC. Effect of fixation stitches on out-of-plane response of textile non-crimp fabric composites. Journal of Industrial Textiles 2019;48(7):1151–66.

[47] Quan D, Alderliesten R, Dransfeld C, Murphy N, Ivanković A, Benedictus R. Enhancing the fracture toughness of carbon fibre/epoxy composites by interleaving hybrid meltable/non-meltable thermoplastic veils. Composite Structures 2020;252:112699.

[48] García-Rodríguez S, Costa J, Rankin K, Boardman R, Singery V, Mayugo J. Interleaving light veils to minimise the trade-off between mode-I interlaminar fracture toughness and in-plane properties. Composites Part A: Applied Science and Manufacturing 2020;128:105659.

[49] Mendikute J, Baskaran M, Aretxabaleta L, Aurrekoetxea J. Effect of voids on the impact properties of non-crimp fabric carbon/epoxy laminates manufactured by liquid composite moulding. Composite Structures 2022;297:115922.

[50] Megson THG. Aircraft structures for engineering students. Butterworth-Heinemann; 2016.

[51] Turon A, Costa J, Maimi P, Trias D, Mayugo J. A progressive damage model for unidirectional fibre-reinforced composites based on fibre fragmentation. part I: Formulation. Composites Science and Technology 2005;65(13):2039–48.

[52] Maimí P, Camanho P, Mayugo J, Dávila C. A continuum damage model for composite laminates: Part I – constitutive model. Mechanics of Materials 2007;39(10):897–908.

[53] Herman M, Leon-Dufour JL, Peters P, Laurin F, Turon A, Arteiro A, et al. Evaluation of advanced approaches based on continuum damage mechanics for composite failure analysis: status and way forward. In: 25^{th} International Conference on Composites, Porto, Portugal. 2019,.

[54] Lopes C, González C, Falcó O, Naya F, LLorca J, Tijs B. Multiscale virtual testing: the roadmap to efficient design of composites for damage resistance and tolerance. CEAS Aeronautical Journal 2016;7:607–19.

[55] Furtado C, Pereira L, Tavares RP, Salgado M, Otero F, Catalanotti G, et al. A methodology to generate design allowables of composite laminates using machine learning. International Journal of Solids and Structures 2021;233:111095.

[56] Vallmajó O, Cózar I, Furtado C, Tavares R, Arteiro A, Turon A, et al. Virtual calculation of the B-value allowables of notched composite laminates. Composite Structures 2019;212:11–21.

[57] Arteiro A, Gray P, Camanho P. Simulation of edge impact and compression after edge impact in CFRP laminates. Composite Structures 2020;240:112018.

[58] Handbook-MIL-HDBK M. 17-3f: Composite materials handbook, volume 3-polymer matrix composites materials usage, design, and analysis. US Department of Defense 2002;:3.

[59] Camanho PP, Maimí P, Dávila C. Prediction of size effects in notched laminates using continuum damage mechanics. Composites science and technology 2007;67(13):2715–27.

[60] Laux T, Gan KW, Tavares RP, Furtado C, Arteiro A, Camanho PP, et al. Modelling damage in multidirectional laminates subjected to multi-axial loading: Ply thickness effects and model assessment. Composite Structures 2021;266:113766.

[61] Davila C, Camanho P. Failure criteria for FRP laminates in plane stress. Report NASA. Tech. Rep.; TM-2003-212663; 2003.

[62] Song K, Li Y, Rose C. Continuum damage mechanics models for the analysis of progressive failure in open-hole tension laminates. In: 52nd AIAA/ASME/ASCE/AHS/ASC Structures, Structural Dynamics and Materials Conference 19th AIAA/ASME/AHS Adaptive Structures Conference 13t. 2011, p. 1861.

[63] Pinho ST, Dávila CG, Camanho PP, Iannucci L, Robinson P. Failure models and criteria for frp under in-plane or three-dimensional stress states including shear non-linearity. Tech. Rep.; 2005.

[64] Ladevèze P, Lubineau G, Violeau D, Marsal D. A computational damage micromodel for laminate composites. In: IUTAM Symposium on Multiscale Modelling of Damage and Fracture Processes in Composite Materials: Proceedings of the IUTAM Symposium held in Kazimierz Dolny, Poland, 23–27 May 2005. Springer; 2006, p. 1–12.

[65] Dávila CG, Rose CA, Iarve EV. Modeling fracture and complex crack networks in laminated

composites. In: Mathematical methods and models in composites. World Scientific; 2014, p. 297–347.

[66] Camanho P, Hallett S. Numerical modelling of failure in advanced composite materials. Woodhead Publishing; 2015.

[67] Iarve EV, Gurvich MR, Mollenhauer DH, Rose CA, Dávila CG. Mesh-independent matrix cracking and delamination modeling in laminated composites. International journal for numerical methods in engineering 2011;88(8):749–73.

[68] Beaumont PW, Soutis C, Hodzic A. The structural integrity of carbon fiber composites: fifty years of progress and achievement of the science, development, and applications. Springer; 2016.

[69] Forghani A, Shahbazi M, Zobeiry N, Poursartip A, Vaziri R. 6 - An overview of continuum damage models used to simulate intralaminar failure mechanisms in advanced composite materials. In: Camanho PP, Hallett SR, editors. Numerical Modelling of Failure in Advanced Composite Materials. Woodhead Publishing Series in Composites Science and Engineering; Woodhead Publishing. ISBN 978-0-08-100332-9; 2015, p. 151–73.

[70] Camanho PP, Arteiro A. Analysis Models for Polymer Composites Across Different Length Scales. Cham: Springer International Publishing. ISBN 978-3-319-46120-5; 2017, p. 199–279.

[71] Arteiro A, Catalanotti G, Melro A, Linde P, Camanho P. Micro-mechanical analysis of the in situ effect in polymer composite laminates. Composite Structures 2014;116:827–40.

[72] Varandas L, Arteiro A, Bessa M, Melro A, Catalanotti G. The effect of through-thickness compressive stress on mode ii interlaminar crack propagation: A computational micromechanics approach. Composite Structures 2017;182:326–34.

[73] Varandas L, Catalanotti G, Arteiro A, Melro AR, Falzon B. 11 - Micromechanical modelling of interlaminar damage propagation and migration. In: Van Paepegem W, editor. Multi-Scale Continuum Mechanics Modelling of Fibre-Reinforced Polymer Composites. Woodhead Publishing Series in Composites Science and Engineering; Woodhead Publishing. ISBN 978-0-12-818984-9; 2021, p. 307–47.

[74] González C, LLorca J. Mechanical behavior of unidirectional fiber-reinforced polymers under transverse compression: Microscopic mechanisms and modeling. Composites Science and Technology 2007;67(13):2795–806.

[75] Peerlings R, de Borst R, Brekelmans W, Geers M. Localisation issues in local and nonlocal continuum approaches to fracture. European Journal of Mechanics - A/Solids 2002;21(2):175–89.

[76] Benvenuti E. A regularized XFEM framework for embedded cohesive interfaces. Computer Methods in Applied Mechanics and Engineering 2008;197(49):4367–78.

[77] Turon A, González E, Sarrado C, Guillamet G, Maimí P. Accurate simulation of delamination under mixed-mode loading using a cohesive model with a mode-dependent penalty stiffness. Composite Structures 2018;184:506–11.

[78] Turon A, Camanho PP, Costa J, Dávila C. A damage model for the simulation of delamination in advanced composites under variable-mode loading. Mechanics of materials 2006;38(11):1072–89.

[79] Chang JB, Goyal VK, Klug JC, Rome JI. Composite structures damage tolerance analysis methodologies. Tech. Rep.; 2012.

[80] Soto Masip A, et al. Development of efficient numerical models for the simulation of low velocity impact and compression after impact on composite structures. Ph.D. thesis; Universitat de Girona; 2018.

[81] Abdel-Monsef S, Tijs B, Renart J, Turon A. Accurate simulation of delamination under mixed-mode loading using a multilinear cohesive law. Engineering Fracture Mechanics 2023;284:109233.

[82] Dugdale DS. Yielding of steel sheets containing slits. Journal of the Mechanics and Physics of Solids 1960;8(2):100–4.

[83] Barenblatt GI. The mathematical theory of equilibrium cracks in brittle fracture. Advances in applied mechanics 1962;7:55–129.

[84] Carreras L, Guillamet G, Quintanas-Corominas A, Renart J, Turon A. Mesoscale modelling of delamination using the cohesive zone model approach. In: Multi-Scale Continuum Mechanics Modelling of Fibre-Reinforced Polymer Composites. Elsevier; 2021, p. 555–77.

[85] Hillerborg A, Modéer M, Petersson PE. Analysis of crack formation and crack growth in concrete by means of fracture mechanics and finite elements. Cement and concrete research 1976;6(6):773–81.

[86] Camanho PP, Davila CG, De Moura M. Numerical simulation of mixed-mode progressive delamination in composite materials. Journal of composite materials 2003;37(16):1415–38.

[87] Sarrado C, Turon A, Costa J, Renart J. An experimental analysis of the fracture behavior of composite bonded joints in terms of cohesive laws. Composites Part A: Applied Science and Manufacturing 2016;90:234–42.

[88] Monsef SA, Ortega A, Turon A, Maimí P, Renart J. An efficient method to extract a mode I cohesive law for bonded joints using the double cantilever beam test. Composites Part B: Engineering 2019;178:107424.

[89] Monsef SA, Pérez-Galmés M, Renart J, Turon A, Maimí P. The influence of mode II test configuration on the cohesive law of bonded joints. Composite Structures 2020;234:111689.

[90] Tvergaard V, Hutchinson JW. The relation between crack growth resistance and fracture process parameters in elastic-plastic solids. Journal of the Mechanics and Physics of Solids 1992;40(6):1377–97.

[91] Goyal VK, Johnson ER, Davila CG. Irreversible constitutive law for modeling the delamination process using interfacial surface discontinuities. Composite Structures 2004;65(3-4):289–305.

[92] Airoldi A, Dávila CG. Identification of material parameters for modelling delamination in the presence of fibre bridging. Composite Structures 2012;94(11):3240–9.

[93] Dávila CG, Rose CA, Camanho PP. A procedure for superposing linear cohesive laws to represent multiple damage mechanisms in the fracture of composites. International Journal of Fracture 2009;158(2):211–23.

[94] Benzeggagh ML, Kenane M. Measurement of mixed-mode delamination fracture toughness of unidirectional glass/epoxy composites with mixed-mode bending apparatus. Composites science and technology 1996;56(4):439–49.

[95] Turon A, Camanho P, Costa J, Renart J. Accurate simulation of delamination growth under mixed-mode loading using cohesive elements: Definition of interlaminar strengths and elastic stiffness. Composite structures 2010;92(8):1857–64.

[96] Sørensen BF, Goutianos S, Jacobsen TK. Strength scaling of adhesive joints in polymer–matrix composites. International Journal of Solids and Structures 2009;46(3-4):741–61.

[97] Harper PW, Sun L, Hallett SR. A study on the influence of cohesive zone interface element strength parameters on mixed mode behaviour. Composites Part A: Applied Science and Manufacturing 2012;43(4):722–34.

[98] Talreja R. Damage development in composites: mechanisms and modelling. The Journal of strain analysis for engineering design 1989;24(4):215–22.

[99] Bažant ZP, Oh BH. Crack band theory for fracture of concrete. Matériaux et construction 1983;16:155–77.

[100] Maimí P, Camanho P, Mayugo J, Dávila C. A continuum damage model for composite laminates: Part II – computational implementation and validation. Mechanics of Materials 2007;39(10):909–19.

[101] Germain N, Besson J, Feyel F. Composite layered materials: Anisotropic nonlocal damage models. Computer Methods in Applied Mechanics and Engineering 2007;196(41-44):4272–82.

[102] Soden P, Hinton M, Kaddour A. A comparison of the predictive capabilities of current failure theories for composite laminates. Composites science and technology 1998;58(7):1225–54.

[103] Hinton M, Soden P. Predicting failure in composite laminates: the background to the exercise. Composites Science and Technology 1998;58(7):1001–10.

[104] Hinton M, Kaddour A, Soden P. Evaluation of failure prediction in composite laminates: background to 'part B' of the exercise. Composites Science and Technology 2002;62(12-13):1481–8.

[105] Soden P, Kaddour A, Hinton M. Recommendations for designers and researchers resulting from the world-wide failure exercise. In: Failure criteria in fibre-reinforced-polymer composites. Elsevier; 2004, p. 1223–51.

[106] Hinton M, Kaddour A, Soden P. Evaluation of failure prediction in composite laminates: background to 'part C' of the exercise. Composites Science and Technology 2004;64(3-4):321–7.

[107] Davila CG, Camanho PP, Rose CA. Failure criteria for FRP laminates. Journal of Composite Materials 2005;39(4):323–45.

[108] Pinho S, Iannucci L, Robinson P. Physically-based failure models and criteria for laminated fibre-reinforced composites with emphasis on fibre kinking: Part I: Development. Composites Part A: Applied Science and Manufacturing 2006;37(1):63–73.

[109] Pinho S, Iannucci L, Robinson P. Physically based failure models and criteria for laminated fibre-reinforced composites with emphasis on fibre kinking. part II: Fe implementation. Composites Part A: Applied Science and Manufacturing 2006;37(5):766–77.

[110] Catalanotti G, Camanho P, Marques A. Three-dimensional failure criteria for fiber-reinforced laminates. Composite Structures 2013;95:63–79.

[111] Camanho P, Arteiro A, Melro A, Catalanotti G, Vogler M. Three-dimensional invariant-based failure criteria for fibre-reinforced composites. International Journal of Solids and Structures 2015;55:92–107.

[112] Ladeveze P, LeDantec E. Damage modelling of the elementary ply for laminated composites. Composites science and technology 1992;43(3):257–67.

[113] Matzenmiller A, Lubliner J, Taylor RL. A constitutive model for anisotropic damage in fiber-composites. Mechanics of materials 1995;20(2):125–52.

[114] Kachanov L. Introduction to continuum damage mechanics; vol. 10. Springer Science & Business Media; 1986.

[115] Lemaitre J, Desmorat R, Sauzay M. Anisotropic damage law of evolution. European Journal of Mechanics-A/Solids 2000;19(2):187–208.

[116] Maimí P. Modelización constitutiva y computacional del daño y la fractura en materiales compuestos. Ph.D. thesis; Universitat de Girona, Dept. d'Enginyeria Mecànica; 2006.

[117] Bessa M. Meso-mechanical model of the structural integrity of advanced composite laminates. Master's thesis; University of Porto; 2010.

[118] González E, Maimí P, Turon A, Camanho P, Renart J. Simulation of delamination by means of cohesive elements using an explicit finite element code. Computers, Materials & Continua (CMC) 2009;9(1):51.

[119] Lopes C, Camanho P, Gürdal Z, Maimí P, González E. Low-velocity impact damage on dispersed stacking sequence laminates. part II: Numerical simulations. Composites Science and Technology 2009;69(7-8):937–47.

[120] González Juan EV, et al. Simulation of interlaminar and intralaminar damage in polymer-based composites for aeronautical applications under impact loading. Universitat de Girona; 2011.

[121] González E, Maimí P, Camanho P, Turon A, Mayugo J. Simulation of drop-weight impact and compression after impact tests on composite laminates. Composite Structures 2012;94(11):3364–78.

[122] Lopes C, Sádaba S, González C, Llorca J, Camanho P. Physically-sound simulation of low-velocity impact on fiber reinforced laminates. International Journal of Impact Engineering 2016;92:3–17.

[123] González E, Maimí P, Martín-Santos E, Soto A, Cruz P, De La Escalera FM, et al. Simulating drop-weight impact and compression after impact tests on composite laminates using conventional shell finite elements. International Journal of Solids and Structures 2018;144:230–47.

[124] Soto A, González E, Maimí P, Mayugo J, Pasquali P, Camanho P. A methodology to simulate low velocity impact and compression after impact in large composite stiffened panels. Composite Structures 2018;204:223–38.

[125] Sasikumar A, Costa J, Trias D, Llobet J, Cózar I, Turon A, et al. A virtual testing based search for optimum compression after impact strength in thin laminates using ply-thickness hybridization and unsymmetrical designs. Composites Science and Technology 2020;196:108188.

[126] Moran P, Liu X, Shih C. Kink band formation and band broadening in fiber composites under compressive loading. Acta metallurgica et Materialia 1995;43(8):2943–58.

[127] Gouskos D, Iannucci L. A failure model for the analysis of cross-ply non-crimp fabric (NCF) composites under in-plane loading: Experimental & numerical study. Engineering Fracture Mechanics 2022;271:108575.

[128] Asp L, Marklund E, Varna J, Olsson R. Multiscale modelling of non-crimp fabric composites. In: ASME International Mechanical Engineering Congress and Exposition; vol. 45196. American Society of Mechanical Engineers; 2012, p. 581–90.

[129] Marklund E, Asp L, Olsson R. Transverse strength of unidirectional non-crimp fabric composites: Multiscale modelling. Composites Part B: Engineering 2014;65:47–56.

[130] Drapier S, Wisnom MR. Finite-element investigation of the compressive strength of non-crimp-fabric-based composites. Composites Science and Technology 1999;59(8):1287–97.

[131] Drapier S, Wisnom MR. A finite-element investigation of the interlaminar shear behaviour of non-crimp-fabric-based composites. Composites Science and Technology 1999;59(16):2351–62.

[132] Edgren F, Asp LE. Approximate analytical constitutive model for non-crimp fabric composites. Composites Part A: Applied Science and Manufacturing 2005;36(2):173–81.

[133] Oakeshott J, Iannucci L, Robinson P. Development of a representative unit cell model for bi-axial ncf composites. Journal of composite materials 2007;41(7):801–35.

[134] Tserpes K, Labeas G. Mesomechanical analysis of non-crimp fabric composite structural parts. Composite Structures 2009;87(4):358–69.

[135] Ferreira LM, Graciani E, París F. Three dimensional finite element study of the behaviour and failure mechanism of non-crimp fabric composites under in-plane compression. Composite Structures 2016;149:106–13.

[136] Edgren F, Asp LE, Joffe R. Failure of NCF composites subjected to combined compression and shear loading. Composites Science and Technology 2006;66(15):2865–77.

[137] Wilhelmsson D, Talreja R, Gutkin R, Asp L. Compressive strength assessment of fibre composites based on a defect severity model. Composites Science and Technology 2019;181:107685.

[138] Molker H, Wilhelmsson D, Gutkin R, Asp LE. Orthotropic criteria for transverse failure of non-crimp fabric-reinforced composites. Journal of Composite Materials 2016;50(18):2445–58.

[139] Shipsha A, Hallström S, Burman M. Effect of stacking sequence and bundle waviness in quasi-isotropic NCF composites subjected to compression. Composites Part B: Engineering 2019;178:107423.

[140] Yin H, Iannucci L. An experimental and finite element investigation of compression-after-impact (CAI) behaviour of biaxial carbon fibre non-crimp-fabric (NCF) based composites. Composite Structures 2022;281:115057.

[141] Alfano G, Sacco E. Combining interface damage and friction in a cohesive-zone model. International Journal for Numerical Methods in Engineering 2006;68(5):542–82.

[142] Catalanotti G, Furtado C, Scalici T, Pitarresi G, Van Der Meer F, Camanho P. The effect of through-thickness compressive stress on mode II interlaminar fracture toughness. Composite Structures 2017;182:153–63.

[143] Malvern LE. Introduction to the Mechanics of a Continuous Medium. Monograph; 1969.

[144] Camanho PP, Dávila CG, Pinho ST, Iannucci L, Robinson P. Prediction of in situ strengths and matrix cracking in composites under transverse tension and in-plane shear. Composites Part A: Applied Science and Manufacturing 2006;37(2):165–76.

[145] Dvorak GJ, Laws N. Analysis of progressive matrix cracking in composite laminates II. first ply failure. Journal of composite materials 1987;21(4):309–29.

[146] Mi Y, Crisfield M, Davies G, Hellweg H. Progressive delamination using interface elements. Journal of composite materials 1998;32(14):1246–72.

[147] ASTM D7136/D7136M-15. Standard Test Method for Measuring the Damage Resistance of a Fiber-Reinforced Polymer Matrix Composite to a Drop-Weight Impact Event. West Conshohocken, PA, USA: ASTM International; 2015.